UCLouvain
Faculté des bioingénieurs
Institute of Condensed Matter and Nanosciences

Synthesis of bulk and supported catalysts by humid air gliding arc plasma

Thèse soutenue en vue de l'obtention du grade de docteur
en sciences agronomiques et ingénierie biologique par

Fanny Hanon

Composition du Jury

Pr. Eric Gaigneaux (UCLouvain/IMCN) – Promoteur
Pr. Arnaud Delcorte (UCLouvain/IMCN) – Président
Pr. Sophie Hermans (UCLouvain/IMCN)
Pr. Michel Devillers (UCLouvain/IMCN)
Pr. Rony Snyders (UMons/ChIPS)
Pr. Renaud Cousin (Université du Littoral Côte d'Opale/UCEIV)

Louvain-la-Neuve
Septembre 2024

IMCN

"Science never solves a problem without creating ten more."

George Bernard Shaw

Remerciements

Après ces 4 années de thèse (+ 1 « année bonus » en mémoire), je tiens à remercier toutes les personnes qui m'ont entourée durant ce parcours (qui fut parfois du combattant).

Je souhaite tout d'abord remercier mon promoteur, Eric Gaigneaux, pour m'avoir permis de réaliser mon mémoire dans son laboratoire, et pour avoir ensuite suffisamment cru en moi pour me laisser tenter le FRIA afin de poursuivre une thèse sur le même sujet. Merci de m'avoir donné la liberté d'orienter le sujet à ma manière, d'avoir fait preuve d'une rapidité inégalable pour tout type de corrections nécessaires, d'avoir su me remonter le moral quand j'en avais parfois besoin, et d'avoir été présent tout au long de cette thèse, quelle qu'en soit la raison.

Merci aux membres du jury d'avoir pris le temps de lire ma thèse (ce qui, vu le nombre de pages, n'était pas une mince affaire) et pour avoir initié une discussion enrichissante ainsi que suggéré des modifications pertinentes lors de ma défense privée (et certainement publique aussi). Merci à Sophie Hermans et Rony Snyders de m'avoir aidé à mieux comprendre et réorienter ma recherche lors de l'épreuve de confirmation. Merci également à Sophie Hermans et Michel Devillers pour avoir pris de leur temps pour répondre à mes (nombreuses) questions tout au long de ma thèse, pour les cours particuliers express de chimie, et pour avoir accepté d'écrire ensemble des articles qui, sans vous, auraient été bien moins intéressants.

Un grand merci au FNRS pour m'avoir accordé une bourse FRIA, qui m'a permis de mener à bien cette thèse.

Un immense merci aux permanents, sans qui le laboratoire ne tournerait pas aussi bien et ne serait pas un endroit aussi agréable pour y travailler. Merci à Nathalie de prendre si bien soin des petits chercheurs et sans qui nos commandes n'arriveraient surement jamais, probablement perdues quelque part avant même d'arriver au magasin Lavoisier. Merci également à Jean-Charles, qui parvient à résoudre n'importe quel problème mécanique ou informatique en moins de 6 centièmes de seconde. Merci également à Pierre et Delphine pour les formations machines et pour leur présence précieuse face à mes nombreuses questions lors de leur utilisation ! Et merci à Fabio pour avoir réalisé mes dernières analyses ICP juste avant la remise de ma thèse, et ce, malgré un timing serré !

Merci à François, toujours présent pour répondre à nos questions, même les plus stupide, et pour contribuer à maintenir une ambiance si joviale au labo. Soyons honnêtes, sans toi, je (et probablement d'autres) n'aurais pas eu autant de motivation pour faire une thèse. Plus personnellement, merci pour les petites discussions dans le train qui rendaient le trajet beaucoup moins ennuyeux, les découvertes culturelles comme « la Bombe » de « Bistouille », les innombrables verres et pauses cafés partagés et les nombreux fous rires. Tu as fait en sorte qu'il soit toujours un plaisir de venir au laboratoire durant ces 5 années !

Merci à Hippolyte pour son soutien indéfectible jusqu'à la fin de ma thèse. Tu as été là dans les moments de joies comme dans les moments de doutes et de stress. Sans ta présence tout au long de ce parcours, ces années auraient été bien moins agréables !

Merci à tous les membres du laboratoire qui ont contribué à faire de cet endroit un lieu où il faisait bon vivre (et non pas juste travailler). À tel point que, même lorsque je pouvais travailler de chez moi, je faisais quand même le trajet juste pour vous voir.

Merci au groupe des « Jeudredi », présents depuis mon mémoire et pendant une bonne partie de la thèse, à savoir Hippolyte, Marty, Denis et Margot. Merci pour ces jeudredi (surtout en période de covid), les petits week-ends à la mer ou dans les Ardennes, les nombreux verres en terrasse, qu'il pleuve ou qu'il vente (de nouveau, covid oblige) et les souvenirs de conférences.

Pour la seconde moitié de ma thèse, un grand merci au groupe de mémorants ayant débarqués en septembre 2022 (Figure R.2). Vous êtes arrivés avec une super entente entre vous, qui a raisonné dans l'ambiance au labo. Merci tout particulièrement à Juliette, Corentin, Doudou, Oscar, Mehdi, Noé et Alexis (je sais vous êtes arrivés l'année d'avant mais on va vous mettre ici), pour être resté, tout d'abord, mais aussi d'avoir créé une nouvelle équipe de « bouts-entrains » avec qui il est presque impossible de ne pas rire au quotidien !

Merci également aux meubles du laboratoire que je n'ai pas encore eu l'occasion de citer. Merci à Cédric, qui m'a permis de voir l'assistant que j'ai eu sous un autre œil, à Damien, qui m'a permis de voir le professeur que j'ai eu sous un autre œil, et à Guillaume (qui finira peut-être un jour par terminer son post-doc) pour avoir gentiment accepté de faire du badminton et de l'escalade avec moi, malgré mon niveau médiocre.

Merci donc à tout le monde pour les nombreux fous rires qui me motivaient à ne jamais rater une pause midi à la cafétéria ! Vous avez été ma 2e maison et vous manquerez surement à mon futur quotidien !

Un merci spécial à 3 filles incroyables que j'ai eu l'occasion de rencontrer durant cette thèse, à savoir Juliette, Sophie et Héloïse. Votre personnalité et votre humour si uniques ont rendu ces années, et ma vie en général, beaucoup plus agréables ! Vous êtes devenues des amies que je n'aurais jamais pensé trouver !

Merci également au groupe de République Dominicaine, devenus une bande d'amis dont je ne pensais pas avoir besoin. Merci tout particulièrement à Lucas pour m'avoir intégrée au groupe, mais aussi pour toutes les soirées films, sushi, indiens, et les matinées escalade. Ces moments étaient ce qu'il me fallait pour me changer les idées.

Un immense merci à ma meilleure amie, Camille, présente dans ma vie depuis si longtemps et d'être toujours là pour moi, peu importe la raison. Merci d'être toi, de trouver les mots justes ou de faire ce qu'il faut pour que je me sente bien !

Merci à mon papa, sans qui je ne serais jamais arrivée au bout de ce chemin. Tu m'as fait confiance quand je me suis lancée dans ces études, du début à la fin, et tu as tout fait pour que ce parcours puisse être réalisé, aussi long et semé d'embûches soit-il.

Merci aux nombreux.ses psys que j'ai consulté au fil de mes études (dont Marty), qui ont clairement été indispensables au maintien de ma santé mentale parfois un peu bancale.

Merci à mon réacteur plasma et benzène de ne pas avoir rendu l'âme avant la fin de ma thèse. Chaque problème me donnait l'impression que j'allais signer leur arrêt de mort, mais vous avez toujours fini par redémarrer à chaque fois (merci à François et Jean-Charles pour avoir contribué à leur santé).

Et enfin, merci à mon chat, Typhon, sans qui mon quotidien serait beaucoup moins agréable. Merci d'être cette petite boule de poils capable de me divertir sans rien faire, et d'être toujours là pour mes séances séries-thé du soir (Fig.R1).

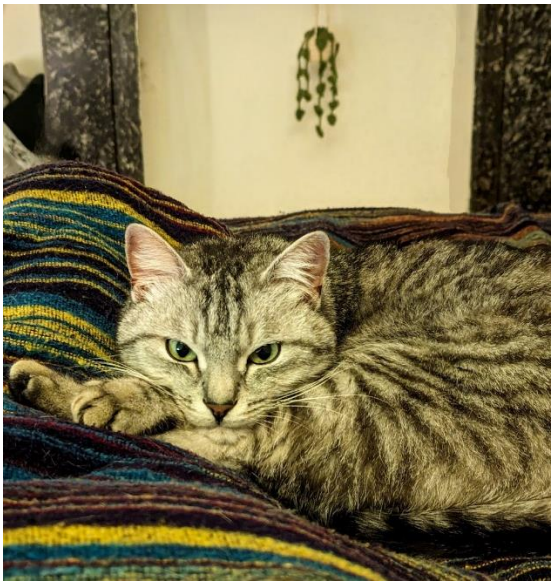


Figure R.1: Illustration du plus beau chat du monde

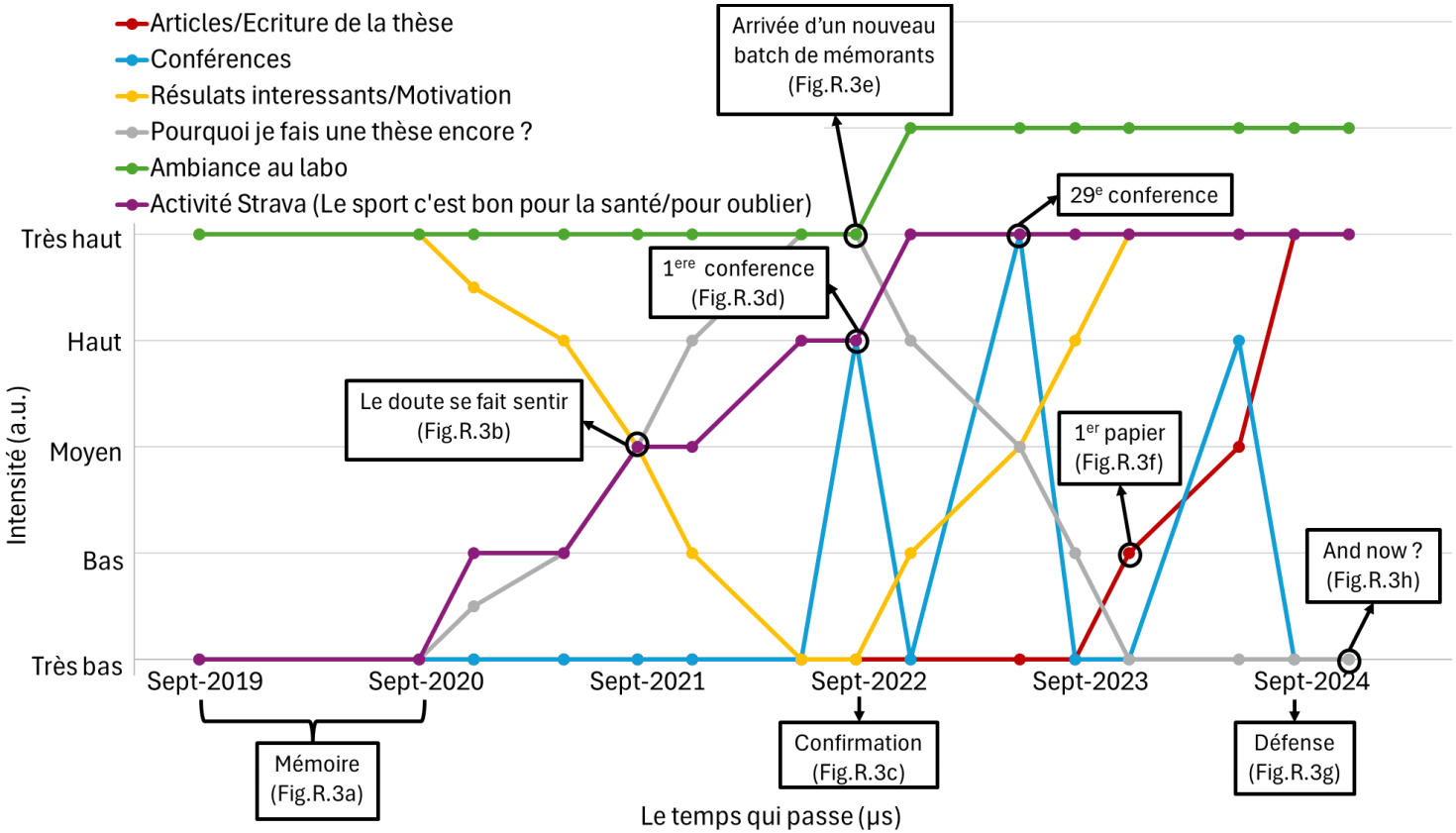


Figure R.2: Intensity of my PhD experiences as a function of the course of my life

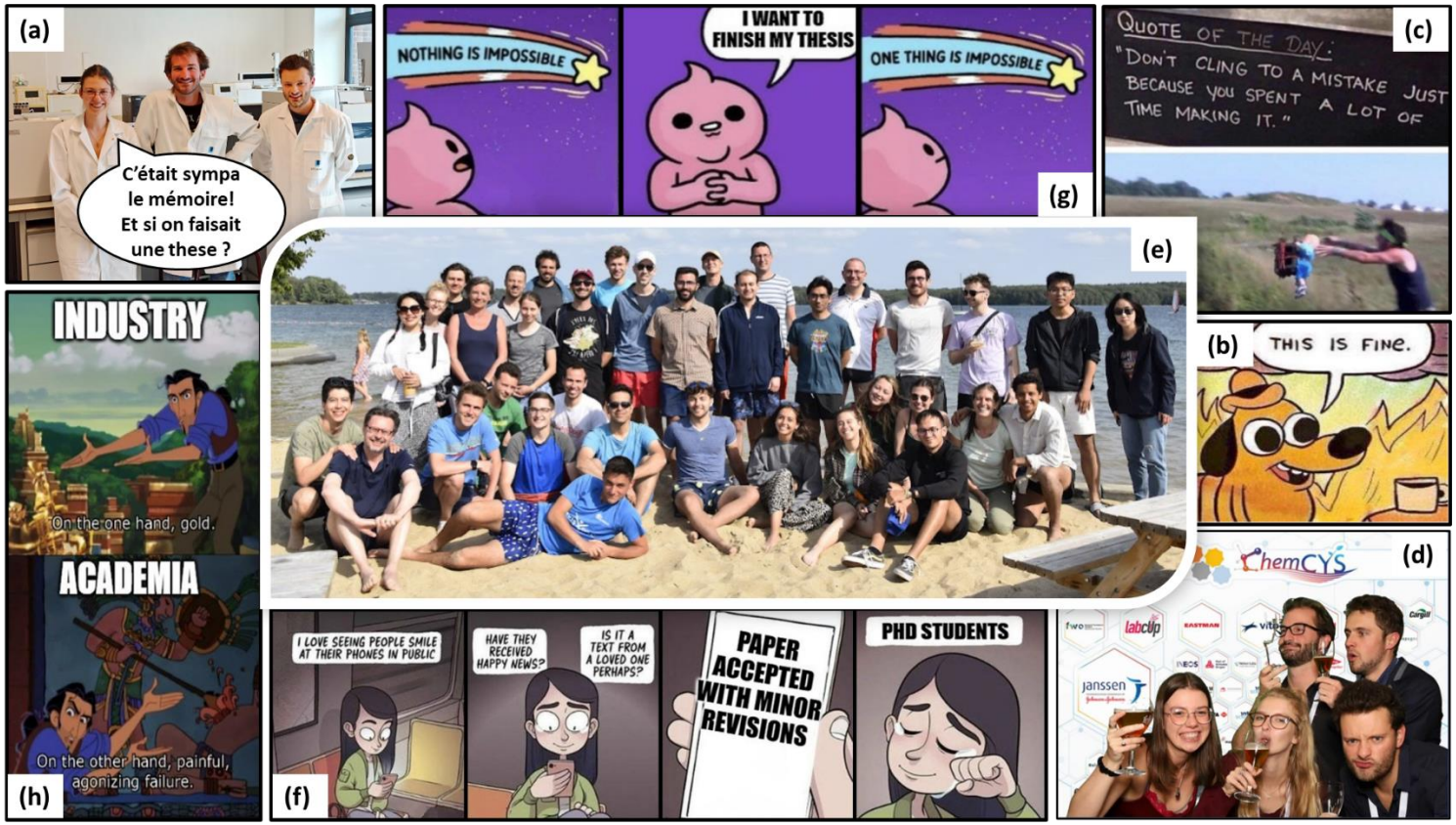


Figure R.3: Scheme of my PhD life

Abstract

Catalysts are used in 85-90% of chemical industries due to their significant economic and environmental impact. Therefore, developing new methods for producing catalyst with better selectivity, stability, and cost-effectiveness is essential. In this context, gliding arc plasma (GP) technology has emerged as a promising, eco-friendly, and cost-effective technique for catalysts synthesis. GP generates reactive species like electrons, cations, and free radicals that drive chemical reactions within and/or on various media. Particularly, when humid air is used as plasma gas, GP produces “reactive oxygen and nitrogen species” (RONS) with strong acidic and redox properties, making it effective for applications such as gas depollution, wastewater treatment, surface modification, and, most notably, heterogeneous catalysts synthesis.

While GP has already shown success in synthesizing metal (hydr)oxides and supported catalysts (FeO_x, MnO_2, SnO_2, TiO_2/SnO_2, …) with excellent properties and catalytic activity, improvements are still needed. The mechanisms behind metal precursor precipitation in GP remain not fully understood, presenting opportunities to enhance both the catalysts and the synthesis conditions. This thesis aims to deepen the understanding of the GP synthesis and optimize its application for diverse catalyst production. To address these goals, the thesis is structured in three parts.

The first part investigates the mechanisms behind metal precursor reaction and precipitation during GP synthesis, examining the roles of OH and NO radicals in the oxidation-reduction reactions of precursors and precipitation into metal (hydr)oxides. This section also explores the factors influencing metal precursors’ ability to react and precipitate under GP exposure, aiming to establish a framework for predicting precursor behavior.

The second part focuses on optimizing the GP synthesis method. It examines a post-treatment (PT) step to understand and optimize its potential to improve catalyst properties, as well as a "no-cooling" system that utilizes the heat generated during GP exposure, and testing Plasma-Activated Water (PAW) as an alternative synthesis medium.

The final part uses GP synthesis to produce novel supported metal/oxide catalysts never synthesized by GP before, such as Au on TiO_2 and SnO_2, demonstrating the ability of GP in producing various catalyst types.

Overall, the research of this thesis contributes to a deeper understanding of GP as catalyst synthesis method, offering new insights and strategies for optimization.

Table of contents

General Introduction..... 1

1. What is catalysis?.....3

2. Classical methods to synthesize heterogeneous catalysts 6

2.1. Bulk catalysts 6

2.2. Supported metal catalysts.....16

2.3. Conclusion on classical methods to synthesize catalysts 19

3. The glidarc plasma as a new way to synthesize catalysts 20

3.1. What is a plasma? 20

3.2. Different types of plasma 20

3.3. The glidarc plasma (GP) 22

4. Context and goal of the thesis 31

5. Strategy and structure of the thesis.....33

Experimental..... 39

1. GP reactor.....41

2. Characterizations of the solids.....42

2.1. X-Ray Diffraction (XRD) 42

2.2. X-Ray Photoelectron Spectroscopy (XPS) 42

2.3. Scanning Electron Microscopy (SEM) and Energy Dispersive X-Ray (EDX).....43

2.4. N_2-physisorption 43

2.5. Catalytic tests – total oxidation of benzene.....43

Part I - Enhancing understanding of the GP catalysts synthesis method 45

Chapter 1 - What are the species involved in the gliding arc plasma synthesis of heterogeneous catalysts?.....47

1. Introduction.....51

2. Materials and methods 53

2.1. Materials....53
2.2. Methods....54
2.3. Characterization of the solids formed....58
3. Results and discussion....59
3.1. Are OH radical responsible for the oxidation of precursors exposed to GP?....59
3.2. Do the long-lived species influence the precipitation process of precursors exposed to the GP?....64
3.3. What is the impact of different types of plasma gases on the precipitation of precursors exposed to the GP?....80
4. Conclusion....84
Chapter 2 - Towards the understanding of parameters allowing to anticipate the precipitation reaction of metallic precursors in humid air gliding arc plasma reactor....87
1. Introduction....91
2. Materials and methods....92
2.1. Materials....92
2.2. Methods....92
2.3. Characterization of the solids formed: X-Ray Diffraction (XRD) 93
3. Results and discussion....93
3.1. Factors influencing the ability of a precursor to react....93
3.2. Application of the identified factors to predict precursors that may react by GP:....116
4. Conclusion....127
Part II - Optimization of the humid air GP catalysts synthesis . 129
Chapter 3 - Post-Treatment: an interesting step to improve heterogeneous catalysts synthesized by glidarc plasma?....131
1. Introduction....135
2. Experimental methods....137

2.1. Materials 137
2.2. Method 137
2.3. Characterization of the solids formed 139
3. Results and discussion 139
3.1. Investigation of the impact of the PT 139
3.2. Elucidation of the mechanism underlying the PT 162
4. Conclusion 170
Chapter 4 - Improving the synthesis of heterogeneous catalysts by gliding arc plasma using the "no-cooling system" 173
1. Introduction 177
2. Materials and methods 179
2.1. Materials 179
2.2. Methods 179
2.3. Characterization of the solids formed 180
3. Results and discussion 180
3.1. Impact of the no-cooling system on the temperature of the exposed solution 180
3.2. Impact of the no-cooling system on solids GP-synthesized .. 181
3.3. Can the no-cooling system replace the PT step in the GP catalysts synthesis? 197
4. Conclusion 199
Chapter 5 - Using "Glidarc Plasma Activated Water" as a new way to synthesize heterogeneous catalysts 201
1. Introduction 205
2. Materials and methods 206
2.1. Materials 206
2.2. Methods 206
2.3. Characterization of the solids formed 209
3. Results and discussion 209

3.1. Lifetime of long-lived species present in PAW 209
3.2. Investigation of the impact of PAW for catalysts synthesis .. 211
3.3. How long after the exposure PAW can be used for the catalysts precipitation ? 221
4. Conclusion 225
Part III - Synthesis of supported metal/metal oxide catalysts through GP 227
Chapter 6 - Synthesis of Au/metal oxides catalysts by humid air GP 227
1. Introduction 231
2. Materials and methods 233
2.1. Materials 233
2.2. Method 233
2.3. Material characterization 240
3. Results and discussion 241
3.1. Au/TiO_2 241
3.2. Au/SnO_2 – 2 steps 254
3.3. Au/SnO_2 – 1 step 264
4. Conclusion 267
General conclusion and future works 271
Supplementary Information 281
References 337
List of publications, communications and awards 353
Publications 353
Conference communications 354
1. Oral communications 354
2. Poster communications 355
Awards 355

List of abbreviations

Samples

NE	Non-exposed
SA	Au/SnO_2 not washed and not dried
SAOP	Au/SnO_2 one-pot
SAWD	Au/SnO_2 washed and dried
SAWH	Au/SnO_2 washed and not dried
Sn	$SnSO_4$
TA	Au/TiO_2

Synthesis conditions

AT	Ambiant Temperature
GP	Glidarc Plasma
NE	Non-exposed
NPs	Nanoparticles
PD	Post-Discharge
PAW	Plasma Activated Water
TOC	Total Organic Carbon content

Chemicals

7HC	7-hydroxycoumarin
cou	coumarin
phen	1,10-phenanthroline

Characterization

BET	Brunauer, Emmet, and Teller
BJH	Barret-Joyner-Halenda
EDX	Energy Dispersive X-Ray
ESR	Electron-spin resonance spectroscopy

FID	Flame Ionization Detector
FWHM	Full Width at Half Maximum
GBH	Beam High Resolution mode
ICP	Inductively Couple Plasma
RF	Radio-Frequency
SEM	Scanning Electron Microscopy
TEM	Transmission Electron Microscopy
UV-vis	UV-visible
VVH	Volume ratio per hour
XPS	X-Ray Photoelectron Spectroscopy
XRD	X-Ray Diffraction

Others

ER	Eley-Rideal
LH	Langmuir-Hinshelwood
LTE	Limit Equilibrium Temperature
PZC	Point of Zero Charge
RONS	Reactive oxygen and nitrogen species
T_e	Temperature of electrons
T_i	Temperature of ions
T_n	Temperature of neutral species

List of synthesized catalysts

Iron precursors	**$FeSO_4$ or $(NH_4)_2Fe(SO_4)_2$**	Classical exposure of iron precursor solution to GP
	$FeSO_4$ + cou10^{-2}	$FeSO_4$ solution exposed to GP in the presence of 10^{-2} mol/L coumarin
	Water 60 min + $FeSO_4$ 60 min after	Water exposed to GP for 60 min and collected before adding the $FeSO_4$ precursor
	$FeSO_4$ PAW	
	$FeSO_4$ + $NaNO_2$ (+HNO_3)	$FeSO_4$ solution stirred at AT for 60 min, with $NaNO_2$ and HNO_3 subsequently added
	$FeSO_4$ or $(NH_4)_2Fe(SO_4)_2$ + PT (3h-100°C)	Iron precursor solution exposed to GP, followed by a Post-Treatment at 100°C for 3 h
	$FeSO_4$ or $(NH_4)_2Fe(SO_4)_2$ + PT (72h-AT)	Iron precursor solution exposed to GP, followed by a Post-Treatment at AT for 72 h
Manganese precursors	**$KMnO_4$**	Classical exposure of $KMnO_4$ precursor solution to GP
	Water 30 min + $KMnO_4$ 30 min after	Water exposed to GP for 30 min and collected before adding the $KMnO_4$ precursor
	$KMnO_4$ PAW	
	$KMnO_4$ + $NaNO_2$ (+HNO_3)	$KMnO_4$ solution stirred at AT for 30 min, with $NaNO_2$ and HNO_3 subsequently added
Tin precursors	**$SnSO_4$ or $SnCl_2$**	Classical exposure of tin precursor solution to GP
	$SnSO_4$ or $SnCl_2$ + PT (3h-100°C)	Tin precursor solution exposed to GP, followed by a Post-Treatment at 100°C for 3 h
	$SnSO_4$ or $SnCl_2$ + PT (72h-AT)	Tin precursor solution exposed to GP, followed by a Post-Treatment at AT for 72 h
	$SnSO_4$ PAW	Water exposed to GP for 120 min and collected before adding the $SnSO_4$ precursor

TiO_2	**P25 60**	P25 exposed to GP for 60 min
	P25 60 NE	P25 stirred at AT for 60 min
Au/TiO_2	**TA 7, 15 or 30**	P25 + $HAuCl_4$ (Au/TiO_2 3% mass) exposed to GP for 7, 15 or 30 min
	TA 7, 15 or 30 NE	P25 + $HAuCl_4$ (Au/TiO_2 3% mass) stirred at AT for 7, 15 or 30 min
SnO_2	**Sn**	$SnSO_4$ solution exposed to GP for 120 min
	Sn NE	$SnSO_4$ solution stirred at AT for 120 min
Au/SnO_2	**SA 15 or 30**	$SnSO_4$ solution exposed to GP for 120 min, followed by the addition of $HAuCl_4$ (Au/SnO_2 0.86% mass) and additional to GP exposure for 15 or 30 min
	SAWD 7 or 15	$SnSO_4$ solution exposed to the GP for 120 min, followed by washing and drying of the formed precipitate. $HAuCl_4$ is then added (Au/SnO_2 3% mass), followed by further GP exposure for 7 or 15 min
	SAWD 7 or 15 NE	$SnSO_4$ solution stirred at AT for 120 min, followed by washing and drying of the formed precipitate. $HAuCl_4$ is then added (Au/SnO_2 3% mass), followed by further GP exposure for 7 or 15 min
	SAWH 7 or 15	$SnSO_4$ solution exposed to the GP for 120 min, followed by washing of the formed precipitate. $HAuCl_4$ is then added (Au/SnO_2 3% mass), followed by further GP exposure for 7 or 15 min
	SAWH 7 or 15 NE	$SnSO_4$ solution stirred at AT for 120 min, followed by washing of the formed precipitate. $HAuCl_4$ is then added (Au/SnO_2 3% mass), followed by further GP exposure for 7 or 15 min

General Introduction

Abstract

This section outlines the context of this research, including a presentation of the classical catalysts synthesis, and of the gliding arc plasma and its applications, particularly in catalysts synthesis. It highlights limitations in current understandings, existing knowledge and synthesis conditions of the method, aligning these with our objectives. Consequently, our strategy is designed in order to address these issues.



Image from "Advanced Metallic System CDT (Youtube)"

1. What is catalysis?

Catalysis did not wait to be discovered to be already used in everyday life. In fact, it has been employed for centuries, even before we called it “catalysis”. An illustrative example of a catalyzed reaction spanning centuries and still in use today is the fermentation process, where yeast catalyzes the transformation of sugar into alcohol, giving rise to the beloved drink we all know [1,2]. However, the earliest formal scientific reports of the use of heterogeneous catalysts were written by Joseph Priestly and Martinus van Marum in the 1800s. They documented the dehydrogenation of ethyl alcohol over a metal catalyst [1]. Yet, we had to wait for Berzelius in 1836 to formally describe these accelerated chemical reactions as “catalysis” [2–5].

A catalyst is defined as a substance that accelerates chemical reactions, or reduces the temperature or pressure required to initiate one, without undergoing any change itself [3,6,7]. Catalysts effectively lower the activation energy of a chemical reaction, making it easier to break and form chemical bonds, thus facilitating the production of new combinations and new substances (Figure I.1) [5–7]. Consequently, the use of a catalyst results in faster and more energy-efficient chemical reactions. Additionally, catalysts can enhance the yield and selectivity of a process by increasing the amount of desired products while reducing the generation of unwanted byproducts. This aspect not only amplifies the environmental sustainability of the chemical reaction but also enhances its economic viability [5,6,8]. Consequently, catalysis plays a key role in chemical industries, significantly contributing to both their economic viability and environmental sustainability. Today, catalysts are utilized in over 90% of all industrial chemical transformations across various sectors, including polymers, pharmaceuticals, agrochemicals, and petrochemicals, as well as for clear-up of environmental pollutants [2,9,10].

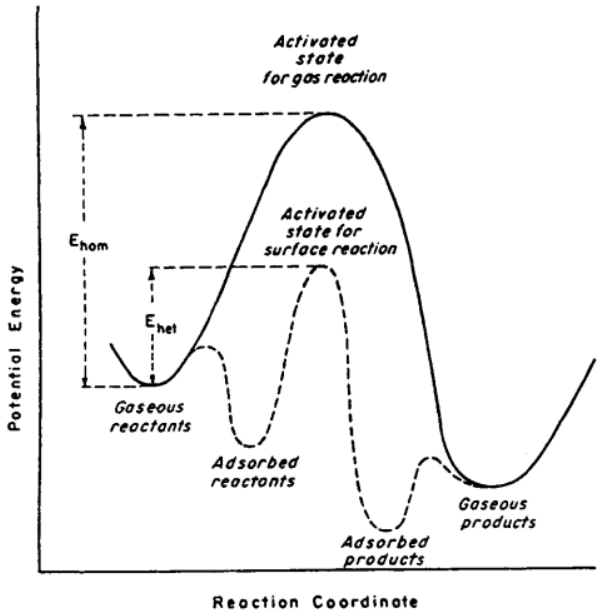


Figure I.1: Potential-energy curves for a reaction proceeding homogeneously (full curve) and on a surface of a catalyst (dotted curve) [2]

There are 3 types of catalysts: enzymatic, homogeneous, and heterogeneous. An enzymatic catalyst is a highly specific protein that accelerates particular chemical reactions by binding to substrate molecules in its unique active site. It typically acts in a homogeneous phase but can become heterogeneous when immobilized on a solid support. A catalyst is categorized as homogeneous when it is in the same phase as the reactants and as heterogeneous when it is dispersed in a distinct phase. Typically, a heterogeneous catalyst consists of a solid in a liquid or gaseous medium [7]. Both homogeneous and heterogeneous catalysis are widespread in certain contexts. Homogeneous catalysts often provide enhanced selectivity and activity, which make them predominantly used in the pharmaceutical industry. However, they require separation steps to be removed from the final product and are sometimes impossible to reuse, making them expensive and environmentally unfriendly. On the other hand, heterogeneous catalysts are generally preferred when possible due to their ease of separation and reusability, which makes them cheaper and less polluting. Additionally, their higher thermal stability allows for operation in harsher conditions [9,11]. Since heterogeneous catalysts are the sole subject of this thesis, only them shall be referred to as "catalysts".

The action of such catalysts can involve various mechanisms, with the Langmuir-Hinshelwood (LH), Eley-Rideal (ER) or Mars-Van Krevelen cycles

being the most common ones. In these cycles, one (ER) or two (LH) reactant molecules adsorb onto the solid surface, undergo conversion into a surface intermediate, and finally form a product, followed by its desorption (Figure I.2). In the case of metal oxides, a Mars-Van Krevelen mechanism can occur. In this case, a reactant A adsorbs on the surface and reacts with and removes an atom of oxygen from the catalyst. When the product desorbs, the resulting vacancy is rapidly refilled by a source of O_2 serving as co-reactant (Figure I.2) [1,10–12]. However, these cycles are simplified. The reality of a catalytic reaction is much more complex and involves several additional steps. These steps can be the diffusion of reactant or product molecules through the boundary layer to the catalyst surface and into the pores of the catalyst, as well as the chemical or physical adsorption of the reactant at the surface of the catalyst [2,11].

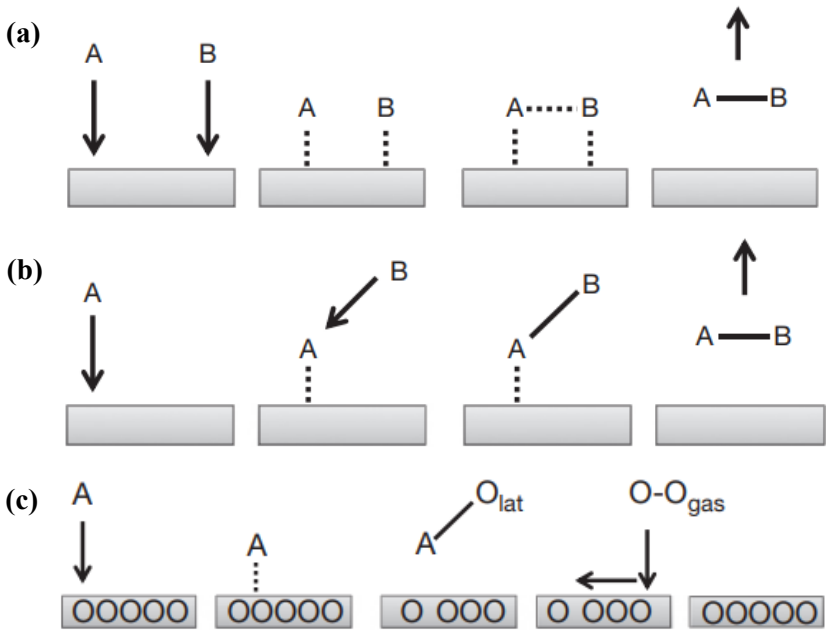


Figure I.2: Schematic illustration of the three main surface mechanisms: (a) Langmuir−Hinshelwood; (b) Eley−Rideal; (c) Mars−Van Krevelen mechanism [12]

Due to their significant environmental and economic impact on chemical industries, ongoing research in catalyst synthesis aims to enhance their properties and performance in a wide variety of reactions. This includes modifying their selectivity, activity, stability, morphology, mechanical and thermal strength, regenerability, reproductivity, originality, and cost [13].

2. Classical methods to synthesize heterogeneous catalysts

There are different categories of heterogeneous catalysts, but the most used are bulk and supported ones. Bulk catalysts are mainly composed of active substances, whereas supported catalysts are usually derived from preformed supports impregnated with the active phase. Supported catalysts are often preferred due to their ability to achieve optimal dispersion of catalytically active component(s) while stabilizing them against sintering. This is economically advantageous, especially considering that the active components are often expensive metals. Additionally, besides providing structural framework and stability to the metal, the support can sometimes introduce new active sites to the system [13–15]. While various types of bulk and supported catalysts exist, this thesis will mostly discuss metal oxides as bulk catalysts that can also potentially serve as supports for supported catalysts. Metal oxides are indeed widely used in various industrial reactions, such as partial oxidation for the synthesis of valuable products and total oxidation for degradation of pollutants. Additionally, metal oxides are frequently employed as supports in many types of supported catalysts for a wide range of catalytic reactions [2,5]. However, in order to develop new types of catalysts using the method presented here, supported metal on metal oxides will also be briefly discussed at the end of this introduction.

The industrial manufacturing process for catalysts typically involves several steps, including synthesis, hydrothermal transformation, separation (decantation, filtration, and centrifugation), washing, crushing, grinding, forming and/or shaping, calcination, impregnation, mixing, and activation or reduction [14,15]. Each of these steps is crucial in developing catalysts with the required characteristics for their intended chemical reactions. However, the synthesis process, being the initial step, largely defines most of the characteristics, which is the main focus point of this thesis.

Considerable research has been and continues to be conducted to develop improved catalysts. This involves developing synthesis methods and studying various parameters that can be altered to impact different characteristics of the catalysts formed. Below, we outline some common methods used in industrial catalyst synthesis, along with their respective advantages and disadvantages.

2.1. Bulk catalysts

Catalysts synthesis methods can be performed in various media. Solid-state and gaseous-phase methods, such as thermal decomposition or flame hydrolysis, are widely used in industrial synthesis. However, since the

synthesis in this thesis occurs in an aqueous medium, we will primarily focus on discussing methods considered as liquid-phase synthesis, being the sol-gel and precipitation process. This approach allows for a fair comparison of methods with similar synthesis conditions, and, consequently, similar advantages and disadvantages.

2.1.1. Sol-gel process

2.1.1.1. Principle of the sol-gel process

The sol-gel method consists of creating a diphasic 3D network trapping the molecules of solvent from the reticulation of a colloidal suspension. The precursor in sol-gel preparation can either be a metal salt or alkoxide dissolved in an appropriate solvent (water or alcohol) or a stable colloidal suspension of preformed sol. The sol, which is a liquid suspension of solid particles from 1 nm to 1 µm, is obtained by the hydrolysis (Eq.I.1) or condensation (Eq.I.2) of the precursor [13–15].

<u>*Hydrolysis:*</u>

$$-M-(OR)_n + xH_2O \rightarrow -M-(OH)_x-(OR)_{n-x} + xROH \qquad (Eq.I.1)$$

<u>*Condensation:*</u>

$$-M-OH + XO-M- \rightarrow -M-O-M + XOH \qquad (Eq.I.2)$$

Where X can be either H or R (alkyl group)

Subsequently, the further condensation of the sol particles into a 3D network produces the gel. The encapsulated liquid is then removed by either evaporative or sublimative drying (xerogel) or drying with supercritical extraction (aerogels) to form the resulting solid. An aging step of the gel can also be added before the drying step, in order to change the properties of the final solid produced. Finally, further heat treatment is necessary to convert the solid into a catalytically useful form, i.e. mainly to burn off any residual organics and/or to oxidize the sample (Figure I.3) [13–15].

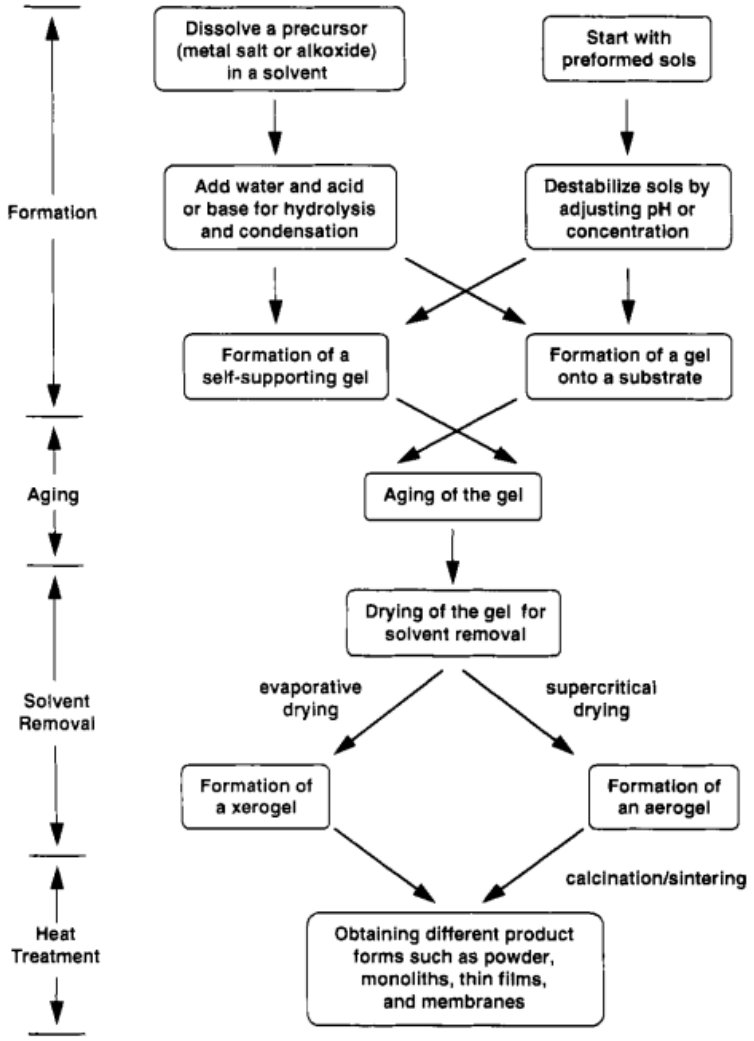


Figure I.3: Schematic diagram showing the various steps of a sol-gel process [13]

2.1.1.2. Parameters that matter

The sol-gel process consists of four steps each having a specific purpose and several experimental parameters that can be varied, leading to solids with specific characteristics (Table I.1).

a. Solution chemistry

The formation of a gel is influenced by several factors. Hydrolysis and condensation are both nucleophilic substitution reactions, meaning that an electro-rich chemical species (nucleophile) replaces a functional group within

another electron-deficient molecule (electrophile). Therefore, the reactivity of metal alkoxides depending on the metal's partial positive charge and coordination number and this reactivity can be controlled by the nature and number of alkyl groups. Additionally, the water quantity and addition rate impact the hydrolysis ratio (moles of water molecules per mole of metal alkoxide), which must be greater than one to form a gel. Finally, temperature, pH, and the choice of solvent also affect reaction rates and can modify the alkoxide properties or the condensation reaction [13–15].

b. Aging

During the aging step, continued condensation between surface functional groups of the gel strengthens the gel's network but can cause shrinkage if excessive. Coarsening may also occur, where particles dissolve and reprecipitate, increasing pore size and reducing specific surface area. Factors influencing the aging step include temperature, time and pH of the pore liquid. To manipulate these parameters and avoid issues during the aging step, different methods were developed such as immersing the gel in or washing it with another liquid, exposing the gel to a different humidity, heating the gel, and using hydrothermal conditions [13].

c. Drying

In a gel, it is common to have a range of pore sizes within the structure, which can create differential capillary pressure across pores and cause structural collapse during the drying step. To reduce this pressure, gels with more uniform pore sizes can be created by adding organic molecules, such as formaldehyde or glycerol, which control hydrolysis and condensation rates to influence pore size distribution. Similarly, surfactants can stabilize particles and control their size, while swelling agents increase the distance between structural components, enlarging the pores. Capillary pressure can also be minimized by using solvents with lower surface tension or a contact angle near 90°, or by removing the liquid-vapor interface altogether through supercritical or freeze drying [13,16].

d. Heat treatment

After liquid removal, heat treatment is needed to burn off residual organics and/or oxidize/reduce the sample, often in the presence of a reactive gas (air, oxygen, or hydrogen). Factors like temperature, heating rate, time, and gas type influence crystallization, sintering, and the final material structure, requiring careful control [13].

Table I.1: Important parameters in the various steps of a sol-gel process [13]

Step	Purpose	Important parameters
Solution chemistry	To form a gel	- Type of precursor - Type of solvent - pH - Water content - Precursor concentration - Temperature
Aging	To allow a gel to undergo changes in properties	- Time - Temperature - Composition of the pore liquid - Aging environment
Drying	To remove solvent from a gel	- Drying method - Temperature and heating rate - Pressure and pressurization rate - Time
Calcination	To change the physical/chemical properties of the solid, often resulting in crystallization and densification	- Temperature and heating rate - Time - Gaseous environment

2.1.1.3. Interest of the sol-gel process

The sol-gel process is used for a wide variety of oxidic materials for catalysis. The main advantage of the sol-gel method is the easiness to control the physical characteristics such as pore size, volume, and distribution, to have a highly pure solid, to vary the compositional homogeneity at a molecular level, to prepare samples at low temperatures, and to produce samples in different physical forms. Furthermore, it is also possible to introduce many components in a single step [13,14]. However, although a wide variety of characteristics for the catalysts can be obtained by this method, the control of the parameters needs to be meticulous and sometimes require long steps and/or difficult conditions to obtain. In fact, as we have seen, the gels formed are metastable, so the drying step needs to be done slowly with not too harsh thermal treatment or exposure to liquid water to avoid sintering, phase transformation, or collapsing of the structure [13]. Furthermore, another issue with the sol-gel method is the cost and stability of the alkoxide metal compound, which has limited its development in high-volume industrial catalyst preparation [16].

2.1.2. Precipitation

2.1.2.1. Principle of the precipitation

The purpose of this method is to precipitate a solid from a liquid solution. The precipitation occurs in different steps: supersaturation, nucleation, growth, and eventually maturation. The supersaturation step is when the system is unstable and a small perturbation triggers precipitate formation, also known as the nucleation step. This is followed by the growth of the solid precipitate that increases in size by adding more solute to the existing particles. A maturation step can eventually be also added in order to restructure and reorganize the formed particles [14,15,17]. The process of forming of a solid from a solution is illustrated in Figure I.4. It shows that nucleation, occurs only when the precursor concentration exceeds a critical point, the nucleation threshold. This nucleus, defined as "the smallest solid-phase aggregate of atoms, molecules or ions which is formed during a precipitation and which is capable of spontaneous growth", initiates the precipitation process [13]. New particles are formed as long as the precursor concentration remains above the nucleation threshold. During this formation, the precursor is consumed, causing its concentration to decrease until it falls below the critical point, at which stage the growth of existing particles begins. It has been deduced that the larger the nucleation regime area, the smaller the resulting particles tend to be due to a higher tendency for nucleation. Additionally, mechanical agitation or other processes can shear growing crystals, further decreasing the particles size [13].

Supersaturation, the prerequisite for nucleation, can be achieved through physical or chemical methods. Physically, supersaturation can be induced by increasing the concentration through solvent evaporation or decreasing the temperature. Chemically, it can be triggered by adding a coprecipitating agent that either changes the pH, leading to precursor condensation into (hydr)oxides, or introduces additional ions that cause the solubility product of a certain precipitate to be exceeded [13].

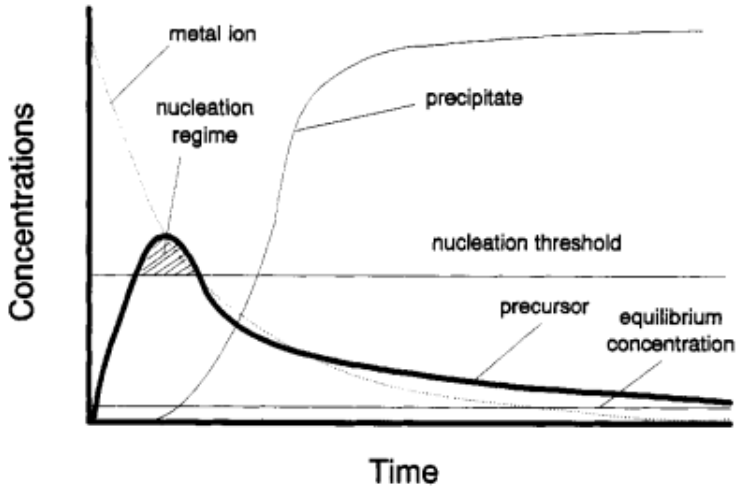


Figure I.4: Simplified scheme for the formation of a solid product from solution [13]

2.1.2.2. Parameters that matter

In the precipitation process, various parameters, including the nature of precursor or precipitating agent, the concentration of the reactants, the solvent, the temperature, and the pH, can significantly influence the characteristics of the final product, such as its purity, particle size, specific surface area, pore size and volume, etc. (Figure I.5). Consequently, these parameters must be carefully adjusted to achieve the desired final catalyst [13,14,16].

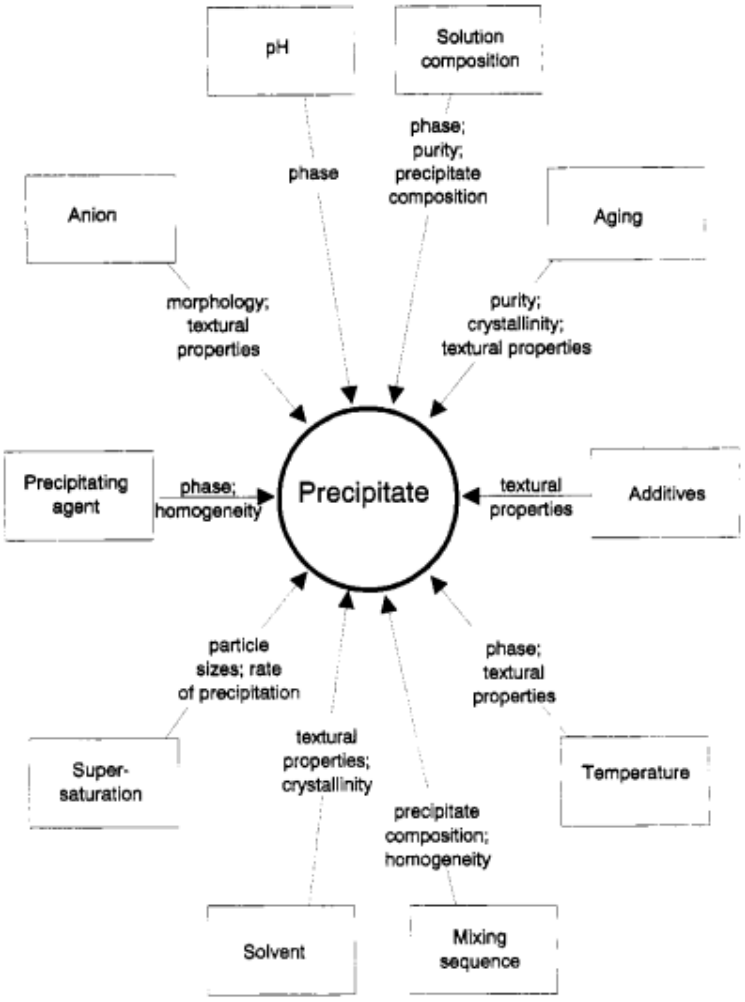


Figure I.5: Parameters affecting the properties of the precipitate and main properties influenced [12]

a. Nature of precursor or precipitating agent

In a common procedure, a metal salt is dissolved in a solution, and, in most cases, the pH is increased by adding a base, such as sodium hydroxide, ammonia, or ammonium carbonate, causing the precipitation of an insoluble metal hydroxide or carbonate. The interest in producing hydroxides and carbonates is that they can be easily decomposed by heat into oxides of high specific surface area without leaving potential catalyst poisons, and that the safety and environmental problems coming from their calcination are minimal. This suggests the importance of choosing the right precursor of the

precipitate to also avoid contaminations. It is preferable to use a precursor salt where the counterions, which may become trapped in the precipitate, can decompose into volatile products during the calcination step. Suitable counterions include nitrates, carbonates, ammonium or carboxylates. If the ions trapped in the solid cannot decompose by heat, careful washing of the precipitate is necessary [4,13,14,16].

The nature of the ions present in the precipitation solution can greatly influence the properties of the final product. In fact, some of these ions, such as chlorides and sulfates, can potentially act as poisons of catalytic reactions. Moreover, these ions can affect the final product's properties, including morphology, particles size, but also lead to the formation of different types of phases [13].

b. Concentration

Working at high concentration for the precipitation process is often preferred for several reasons. Firstly, supersaturation occurs rapidly at higher concentration, leading to faster precipitation. Additionally, higher supersaturation rates result in a higher nucleation rate, producing smaller particles with a greater specific surface area. Lastly, using higher concentration allows for a reduction in the volume of the vessel needed for the same mass of precipitate, thereby lowering the cost of plant investment [13].

c. Solvent

For economic and environmental reasons, water is typically preferred as a solvent. However, sometimes, organic solvents are chosen despite their disadvantages to synthesize products of superior qualities that cannot be achieved by other means. Nonetheless, the use of organic solvents in precipitation processes is rare and is reserved for special cases where the superior properties of the final catalysts justify the higher costs and associated challenges [13].

d. Temperature

An important factor in determining the crystallite sizes, specific surface area and phases of the produced solid is the temperature at which precipitation occurs, as it influences the nucleation rate. However, selecting the appropriate temperature to achieve specific characteristics of the solid is difficult to predict otherwise than experimentally. Additionally, for some systems, it is possible to predict the phases that will develop based of the temperature of precipitation thanks to chemical considerations [13].

e. pH

If hydroxides are precipitated, the pH directly influences the degree of supersaturation by affecting the amount of OH^- available in the solution, which participate in the formation of the precipitate. As for the temperature, the influence of the pH on the properties of the solid is difficult to predict other than experimentally [13].

f. Additives

An additive is a substance added to the precursor solution that influences the product properties without being essential to the precipitation process. Most of the time, these additives are organic molecules that become trapped in the solid during the precipitation and are subsequently removed during the calcination step, leaving behind a certain porosity [13].

2.1.2.3. Industrial implementation

In industrial catalyst synthesis, the simplest method is batch operation, where a precipitating agent is added to a metal salt solution in a vessel (Figure I.6 (a)). It is a very simple way to make the synthesis, however, it can result in a heterogeneous product due to variations in batch composition. To improve homogeneity, both reagents can be added simultaneously under controlled pH and reagent ratios. The homogeneity of the product is better but might still vary due to the different concentrations of other ions present in the solution, which are not precipitated and might be occluded in the solid. Furthermore, the precipitates first formed are aged for a longer time in the solution than the others, which can already lead to phase transitions (Figure I.6 (b)). All these issues can be avoided by using a continuous process (Figure I.6 (c)). However, this makes higher demands on the process control of parameters such as temperature, concentration, pH, and residence times of precipitate [13].

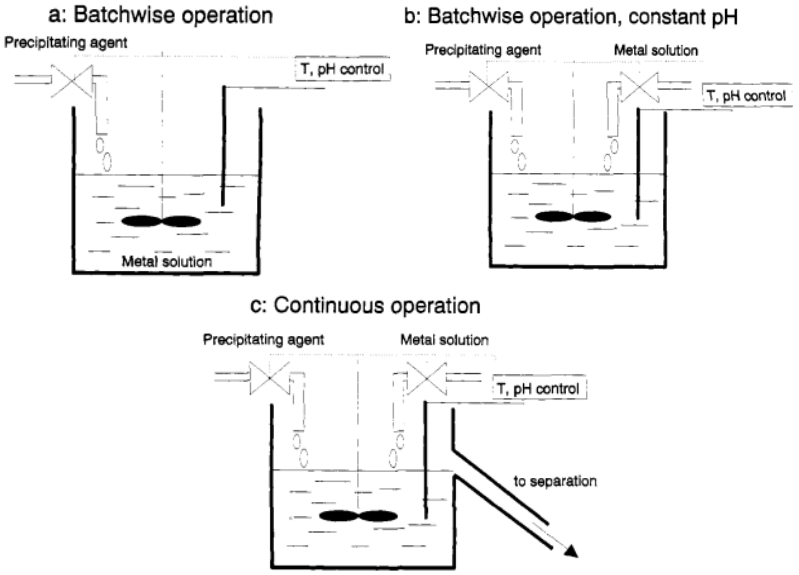


Figure I.6: Possible implementation of precipitation process in (a) batch where precipitating agent is added slowly in a vessel containing the metal solution ; (b) batch where precipitating agent and metal solution are added in a vessel ; (c) continuous operation [13]

2.1.2.4. Interest of the precipitation process

The precipitation process is the most widely used one to synthesize a wide variety of catalysts because of its easiness and economic value. In fact, most supports materials, such as alumina and zirconia, as well as some specific oxides like iron or titanium, are synthesized using this method. The main advantage of precipitation for preparing these materials is the possibility of creating very pure solids. Furthermore, as it is well known, we know which parameters must be changed in order to develop catalysts with specific characteristics. However, the method is highly demanding as it requires meticulous parameters control during the synthesis and a separation step after precipitation. Moreover, this method possesses ecological issues as the addition of strong chemical components (considered with high environmental impact in both their production and their treatment in wastewater) is sometimes required to trigger the precipitation, and a large volume of salt-containing solutions is formed from the washing steps [15,18].

2.2. Supported metal catalysts

It is possible to synthesize supported catalysts in a single step by sol-gel or by co-precipitation process. In co-precipitation, salts of the active metal and support are dissolved and mixed so that the nucleation and growth of a

combined solid precursor of the active metal and support are obtained at the same time [19]. By sol-gel, a metal precursor is usually added directly to the solution containing the oxide precursor prior to the gelling process. The metal precursor becomes part of the network of the gel by being hydrolyzed or condensed [13].

However, in most cases, the preparation of a supported catalyst is done by first synthesizing the support before incorporating the supported synthesis method. These are called “impregnations” and are described below.

All the methods presented here are solution-based, so the addition of a chemical reduction or thermal decomposition step is needed to transform the precursor into the catalytically active phase. This is done in order to transform the metal precursor deposited on the surface into pure metal and/or to decompose and desorb the possible residues coming from this metal precursor synthesis [20,21].

Gas phase deposition of metal on support also exists but will not be discussed here, as only wet impregnations are possible in the GP reactor used for the catalyst synthesis in this thesis.

2.2.1. Impregnation without chemical support-precursor bond

This technique consists in introducing, into the pore space of a support, a solution of an inert precursor that does not interact chemically with the solid surface. The precursor therefore remains in the dissolved state in the solution and is not fixed to the surface before the evaporation of this solution occurs in the subsequent drying steps [13].

We call the impregnation “capillary” or “dry” if the volume of the impregnation solution introduced is equal to or less than the volume of the pores of the support. In this case, the main advantages are the simplicity of the method (no filtration step), the low amount of solvent and consequently waste, and above all, a thorough control of the active phase loading since the amount of active phase is dictated by the concentration of the impregnation solution [1,16]. However, the main limitations may arise from poor spreading of the active phase, poor control of the solution pH, and the use of highly concentrated (and hence poorly stable) solutions due to the low amount of solution used [1,16]. Furthermore, dry impregnation is characterized by its exothermicity, the capillary pressure developed in the pores, and the speed with which the pore space is filled. These parameters need to be carefully

studied to obtain good homogeneity in the deposition while avoiding the collapsing of the pores [13].

If this volume is greater than that required to fill the pores, the impregnation is called “diffusional” or “wet”. In this case, we no longer have the issue of exothermicity, and pressure developed in the pores. However, the precursor salt migrates progressively from the solution into the pores of the support, which requires a longer time of synthesis and may result in poor dispersion of the active phase [1,13].

The main issue with impregnation without chemical support-precursor interaction is that no washing step is possible to avoid “washing away” the metal precursor deposited at the surface.

2.2.2. Impregnation with chemical support-precursor bond

Impregnation with chemical support-precursor interaction can be done by ion exchange, grafting or deposition-precipitation.

Ion exchange involves replacing an ion A in electrostatic interaction with a support surface by another ion B from a precursor solution. This is possible to achieve because the oxide supports behave like ion exchangers when their surface bears electric charges. They are natural exchangers when they are composed of a framework bearing electric charges neutralized by ions of the opposite sign, such as zeolites, clays, and silicates. These ions can be exchanged with others from the precursor during the operation. Amphoteric oxides with hydroxyl groups (S-OH) can also participate in ion exchange, as their surface charge varies with pH. Above their point of zero charge (PZC), oxide particles become negatively charged, favouring cation adsorption, while below PZC, anion adsorption is preferred. Thus, the pH determines which ions from the precursor interact with the support [13].

Grafting consists in forming a covalent bond between the support and the metal complex, which immobilizes the active species and enhances stability. This grafting process can be implemented in various ways: by creating functional groups on the support surface that serve as binding sites for the metal, or by adding ligands to the metal that react with the functional groups on the support surface.

The advantages of these 2 methods (ion exchange and grafting) are the high dispersion of the metal ions, the avoidance of migration, agglomeration, and sintering of the metal particles during the subsequent thermal treatment, and the control of the metal loading [21].

The deposition-precipitation method, similar to co-precipitation, involves depositing metal compounds onto a support surface by changing the pH of the metal precursor solution at the surface of the support, often resulting in metal hydroxide precipitation. Selective precipitation is achieved if two conditions are met: (1) the soluble precursor adsorbs onto the support to create preferential nucleation sites, and (2) supersaturation is kept below the homogeneous supersaturation threshold. This requires gradual adjustment of the precipitating agent (pH, temperature, or concentration) to prevent bulk precipitation. The method enables controlled deposition of the catalyst precursor, leading to highly dispersed metal phases after activation [16,19].

The advantage of these impregnations is that, as a chemical interaction between the support and the precursor exists, it is possible to add a washing step to the synthesis to remove the non-specifically adsorbed species without losing the active phase [16].

2.3. Conclusion on classical methods to synthesize catalysts

As we have seen, the development of catalysts with interesting properties aimed at reducing the environmental and economic impacts of chemical reactions constitutes a significant area of research. This explains the intense investigation and ongoing studies in this field. Numerous techniques have been developed to create these catalysts of interest. However, despite their notable advantages, such as their well-established nature and ability to generate catalysts with a wide range of interesting properties (including porosity, specific surface area, stability, etc.), they also possess inherent drawbacks.

Among the primary disadvantages, we can highlight the cost of the precursor materials, the time-consuming nature of the synthesis, the meticulous parameters control during the whole synthesis, the necessity of adding numerous substances that induce precipitation, and the utilization of environmentally harmful solvents. Consequently, the pursuit of new synthesis methodologies capable of mitigating these shortcomings while still yielding catalysts with interesting properties remains an exciting field of research.

It is within this context that the utilization of plasma, particularly glidarc plasma (GP), as a novel synthesis method for catalysts emerges as promising.

3. The glidarc plasma as a new way to synthesize catalysts

3.1. What is a plasma?

Plasma is defined as a globally neutral ionized gas composed of "light" species, such as electrons and photons, and "heavy" species, such as molecules, atoms, ions, and radicals. When generated in laboratory, far from the electrodes or reactor walls, it is considered neutral because the density of electrons and ions present in the plasma are balanced. It is observed in nature (stars, lightning, fire, solar corona, etc.) or artificially when the thermal energy supplied is sufficient for the collisions between gas atoms to cause the expulsion of their electrons [22,23].

Artificially, plasma is formed through an energy transfer between a source, often an electrical discharge, and a gas. As the energy is applied, electrons in the gas atoms or molecules are excited, and some gain enough energy to escape. These electrons then collide with other gaseous species, knocking electrons off from additional atoms and molecules. The result is a gas consisting of a mixture of positively charged ions, free electrons, and neutral particles, thus forming a plasma. [22]. The experimental setup used for this purpose includes a voltage source (U_0), a resistance (R), and a tube filled with gas at a certain pressure (P). The tube consists of 2 or more conductive electrodes (E) between which an electrical discharge of intensity I and voltage U can occur (Figure I.7) [24,25].

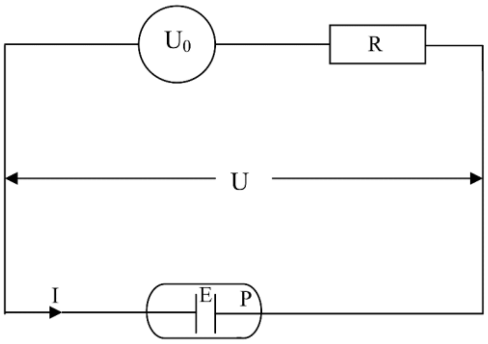


Figure I.7: Experimental set-up of a plasma [25]

3.2. Different types of plasma

There are three types of plasma: hot/thermal, cold/non-thermal, and moderate/temperate. The first step in forming a plasma is the creation of free electrons from gas species, which then collide with and ionize other molecules. Initially, due to the significantly lighter mass of electrons

compared to heavier molecules, electrons lose only a small fraction of their energy when colliding with these heavier species. Therefore, at the beginning of the process, the temperature of electrons (T_e) is much higher than that of heavy particles (T_i and T_n). However, with sufficient time and energy, collisions between electrons and heavy species lead to an equilibrium in their temperatures (LTE). In fact, the temperature differential between electrons and heavy particles is directly proportional to the ratio of the electric field (E) to the pressure of the system (P). When E/P is low (at high pressure), the temperatures of electrons and heavy species are similar (>10^5 K ; T_e=T_i=T_n), leading to a state known as local thermodynamic equilibrium (LTE) (Figure I.8). Such plasmas are referred to as "thermal plasma". In these plasmas, ionization and chemical processes are dictated by the system's temperature. Due to the high temperature, they contain a large quantity of ionized species, making them highly reactive. However, utilizing this type of plasma in laboratory settings is challenging due to the high energy requirements for generation, the need for reaction media and materials capable of withstanding high temperatures, and the rapid electrode degradation [22–24,26,27].

Non-thermal plasmas, on the other hand, do not achieve LTE due to insufficient time or energy. Consequently, the electron temperature (>10^4 K) is much higher than that of heavy particles (around room temperature) (T_e>>T_i and T_n) (Figure I.8). In these plasmas, ionization and chemical processes primarily depend on electron temperature and are less sensitive to thermal processes and gas temperature. Generating such plasmas does not demand excessively high energy, and the reaction medium can remain at low temperatures during reactions. However, achieving pressures lower than atmospheric pressure is necessary, which might pose challenges for industrial-scale implementation [22,24,26–30].

At pressures around atmospheric pressure, LTE is not strictly maintained, leading to the emergence of "moderate" plasma (Figure I.8). These plasmas exhibit characteristics of thermal plasma due to the type of species formed in the gas and of non-thermal plasma due to the ambient temperature of heavy species (around room temperature). They are of industrial interest as they operate at atmospheric pressure and room temperature, facilitating energy-efficient operations with aqueous media that do not vaporize. GP belongs to this category. [22,24,27,31–34].

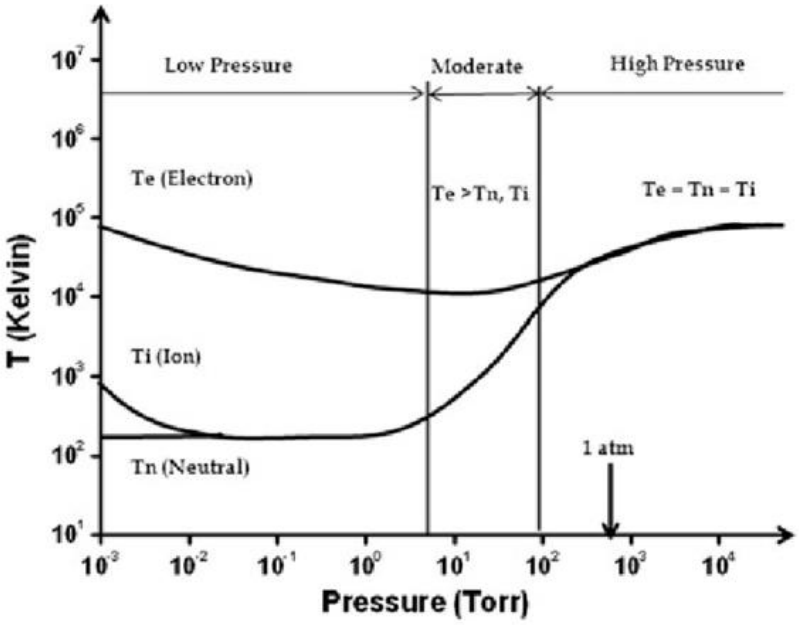


Figure I.8: Types of plasmas as a function of the thermal energy of the species present and the pressure [35]

3.3. The glidarc plasma (GP)

3.3.1. What is it?

The GP reactor was invented by H. Lesueur and further developed by A. Czernichowski in 1988 [30,36]. It comprises two stainless steel electrodes with a divergent profile, linked to a high-voltage generator. Upon activation of the generator, an arc forms at the smallest distance between the electrodes. Subsequently, a flow of gas (plasma gas) is directed perpendicular to the arc, pushing it along the electrodes. At the end of these electrodes, the distance becomes too big to sustain the arc, and a new discharge can initiate at the electrodes' beginning. All these arcs form the "plume" (Figure I.9) [30,34,37–40].

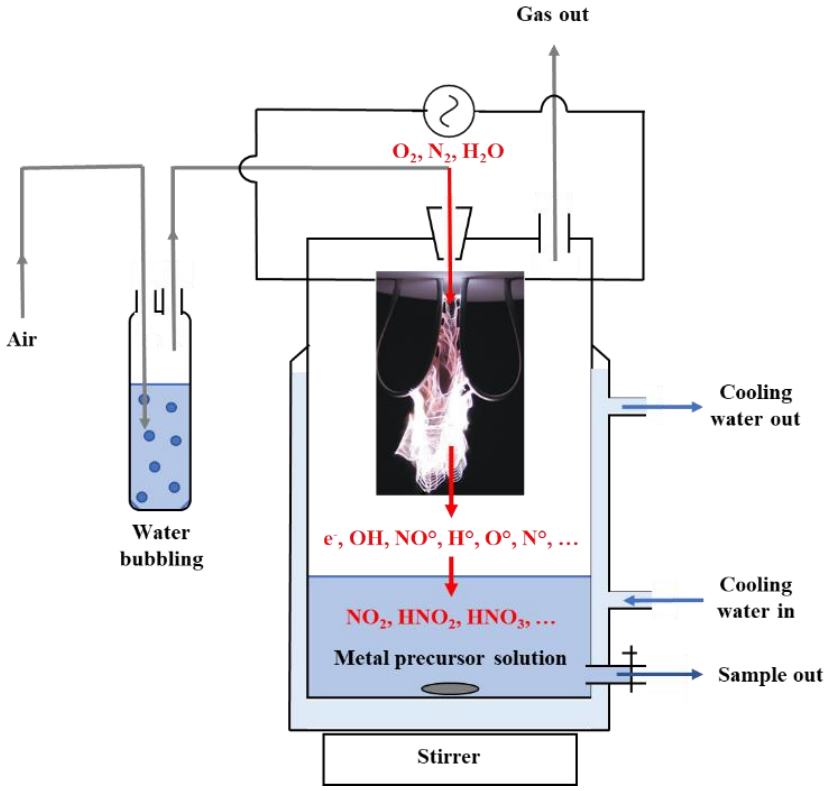


Figure I.9: Scheme and species created in humid air GP reactor; plasma plume from [41]

The plasma gas, upon encountering the arc, forms the thermal plasma. This gas gradually cools as it moves along the electrodes, transitioning into a non-thermal plasma. Hence, the glidarc constitutes both types of plasmas, earning it the classification of "moderate." This technique was created to extend the lifespan of the electrodes while still facilitating reactions characteristic of thermal plasma [30,32,37,39,42–44].

Various types of reactions occur within a plasma reactor, including excitations, ionizations, dissociations, recombinations, etc. (Table I.2) [33]. Excitations of a molecule in a plasma can occur through electron impact collisions, resulting in energy transfer to excitation modes such as electronic, vibrational, or rotational. However, in addition to direct electron impact excitation, molecules in a plasma can also experience energy transfer mechanism through collisions with heavy species (Table I.2) [23].

Table I.2: Typical reactions occurring in plasma phase [33]

Reaction type	**Source**	**Reaction**
Excited by	Molecules	$A + B \rightarrow A^* + B$ or $A + B^* \rightarrow A^* + B$
	Photon	$A + h\upsilon \rightarrow A^*$
	Electron	$A + e^- \rightarrow A^* + e^-$
Relaxation		$A^* \rightarrow A + h\upsilon$
Ionisation by	Impact of molecules	$A + B \rightarrow A^+ + B + e^-$
	Attachment of an electron	$A + e^- \rightarrow A^-$
	Photon impact	$A + h\upsilon \rightarrow A^+ + e^-$
	Electron impact	$A + e^- \rightarrow A^+ + 2e^-$
Recombination of	Atoms	$A + A + B \rightarrow B + A_2$
	Electron + ion	$A^+ + e^- \rightarrow A + h\upsilon$
	Ion + ion	$A^- + B^+ \rightarrow AB$
	Radicals	$R + H \rightarrow RH$
	Ion + molecule	$A^+ + B \rightarrow AB^+$
Charge transfer		$A + B^+ \rightarrow A^+ + B$
Dissociation by	Impact of molecules	$A_2 + B \rightarrow A + A + B$
	Photon impact	$A_2 + h\upsilon \rightarrow A + A + h\upsilon$
	Electron impact	$A_2 + e^- \rightarrow A + A + e^-$

The species produced through these reactions are contingent upon the plasma gas introduced between the electrodes. In our setup, humid air serves as the gas source. When humid air is used as plasma gas, the species generated are known to predominantly exhibit acidic and oxidant effects on the target (Figure I.10). As plasma gas interacts with the electrons (and photon) of the arc, it leads to the formation of activated species, ions, and radicals, called "primary species", such as OH, NO, H_2O_2, O, O_3. In addition to these species, "secondary species", such as OH, NO_2, HNO_3, HNO_2, can be created by the reaction of primary species together or with parent species (Figure I.10). Emission spectroscopy measurements of the plume have revealed that the main species created in such plasmas are the radicals OH and NO [33]. It has been suggested that a part of the thermal energy from the arc is transferred through electron impact to the plasma gas molecules causing the cleavage of H_2O and O_2, resulting in the creation of OH and O radicals (Eq.I.3, Eq.I.4 Eq.I.5). The formation of these radicals can occur in more than one stage, depending on the energy of the impacting electron. For instance, the O_2 molecule may first be excited to different vibrational state before dissociating (Eq.I.6) [23].

$$H_2O + e^- \rightarrow OH + H + e^- \quad (Eq.I.3)$$
$$O_2 + e^- \rightarrow 2O + e^- \quad (Eq.I.4)$$
$$O + H_2O \rightarrow OH + OH \quad (Eq.I.5)$$
$$O_2(v = 0) + e^- \rightarrow O_2(v > 0) + e^- \rightarrow 2O + e^- \quad (Eq.I.6)$$

The formation of NO radicals is more complex because the N_2 bond is very strong, requiring high-energy electrons to efficiently break it by electron impact alone. However, in GP, the energy of the generated electron is not high enough to explain N_2 bond breaking through electron impact alone. Instead, another mechanism predominantly triggers the breaking of the N-N bond. First, O radicals must be created before reacting and breaking the N_2 triple bond, a process known as the "Zeldovich mechanism", assuming the N_2 is in its ground state before the impact. If the N_2 is vibrationally excited before the bond is broken by the O, this mechanism is referred to as the "vibrationally-enhanced Zeldovich mechanism". The advantage of this mechanism is that it is more efficient, as part of the energy barrier is already provided by the excitation energy, making the bond easier to break (Eq.I.7) [23,45,46].

$$N_2(g, v) + O \rightarrow NO + N \quad (Eq.I.7)$$

From the dissociation of the N_2 molecule, NO can also be formed by the reaction of N with OH or O radicals previously formed (Eq.I.8, Eq.I.9) [23,47].

$$O_2 + N \rightarrow NO + O \quad (Eq.I.8)$$
$$N + OH \rightarrow NO + H \quad (Eq.I.9)$$

Finally, other types of plasma-species can be formed through various reactions of previously formed radicals, some of which are proposed below, among many others (Eq.I.10-Eq.I.19) [23,31,33,39,48,49].

$$H + NO \rightarrow N + OH \quad (Eq.I.10)$$
$$OH + NO \rightarrow HNO_2 \quad (Eq.I.11)$$
$$NO + O \rightarrow NO_2 \quad (Eq.I.12)$$
$$NO + O_2 \rightarrow 2NO_2 \quad (Eq.I.13)$$
$$3NO_2 + H_2O \rightarrow 2H^+ + 2NO_3^- + NO \quad (Eq.I.14)$$
$$NO + NO_2 + H_2O \rightarrow 2HNO_2 \quad (Eq.I.15)$$
$$NO_2 + OH \rightarrow HNO_3 \quad (Eq.I.16)$$
$$2H + 2O_2 \rightarrow 2HO_2 \rightarrow H_2O_2 + O_2 \quad (Eq.I.17)$$
$$O + O_2 \rightarrow O_3 \quad (Eq.I.18)$$
$$OH + OH \rightarrow H_2O_2 \quad (Eq.I.19)$$

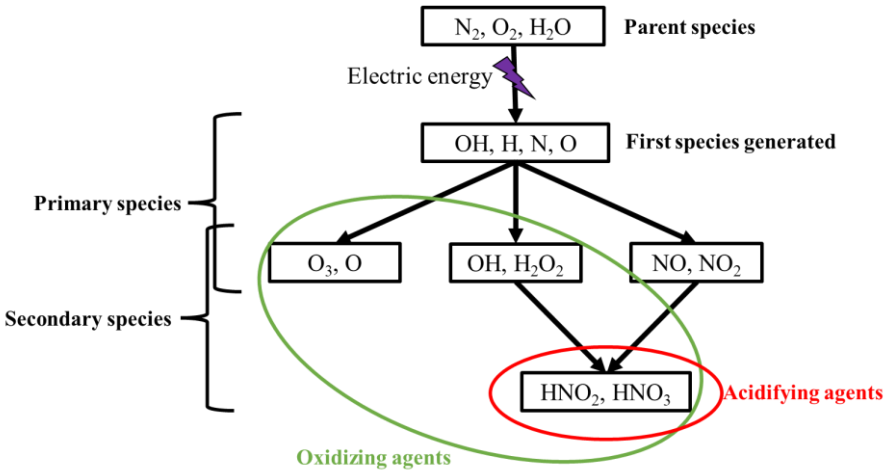


Figure I.10: Main molecular species formed in humid air plasma (inspired form [39])

Knowing this, it is important to note that another significant aspect of GP lies in the formations of vibrationally excited N_2 molecules, which are essential for producing reactive NO_x species. Recent studies have highlighted that the reduced electric field (E/N), where E represents the electric field and N is the concentration of neutral species, is a key factor to distinguish different plasma types and in understanding how electron energy is transferred to neutral species in the plasma. These studies indicate that, to enhance N_2 conversion via the vibrationally-enhanced Zeldovich mechanism, the E/N must range between 5 and 100 Townsend (Td) (Figure I.11). In fact, GP generates a reduced electric field below 100 Td, making it optimal for forming vibrationally excited N_2 molecules, and, consequently, producing more NO_x species [23,45,46].

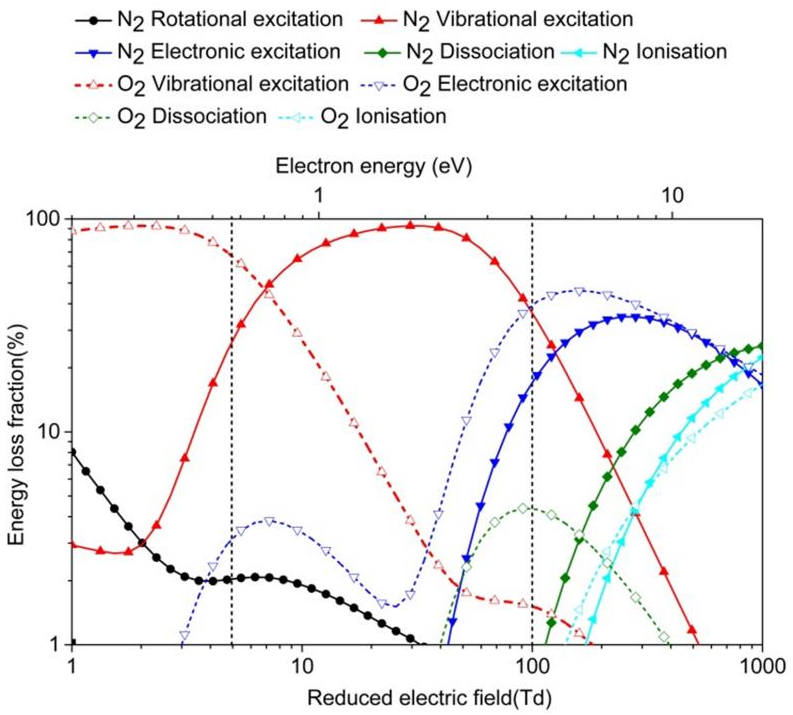


Figure I.11: Fraction of energy transferred from free electrons to different channels of excitation, dissociation, and ionization of N_2 and O_2 as a function of E/N and of the electron energy [46]

Among all these species formed in humid air plasma, some are considered as "short-lived species" (with lifetime in the millisecond range) and some as "long-lived species" (lifetime > 1s). Only species with longer lifespans have the capacity to traverse through and react within the bulk liquid, whereas

shorter-lived species only cause reactions at the gas-liquid interface (Figure I.12) *[31,33,37,39,48–54]*.

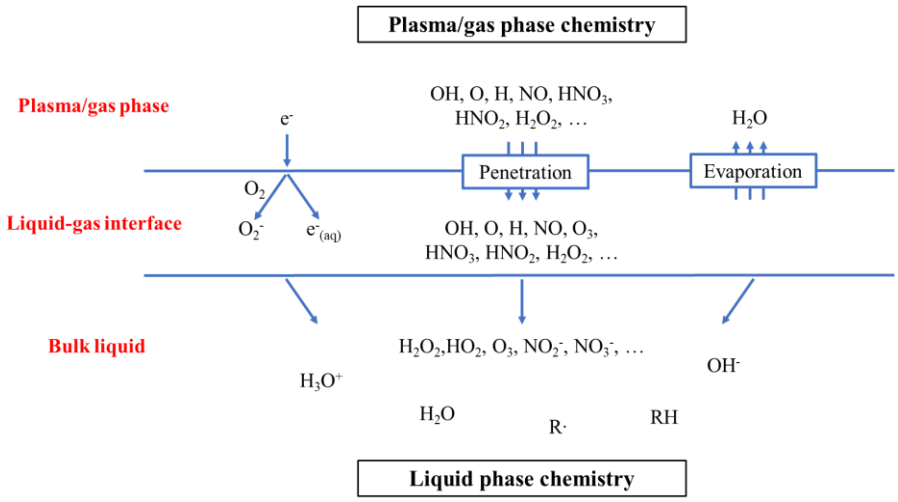


Figure I.12: Schematic diagram of some of the most important species and mechanism for a humid air plasma in contact with water (adapted from [54])

3.3.2. Applications and previous research in GP applications

The GP has garnered particular interest among industrialists compared to other types of plasmas for several reasons:

- Its application takes place at atmospheric pressure and ambient temperature, thus requiring lower energy input compared to applications utilizing other types of plasma [33].
- Among the various plasma technologies, GP is known for generating the highest number of NO_x species due to its ability to efficiently impact the vibrational excitation of N_2 [23,45,46].
- Intense research is being undertaken to improve the plasma setup, with promising results. Several possibilities have been explored, such as changing the nature and flow of plasma-gases, increasing the number of electrodes, employing circulating reactors instead of batch reactors, and modifying the method for introducing reactants into the reactor (via injection). These adjustments aim to improve the efficiency of the GP method while maintaining its economic and ecological advantages [43,44].

The species generated by humid air GP exhibit a wide range of properties, including acidifying, oxidizing, and reducing characteristics, among others. These properties make it highly interesting for a variety of applications such

as water and air depollution, hydrogen production, hydrocarbon oxidation and conversion, and modification of solid surface properties [30,33,39,55].

However, it is the oxidizing and reducing properties of the GP that are of particular interest in this thesis. This is this feature that researchers have exploited to synthesize metal (hydr)oxide catalysts using GP (TiO_2, TiO_2/SnO_2, FeOOH, Fe_2O_3, FeO_x/kaolinite, SnO_2, polymorphs of MnO_2) (Table I.3) [24,25,56,57]. Various precursor materials solutions undergo reduction or oxidation processes when exposed to the discharge, ultimately forming the desired catalyst (Table I.3). Recently, the acidifying characteristic of the humid air GP was also exploited for the synthesis of WO_3 (Table I.3) [58]. The solid precipitates during exposure to the plasma, subsequently undergoes drying and, in some cases, calcination before being utilized in catalysis. Notably, catalysts synthesized through this approach demonstrate comparable or even superior catalytic activity compared to those produced via conventional methods [24,25,56,57].

Table I.3: Catalysts synthesized by humid air GP in the literature [24,25,42,56–63]

Precursor	Catalyst synthesized	Synthesis reaction
$TiCl_3$	TiO_2 [57,60,62]	$TiCl_3 + OH + H_2O \rightarrow TiO_2 + 3HCl$
$TiCl_3$ + $SnCl_2.2H_2O$	TiO_2/SnO_2 [64]	$TiCl_3 + SnCl_2 + 3OH + H_2O \rightarrow TiO_2/SnO_2 + 5HCl$
$(NH_4)_2Fe(SO_4)_2.6H_2O$	FeOOH [25,61]	(1) $Fe^{2+} + OH \rightarrow Fe^{3+} + OH^-$ (2) $Fe^{3+} + 2OH^- + H_2O \rightarrow FeOOH + H_3O^+$
	Fe_2O_3 [25,63]	$2FeOOH \xrightarrow{calcination} Fe_2O_3 + H_2O$
Mayouom Kaolinite + $(NH_4)_2Fe(SO_4)_2.6H_2O$	FeO_x/kaolinite[25]	(1) $Fe^{2+} + OH \rightarrow Fe^{3+} + OH^-$ (2) $Fe^{3+} + 2OH^- + H_2O \rightarrow FeOOH + H_3O^+$
$KMnO_4$	α-MnO_2 and γ-MnO_2 [24,42,59]	$MnO_4^- + NO \rightarrow MnO_2 + NO_3^-$
$Mn(CH_3COO)_3.2H_2O$	γ-MnO_2 et β-MnO_2 [24,59]	$Mn^{3+} + OH + H_2O \rightarrow MnO_2 + H^+$
$SnCl_2$	SnO_2 [64]	(1) $SnCl_2 + H_2O \rightarrow Sn(OH)Cl + HCl$ (2) $Sn(OH)Cl + 3OH \rightarrow SnO_2 + 2H_2O + \frac{1}{2}Cl_2$
Na_2WO_4•$2H_2O$	WO_3 [58]	$Na_2WO_4.2H_2O + 2\,NO \rightarrow WO_3.2H_2O + 2\,(Na^+ + NO_3^-)$

4. Context and goal of the thesis

GP appears to be an interesting technique for synthesizing catalysts with good catalytic activities. Indeed, when compared to other methods, numerous advantages emerge. Firstly, the creation of reactive species is made straightforward in the reactor, and the source to generate them only necessitates electricity, air and water, which can be considered as cheap and renewable reactants. No additional substance is required, unlike other methods that typically necessitate the addition of a chemical reactant. Therefore, it makes the GP process cost-effective and environmentally friendly in comparison to some other methods.

Moreover, the catalyst precursors employed until now for GP synthesis are largely common, inexpensive, and readily soluble in water. This aspect significantly contributes to the cost-effectiveness of the method when compared to approaches like sol-gel.

Furthermore, the GP proves to be remarkably convenient in terms of facility and synthesis time. The industrial manufacturing process for catalysts usually entails multiple steps such as separation, washing, drying, etc., which are almost ubiquitous across various synthesis methods and cannot be removed in GP synthesis either. However, the synthesis method itself only requires exposing the metal precursor solution until it precipitates. Thus far, exposure time has not exceeded 2 hours (for SnO_2 synthesis from $SnCl_2$) and can be as short as 4 minutes (for MnO_2 synthesis from $KMnO_4$), making it an unbeatable synthesis time compared to other methods [42,64]. Additionally, during exposure to the plasma discharge, no parameter adjustments are necessary, unlike other methods, simplifying the process as we can simply “let it turn” until precipitation happens.

However, GP catalysts synthesis is not perfect, and many aspects remain to be explored.

To begin, hypotheses have been proposed to explain the mechanism underlying the precipitation process of a metal precursor exposed to the GP, with the radicals OH and NO being responsible for the reaction. This proposition is based on the observation that among the various species generated by humid air GP, OH and NO are produced abundantly and possess distinct characteristics: OH is a potent oxidizer, whereas NO functions as a strong reducer (OH/H_2O: 2.85 V/ENH; NO_3^-/NO: 0.94 V/ENH) [24,33,37,39]). To be more specific, it has been said that “When directed to metallic aqueous solutions, thanks to the oxidizing (HO) and reducing (NO)

characters of the radicals it contains, the discharge induces the precipitation of the corresponding metal (hydr)oxides" [59]. Even when acidification seems to trigger the reaction, NO was also mentioned as the species responsible for the precipitation [58]. Nevertheless, these radicals do not reflect all the so-called "Reactive oxygen and nitrogen species" (RONS) produced. Numerous other "short-lived" and "long-lived" species are generated, and they can also act as oxidizing/reducing, and/or precipitating agents (Figure I.10) [31,37,39,48,49,51–53]. However, to the best of our knowledge, none of these extra species have ever been considered to have an impact on the precipitation process. In fact, the proposed hypothetical reactions have not been confirmed, putting us in a state of uncertainty about which species activate the oxidoreduction that leads to precipitation or how the associated reactions occur inside the GP system. As a result, the mechanism of solid production by humid air GP is still not fully understood and is primarily dependent on hypotheses.

Furthermore, different types of precursors have been utilized in previous literature and have demonstrated efficacy in precipitating oxides or hydroxides. However, we still lack understanding regarding why these precursors precipitate and whether it implies that every type of metal precursor is capable of reacting and forming a precipitate via GP. This issue is directly linked to the previous point where, without comprehending the mechanism of solid formation, we cannot predict or understand why certain precursors react while others do not. Consequently, it is challenging to ascertain at this juncture the potential versatility of the method in synthesizing various types of catalysts, such as bulk oxides, mixed oxides, as well as supported oxide/oxide or metal/oxide configurations.

Additionally, while the GP synthesis appears promising given the synthesis conditions and the synthesized catalysts, there is still room for improvement to enhance the method's interest. This improvement can be achieved either by synthesizing better catalysts or by utilizing more interesting synthesis parameters. One approach improving catalysts has previously been proposed in the literature as "the post-discharge step" (PD, that will be later referred to in this thesis as the "post-treatment" step (PT)) [61,65]. This involves allowing the precursor solution, after exposure to GP and deactivation of the discharge, to stand outside the reactor for a defined duration and at a fixed temperature. It has been demonstrated that this step can impart new valuable properties such as phase transformation, increased specific surface area, and enhanced catalytic activity [61,65]. However, this step is not fully understood yet,

making it difficult to determine its relevance to various types of synthesized catalysts and the appropriate conditions for its implementation. Furthermore, this step prolongs the synthesis time of the catalysts and may sometimes necessitate additional energy input, such as heat, which could pose constraints for industrial purposes. Hence, there are still opportunities for discovering improvements to enhance both the method itself and the synthesized catalysts.

The primary objective of this thesis is to enhance the understanding of the entire GP synthesis method by comprehending its functioning. This research aims to facilitate improvements not only in the nature and properties of the synthesized catalysts but also in the synthesis parameters employed. Enhancing the understanding of the method will significantly contribute to elevating its value as an innovative approach for synthesizing heterogeneous catalysts.

5. Strategy and structure of the thesis

To achieve the mentioned objectives, the strategy pursued throughout this thesis can be illustrated, as depicted in Figure I.13. It revolves around 3 parts and 6 chapters, each addressing a specific objective, as detailed in the following paragraphs (Figure I.13).

The Part I aims to enhance the understanding of the complete GP synthesis method by thoroughly exploring its functioning. This part is divided into 2 chapters. The Chapter 1 is dedicated to comprehending the mechanism underlying the precipitation process of a metal precursor when exposed to GP. The aim is to ascertain the plasma species responsible for initiating the oxidoreduction leading to precipitation and to understand how the associated reactions occur within the GP system. Specifically, this involves confirming or refuting the hypothesis proposed in the literature regarding the role of the radicals OH and NO in the reaction, followed by the identification of at least some of the plasma species that trigger the precipitation process. The Chapter 2 consists in investigating the parameters influencing the ability of certain precursors to react or not via humid air GP. Various factors impacting a precursor's ability to undergo precipitation through GP are examined, including solubility, medium pH, the potential of redox reactions, and the nature of the metal precursor. The aim is to enhance comprehension of the method, creating a dichotomous key allowing us to predict the precipitation of any type of metal precursor, and ultimately enabling the synthesis of a broader range of catalysts, as detailed in Chapter 6.

The Part II of the thesis primarily focuses on optimizing GP synthesis to produce more interesting catalysts and/or employing more favourable synthesis conditions. This part is structured into 3 chapters (numbered from 3 to 5 in continuity of the chapter numbers initiated in Part I). The Chapter 3 discusses the previously proposed PD step found in the literature (that will be referred to in this thesis as the "post-treatment" step (PT)). The objective is to understand the mechanism of this step and assess its potential applicability to each type of solid synthesized, as well as to determine the optimal conditions, if applicable. The Chapter 4 is based on observations from the Chapter 3, aiming to replicate the desirable characteristics achieved through the PD step but with reduced synthesis time and energy input, by utilizing what we called the "no-cooling system". In fact, in conventional plasma synthesis, the GP reactor and the exposed solution are cooled down using a double jacket with circulating cold water. Consequently, we explored the idea of omitting this cooling system, i.e. allowing the solution to get heated by the energy spontaneously provided by the plasma, and checked whether this is enough to induce rapid maturation. Finally, the Chapter 5 entails enhancing the ease of the method by using a Plasma-Activated Water (PAW). This system involves exposing water to the discharge to activate it and then recovering it prior to adding the metal precursor, which initiates the precipitation process using the long-lived species created in the PAW. These experiments aim to propose a simplified set-up for GP catalyst synthesis, potentially yielding similar catalysts as those obtained through direct exposure to the discharge, without the need for reactor washing between different metal precursor exposures.

The final part of the thesis (Part III) builds upon the insights gained from the preceding chapters 1 and 2, demonstrating the utility of GP for catalyst synthesis by developing novel catalyst types. This section proposes the synthesis of supported metal/oxide catalysts through this method. More specifically, the synthesis of metallic Au on 2 types of support, TiO_2 as P25 and SnO_2 precipitated from the plasma-exposure of $SnSO_4$, were developed through the exposure of a specific gold precursor, $HAuCl_4$.

Finally, this thesis concludes with a general conclusion and suggestion for future work based on the finding presented throughout the study.

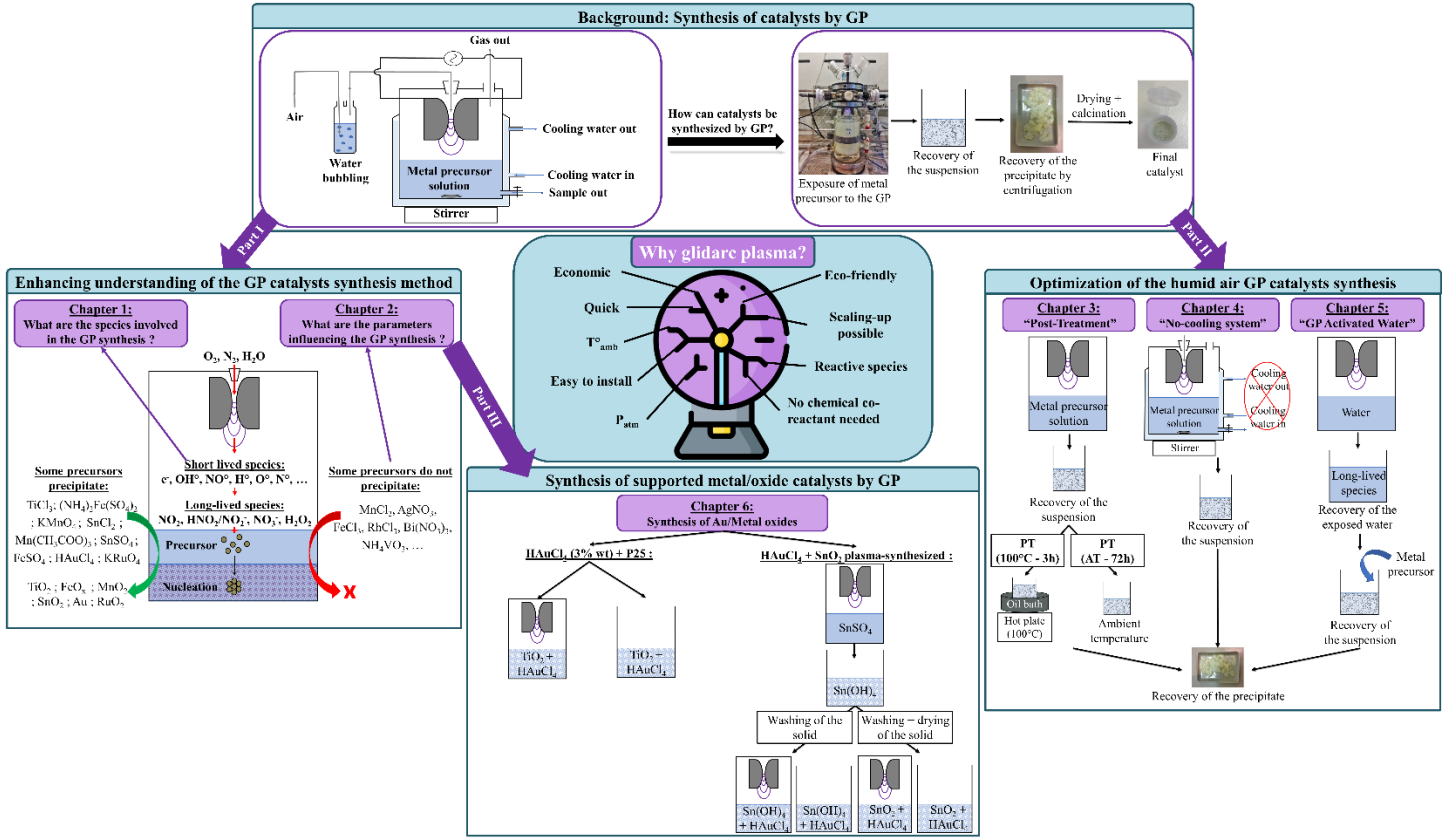


Figure I.13: Schematic representation of the strategy and structure of the thesis

Experimental

Abstract

This section outlines the primary experimental procedures employed throughout the thesis, including the GP reactor system and the conditions under which it was used. Additionally, it describes the characterization techniques utilized to analyse the solids formed by the GP process, as well as the catalytic tests conducted to evaluate the activity of the synthesized catalysts. Specific synthesis methods, techniques, and parameters pertinent to particular chapters are detailed in separate "Materials and Methods" sections at the beginning of each respective chapter.

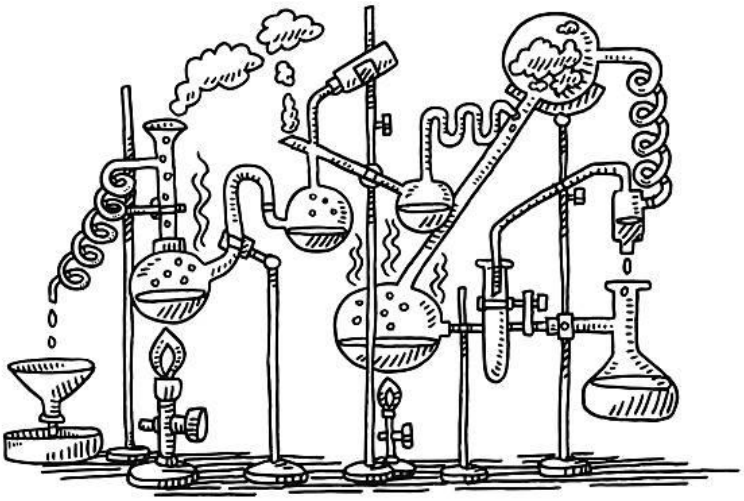


Image from "iStock"

1. GP reactor

The gliding arc plasma system employed in this study comprises the following components (Figure E.1):

- A high voltage generator (ABL Transformer; 9 kV; 100 mA) connected to both stainless-steel electrodes with a divergent profile, positioned within the reactor.
- A gas supply setup consisting of a compressed air source, a saturator filled with water in which air is bubbled, and a flowmeter controlling the gas flow rate (fixed at ≈ 400 L/h).
- A central reactor in the form of a double-walled cylindrical glass tube. It features inlets and outlets for the circulation of an external cooling fluid (water), an additional inlet for the nozzle to direct the air flow between the electrodes, and an opening for the gas exhaust (to prevent exceeding pressure within the reactor). An outlet valve is also present to facilitate retrieval of the reactor content following plasma exposure.

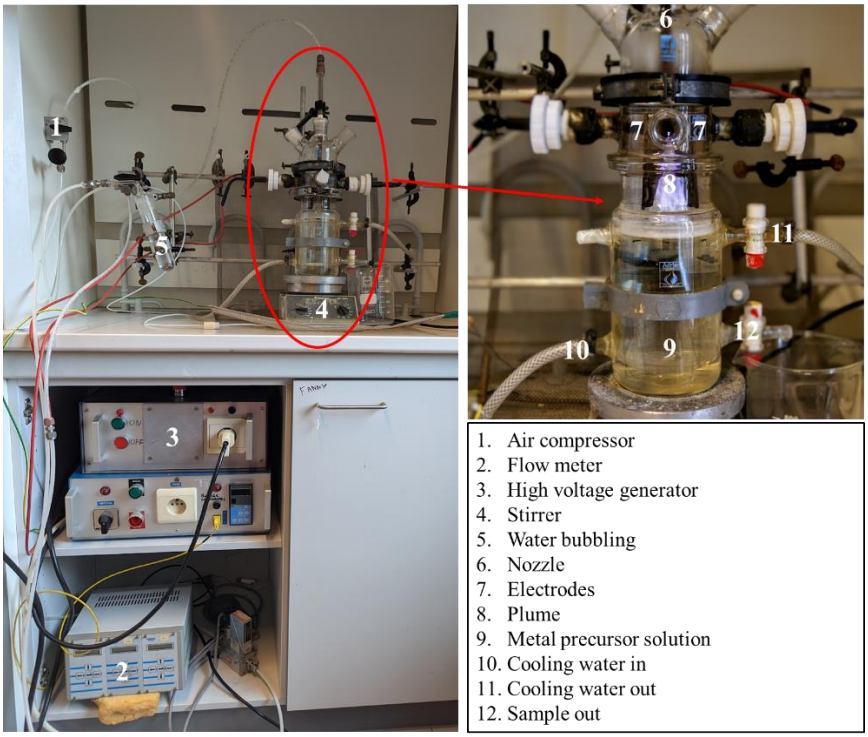


Figure E.1: GP reactor used for this thesis

When solution is exposed to the GP, 450 mL is added to the pre-washed reactor. This ensures that the distance between the liquid surface and the end of the electrodes is approximately 2 cm. The solution is agitated

throughout the entire exposure using a magnetic stirrer at approximately 1 turn/second.

2. Characterizations of the solids

2.1. X-Ray Diffraction (XRD)

The catalyst, previously ground, is placed on a polished Si single crystal sample holder covered with a thin layer of Nivea© cream and is introduced into a Bruker-D8 Advance diffractometer with a Bragg-Brentano geometry. The X-rays sent to the sample are produced using a copper anode (λ of Kα=0.15418 nm). The analysis is performed for angles 2θ = 5° to 80° with an increment of 0.015° and 0.15 s integration time. Detection is performed using a LynxEye XE-T Technology detector. The diffractograms are then processed using the ICDD-PDF2-2004 database [66].

2.2. X-Ray Photoelectron Spectroscopy (XPS)

The samples, previously crushed, are placed on a double-sided insulated plastic sticker, which is itself placed on a 4 mm diameter stainless steel sample holder placed in an aluminum carousel. The samples are then degassed under ultra-high vacuum at 10^{-5} Pa for 12 hours in order to eliminate the physisorbed compounds before being analyzed. The machine used is an SSX 100/206 Photoelectrons Spectrometer from Surface Science Instruments (USA). It is equipped with a micro-focused monochromatic Al X-ray source powered at 20 mA and 10 kV. The pressure inside the analysis chamber is 10^{-8} Pa, and the analysis angle is 55°. An electron gun operating at 8 eV and a Ni grid placed 3 mm above the sample surface are used to ensure that the sample charge is stabilized during analysis. The data are processed using the CasaXPS program from Casa Software Ltd, UK. To calibrate the binding energy, the C-(C,H) component of the C 1s peak is positioned at 284.8 eV. The atomic percentages are obtained using the normalized peak areas, the sensitivity factors provided by the manufacturer, and a Shirley-type baseline. The atomic percentages of each element are recalculated by removing the carbon contamination due to the experimentation. From the percentage obtained for O 1s, the quantity of O atoms bound to the carbon contamination is deduced, considering 3 types of carbon-oxygen bonds: O-C=O, O-C-O and C=O, and C-O. The remaining percentages of the elements not coming from the contamination are then brought back to 100%.

2.3. Scanning Electron Microscopy (SEM) and Energy Dispersive X-Ray (EDX)

The ground solids are placed on an adhesive carbon sticker, which is itself deposited on an aluminum support. The scanning electron microscope used is a JEOL 7600F operating at 2 kV for the SEM images in Gentle Beam High Resolution mode (GBH) and at 15 kV for the EDX analyses. The atomic percentages of each element are recalculated by removing carbon and aluminum contamination (considered to come exclusively from the sample holder and the sticker). All remaining percentages are then brought back to 100%.

2.4. N_2-physisorption

N_2-physisorption is used to measure the specific surface area by the BET method (Brunauer, Emmett, and Teller) in the usual relative pressure range of 0.05-0.30. and the pore volume by the BJH method (Barrett-Joyner-Halenda). In practice, the weighed ground solids are introduced into glass tubes with a filler rod to limit the error in the measurement due to the dead volume of the glass tubes. A vacuum degassing of at least 6 hours at 150 °C is carried out at a vacuum of approximately 10 mbar. After degassing, the powder is weighed again. Then the glass tube is introduced into a specific surface area and porosity analyzer (TriStar 3000 from Micromeritics). The analysis is carried out at -196°C in the range of relative pressures from 0.01 to 0.99.

2.5. Catalytic tests – total oxidation of benzene

Since most of the catalysts synthesized in this thesis are oxidizing, their catalytic activity is tested in VOCs degradation, by comparing their ability to totally oxidize benzene in the gas phase at different temperatures (Eq.E.1). The primary purpose of this test is to evaluate the impact of the modifications introduced in the synthesized solids, rather than to develop the best catalysts for this specific reaction.

$$C_6H_6 + \frac{15}{2}O_2 \rightarrow 6CO_2 + 3H_2O \qquad (Eq.E.1)$$

The catalysts tested are sieved to achieve a particle size ranging between 200 and 315 µm. A constant mass of 100 mg of catalyst, mixed with 400 mg of glass beads measuring between 350 and 500 µm, is introduced into the reactor between 2 layers of quartz wool so that the different compared catalysts always occupy the same volume within the reactor. The reaction gas, containing 200 ppm by volume of benzene (from a gas bottle of 2000

ppm, diluted with He, from Nippon gases) and 10 vol% O_2 (gas bottle from Air Liquid, purity ≥ 99.995%), is continuously supplied to the reactor at a flow of 100 mL/min throughout the analysis, with He serving as the carrier gas. The reagent-to-catalyst volume ratio per hour (VVH) is maintained at approximately 60000 h^{-1}. The reactor operates within a temperature range from 50 to 400°C, with increments of 50°C per stage. At the outlet of the reactor, the gas effluent is directed to a Varian CP-3800 gas chromatograph equipped with a CP-sil 8CB column and a flame ionization detector (FID). He is used as the GC carrier gas and the analysis is conducted at a constant temperature of 80°C. To calculate the remaining (not converted) benzene, we maintain each tested temperature for 90 min. During this time, six injections of the reactor outlet gas are performed, but only the 4 last injections (when the tested temperature is stabilized) are considered.

The quantification assumed that at the initial reactor temperature, i.e. 50°C, benzene does not undergo any conversion, and that the peak area at this temperature signifies 0% conversion. Using this reference area, the benzene conversion for each temperature stage is calculated using Eq.E.2:

$$\frac{peak\ area\ at\ 50°C - peak\ area\ at\ a\ given\ temperature}{peak\ area\ at\ 50°C} * 100 \quad (Eq.E.2)$$

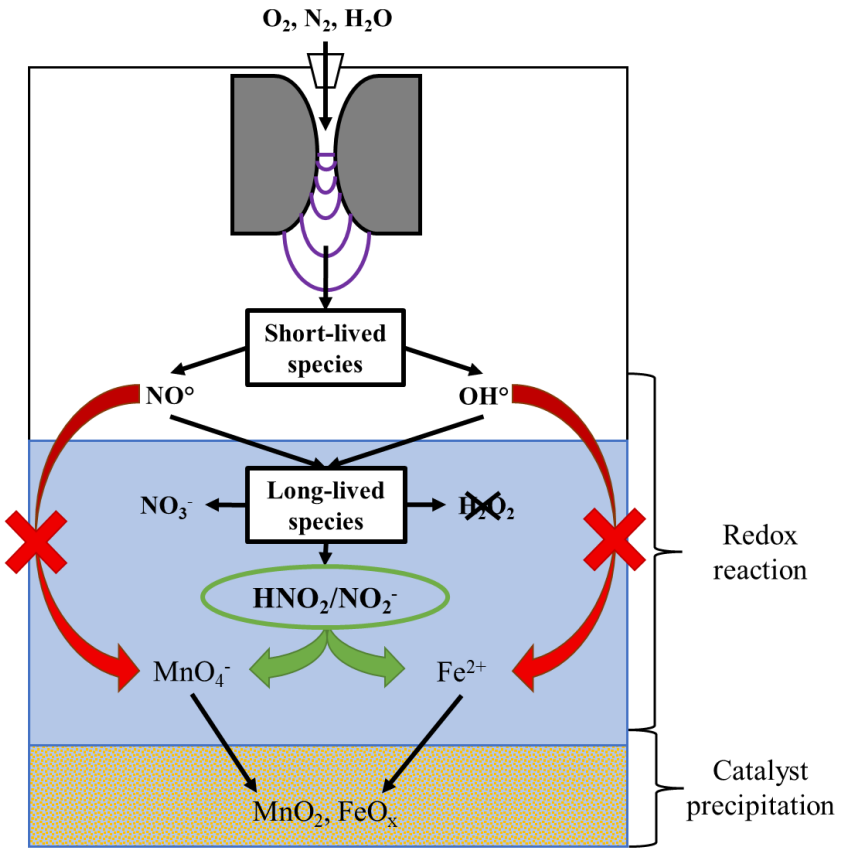
A blank test is conducted under the previously described catalytic conditions, using 500 mg of glass beads measuring between 350 and 500 µm in place of a catalyst.

Part I - Enhancing understanding of the GP catalysts synthesis method

Abstract

The purpose of the Part I is to enhance the understanding of the complete GP synthesis method by thoroughly exploring its functioning. This part is divided into 2 chapters. The first chapter (Chapter 1) is dedicated to comprehending the mechanism underlying the precipitation process of a metal precursor when exposed to GP. The aim is to ascertain the plasma species responsible for initiating the oxidoreduction leading to precipitation and to understand how the associated reactions occur within the GP system. We discovered that, contrary to what was stated in the literature before, OH radicals are not responsible for oxidizing the exposed precursors. Instead, we found that long-lived species, particularly HNO_2 and/or NO_2^-, are the main active agents. Additionally, we observed that oxygen-based species significantly impact the reaction. The second chapter (Chapter 2) consists in investigating the parameters influencing the ability of certain precursors to react or not via humid air GP. Various factors impacting a precursor's ability to undergo precipitation through GP are examined, including solubility, medium pH, the standard potential of redox reactions, and the nature of the metal precursor. The aim is to enhance comprehension of the method, creating a dichotomous key allowing us to predict the precipitation of any type of metal precursor, and ultimately enabling the synthesis of a broader range of catalysts.

Chapter 1 - What are the species involved in the gliding arc plasma synthesis of heterogeneous catalysts?



Abstract

Gliding arc plasma (GP) is an innovative method for synthesizing heterogeneous catalysts, but the exact reactions involved in catalyst formation remain unclear. The hypothetical reaction from the literature currently considers OH and NO radicals in the catalyst formation (metal (hydr)oxide) when precursors (metal salts) are exposed to plasma. Yet, these reactions remain unverified, and other reactive plasma species have never been considered to exert an influence on the precipitation. Therefore, this chapter investigates which species are responsible for the oxidoreduction of precursors exposed to the GP. Experiments with a OH radical scavenger (coumarin) in presence of iron precursors showed that theses radicals are not the sole contributors in the oxidation of the precursors, suggesting that other plasma-generated species might contribute to the oxidation process, such as long-lived species. Further studies showed that $FeSO_4$ and $KMnO_4$ formed similar precipitates when added in demineralized water pre-exposed to plasma as when directly exposed to the GP. This suggests that the predominant initiators of the precipitation are the long-lived species, identified as NO_3^- and HNO_2/NO_2^- in our system. We then demonstrate indeed that HNO_2/NO_2^- species play a prominent role in the plasma precipitation process, which has never been reported before. However, further tests indicates that a higher yield of precipitate is obtained by exposing $KMnO_4$ and $FeSO_4$ to O_2 as plasma gases, suggesting that oxygen-based species also influence the precipitation.

The results presented in this chapter have been published in:

Fanny Hanon, Sophie Hermans, Eric M. Gaigneaux, What are the species involved in the gliding arc plasma synthesis of heterogeneous catalysts?, Catalysis Today, Volume 430, 2024, 114550

https://doi.org/10.1016/j.cattod.2024.114550



1. Introduction

As mentioned in the General Introduction, section 3.3.2, the GP reactor is currently employed in various applications, including heterogeneous catalysts synthesis [31,33,42,48,50,57,61]. This method has already demonstrated its potential for synthesizing metal (hydr)oxides (TiO_2, $FeOOH/FeO_x$, MnO_2, SnO_2, WO_3) and supported catalysts (FeO_x/Kaolinite, TiO_2/SnO_2) with good properties and interesting catalytic activity when used for pollutant degradation in both gaseous and liquid phases (Table I.3) [42,56–61,64]. Currently, all the hypothetical reactions suggested in the literature to depict the formation of solid catalysts when their precursors (usually soluble metal salts) are exposed to GP, involve only the radicals OH and NO (Table I.3). It has been stated that "When directed to metallic aqueous solutions, thanks to the oxidizing ($HO^{\cdot}$) and reducing ($NO^{\cdot}$) characters of the radicals it contains, the discharge induces the precipitation of the corresponding metal (hydr)oxides" [59]. Nevertheless, these radicals do not represent all the so-called "Reactive oxygen and nitrogen species" (RONS) generated. Numerous other "short-lived" (with lifetime in the nanosecond-millisecond range) and "long-lived" species (lifetime > 1s) are formed, as already mentioned in the General Introduction, section 3.3.1 (Figure I.12, Table 1.1). And these species can also have a role as oxidizing/reducing and/or precipitating agents (Figure I.10) [31,37,39,48,49,51–53]. However, to the best of our knowledge, none of these additional species have ever been considered to exert an influence on the precipitation process. In fact, the proposed hypothetical reactions have not been proven, leaving us in a state of uncertainty regarding which species do trigger the oxidoreduction leading to the precipitation and how the corresponding reactions do occur within the GP system.

Table 1.1: Overview of the short and long-lived RONS generated in liquid media exposed to humid air plasma and how these species have been quantified in the literature ; adapted from [52] ; completed with [53]

	Short-lived RONS			**Long-lived RONS**	
	Species	**Detection methods**		**Species**	**Detection methods**
From dissociation of water molecules	OH, HOO	• Fluorospectrophoto-metry using coumarin as OH radical scavenger • Electron-spin resonance spectroscopy (ESR) with 5,5-Dimethyl-1-pyrroline N-oxide (DMPO) used as scavenger of OH and O_2^- radicals	➔	H_2O_2	• UV-vis absorption spectroscopy using $TiOSO_4$ • Fluorescence method with Amplex red hydrogen peroxide assay kit • Commercial peroxide test strips
	$e^-_{solvated}$, H			O_3, O_2, O_2^-	
In presence of air	$ONOO^-$	UV-vis absorption spectroscopy		HNO_3/NO_3^-	• Nitrate assay kit • Nitrate selective electrode • UV-vis spectroscopy
	NO	Electron-spin resonance spectroscopy (ESR)	➔	HNO_2/NO_2^-	• Nitrite assay kit • UV-vis spectroscopy • Colorimetric method using Griess reagent • Nitrite test strips

Therefore, the objective of this chapter is to progress in the identification of which species, among those various ones generated by humid air GP, are truly accountable for the oxidation or reduction of precursors leading to the precipitation of (hydr)oxides when metal salts in solubilized forms are exposed to the plasma.

To test the validity of the hypothesis suggested in the literature that NO and OH radicals are accountable for the oxidation or reduction of precursors that is needed for (hydr)oxides formation, we will check whether precipitation occurs or not within the GP reactor in the absence of these species. The role of OH was the centre of our attention as we here after report experiments in which OH is removed from the medium thanks to the use of a specific OH radical scavenger, namely coumarin (cou), and the concomitant fluorospectrophotometric quantification of their product, 7-hydroxycoumarin (7HC) (Figure 1.1) [67–75].



Figure 1.1: Formation of the 7-hydroxycoumarin from the reaction between coumarin and OH radical

After clarifying the role of OH in the precipitation of precursors exposed to GP, our investigation extended to the identification of alternative species among the long-lived species plasma-generated ones that contribute to the precipitation process. By a UV-visible spectroscopic analysis and additional dedicated experiments, the role of H_2O_2, NO_3^- and NO_2^- was addressed.

Finally, the use of other types of plasma gases (He, Ar, O_2, and N_2) was explored to observe the impact of different types of plasma species on the precipitation of the metal precursors exposed to the GP.

2. Materials and methods

2.1. Materials

$FeSO_4.7H_2O$ (≥ 99%) and 1,10-phenanthroline (1,10-phenanthroline monohydrate, ≥ 99.0%) were purchased from Sigma Aldrich.

$KMnO_4$ (≥ 99%), $NaNO_2$ (≥ 98%) and HNO_3 (65%) were obtained from Roth, $NaNO_3$ (≥ 99%) from Merck and the coumarin (≥ 99%) from Thermo Scientific.

All the solutions were prepared with demineralized water as solvent.

2.2. Methods

2.2.1. Conditions used when a solution is exposed to the GP

The gliding arc plasma system used in this study is the same as the one presented in Experimental, section 1.

2.2.2. Are OH responsible for the oxidation of precursors exposed to GP?

Before challenging the hypothesis that OH are responsible for the oxidation of precursors exposed to GP, our initial step involved observing the formation of OH in an aqueous solution when exposed to the plasma. For this purpose, a 10^{-3} mol/L solution of coumarin (cou) was subjected to plasma exposure for 120 min. Determining the appropriate concentration of coumarin to effectively react with OH radicals is challenging as if the concentration is too low, the reaction may be too slow, allowing OH to react non-specifically with coumarin. Conversely, if the concentration is too high, the coumarin may either fail to dissolve adequately in water or create steric hindrance, preventing rapid interaction with OH radicals. Therefore, this concentration was selected based on previous literature to facilitate a rapid reaction between cou and OH while minimizing the potential consumption of OH by compounds other than cou [68,71]. 10 mL of the solution was collected at 30 min intervals for 2h and analysed by fluorospectrophotometry (Cary Eclipse fluorescence spectrophotometer (from Agilent)) with a slit of 10. The resulting 7HC produced through the reaction between cou and OH was analysed using an excitation wavelength of 346 nm, with the emission wavelength being observed around 456 nm [67–75]. It is worth noting that quantifying the 7HC formed does directly give the amount of OH generated in the medium, as the reaction between cou and OH produces multiple products. Indeed, several hydroxycoumarins can form alongside 7HC, though none are fluorescent and therefore do not interfere with the 7HC measurement [76]. While these additional products can be observed using UV-vis spectroscopy, their overlapping absorption wavelengths make it impossible to quantify each individually. Consequently, we relied on the qualitative observation of 7HC formation as sufficient evidence of OH radicals presence during exposure.

Afterwards, we explored whether the oxidation of precursors exposed to GP remains feasible in the absence of OH. To do that, we exposed a 10^{-2} mol/L solution of $FeSO_4.7H_2O$ in the presence of 10^{-2} mol/L of cou to the GP for 1h (solution named "$FeSO_4$ + cou 10^{-2}"). This precursor was

selected because Fe^{2+} precursor was already known to oxidize into FeOOH upon exposure to GP [61]. Furthermore, this concentration of cou was chosen to effectively block as much OH in the system as possible without exceeding the solubility limit of cou in water. The resulting precipitate was collected through centrifugation (24490 G for 30 min), subjected to two washing cycles with demineralized water, dried in an oven under air at 110°C for 22h ± 2h and then calcined in a muffle furnace under air at 400°C for 2h.

2.2.3. Do the long-lived species influence the precipitation process of precursors exposed to the GP?

In order to identify other species implicated in the GP assisted precipitation, we conducted a two-step experimental approach. Our initial focus was on determining the eventual involvement of long-lived species. To confirm their role in the oxidation of precursors, we exposed 450 mL of demineralized water to plasma for 1h, recovered it and then introduced 10^{-2} mol/L of $FeSO_4.7H_2O$ in it, as Fe^{2+} precursor is known to oxidize upon GP exposure. The resulting mixture was stirred at room temperature for 1h (named "water 60 min + $FeSO_4$ 60 min after"). To ascertain whether these long-lived species participate in precursor reduction, we exposed 450 mL of demineralized water to GP for 30 min, collected it and then introduced 10^{-2} mol/L of $KMnO_4$ in it (named "water 30 min + $KMnO_4$ 30 min after"), as $KMnO_4$ precursor is known to reduce into MnO_2 upon GP exposure [59]. The resulting mixture was stirred at room temperature for 30 min.

Subsequently, our focus shifted toward the identification of long-lived species generated within our GP reactor and which of them is involved in precursor precipitation. To achieve this, we subjected demineralized water to plasma exposure for 1h and performed UV-visible spectroscopic analysis (Shimadzu UV-3600 PLus) at 15 min intervals for 1h. The samples are contained in a quartz cuvette (100-QS, Hellma Analytics) of a standard optical path of 10 mm. The transmission spectrum is recorded from 200 to 300 nm with photomultiplier tube (PMT) detector since the absorption spectrum of long-lived species extends below 300 nm and that no absorption occurs in the visible and near infrared ranges (400–900 nm) [77]. For the quantification of NO_3^- and NO_2^-, calibration curves using $NaNO_2$ and $NaNO_3$ were established (Supplementary Information SI.1). The matrix used to measure the blank is pure demineralized water. The concentrations of the species are determined from an absorbance spectrum (intensity versus wavelength) using the Beer-Lambert law where ε is the

molar absorptivity of the chemical species at a certain wavelength, l is the optical path length, and C is the concentration of the species (Eq.1.1).

$$A = \varepsilon l C \qquad (Eq.1.1)$$

The measurement of NO_2^- intensity absorbance was performed at 240 nm, as it exclusively absorbs at this wavelength. Quantification of NO_3^- was performed by measuring the absorbance at 210 nm, with the contribution from previously calculated NO_2^- absorbance subtracted (Supplementary Information SI.2). Along the experiment, the pH of the solution was measured at 15 min intervals. The impact of pH on this quantification was previously reported in the literature and taken into account here to select the appropriate wavelengths for our analysis [77].

To identify the long-lived species accountable for the precipitation process, we stirred 450 mL of a 10^{-2} mol/L solution of $KMnO_4$ or $FeSO_4$ and introduced at 15 min intervals a precise amount of HNO_3 or $NaNO_2$ (experiments named "$FeSO_4$+$NaNO_2$ (+HNO_3)" and "$KMnO_4$+$NaNO_2$ (+HNO_3)"). The quantity added was chosen to align with the amount of NO_3^- and NO_2^- formed during the plasma exposure (Figure 1.8, Table 1.2). This protocol was executed over a duration of 30 min for $KMnO_4$ and 60 min for $FeSO_4$. It should be noted that during the addition of $NaNO_2$, a small quantity of HNO_3 was also introduced to maintain a pH similar to the value attained during plasma exposure of pure demineralized water (Figure 1.8).

Table 1.2: Quantity of $NaNO_2$ and HNO_3 added in the experiment aiming at identifying the long-lived species accountable for the precipitation process

	Duration of the experiment (min)	**HNO_3**		**$NaNO_2$**	
		Concentration of HNO_3 added in the solution in total (mol/L)	**pH**	**Concentration of $NaNO_2$ added in the solution in total (mol/L)**	**pH**
$FeSO_4$	0	0	4	0	4.1
	15	$3.2*10^{-5}$	3.5	$1.6*10^{-3}$	3.5
	30	$4.0*10^{-4}$	3.4	$2.5*10^{-3}$	3.4
	45	$4.4*10^{-4}$	3.2	$3.7*10^{-3}$	3.2
	60	$5.6*10^{-4}$	3	$4.0*10^{-3}$	3
$KMnO_4$	0	0	6.2	0	6.3
	15	$3.2*10^{-5}$	3.9	$1.6*10^{-3}$	3.5
	30	$4.0*10^{-4}$	3.4	$2.5*10^{-3}$	3.2

For all the experiments presented above, we subjected the $FeSO_4.7H_2O$ solution to a 1h synthesis and the $KMnO_4$ solution to a 30 min synthesis because these durations represent the respective optimal plasma exposure periods to obtain the highest yield and quality of catalyst synthesized using these precursors. Furthermore, the resulting precipitate was collected through centrifugation (24490 G for 30 min), subjected to two washing cycles with demineralized water, dried in an oven under air at 110°C for 22h ± 2h and then calcined in a muffle furnace under air at 400°C for 2h.

Moreover, for all the experiments presented here, the quantity of precursor transformed into a precipitate was quantified by UV-visible spectroscopy (in the same conditions as explained before). MnO_4^- ions absorb within the wavelength range of 425 to 625 nm, with a maximum absorbance at 525 nm. Therefore, it is possible to determine the quantity of $KMnO_4$ that has reacted by analyzing the solution before and after the solid synthesis. To avoid an absorbance saturation, all $KMnO_4$ solutions were diluted 20 times. On the other hand, to observe the Fe^{2+} ions from the iron precursor, the introduction of a complexing agent is imperative. When combined, Fe^{2+} and 1,10-phenanthroline (phen) interact in a 1:3 ratio, forming an orange-red coloured complex $[Fe(phen)_3]$ when in aqueous medium (Eq.1.2) [78]. To quantify this complex, the absorbance is gauged at 510 nm via UV-visible spectroscopy. As for $KMnO_4$ quantification, the evaluation of reacted Fe^{2+} necessitates an analysis of the solution before and after the solid synthesis. To perform this experiment, a solution containing 66 µL of the sample is mixed with 5 mL of a phen solution (100 mg of phen in 100 mL of demineralized water) within a 100 mL flask. After a mixing period of 15 min to allow a full colour development, the flask is then filled to the mark with deionized water.

$$Fe^{2+} + 3phen \rightarrow [Fe(phen)_3]^{2+} \qquad (Eq.1.2)$$

The final yield of formed precipitate for each precursor was computed using Eq.1.3.

$$Yield(\%) = \left(\frac{[precursor]_i - [precursor]_f}{[precursor]_i}\right) * 100 \qquad (Eq.1.3)$$

A calibration curve was established for both precursors in order to determine the quantity of MnO_4^- and Fe^{2+} within the solutions (Supplementary Information SI.3).

2.2.4. What is the impact of the type of plasma gas on the precipitation of precursors exposed to the GP?

To determine whether plasma species other than nitrogen-based ones could trigger the precipitation of the exposed precursors, various types of plasma gases were tested. The plasma gases used were He (≥ 99.999%, Air liquide), Ar (≥ 99.999%, Air liquide), O_2 (≥ 99.995%, Air liquide), N_2 (≥ 99.999%, Air liquid), dry air (N_2+O_2 ≥ 99.999%, Air liquid), and humid air (obtained by passing dry air N_2+O_2 ≥ 99.999%, Air liquid, by a saturator filled with demineralized water maintained at room temperature, i.e. about 15-20°C). The gas flow rates were chosen to achieve a plume length similar to that of humid air (He: 433 L/h, Ar: 316 L/h, O_2: 200 L/h, N_2: 400 L/h, dry air: 400 L/h, humid air: 400 L/h). For O_2, the chosen flow rate was insufficient to create a long enough plume for comparison with other experiments. However, to maintain a stable plume and avoid unstable arc forming at the liquid surface, a lower flow rate was used during the experiment with O_2.

To assess the impact of these other species on the oxidation of the precursors, we exposed 450 mL of 10^{-2} mol/L of $FeSO_4.7H_2O$ for 1 h. For the reduction of the precursors, 450 mL of 10^{-2} mol/L of $KMnO_4$ was exposed for 30 min. These precursors were dissolved in ultrapure water (18.2 MΩ, 3 ppb of total organic carbon content (TOC)) to eliminate any potential nitrogen sources present in the demineralized water previously used. The quantity of precursor transformed into a precipitate was quantified by UV-visible spectroscopy, following the same conditions outlined in the Part I, Chapter 1, section 2.2.3.

Additionally, the formation of potential NO_3^- and NO_2^- species was investigated by exposing 450 mL of ultrapure water to the GP exposure for 60 min with each type of plasma gas. The exposed water was analyzed using UV-visible spectroscopy every 15 min, as described in Part I, Chapter 1, section 2.2.3.

The pH of the solution was also measured every 15 min for each type of plasma gas used. Each experiment was performed twice for each plasma gas to obtain an average quantity of plasma species formed.

2.3. Characterization of the solids formed

All the instrumental characterizations used here (XRD, XPS, SEM, EDX, N_2-physisorption) were done after calcination of the solids formed, except for XRD that was done both before and after the calcination step.

All the characterizations performed in this chapter were carried out as presented in Experimental, section 2.

3. Results and discussion

3.1. Are OH radical responsible for the oxidation of precursors exposed to GP?

Before using cou as radical scavenger in the presence of precursors, we confirmed that OH radicals are generated in an aqueous solution exposed to humid air GP in our conditions. The emission peak of 7HC (around 456 nm) indeed increases over time when a 10^{-3} mol/L solution of cou is subjected to plasma exposure (Figure 1.2). This observation signifies an augmentation in the quantity of OH generated within the solution throughout the exposure period.

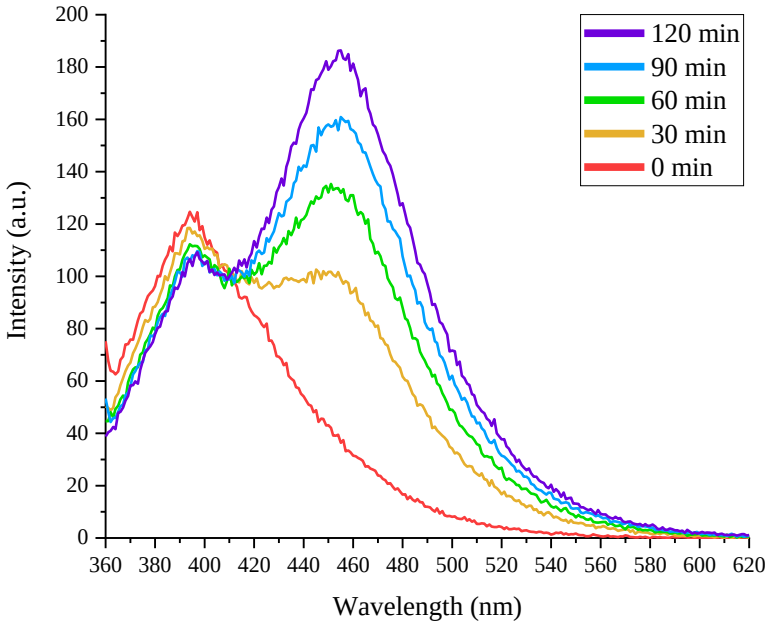


Figure 1.2: Evolution with time of fluorescence emission peak of the 7HC produced when a 10^{-3} mol/L solution of cou is exposed to humid air GP

With the presence of cou in a $FeSO_4$ solution, the formation of a precipitate occurs slightly more slowly than without. The yield of formed precipitate is also slightly lower but the formed solids develop identical specific surface areas and pore volumes in both cases (Table 1.3).

Table 1.3: Time required for the appearance of a precipitate, yield of formed precipitate, specific surface area and pore volume of solid obtained after calcination, for $FeSO_4$ exposed to GP with or without cou

	Time required for the formation of a precipitate (min)	**Yield of formed precipitate (%)**	**Specific surface area (m^2/g)**	**Pore volume (cm^3/g)**
$FeSO_4$	± 15	53 ± 1	49	0.14
$FeSO_4$ + cou 10^{-2}	± 20	48 ± 1	49	0.15

Furthermore, the diffractograms of both solids exhibit identical peaks corresponding to goethite (FeOOH) before calcination (Figure 1.3) and hematite (Fe_2O_3) and $FeOHSO_4$ after calcination (Figure 1.4).

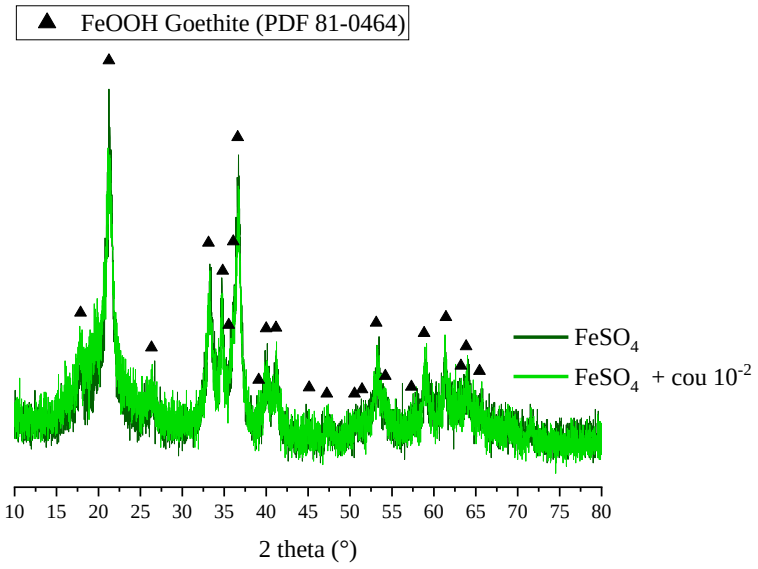


Figure 1.3: XRD data of solids formed before calcination, in the case of $FeSO_4$ exposed to GP with or without cou

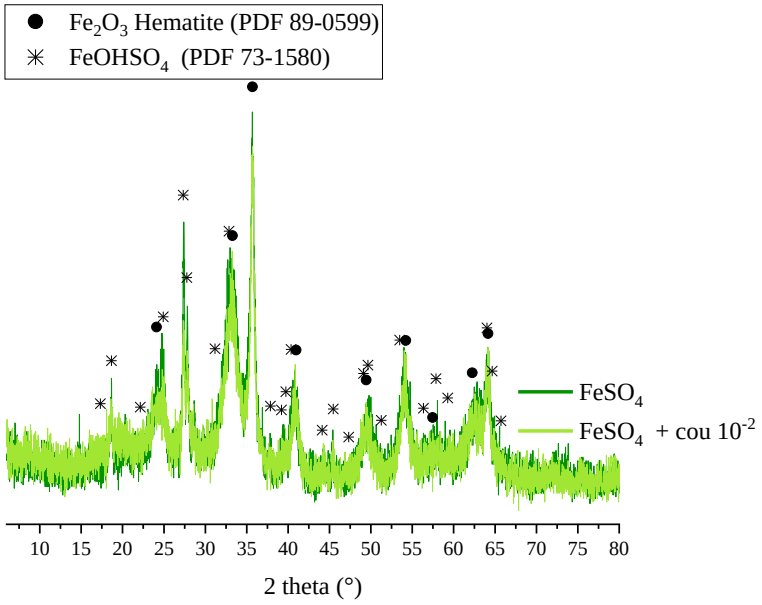


Figure 1.4: XRD data of solids formed after calcination, in the case of $FeSO_4$ exposed to GP with or without cou

As the time to observe the formation of the precipitate increases and the yield of recovered solid at the end of the synthesis decreases when the exposure is done in the presence of the radical scavenger, it suggests that OH indeed potentially facilitates the oxidation of the precursor, and therefore its precipitation. Furthermore, the composition of the 2 solids is different. The solid formed in the presence of the radical scavenger possesses less Fe and more S both at its surface (as measured by XPS) and in its bulk (as measured by EDX) (Table 1.4). The percentages of each phase can be computed by assessing the quantity of Fe linked to the $FeOHSO_4$ phase (1S for 1Fe) and the remaining amount of Fe being from the Fe_2O_3 phase. Through this calculation, we observe that a higher proportion of $FeOHSO_4$ (and correspondingly a lower proportion of Fe_2O_3) is developed in presence of the cou (Table 1.4). The fact that the proportions of phases differ when the exposure is done with or without OH scavenger can be explained by examining the formation mechanism of these 2 phases within the plasma system. Both the $FeOHSO_4$ and Fe_2O_3 phases consist of Fe^{3+} species, indicating that the precursor must undergo oxidation in the solution before being capable of precipitating. Specifically, when $FeSO_4$ is introduced into the solution, it dissociates into Fe^{2+} and SO_4^{2-} ions. Subsequently, the plasma species oxidize Fe^{2+} to Fe^{3+}. When present in water, Fe^{3+} ions are unstable, leading to their spontaneous hydrolysis into FeOOH (later transformed to Fe_2O_3 through calcination)

(Eq.1.4). Fe^{3+} may also engage in reactions with other ions within the medium, including SO_4^{2-} coming from the precursor (Eq.1.5). Given that the concentration of SO_4^{2-} is lower that of H_2O, the occurrence of this reaction becomes less probable. Consequently, less $FeOHSO_4$ phase is formed, likely as an amorphous phase before calcination, as it is not detected by XRD before calcination. The observed decrease in the formation of the $FeOHSO_4$ phase in the presence of OH radicals may indicate an interaction between the OH and the sulfates. Precisely, the literature reports that within a medium housing reactive species like solvated electrons or radicals, SO_4^{2-} ions might transform into SO_3^{2-}, subsequently evolving into the radical SO_4^{-} [79,80]. In fact, this radical exhibits higher oxidation potential and longer lifetime compared to OH, which can, in turn, provide an explanation for the slightly increased amount of solid formed in absence of the radical scavenger [79,80].

$$Fe^{3+} + 2H_2O \rightarrow FeOOH + 3H^+ \qquad (Eq.1.4)$$

$$Fe^{3+} + SO_4^{2-} + H_2O \rightarrow FeOHSO_4 + H^+ \qquad (Eq.1.5)$$

Table 1.4: Bulk (EDX) and surface (XPS) composition and % of each phase developed (calculated from the at% of Fe and S obtained by EDX analysis) in solids formed after calcination in the case of $FeSO_4$ exposed to glidarc plasma with or without cou

	Fe (at%)		**O (at%)**		**S (at%)**		**% of each phase formed (%)**	
	XPS (Fe2p)	**EDX**	**XPS (O1s)**	**EDX ***	**XPS (S2p)**	**EDX**	**$FeOHSO_4$ ****	**Fe_2O_3**
$FeSO_4$	34.3	19	62.3	73	3.5	2	11	89
$FeSO_4$ + cou 10^{-2}	27.6	14	66.2	83	6.2	3	21	79

* The at % of O obtained by EDX is likely overestimated due to the underlying adhesive carbon tape used to fix the sample.

** $\%\ of\ FeOHSO_4 formed = \left(\frac{\%Fe_{(from\ FeOHSO_4)}}{\%Fe_{(total)}}\right) * 100\ where\ \%Fe_{(from\ FeOHSO_4)} = \%S_{(total)}$

These results show that OH radicals have an impact on the reaction of the precursor under GP exposure, as when its presence is diminished in the medium, the yield of formed solid decreases slightly and the amount of each phases developed changes (due to the potential interaction between OH and ions from the precursors). Nevertheless, considering that even without OH in the medium, we still obtain almost the same yield and developed solids with similar features, it suggests that other plasma-generated species may exert a similar oxidation effect as these OH radicals. Consequently, the presence of the latter is not absolutely required to trigger the precipitation process.

3.2. Do the long-lived species influence the precipitation process of precursors exposed to the GP?

3.2.1. Can the long-lived species initiate the precipitation?

The hypothesis emitted after the conclusion drawn above regarding the OH is that long-lived species generated by GP also take part in the precipitation of products from the exposed precursors. To test this hypothesis, we exposed demineralized water to the plasma discharge, recover the treated water and then introduced in it $FeSO_4$ or $KMnO_4$ as metal precursors. In these conditions, only the long-lived species are expected to persist in the water, and consequently, they alone could potentially initiate the precipitation of some solid products. Furthermore, since $FeSO_4$ is oxidized and $KMnO_4$ reduced upon plasma exposure, the use of these 2 precursors in comparison allows determining whether long-lived species have the capacity to undergo both reduction and oxidation processes.

In this experiment, a precipitate was formed from both solubilized precursors, appearing after approximately the same exposure duration as when directly exposed to the GP (Table 1.5). The formed solids also develop similar specific surface areas and pore volumes in both cases, although the values are slightly higher when $FeSO_4$ is introduced to the demineralized water after the exposure (Table 1.5). The yield of solid formed is approximately the same for $KMnO_4$ when directly exposed to the discharge or when added in a pre-exposed water. On the other hand, the solid recovered is more abundant with $FeSO_4$ precursor is added in the pre-exposed water (Table 1.5). Therefore, the fact that the yield for both precursors is either similar or higher when introduced into pre-exposed water suggests that the long-lived species alone possess the capability to initiate the precipitation reaction. Furthermore, it confirms that OH

radicals are indeed not necessary to initiate to precipitation of precursors, as their lifetime is too short to ensure their presence in a pre-exposed water.

Table 1.5: Time required for the appearance of a precipitate, yield of formed precipitate, specific surface area and pore volume of solid obtained after calcination, when $FeSO_4$ and $KMnO_4$ undergo a) direct exposure to the GP or b) introduction after demineralized water has been exposed independently

	Time required for the formation of a precipitate (min)	**Yield of formed precipitate (%)**	**Specific surface area (m^2/g)**	**Pore volume (cm^3/g)**
a) $FeSO_4$	± 15	53 ± 1	49	0.14
b) Water 60 min + $FeSO_4$ 60 min after	± 15	79 ± 5	59	0.2
a) $KMnO_4$	± 5	18 ± 1	≈ 0	/
b) Water 30 min + $KMnO_4$ 30 min after	± 5	15 ± 2	≈ 0	/

Regarding the diffractograms of the obtained solids, they exhibit identical patterns whenever the precursor is added in the direct exposure mode or after the preexposure of water to the glidarc. In the case of $FeSO_4$, the resulting solid is identified as the FeOOH phase before calcination and a mixture of Fe_2O_3 and $FeOHSO_4$ after calcination, while for $KMnO_4$, the formed solid corresponds to the $KMnO_2$ phase both before and after calcination (Figure 1.5, Figure 1.6).

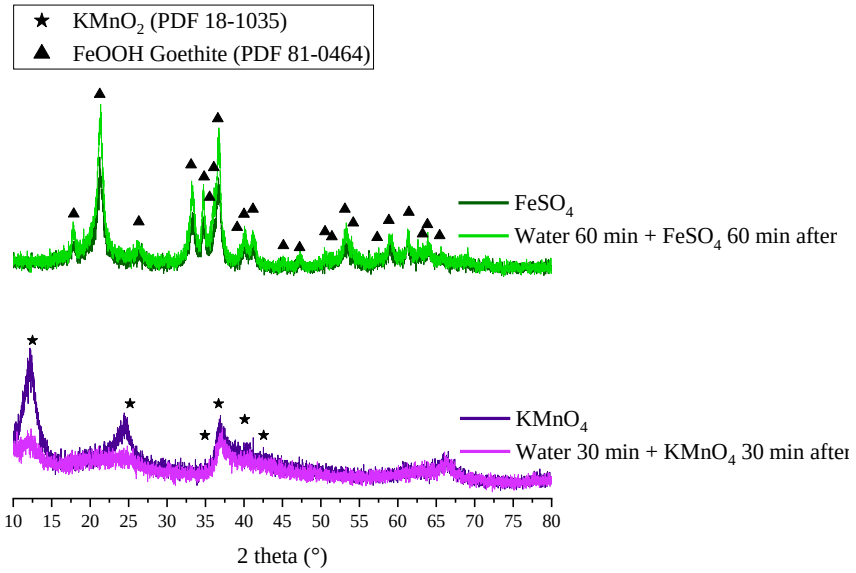


Figure 1.5: XRD data of solids obtained before calcination when $FeSO_4$ and $KMnO_4$ undergo direct exposure to the GP or introduction after demineralized water has been exposed independently

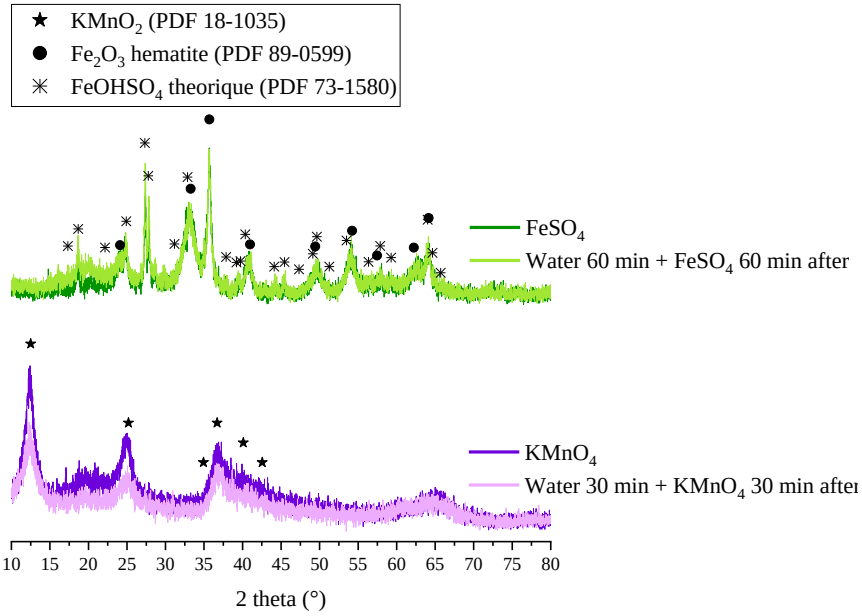


Figure 1.6: XRD data of solids obtained after calcination when $FeSO_4$ and $KMnO_4$ undergo direct exposure to the GP or introduction after demineralized water has been exposed independently

Within its error margin (1 at%), EDX shows that the solids obtained along the two different procedures have the same bulk composition. On the other

hand, the variations in their surface compositions measured by XPS exceed the method's error margin. More precisely, when the precursors are introduced subsequently to the exposure of demineralized water to the plasma, the resulting solids exhibit less Fe or Mn and more S or K at their surface. For the $FeSO_4$ precursor, it is possible to calculate the quantity of each phase developed. Slightly more $FeOHSO_4$ is generated at the surface when the precursor is introduced after the glidarc pre-exposure of water (Table 1.6). This phenomenon can be explained on the basis of the previously proposed hypothesis. As SO_4^{2-} ions could interact with OH, introducing the precursor after water exposure, wherein no OH is present anymore, results in a greater abundance of these ions available for the formation of the $FeOHSO_4$ phase. However, regarding the solids formed from $KMnO_4$, the observed variation in the surface % of K is likely due to the washing step. $KMnO_4$ forms small $KMnO_2$ particles that are difficult to recover completely by centrifugation. Consequently, to retain more particles during the washing step and prevent excessive loss, less fresh water is used than with other precursors. This reduced washing may result in a higher residual amount of K^+ remaining after the drying step, leading to an increased presence of K^+ at the solid's surface. Therefore, we believe that the amount of K remaining at the surface of the solid is not influenced by the plasma exposure.

Considering these results, we can assert that the predominant initiators of the precipitation for exposed precursors in the GP reactor are more likely the long-lived species.

Table 1.6: Bulk (EDX) and surface (XPS) composition and % of each phase developed (calculated from the at% of Fe and S obtained by EDX data) of solids obtained after calcination when $FeSO_4$ and $KMnO_4$ undergo a) direct exposure to the GP or b) introduction after demineralized water has been exposed independently

	Fe or Mn (at%)		**O (at%)**		**S or K (at%)**		**% of each phase formed (%)**	
	XPS (Fe2p or Mn2p)	**EDX**	**XPS (O1s)**	**EDX***	**XPS (S2p or K2p)**	**EDX**	**$FeOHSO_4$ ****	**Fe_2O_3**
a) $FeSO_4$	34.3	19	62.3	73	3.5	2	11	89
b) Water 60 min + $FeSO_4$ 60 min after	31.3	21	64.6	76	4.1	2	10	90
a) $KMnO_4$	28.5	22	62.0	72	9.5	6	/	/
b) Water 30 min + $KMnO_4$ 30 min after	27.0	23	60.8	70	12.1	7	/	/

** The at % of O obtained by EDX is likely overestimated due to the underlying adhesive carbon tape used to fix the sample.*

** $\%\ of\ FeOHSO_4 formed = \left(\frac{\%Fe_{(from\ FeOHSO_4)}}{\%Fe_{(total)}}\right) * 100\ where\ \%Fe_{(from\ FeOHSO_4)} = \%S_{(total)}$ $(Eq.1.7)$

3.2.2. What are the long-lived species created in aqueous medium exposed to humid air GP?

As mentioned in the introduction, the long-lived RONS produced by plasma, which are highlighted in the literature for their significant roles in the liquid phase, mainly include H_2O_2, HNO_3/NO_3^- and HNO_2/NO_2^- (exhibiting oxidizing and acidifying effects) [52]. However, at this stage we are uncertain about the presence of these species within our GP reactor. Therefore, a part of our study aimed at ascertaining whether these 3 key species are indeed generated within our system, prior to determining which among them is responsible for precipitating the solid products.

After exposing demineralized water to the GP and subjecting it to UV-vis spectroscopic analysis, several observations came to light. Firstly, no peaks are present beyond 250 nm, indicating the absence of H_2O_2 generation in our system (Figure 1.7). To firmly establish this, an alternative H_2O_2 detection method was employed, involving the exposure of Ti(IV) to the plasma and subsequently analysing the solution in UV-vis spectroscopy. If H_2O_2 is indeed produced in the medium, it leads to the formation of the yellow complex $[Ti(O_2)SO_4]xH_2O$, which absorbs around 400 nm [81,82]. To validate the absence of H_2O_2 formation in aqueous solution exposed to our GP, a solution consisting of 450 mL of 50 mL/L $Ti(SO_4)_2$ (15% solution, Fisher) was exposed to the plasma for 45 min. After that, direct analysis of the solution was conducted using UV-visible spectroscopy within the wavelength range of 300 to 600 nm. A blank solution of 50 mL/L $Ti(SO_4)_2$ in demineralized water served as the reference. Under these conditions, the creation of the $[Ti(O_2)SO_4]xH_2O$ complex was never observed. To confirm that $Ti(SO_4)_2$ is not decomposed by the GP, potentially explaining the lack of complex formation, a non-negligible quantity of H_2O_2 was introduced to the solution after the exposure. This led to a distinct shift in colour solution to a vibrant yellow, confirming the effectiveness of the complexation even after exposure. Consequently, these observations conduct to the conclusion that no H_2O_2 is generated within our experimental medium when exposed to the humid air GP.

This phenomenon can be explained if NO_2^- is generated within the system. In such instances, NO_2^- would quickly react with and consume the formed H_2O_2, offering an explanation for its non-observation (Eq.1.6). This has been previously proposed in the literature, pointing that the presence of N_2 species in the plasma gas hinders the observation of H_2O_2 resulting from its reaction with said species [83–85], as follows (Eq.1.6):

$$NO_2^- + H_2O_2 \rightarrow NO_3^- + H_2O \qquad (Eq.1.6)$$

On the other hand, we observe an increase in the absorption peak below 250 nm with the exposure time. This reflects the augmentation of NO_2^- and/or NO_3^- concentration (Figure 1.7). Quantifying these 2 species reveals a greater formation of NO_2^- in comparison to NO_3^- yet both building up with exposure time (Figure 1.8). The solution's pH decreases with the exposure time, corresponding to the formation of acids like HNO_2 and HNO_3. However, the pH appears to stabilize around 3, likely due to the buffering effect of HNO_2/NO_2^-, which has a pKa of 3.15. This means that, within this pH range, both HNO_2 and NO_2^- species coexist [86].

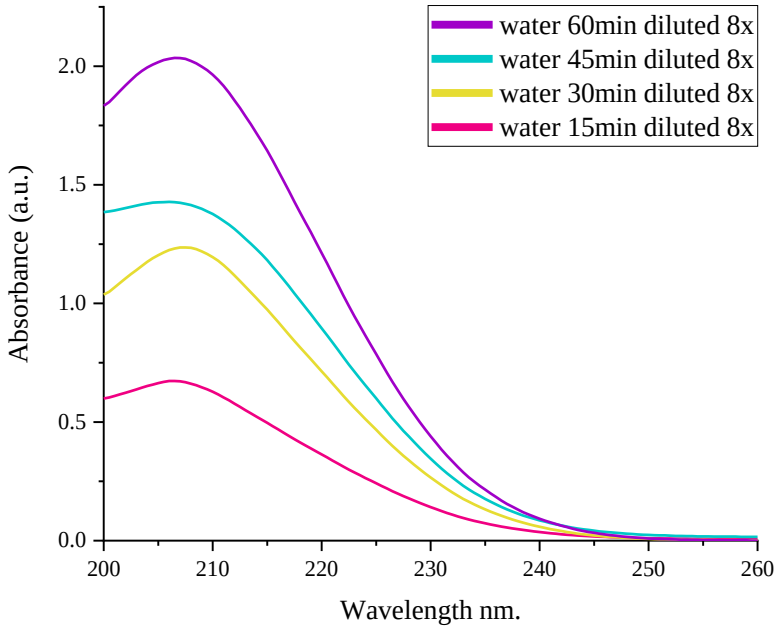


Figure 1.7: Evolution of the UV-visible spectrum absorbance of demineralized water along its exposure to the GP

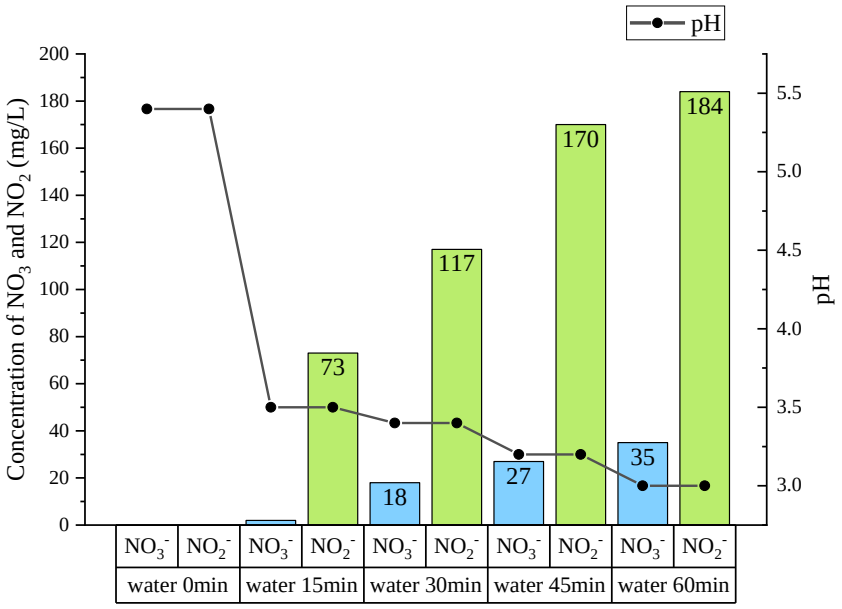


Figure 1.8: Concentration of NO_2^- and NO_3^- in demineralized water exposed to the GP for 1h and pH of the medium

3.2.3. Among the long-lived species, which ones do exert an influence on the redox and precipitation process?

Having established the composition and quantity of some long-lived species within our medium, we can now ascertain whether NO_3^- and/or HNO_2/NO_2^- are accountable for the precipitation phenomenon.

Upon introducing HNO_3 into solutions of $KMnO_4$ or $FeSO_4$, matching the concentration generated by GP, no precipitation was observed in either scenario. This reveals that NO_3^- does not trigger the precipitation. On the other hand, when $NaNO_2$ (along with HNO_3 to attain an equivalent pH as during the plasma exposure) is introduced to these precursor solutions, a precipitate forms in both cases. The solid appears after approximately the same time but the yield of formed precipitate in the case of $FeSO_4$ is higher when $NaNO_2$ is added, and lower in the case of $KMnO_4$. For both precursors, the formed solids develop similar specific surface areas and pore volumes as those recovered in the direct exposure experiments (Table 1.7).

Table 1.7: Time required for the appearance of a precipitate, yield of formed precipitate, quantity formed, specific surface area and pore volume of solid obtained after calcination when $FeSO_4$ and $KMnO_4$ undergo a) direct exposure to the GP or b) introduction of $NaNO_2$ ($+HNO_3$) without plasma exposure

	Time required for the formation of a precipitate (min)	**Yield of formed precipitate (%)**	**Specific surface area (m^2/g)**	**Pore volume (cm^3/g)**
a) $FeSO_4$	± 15	53 ± 1	49	0.14
b) $FeSO_4$ + $NaNO_2$ ($+HNO_3$)	± 15	69 ± 2	54	0.15
a) $KMnO_4$	± 5	18 ± 1	≈ 0	/
b) $KMnO_4$ + $NaNO_2$ ($+HNO_3$)	± 5	7 ± 1	≈ 0	/

Regarding the diffractograms of the obtained solids, they exhibit identical patterns irrespective of whether the precursor is exposed to the GP or if $NaNO_2$ ($+HNO_3$) is added to the solution. As observed before, in the case of $FeSO_4$, the resulting solid is identified as the FeOOH phase before calcination and a mixture of Fe_2O_3 and $FeOHSO_4$ after calcination, while for $KMnO_4$, the formed solid corresponds to the $KMnO_2$ phase before and after calcination (Figure 1.9, Figure 1.10).

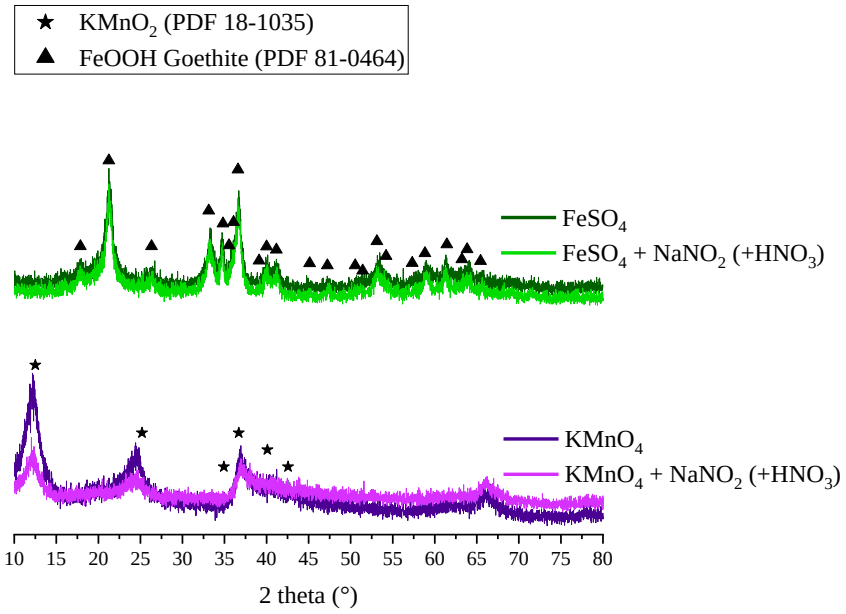


Figure 1.9: XRD data of solids obtained before calcination when $FeSO_4$ and KMnO4 undergo direct exposure to the GP or introduction of $NaNO_2$ ($+HNO_3$) without plasma exposure

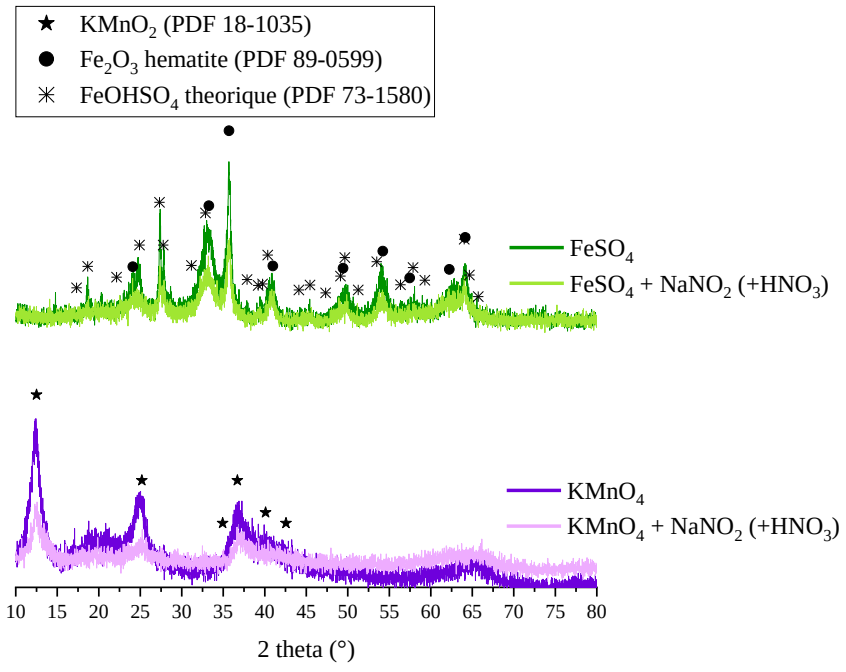


Figure 1.10: XRD data of solids obtained after calcination when $FeSO_4$ and KMnO4 undergo direct exposure to the GP or introduction of $NaNO_2$ ($+HNO_3$) without plasma exposure

Regarding the composition of the solids, differences are noticeable both in terms of surface and bulk compositions (Table 1.8). The solids resulting from the introduction of $NaNO_2$ (+HNO_3) into the precursors solution exhibit higher content of Fe or Mn in their bulk but lesser at their surface. Additionally, these solids possess higher content of S in both their bulk and surface in the case of $FeSO_4$, whereas those generated from $KMnO_4$ exhibit increased K content at the surface. Upon analyzing the phase distribution in the solid created from $FeSO_4$, we observe that a greater proportion of $FeOHSO_4$ is generated by adding $NaNO_2$ without plasma (Table 1.8). These observations align with earlier hypotheses based on the interaction between SO_4^{2-} and OH. When the precursor is just exposed to long-lived species, a precipitate with more $FeOHSO_4$ is likely to form, mirroring our findings when a radical scavenger is introduced to the system or when the precursor is added to glidarc pre-exposed water. In the case of $KMnO_4$, the observed variations can potentially be attributed more likely to the subsequent washing step rather than the plasma exposure itself.

Table 1.8: Bulk (EDX) and surface (XPS) composition and % of each phase developed (calculated from the at% of Fe and S obtained by EDX data) of solids obtained after calcination when $FeSO_4$ and $KMnO_4$ undergo a) direct exposure to the GP or b) introduction of $NaNO_2$ (+HNO_3) without plasma exposure

	Fe or Mn (% at)		**O (% at)**		**S or K (% at)**		**% of each phase formed (%)**	
	XPS (Fe2p or Mn2p)	**EDX**	**XPS (O1s)**	**EDX***	**XPS (S2p or K2p)**	**EDX**	**$FeOHSO_4$ ****	**Fe_2O_3**
a) $FeSO_4$	34.3	19	62.3	73	3.5	2	11	89
b) $FeSO_4$ + $NaNO_2$ (+HNO_3)	27.9	24	66.2	72	5.9	4	17	83
a) $KMnO_4$	28.5	22	62.0	72	9.5	6	/	/
b) $KMnO_4$ + $NaNO_2$ (+HNO_3)	23	26	65.6	68	11.5	6	/	/

* The at % of O obtained by EDX is likely overestimated due to the underlying adhesive carbon tape used to fix the sample.

** $\%\ of\ FeOHSO_4\ formed = \left(\frac{\%Fe_{(from\ FeOHSO_4)}}{\%Fe_{(total)}}\right) * 100\ where\ \%Fe_{(from\ FeOHSO_4)} = \%S_{(total)}$ $(Eq.1.7)$

Again, acknowledging the numerous similarities observed within the generated solids, we can assert that the predominant initiators of the precipitation from exposed precursors in the GP reactor are likely the HNO_2/NO_2^- species. As explained in the introduction, hypothetical precipitation reactions of the precursors when exposed to the GP proposed previously in the literature always involve the reaction of OH and NO radicals with MnO_4^-, Fe^{2+}, Sn^{2+} or Ti^{3+} precursors. However, now that we have understood that HNO_2/NO_2^- also contribute to the precipitation of these species, it is possible to propose additional hypothetical precipitation reactions involving MnO_4^-, Fe^{2+} precursors with HNO_2/NO_2^- species. Actually, HNO_2 and NO_2^- exhibit dual properties and can function either as oxidants (Table 1.9) or reducers (Table 1.10) in diverse types of redox couples [86]. In this first approach, as redox reactions are known to be kinetically favoured when less electrons are involved, we focused on reactions involving a single electron transfer for the redox couple where HNO_2 or NO_2^- species are involved (Eq.1.11, Eq.1.12, Eq.1.19, Eq.1.20). Knowing this, it is possible to evaluate the ability of the precursors to undergo a redox reaction by calculating the difference in standard potential ($\Delta E°$) and equilibrium constant (K) of the 2 couples reacting together (Eq.1.21). By doing so, we observe that all the redox reactions involving the HNO_2/NO_2^- species are indeed feasible, as $\Delta E°>0$ and $K>10^3$. This indicates that these species can function as both oxidizing and reducing agents for precursors exposed to the GP (Table 1.11). Out of curiosity, we also considered the hypothetical reactions involving other precursors (Sn^{2+} and Ti^{3+}) previously mentioned in the literature, when exposed to the GP. By doing so, we also confirmed that the redox reaction with HNO_2/NO_2^- species are feasible, as $\Delta E°>0$ and $K>10^3$ (Table 1.11).

$$K = \exp\left(\frac{nF\Delta E°}{RT}\right) \qquad Eq.1.21$$

where F=96485 C ; R=8.314 J/mol ; T=298 K ; $\Delta E° = E°_{ox} - E°_{red}$

Table 1.9: redox couples where HNO_2 or NO_2^- act as oxidants [86]

Oxidant	Reducer	E° (V/ESH)	Equation number
$2NO_2^- + 8H^+ + 6e^-$	$N_{2(g)} + 4H_2O$	1.52	Eq.1.8
$2HNO_2 + 6H^+ + 6e^-$	$N_{2(g)} + 4H_2O$	1.45	Eq. 1.9
$2NO_2^- + 6H^+ + 4e^-$	$N_2O_{(g)} + 3H_2O$	1.40	Eq. 1.10
$NO_2^- + 2H^+ + e^-$	$NO_{(g)} + H_2O$	1.20	Eq. 1.11
$HNO_2 + H^+ + e^-$	$NO_{(g)} + H_2O$	1.00	Eq. 1.12
$HNO_2 + 6H^+ + 6e^-$	$NH_{3(aq)} + 2H_2O$	0.76	Eq. 1.13
$NO_2^- + 7H^+ + 6e^-$	$NH_{3(aq)} + 2H_2O$	0.79	Eq. 1.14

Table 1.10: Redox couples where HNO_2 or NO_2^- act as reducers [86]

Oxidant	Reducer	E° (V/ESH)	Equation number
$NO_3^- + 2H^+ + 2e^-$	$NO_2^- + H_2O$	0.86	Eq. 1.15
$N_2O_{4(g)} + 2e^-$	$2NO_2^-$	0.87	Eq. 1.16
$NO_3^- + 3H^+ + 2e^-$	$HNO_2 + H_2O$	0.93	Eq. 1.17
$N_2O_{4(g)} + 2H^+ + 2e^-$	$2HNO_2$	1.07	Eq. 1.18
$NO_{2(g)} + e^-$	NO_2^-	0.90	Eq. 1.19
$NO_{2(g)} + H^+ + e^-$	HNO_2	1.09	Eq. 1.20

Table 1.11: Redox reactions between HNO_2/NO_2^- species and precursors exposed to the GP

Reduction of the precursors		
$KMnO_4$ [86]**:** $\boldsymbol{MnO_4^- + 4H^+ + 3e^- \rightleftharpoons MnO_2 + 2H_2O}$ $\boldsymbol{E° = 1.692\ V}$		
NO_2/NO_2^- (Eq. 1.19) $E° = 0.9$ V	$MnO_4^- + 4H^+ + 3NO_2^- \rightleftharpoons MnO_2 + 2H_2O + 3NO_2$ $\Delta E° = 0.79\ V$	$K = 1 * 10^{40}$
NO_2/HNO_2 (Eq. 1.20) $E° = 1.09$ V	$MnO_4^- + H^+ + 3HNO_2 \rightleftharpoons MnO_2 + 2H_2O + 3NO_2$ $\Delta E° = 0.60$ V	$K = 3 * 10^{30}$

Oxidation of the precursors		
$FeSO_4.7H_2O$; $(NH_4)_2Fe(SO_4)_2.6H_2O$ [86]**:** $\boldsymbol{FeOOH + 3H^+ + e^- \rightleftharpoons Fe^{2+} + 2H_2O}$ $\boldsymbol{E° = 0.77\ V}$		
NO_2^-/NO (Eq.1.11) $E° = 1.2$ V	$Fe^{2+} + H_2O + NO_2^- \rightleftharpoons FeOOH + H^+ + NO$ $\Delta E° = 0.43\ V$	$K = 2 * 10^7$
HNO_2/NO (Eq.1.12) $E° = 1.00$ V	$Fe^{2+} + H_2O + HNO_2 \rightleftharpoons FeOOH + 2H^+ + NO$ $\Delta E° = 0.23\ V$	$K = 8 * 10^3$
$SnSO_4$; $SnCl_2$ [86]**:** $\boldsymbol{SnO_2 + 4H^+ + 2e^- \rightleftharpoons Sn^{2+} + 2H_2O}$ $\boldsymbol{E° = -0.077\ V}$		
NO_2^-/NO (Eq.1.11) $E° = 1.2$ V	$Sn^{2+} + 2NO_2^- \rightleftharpoons SnO_2 + 2NO$ $\Delta E° = 1.28$ V	$K = 2 * 10^{43}$
HNO_2/NO (Eq.1.12) $E° = 1.00$ V	$Sn^{2+} + 2HNO_2 \rightleftharpoons SnO_2 + 2NO + 2H^+$ $\Delta E° = 1.08\ V$	$K = 3 * 10^{36}$
$TiCl_3$ [86]**:** $\boldsymbol{TiO_2 + 4H^+ + e^- \rightleftharpoons Ti^{3+} + 2H_2O}$ $\boldsymbol{E° = -0.666\ V}$		
NO_2^-/NO (Eq.1.11) $E° = 1.2$ V	$Ti^{3+} + H_2O + NO_2^- \rightleftharpoons TiO_2 + 2H^+ + NO$ $\Delta E° = 1.87$	$K = 4 * 10^{31}$
HNO_2/NO (Eq.1.12) $E° = 1.00$ V	$Ti^{3+} + H_2O + HNO_2 \rightleftharpoons TiO_2 + 3H^+ + NO$ $\Delta E° = 1.67$	$K = 2 * 10^{28}$

There is a growing interest in synthesizing catalysts through humid air GP, as opposed to simply introducing HNO_2/NO_2^- synthesized by alternative methods into a metal salt solution. The most conventional approach to nitrous acid synthesis involves the interaction of strong acids with nitrite salt at very low temperatures. However, HNO_2 tends to undergo decomposition into nitric acid and nitric oxide, displaying stability only in diluted, cold aqueous solution and in the form of nitrite salt [33,87]. This inherent instability poses challenges in practical applications. In contrast, GP offers a more straightforward method for utilizing HNO_2/NO_2^- as it is directly produced from an abundant source, air, and is consumed *in situ*. Furthermore, this approach addresses the instability issue associated with this molecule, making the [33,87]humid air GP an attractive alternative for synthesizing catalysts.

Nevertheless, since some differences in the composition of the resulting solids appear when no short-lived species are present in the medium (vs when they are obtained via the direct exposure procedure), it indicates that HNO_2/NO_2^- is not the sole agent responsible for initiating the precipitation of the precursors. Moreover, we can also note that the yield is diminished for both precursors when solely $NaNO_2$ is introduced into the medium, as opposed to when they are incorporated into pre-exposed water (Table 1.5, Table 1.7). This suggests the involvement of other long-lived species in initiating the precipitation reaction.

3.3. What is the impact of different types of plasma gases on the precipitation of precursors exposed to the GP?

For each type of plasma gas tested, precipitation occurs for both $FeSO_4$ and $KMnO_4$ precursors. Based on this information, we quantified the amount of NO_3^- and NO_2^- species eventually formed in water exposed to these different plasma conditions to determine if HNO_2 and/or NO_2^- species might be present in the medium and initiate the precipitation. Our findings indicate that both NO_3^- and NO_2^- are indeed created in the medium for each type of plasma gas (Figure 1.11). This might be due to the fact that the plasma reactor used in this thesis is not airtight, allowing a small amount of environmental gas to enter and create nitrous and nitric ions.

We observe that the amount of nitrogen-based species formed is smaller for He, Ar and O_2 which is expected as the source of nitrogen can only be from the environmental gas. On the other hand, the amount of nitrogen-based species is approximately the same for N_2, dry air and humid air, with the highest amount observed for humid air. Referring to the equations

proposed in General Introduction, section 3.3.1, we see that to form HNO_3/NO_3^- and HNO_2/NO_2^- species, we need OH, NO, O, NO_2 (derived from NO and O), and water. From equation I.4, we see that O comes from O_2 molecules, OH from H_2O, and NO from N_2 and O. Therefore, to create HNO_3/NO_3^- and HNO_2/NO_2^-, oxygen, nitrogen, and water are required. This explains why the highest amount of these species is created with humid air, as the reactive species needed to form these species are directly supplied by the plasma gas. With other gases, the source of air can come from the environmental air, and it seems like this source of O_2 is sufficient to create a high amount of nitrous and nitrate ions with the N_2 gas. Furthermore, it is possible that the source of H_2O comes from water below the plume that evaporates during the discharge exposure [31,49].

Therefore, with these observations, it is possible that the HNO_2/NO_2^- species formed under each synthesis condition are sufficient to trigger the precipitation of both $KMnO_4$ and $FeSO_4$ exposed to the plasma gases.

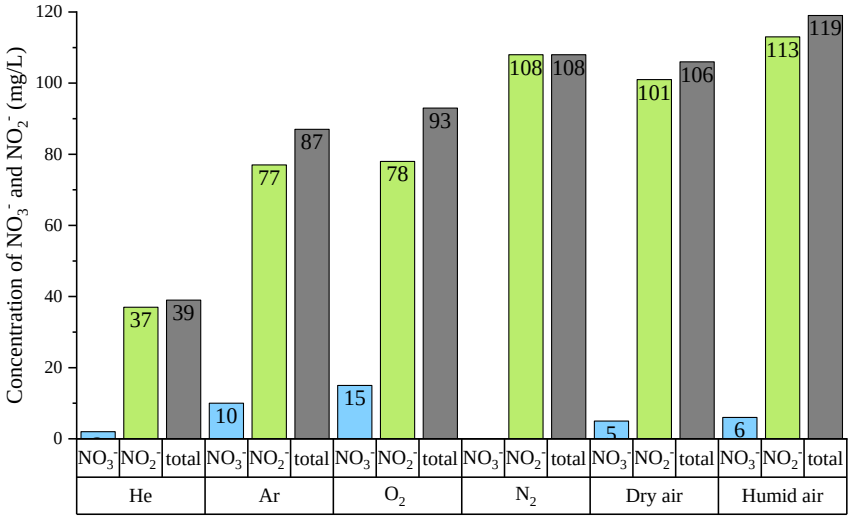


Figure 1.11: Concentration of NO_2^- and NO_3^- in ultrapure water exposed to the GP with different plasma gases for 1h

Since it is not possible to remove all nitrogen-based species under our synthesis conditions, we wondered if it would be possible to correlate the yield of the formed precipitate with the amount of NO_2^- species created (Figure 1.12, Figure 1.13). By plotting the amount of NO_2^- generated with different plasma gases and the yield of formed precipitate using $KMnO_4$ and $FeSO_4$ as precursors, we observe that, for nearly all the plasma gases tested, the yield of the precipitate increases with the amount of NO_2^- present in the medium (He < Ar < N_2 - dry air - humid air) (Figure 1.12,

Figure 1.13). However, a different trend is observed with O_2. In fact, when using O_2 as the plasma gas, the yield of the formed precipitate for both $FeSO_4$ and $KMnO_4$ is higher than when humid air is used, even though less NO_2^- species are present in the medium. This suggests that O_2 as a plasma gas may create new plasma species that more effectively promote the precipitation of the precursor. Different other species might be created when O_2 is used as plasma gas such as O_3 or H_2O_2 [49]. We have previously observed that H_2O_2 is not created when humid air is used in GP (Part I, Chapter 1, section 3.2.2). However, it is possible that H_2O_2 is formed when O_2 is used as plasma gas, and this might explain the increase yield of precipitate under this condition. To investigate this, we tested the formation of H_2O_2 by exposing 450 mL of 50 mL/L $Ti(SO_4)_2$ (15% solution, Fisher) to the plasma for 45 min using O_2 as plasma gas. After the exposure, the solution was analyzed directly using UV-visible spectroscopy within the wavelength range of 300 to 600 nm, in the same conditions as described in Part I, Chapter 1, section 3.2.2. Under these conditions, the creation of the $[Ti(O_2)SO_4]xH_2O$ complex was never observed, indicating that H_2O_2 is not created and is therefore not responsible for the observed increase in yield when using O_2 as plasma gas. Concerning O_3, we did not attempt to determine if this species might be formed under these conditions, but it has been reported that O_3 reacts readily in water, typically producing OH radicals. [49]. Therefore, it is unlikely that O_3 is the species responsible for the increased yield.

Nevertheless, the presence of O_2 still seems to produce other species that increase the yield of formed precipitate. This observation aligns with the fact that the yield is higher for both dry air and humid air than compared to pure N_2, even though the amount of NO_2^- species is approximately the same. This indicates that introducing O_2 in the plasma gas generates other species, in addition to nitrogen-based ones, that enhance the amount of precipitate formed. This correlates with our previous conclusion that while HNO_2/NO_2^- seems to be the main species responsible for the precipitation in humid air GP, they are probably not the only species driving the reaction.

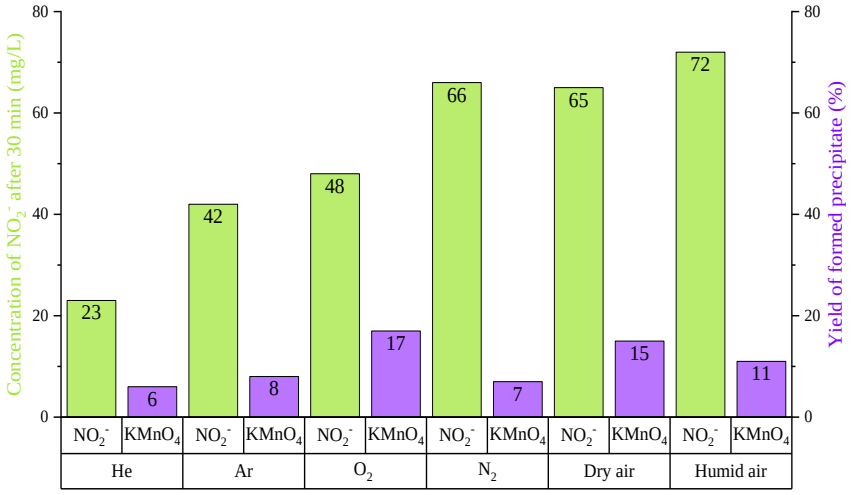


Figure 1.12: Concentration of NO_2^- in ultrapure water exposed to the GP with different plasma gases for 30 min and yield of formed precipitate when $KMnO_4$ undergo exposure to the GP for 30 min with different plasma gases

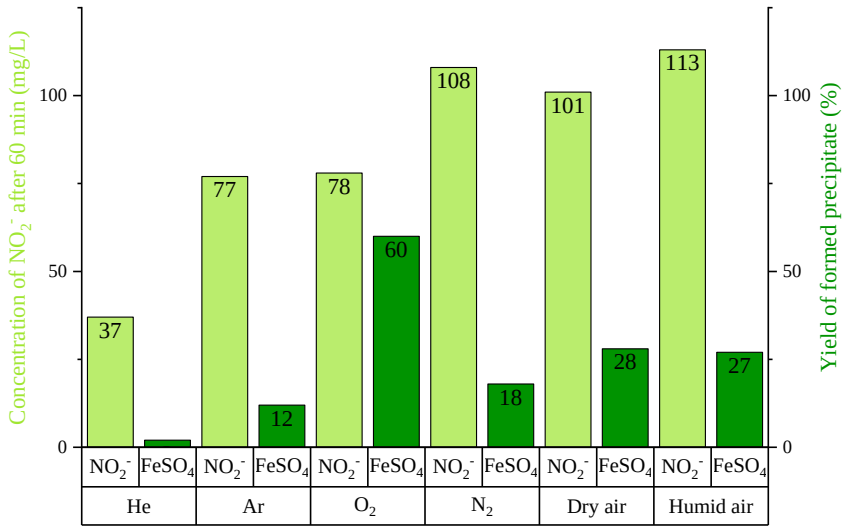


Figure 1.13: Concentration of NO_2^- in ultrapure water exposed to the GP with different plasma gases for 1h and yield of formed precipitate when $FeSO_4$ undergoes exposure to the GP for 1h with different plasma gases

4. Conclusion

The purpose of the research conducted here was to progress in the identification of the GP generated species that induce the precipitation of (hydr)oxides in exposed metal salts precursors solutions. In existing literature, only OH and NO radicals had been proposed as potential oxidant and reducer plasma species, respectively, yet without experimental proofs.

Our experiment involving the exposure of $FeSO_4$ to GP in the presence of an OH radical scavenger, revealed that its precipitation is not completely blocked, indicating that OH radicals are not the sole agents responsible for the oxidation reaction.

Our hypothesis that other species, specifically long-lived ones, might trigger the precipitation of the precursors is confirmed as precursors introduced into water pre-exposed to GP, precipitated. Precisely, it is demonstrated that HNO_2/NO_2^- do initiate the precipitation. This underscores the interest of GP as an alternative method for generating these reactive species, utilizing only humid air as the chemical source. Additionally, HNO_2 can be directly consumed *in situ* for catalysts synthesis, removing the instability issue associated with this molecule.

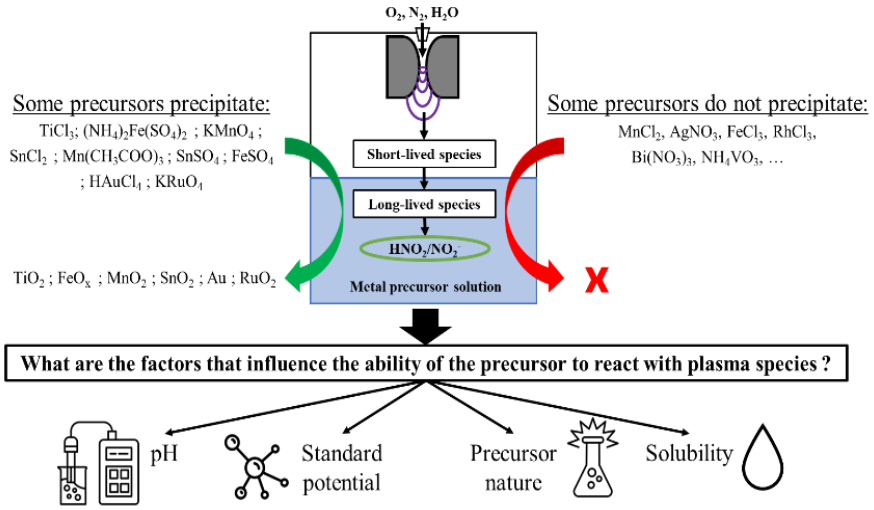
Slight differences in the composition of the solids produced when precipitation was triggered by the sole HNO_2/NO_2^- addition without plasma exposure, *vs* when introduced into water pre-exposed to GP, *vs* when the OH radicals were removed, allows concluding that HNO_2/NO_2^- are not the only responsible for the precipitation of exposed precursors solutions. Nevertheless, the similarities in the solids formed by solely adding HNO_2/NO_2^- to a precursor solution to the ones obtained by direct plasma exposure, allows asserting that these species are the primary agents responsible for (hydr)oxides catalysts formation through exposure to humid air GP.

By exposing $KMnO_4$ and $FeSO_4$ to different types of plasma gases, we observed that the amount of precipitate formed is not always correlated with the amount of HNO_2/NO_2^- species produced by the various gases. In fact, since the yield of the formed precipitate is the highest for both precursors when pure O_2 is used as the plasma gas, we conclude that oxygen-based species might also influence the precipitation of the precursor upon plasma exposure. This explains why the yield of the formed precipitate is higher for both dry air and humid air than compared

to pure N_2, even though the amount of NO_2^- species is approximately the same.

In fact, in complex system like plasma, where a variety of reactive species are generated, and where complex reactions and mechanisms take place, such as redox processes and precipitation involving nucleation and growth, it is unlikely that a single species alone drives the reaction. This highlights the complexity of GP synthesis compared to simply introducing a single chemical reagent. Such complexity may give rise to unique properties that would not be achievable if a conventional chemical reagent was used as the sole agent to trigger the precipitation of the metal precursor salt. Therefore, this underscores the unique value of the GP catalyst synthesis approach compared to other methods.

Chapter 2 - Towards the understanding of parameters allowing to anticipate the precipitation reaction of metallic precursors in humid air gliding arc plasma reactor



Abstract

The humid air gliding arc plasma (GP) has demonstrated its capability to synthesize catalysts (metal (hydr)oxides and supported catalysts) with intriguing properties and significant catalytic activity while employing interesting synthesis conditions compared to conventional catalyst synthesis. However, previous studies exposed various precursors to the plasma without prior knowledge of their reactivity through GP. The objective of this chapter is to investigate the parameters influencing precursor reactivity and precipitation under humid air GP, by identifying commonalities between reactive and non-reactive precursors. Several factors were identified as predominant: the solubility of the precursor and precipitate, the acidification of the medium along exposure, the redox potential of reactions between the precursor and HNO_2/NO_2^- species plasma-generated, and the metal precursor nature. These identified factors have enabled us to create a dichotomous key that can be used for any type of precursors, allowing to anticipate their potential precipitation when exposed to the GP. By utilizing this key, we have identified two new precursors that react, forming new types of solids never synthesized before by GP: Au and Ru-based solids. This demonstrates that GP may be a promising method for developing new types of catalysts, such as metal-supported catalysts, but also indicates that a limited number of precursors may react, at least without changing the conventional synthesis parameters. Therefore, this chapter highlights both the possibilities and limitations of GP catalyst synthesis.

The results presented in this chapter have been published in:

Fanny Hanon, Michel Devillers, Eric M. Gaigneaux, Towards the Understanding of Parameters Allowing to Anticipate the Precipitation Reaction of Metallic Precursors in Humid Air Gliding Arc Plasma Reactor, Plasma Chemistry and Plasma Processing, 2024

https://doi.org/10.1007/s11090-024-10516-1



1. Introduction

As mentioned in the introduction, the humid air GP reactor's acidifying, oxidizing, and reducing capabilities make it highly interesting for a wide variety of applications, including the synthesis of catalysts such as metal (hydr)oxides (TiO_2, $FeOOH/FeO_x$, MnO_2, SnO_2, WO_3) and supported catalysts (FeO_x/Kaolinite, TiO_2/SnO_2) with good properties and interesting catalytic activity when used for pollutant degradation in both gaseous and liquid phases (Table I.3) [42,56,57,59–61,64]. However, despite the utilization of various types of precursors in previous literature, which have demonstrated the efficacy in precipitating oxides or hydroxides, we still lack understanding regarding why these precursors precipitate. It remains uncertain indeed whether every type of metal precursor is capable of reacting and forming a precipitate via GP. Until now, we have simply exposed precursors to the plasma without prior knowledge of whether they were the right choice. Consequently, we are unable to explain why certain precursors react while others do not. This lack of understanding makes it challenging to ascertain the potential versatility of the method in synthesizing various types of catalysts.

Therefore, the objective of this chapter is to investigate the parameters influencing the ability of certain precursors to react via humid air GP, forming a precipitate. The aim is to enhance our understanding of the method, ultimately enabling the synthesis of a broader range of catalysts. This, in turn, could enhance the interest of GP as an innovative method for catalysts synthesis.

To fulfil this objective, the strategy was to identify commonalities between precursors that do form a precipitate via GP and those that do not react. To achieve this, several precursors were tested to establish a pool of both reactive and non-reactive precursors.

To determine the factors dictating the ability of the precursors to react, the strategy was to draw inspiration from the factors that affect the classical synthesis of catalysts by precipitation, which shares many similarities with synthesis via GP exposure. Furthermore, it involved revisiting the basics of chemistry and conducting calculations to theoretically rationalize the reactions upon plasma exposure. Additionally, insights from previous results in Chapter 1 were valuable as it was found that among the plasma species created, the long-lived species, especially HNO_2/NO_2^-, predominantly impact the oxidoreduction of the precursors [88].

Several factors were identified as predominant, including medium pH, redox potential of reactions between the precursor and HNO_2/NO_2^- species plasma-generated, precipitate solubility and of course the nature of the metal precursor.

2. Materials and methods

2.1. Materials

$Al(NO_3)_3.9H_2O$ (≥ 95%), $AlCl_3$ (99%), $HAuCl_4.3H_2O$ (99%), $K_2Cr_2O_7$ (≥ 99%), $Fe(NO_3)_3.9H_2O$ (≥ 98%), $FeCl_3.6H_2O$ (≥ 99%), $FeSO_4.7H_2O$ (≥ 99%), $Mn(CH_3COO)_3.2H_2O$ (97%), $Mn(CH_3COO)_2.3H_2O$ (99.99%), $NaMnO_4$ (solution 40% wt in H_2O), $MnSO_4.H_2O$ (≥ 99%), $Na_2MoO_4.2H_2O$ (≥ 99%), $Ni(NO_3)_2.6H_2O$ (≥ 97%), $Ni(CH_3COO)_2.4H_2O$ (98%), $SnSO_4$ (≥ 95%), $SnCl_2$ (≥ 99%), $TiCl_3$ (solution 10-15% in HCl) were purchased from Sigma Aldrich.

$Bi(NO_3)_3.5H_2O$ (≥ 98%), $Co(NO_3)_2.6H_2O$ (≥ 98%), $(NH_4)_2Fe(SO_4)_2.6H_2O$ (≥ 99%), $KMnO_4$ (≥ 99%), $Mn(NO_3)_2.4H_2O$ (≥ 98%), $MnCl_2$ (97%), $Na_2WO_4.2H_2O$ (≥ 99%) were obtained from Roth.

$AgNO_3$ (99.9%), $AgCH_3COO$ (99%), $Fe(CH_3COO)_2$ (95%), $MnCl_2$ (97%), $(NH_4)_2PtCl_4$ (99.99%), $Ti(SO_4)_2$ (15% (w/v) solution in diluted sulfuric acid), $KRuO_4$ (97%) were obtained from Thermo Scientific.

All the solutions were prepared with demineralized water as solvent.

2.2. Methods

2.2.1. Synthesis device: the GP reactor

The gliding arc plasma system used in this study is the same as the one presented in Experimental, section 1.

2.2.2. Precursors exposure and solid recovery

Various metal precursors were exposed to the GP to establish a pool of both reactive and non-reactive precursors (Table 2.1).

The precursor solutions were prepared by dissolving these compounds in deionized water to obtain a certain concentration of metal (Table 2.1). Subsequently, 450 mL of the respective solutions were introduced into the reactor, stirred magnetically (1 rotation/s), and exposed to the plasma discharge for maximum 2h. If no solid formed within this time frame, we assumed that the precursors did not react to form a precipitate via GP.

The pH of the precursor solution was measured using a pH meter before and after exposure to the plasma.

Table 2.1: Type and concentrations of precursors exposed to the GP

Concentration (mol/L)	Metal	Precursor
10^{-3}	Au, Ru, Bi, Pt	$HAuCl_4.3H_2O$, $KRuO_4$, $Bi(NO_3)_3.5H_2O$, $(NH_4)_2PtCl_4$
10^{-2}	Ag, Cr, Co, Fe, Mn, Mo, Ni, Sn, Ti, W	$AgNO_3$, $AgCH_3COO$, $K_2Cr_2O_7$, $Co(NO_3)_2.6H_2O$, $Fe(NO_3)_3.9H_2O$, $FeCl_3.6H_2O$, $FeSO_4.7H_2O$, $Fe(CH_3COO)_2$, $(NH_4)_2Fe(SO_4)_2.6H_2O$, $Mn(NO_3)_2.4H_2O$, $MnCl_2$, $MnSO_4.H_2O$, $Mn(CH_3COO)_3.2H_2O$, $Mn(CH_3COO)_2.3H_2O$, $KMnO_4$, $NaMnO_4$, $Ni(NO_3)_2.6H_2O$, $Ni(CH_3COO)_2.4H_2O$, $SnCl_2$, $SnSO_4$, $Ti(SO_4)_2$, $Na_2WO_4.\ 2H_2O$
$2*10^{-2}$	Al	$Al(NO_3)_3.9H_2O$, $AlCl_3$
$3*10^{-2}$	Mo	$Na_2MoO_4.2H_2O$
2	Ti	$TiCl_3$

If a solid precipitate was obtained after exposure to the plasma discharge, it was recovered by centrifugation (24490 G, 30 min) and subjected to two washing cycles with distilled water. The solids obtained after centrifugation were subsequently dried in an oven under air at 110°C for 22h ± 2h.

2.3. Characterization of the solids formed: X-Ray Diffraction (XRD)

XRD is the only instrumental characterization used here. It was done after drying of the solids formed. It was performed as presented in Experimental, section 2.

3. Results and discussion

3.1. Factors influencing the ability of a precursor to react

As previously explained, the GP catalysts synthesis shares many similarities with the classical synthesis involving a precipitation process. Therefore, it was anticipated that similar factors influencing the precipitation method would also be important in our case. Among these factors, the pH of the medium, the nature of the precursor used, and the solubility of the precipitate will be discussed. However, one specific factor arises from the plasma species, namely HNO_2 and NO_2^-, generated from the humid air GP and which trigger

the redox reaction of precursor exposed to the medium. This factor might be rationalized from the potential of the redox couple involved in the reaction.

3.1.1. pH of the medium

As suggested in previous literature, acidic species such as HNO_3 and HNO_2 are among those created by the plasma [33,48,88]. These species decrease the pH of the solution during the exposure, reaching a pH around 3, if only distilled water is exposed. The pH stabilizes around this value due to the buffering effect of the HNO_2/NO_2^- couple (pKa=3.3) [89]. In fact, as shown in Table 2.2, the final pH of the exposed precursor solution often stabilizes around this value, except when the metal precursor can act as a secondary buffer, as observed with acetate precursors. However, not all types of solids form under such acidic conditions. Therefore, we suggest that the first factor influencing the ability of a precipitate to form under GP is this acidification of the medium during the exposure.

Table 2.2: Precursors exposed to the GP, solution's pH before and after exposure, and type of solid that can be formed in water with the pH range of their existence

Metal	Precursor	Initial pH	Precipitate ?	Final pH	Precipitate that can be formed in water [86]	
					Type	pH range
Ag	$AgNO_3$	5	No	3	Ag	[0-14]
	$AgCH_3COO$	6.4	No	5.2	Ag_2O	[8-14]
Al	$Al(NO_3)_3.9H_2O$	3.5	No	2	Al_2O_3	[2.5-12.5]
	$AlCl_3$	3.6	No	3.2		
Bi	$Bi(NO_3)_3.5H_2O$	2	No	2.4	Bi_2O_3	[4.5-14]
					Bi	[0-14]
Co	$Co(NO_3)_2.6H_2O$	2.5	No	2	$Co(OH)_3$	[5-14]
					$Co(OH)_2$	[7-14]
					Co	[5-14]
Cr	$K_2Cr_2O_7$	4.3	No	2.9	Cr_2O_3	[3.5-14]
Fe	$Fe(NO_3)_3.9H_2O$	2.5	No	2.3	Fe_2O_3	[1-14]
	$FeCl_3.6H_2O$	2.5	No	2.4		
	$Fe(CH_3COO)_2$	5.4	No	5.2	Fe_3O_4	[7-14]
	$FeSO_4.7H_2O$	4.1	Yes (FeOOH)*	3		
	$(NH_4)_2Fe(SO_4)_2.6H_2O$	3	Yes (FeOOH)* [61]	3		
Mn	$Mn(NO_3)_2.4H_2O$	4.1	No	3.1	MnO_2	[0-14]
	$MnCl_2$	4.9	No	3.2	Mn_2O_3	[4.5-14]
	$MnSO_4.H_2O$	5.4	No	3.3	Mn_3O_4	[7-14]
	$Mn(CH_3COO)_3.2H_2O$	5	Yes ($MnO(OH)$, MnO_2)* [59]	4.8	$Mn(OH)_2$	[8.5-14]

	$Mn(CH_3COO)_2.3H_2O$	6.1	No	5.4			
	$KMnO_4$	6.9	Yes: ($KMnO_2$)** [59]	3.2			
	$NaMnO_4$	6.8	Yes: (MnO_2)*	3.2			
Mo	Na_2MoO_4	6.7	No	5.4		MoO_3 MoO_2	[0-1.5] [3-8.5]
Ni	$Ni(NO_3)_2.6H_2O$	5.2	No	3.2		Ni_3O_4 $Ni(OH)_2$ Ni	[4.5-14] [7-14] [5.5-14]
	$Ni(CH_3COO)_2.4H_2O$	6	No	5.7			
Pt	$(NH_4)_2PtCl_4$	6.2	No	2.7		PtO_2 $Pt(OH)_2$ Pt	[0-14]
Sn	$SnCl_2$	2.5	Yes (SnO_2)* [56]	1.9		SnO_2	[0-14]
	$SnSO_4$	2.6	Yes (SnO_2)*	2.1			
Ti	$Ti(SO_4)_2$	1.7	No	1.6		TiO_2	[0-14]
	$TiCl_3$		Yes (TiO_2) [60]	1.8			
W	Na_2WO_4. $2H_2O$	6.7	No	6.2		WO_3	[0-6]

** The diffractograms of the formed solids, which enable us to identify the developed phases, are presented in Figure 2.1, Figure 2.2, and Figure 2.3.*

*** The $KMnO_2$ phase is actually a polymorph of MnO_2 (birnessite) that is a non-stoichiometric oxide. In this structure, K^+ ions are inserted into the channel of the materials, and some Mn^{4+} ions are either missing, or replaced by Mn^{3+} ions [24].*

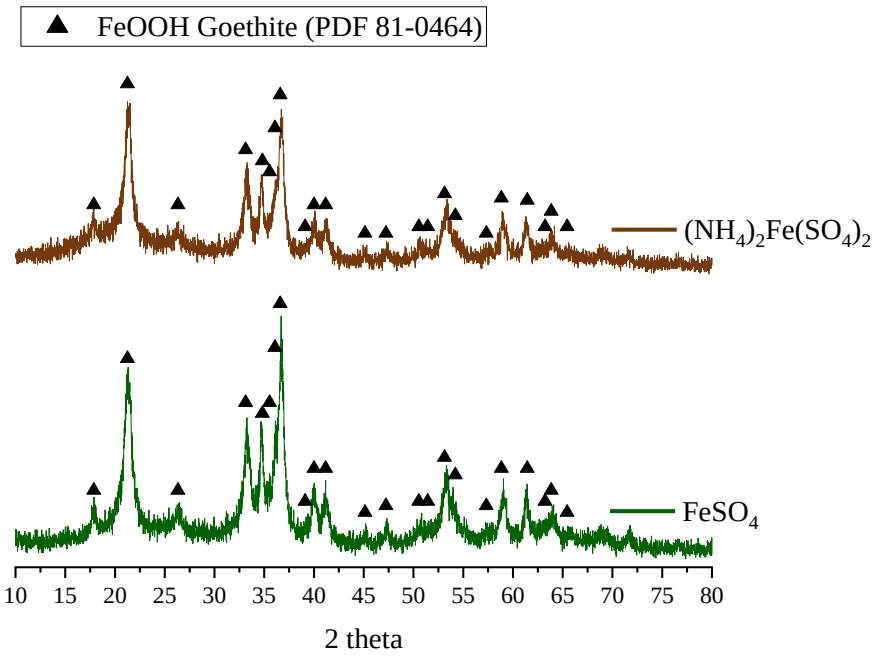


Figure 2.1: XRD data of solids formed in the case of $FeSO_4$ and $(NH_4)_2Fe(SO_4)_2$ exposed to GP

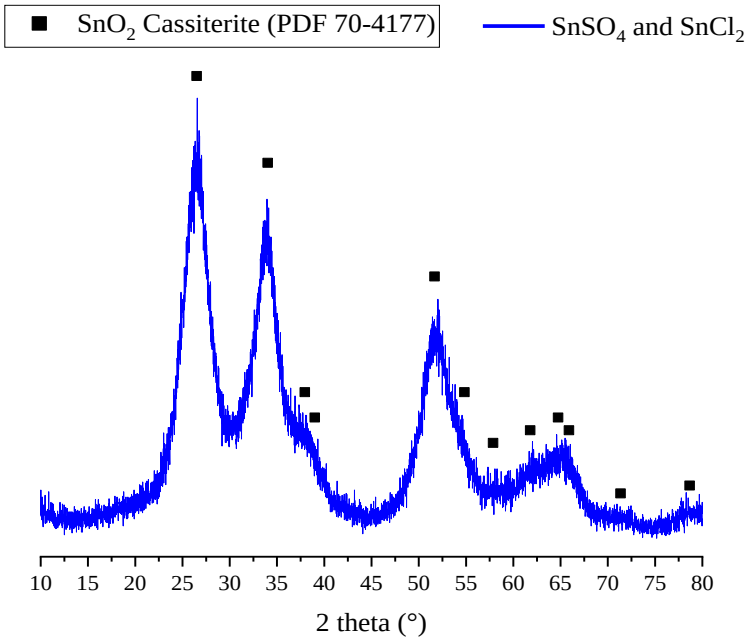


Figure 2.2: XRD data of solids formed in the case of $SnSO_4$ and $SnCl_2$ exposed to GP

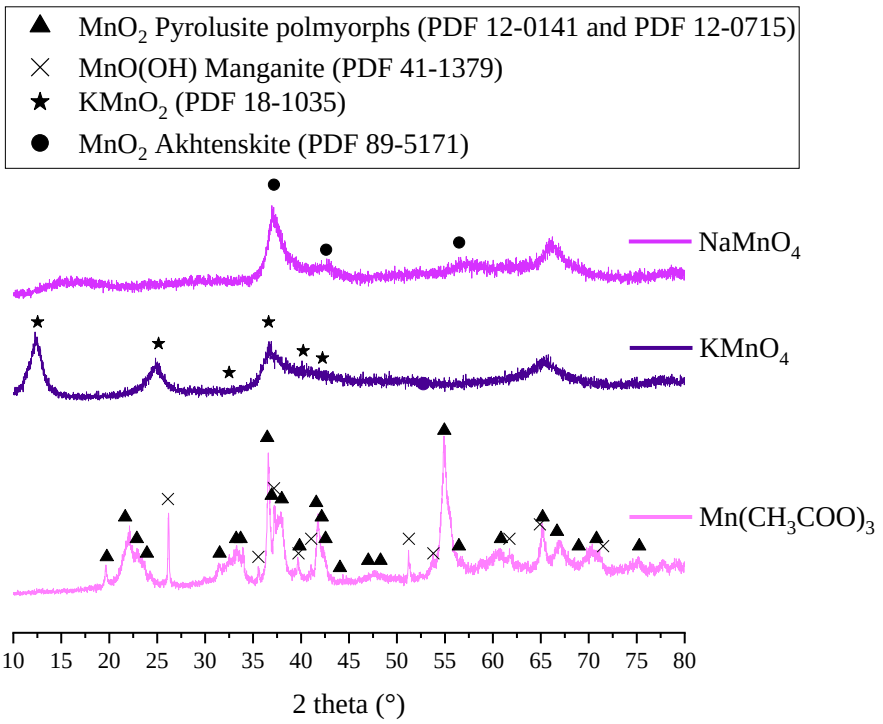


Figure 2.3: XRD data of solids formed in the case of $Mn(CH_3COO)_3$, $KMnO_4$ and $NaMnO_4$ exposed to GP

To investigate this hypothesis, the Pourbaix diagrams of the various metals tested by GP are of primary interest (Figure 2.4 as example, Supplementary information SI.4 for other metals) [86]. In these diagrams, the x-axis represents the pH of the medium, while the y-axis represents the voltage potential with respect to the standard hydrogen electrode. Furthermore, it should be noted that the dashed "a" and "b" lines in this diagram refer to the thermodynamic limitations corresponding to the redox behaviour of water itself, which is here the solvent. From a thermodynamic point of view, only species comprised between these lines should therefore exist in water. However, kinetic limitations could allow for the stabilization of metastable species under certain conditions [86].

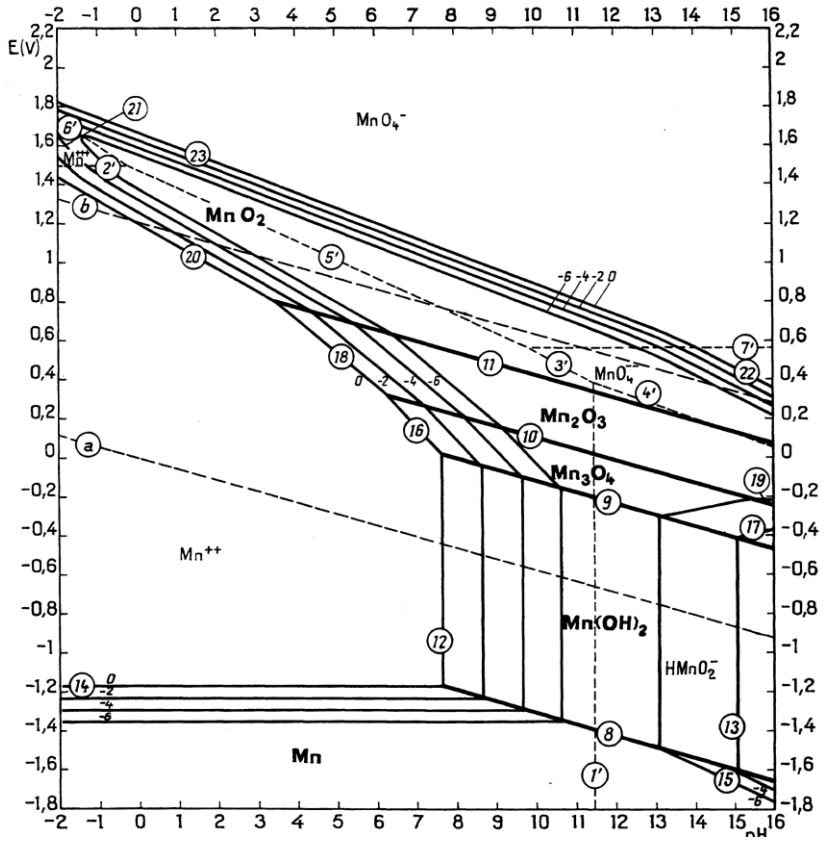


Figure 2.4: Pourbaix diagram of Mn-water at 25°C (considering β-MnO_2 (pyrolusite)) [86]

To simplify the interpretation of these diagrams and understand the types of precipitates that can potentially form, we have compiled in Table 2.2 the solids that can form in water for all the metal tested, along with the approximate pH range where they can be created. To determine this range, we used the "-2" line on the Pourbaix diagram as a limit, as it represents the equilibrium between solid and soluble substances when the concentration of the dissolved substance is 10^{-2} mol/L, corresponding to the quantity of metal ions in our solution due to the initial concentration of precursors we chose (Figure 2.4, Supplementary Information SI.4) [86]. By comparing this range to the final pH of the exposed solution, we observe that some precipitates cannot form at such pH which explains why they are not formed (marked in black in Table 2.2). Furthermore, it is worth noting that all the precursors reacting via GP have a final pH within the range of the corresponding solid formed (marked in green in Table 2.2). This indicates that the pH of the medium is an important

factor in determining whether a precursor can react via GP to form a precipitate.

However, we also observed that some precursors can normally form certain solids at the final pH of the solution after exposure but still do not produce any precipitate (marked in red in Table 2.2). This suggests that other factors need to be considered.

3.1.2. Potential of the redox reaction

The second important factor can be illustrated using the Mn precursors as an example. While Mn(III) and Mn(VII) precursors react by plasma to form MnO_2, Mn(II) does not. This underlines the significance of another important factor: the oxidation state, or more precisely, the potential of the redox couple in which the metallic ion is involved (M^{n+}/precipitate).

As mentioned in the introduction, we previously discovered that the long-lived species, especially HNO_2 and/or NO_2^-, are the main species initiating the precipitation process of precursors exposed to the GP [88]. These species have the ability to undergo redox reactions with the precursor, that could induce precipitation. Actually, HNO_2 and NO_2^- exhibit dual properties and can function either as oxidants or reducers in diverse types of redox couples [86]. In this first approach, as redox reactions are known to be kinetically favoured when less electrons are involved, we focused on reactions involving a single electron transfer for the redox couple where HNO_2 or NO_2^- species are involved (Table 2.3) [90]. Knowing this, it is possible to evaluate their ability to undergo a redox reaction by calculating the difference in standard potential ($\Delta E°$) and equilibrium constant (K) of the 2 couples reacting together (Eq.2.1). In the Part I, Chapter 1, section 2.2.3, we already performed this analysis for all the precursors known to undergo a redox reaction by GP (Fe^{2+}, MnO_4^-, Sn^{2+} and Ti^{3+}), demonstrating that the redox reaction followed by the precipitation process of precursors triggered by the HNO_2 or NO_2^- species is indeed theoretically feasible, as $\Delta E° > 0$ and $K > 10^3$ (Eq.2.1, Table 1.11) [88].

$$K = \exp\left(\frac{nF\Delta E°}{RT}\right) \qquad (Eq.\,2.1)$$

where F=96485 C ; R=8.314 J/mol ; T=298 K ; $\Delta E° = E°_{ox} - E°_{red}$

However, previous calculations were made considering the E°, the standard equilibrium potential of the reaction at 25°C. This value does not account for the actual concentration of ionic species or the pH of the medium. The real E

in our medium for a couple "$aA + mH^+ + ne^- \rightleftharpoons bB + cH_2O$" can be calculated using the equation 2.2 [86]:

$$E = E° + \frac{0.059}{n}\log\left(\frac{(C_A)^a}{(C_B)^b}\right) - 0.059\left(\frac{m}{n}\right)pH \qquad (Eq.\ 2.2)$$

Given that we know the pH of the medium after exposure of each precursor and the concentration used for each, it is possible to calculate the actual E for all the redox couples considered. However, since the exact concentration of HNO_2 and NO_2^-, as well as the partial pressures of the gaseous species in our medium are unknown, calculating the actual E for their redox couple is challenging. Therefore, we will use the standard electrode potential (E°) for these species instead. Consequently, ΔE for each redox reaction was calculated based on these E and E° values (Table 2.4, Table 2.5).

By considering the correct E value for the precursors reacting through GP (marked in green in the Table 2.2), calculated from the final pH obtained after exposure (Table 2.2) and the initial concentration of the precursor (Table 2.1), we still obtain ΔE>0 corresponding to a negative free enthalpy change ΔG, indicating that they can indeed theoretically react with HNO_2 or NO_2^- species (Table 2.4).

Table 2.3: Redox couples where HNO_2 or NO_2^- act as oxidants and reducers with only 1 electron involved [86]

	When HNO_2 or NO_2^- act as oxidant	**When HNO_2 or NO_2^- act as reducer**	**E° (V/NHE)**	**Equation number**
Oxidant	$NO_2^- + 2H^+ + e^-$	$NO_{(g)} + H_2O$	1.2	Eq.1.11
	$HNO_2 + H^+ + e^-$	$NO_{(g)} + H_2O$	1.00	Eq.1.12
Reducer	$NO_{2_{(g)}} + e^-$	NO_2^-	0.90	Eq.1.19
	$NO_{2_{(g)}} + H^+ + e^-$	HNO_2	1.09	Eq.1.20

Table 2.4: Redox reactions between HNO_2 or NO_2^- species and precursors exposed to the GP that give a precipitate [88]

Reduction of the precursors		
<u>$KMnO_4$; $NaMnO_4$</u> [86]**<u>:</u>** $\boldsymbol{MnO_4^- + 4H^+ + 3e^- \rightleftharpoons MnO_2 + 2H_2O}$ $\boldsymbol{E = 1.692 - 0.0788pH + 0.0197log\left(C_{MnO_4^-}\right) = 1.41\ V}$		
NO_2/NO_2^- (Eq. 1.19) $E° = 0.9$ V	$MnO_4^- + 4H^+ + 3NO_2^- \rightleftharpoons MnO_2 + 2H_2O + 3NO_2$	$\Delta E = 0.51$ V
NO_2/HNO_2 (Eq. 1.20) $E° = 1.09$ V	$MnO_4^- + H^+ + 3HNO_2 \rightleftharpoons MnO_2 + 2H_2O + 3NO_2$	$\Delta E = 0.32$ V

Oxidation of the precursor		
$FeSO_4.7H_2O$; $(NH_4)_2Fe(SO_4)_2.6H_2O$ [86]**:** $\boldsymbol{FeOOH + 3H^+ + e^- \rightleftharpoons Fe^{2+} + 2H_2O}$ $\boldsymbol{E = 0.77 - 0.1773pH - 0.0591log\left(C_{Fe^{2+}}\right) = 0.36\ V}$		
NO_2^-/NO (Eq.1.11) $E° = 1.2$ V	$Fe^{2+} + H_2O + NO_2^- \rightleftharpoons FeOOH + H^+ + NO$	$\Delta E = 0.84$ V
HNO_2/NO (Eq.1.12) $E° = 1.00$ V	$Fe^{2+} + H_2O + HNO_2 \rightleftharpoons FeOOH + 2H^+ + NO$	$\Delta E = 0.64$ V
$SnSO_4$; $SnCl_2$ [86]**:** $\boldsymbol{SnO_2 + 4H^+ + 2e^- \rightleftharpoons Sn^{2+} + 2H_2O}$ $\boldsymbol{E = -0.077 - 0.1182pH - 0.0295log\left(C_{Sn^{2+}}\right) = -0.26\ V}$		
NO_2^-/NO (Eq.1.11) $E° = 1.2$ V	$Sn^{2+} + 2NO_2^- \rightleftharpoons SnO_2 + 2NO$	$\Delta E = 1.46$ V
HNO_2/NO (Eq.1.12) $E° = 1.00$ V	$Sn^{2+} + 2HNO_2 \rightleftharpoons SnO_2 + 2NO + 2H^+$	$\Delta E = 1.26$ V
$TiCl_3$ [86]**:** $\boldsymbol{TiO_2 + 4H^+ + e^- \rightleftharpoons Ti^{3+} + 2H_2O}$ $\boldsymbol{E = -0.666 - 0.2364pH - 0.0591log\left(C_{Ti^{3+}}\right) = -1.11\ V}$		
NO_2^-/NO (Eq.1.11) $E° = 1.2$ V	$Ti^{3+} + H_2O + NO_2^- \rightleftharpoons TiO_2 + 2H^+ + NO$	$\Delta E = 2.31$ V
HNO_2/NO (Eq.1.12) $E° = 1.00$ V	$Ti^{3+} + H_2O + HNO_2 \rightleftharpoons TiO_2 + 3H^+ + NO$	$\Delta E = 2.11$ V

Therefore, it may be possible to theoretically explain, with the same calculations, why all the other precursors, which are normally capable of forming a solid with a different oxidation state (OS) under the final pH obtained after exposure, do not seem to react by GP (marked in red in the Table 2.2). By doing this, we observe that in all cases, the redox reaction of these precursors with HNO_2 or NO_2^- species yields $\Delta E < 0$ (Table 2.5). Consequently, it is evident that these reactions cannot occur. This implies that the reason why these precursors do not yield to a solid after exposure to the GP is because they cannot undergo a redox reaction with the HNO_2 or NO_2^- species, which have been identified as the primary active species in the observed redox reactions [88].

Table 2.5: Redox reactions between HNO_2 or NO_2^- species and precursors exposed to the GP that do not give a precipitate

Reduction of the precursors		
<u>$AgNO_3$; $AgCH_3COO$</u> [86]**:** $\boldsymbol{Ag^+ + e^- \rightleftharpoons Ag}$ $\boldsymbol{E_0 = 0.799 + 0.0591 log\left(C_{(Ag^+)}\right) = 0.68\ V}$		
NO_2/NO_2^- (Eq. 1.19) $E° = 0.9$ V	$Ag^+ + NO_2^- \rightleftharpoons Ag + NO_2$	$\Delta E = -0.22$ V
NO_2/HNO_2 (Eq. 1.20) $E° = 1.09$ V	$Ag^+ + HNO_2 \rightleftharpoons Ag + NO_2 + H^+$	$\Delta E = -0.41$ V
<u>$Bi(NO_3)_3$</u> [86]**:** $\boldsymbol{Bi^{3+} + 3e^- \rightleftharpoons Bi}$ $\boldsymbol{E_0 = 0.215 + 0.0197 log\left(C_{Bi^{3+}}\right) = 0.16\ V}$		
NO_2/NO_2^- (Eq. 1.19) $E° = 0.9$ V	$Bi^{3+} + 3NO_2^- \rightleftharpoons Bi + 3NO_2$	$\Delta E = -0.74$ V
NO_2/HNO_2 (Eq. 1.20) $E° = 1.09$ V	$Bi^{3+} + 3HNO_2 \rightleftharpoons Bi + 3NO_2 + 3H^+$	$\Delta E = -0.93$ V

Na_2MoO_4 [86]**:** $\boldsymbol{MoO_4^{2-} + 4H^+ + 2e^- \rightleftharpoons MoO_2 + 2H_2O}$ $\boldsymbol{E_0 = 0.606 - 0.1182pH + 0.0295log\left(C_{MoO_4^{2-}}\right) = -0.09\ V}$		
NO_2/NO_2^- (Eq. 1.19) $E° = 0.9$ V	$MoO_4^{2-} + 4H^+ + 2NO_2^- \rightleftharpoons MoO_2 + 2H_2O + 2NO_2$	$\Delta E = -0.99\ V$
NO_2/HNO_2 (Eq. 1.20) $E° = 1.09$ V	$MoO_4^{2-} + 2H^+ + 2HNO_2 \rightleftharpoons MoO_2 + 2H_2O + 2NO_2$	$\Delta E = -1.18\ V$
$Ni(CH_3COO)_2$ [86]**:** $\boldsymbol{Ni^{2+} + 2e^- \rightarrow Ni}$ $\boldsymbol{E_0 = -0.250 + 0.0295log\left(C_{Ni^{2+}}\right) = -0.31\ V}$		
NO_2/NO_2^- (Eq. 1.19) $E° = 0.9$ V	$Ni^{2+} + 2NO_2^- \rightarrow Ni + 2NO_2$	$\Delta E = -1.21$ V
NO_2/HNO_2 (Eq. 1.20) $E° = 1.09$ V	$Ni^{2+} + 2HNO_2 \rightarrow Ni + 2NO_2 + 2H^+$	$\Delta E = -1.4$ V
Oxidation of the precursor		
$Ni(CH_3COO)_2$ [86]**:** $\boldsymbol{Ni_3O_4 + 8H^+ + 2e^- \rightleftharpoons 3Ni^{2+} + 4H_2O}$ $\boldsymbol{E_0 = 1.977 - 0.2364pH - 0.0886log\left(C_{Ni^{2+}}\right) = 1.40\ V}$		
NO_2^-/NO (Eq.1.11) $E° = 1.2$ V	$3Ni^{2+} + 2H_2O + 2NO_2^- \rightleftharpoons Ni_3O_4 + 4H^+ + 2NO$	$\Delta E = -0.2\ V$
HNO_2/NO (Eq.1.12) $E° = 1.00$ V	$3Ni^{2+} + 2H_2O + 2HNO_2 \rightleftharpoons Ni_3O_4 + 6H^+ + 2NO$	$\Delta E = -0.4\ V$

However, it is important to note that by calculating the ΔE using the E° of the redox couple involving HNO_2 and NO_2^- species rather than the actual E under our specific conditions, we may have overlooked crucial information. As previous mentioned, determining the precise E requires knowledge of the exact conditions of our medium, which we currently lack. Nonetheless, out of curiosity, we attempted to calculate the ΔE using the approximate conditions available to us. Specifically, we considered the medium's pH after exposure for each precursor, the concentration of HNO_2 and NO_2^- determined in Chapter 1, section 3.2.2, and assumed a partial pressure of the gaseous species to be 1 (acknowledging that this assumption is not realistic). This recalculation aimed to include as many known factors as possible to verify that no significant information was missed (Supplementary information SI.5). This approach yielded the same conclusions as those previously found, indicating that additional parameters do not alter the outcome. Nevertheless, it is worth noting that in the future, if more accurate measurements of the concentrations and partial pressure of the species created by GP become available, it may be possible to incorporate all the corresponding values in a more detailed analysis of the redox reactions considered.

3.1.3. Nature of the precursor:

Another aspect that we did not previously consider is the chemical speciation of the components present in the medium. In fact, some precursors introduce other types of species that can impact the reactions occurring in the medium. In our earlier discussions, we only considered that the precursors dissolved to yield aqua ions when reacting with water molecules ($[M(OH_2)_N]^{z+}$, here noted as M^{z+}). However, some precursors are made of complex ions involving coordinating species like Cl^- and NH_3, and appear as such upon dissolution.

That is indeed what happens with $(NH_4)_2PtCl_4$. Upon dissolution, $[PtCl_4]^{2-}$ ions are present, as a result of the dissociation of the precursor [91]. To understand the influence of these complexes, we have to examine the Pourbaix diagram of Pt, both without and with the presence of Cl^- ions, as shown in Figure 2.5 [92]. We observe that when Pt^{2+} is present as a complex $[PtCl_4]^{2-}$, its stability range is extended to a higher pH value (up to around 6). This diagram also shows that for Cl-Pt complexes, at the pH obtained after the exposure of the Pt precursor (2.7), PtO_2 can no longer be formed, and Pt is the only solid that can precipitate at this pH. This highlights the importance of considering the ions actually present in the solution after the dissolution of the precursor, and of taking into account, when necessary, the possible reactions these ions could undergo in solution.

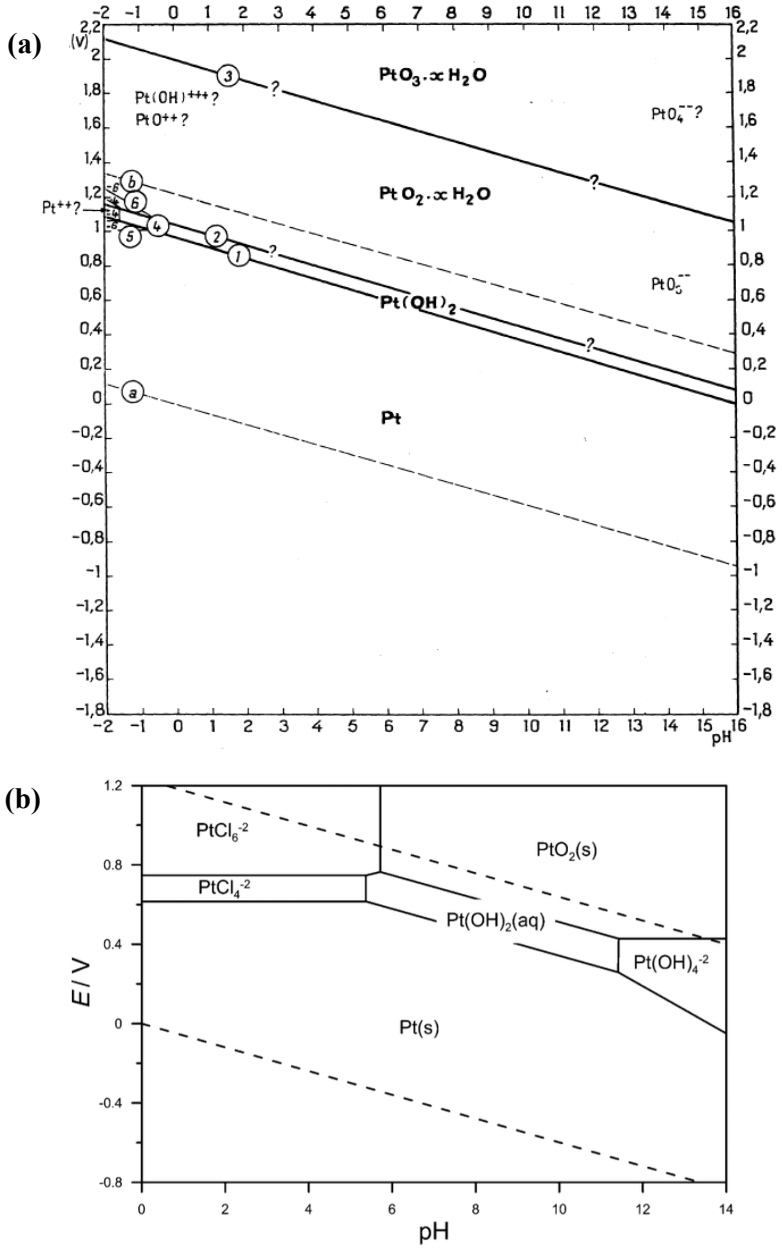


Figure 2.5: Pourbaix diagram of (a) Pt-water at 25°C [86] ; (b) Pt-water containing 0.5M of HCl at 25°C [92]

Knowing this, it is possible to calculate ΔE for the redox reaction of $[PtCl_4]^{2-}$ with HNO_2 or NO_2^- to eventually form Pt (Table 2.6), calculated from the final pH obtained after GP exposure (Table 2.2) and the initial concentration of the precursor (Table 2.1). To do so, we need to consider the potential of the couple

ML_y/M (Eq.2.6) that can be calculated thanks to the formation constant (K_f) of the ML_y complex (Eq.2.3) and the potential of the redox couple that does not imply the ligand, M^{n+}/M (Eq.2.4).

For a neutral L ligand, the corresponding equations are:

$$M^{z+} + yL \rightleftharpoons \left[ML_y\right]^{z+} \quad with\ K_f = \frac{\left[\left[ML_y\right]^{z+}\right]}{[M^{z+}][L]^y} \qquad (Eq.2.3)$$

$$M^{z+} + ne^- \rightleftharpoons M \quad with\ \mathrm{E}_{\left(\frac{M^{z+}}{M}\right)} = E°_{\left(\frac{M^{z+}}{M}\right)} - \frac{RT}{nF}\ln\left(\frac{1}{[M^{z+}]}\right) \qquad (Eq.2.4)$$

$$\left[ML_y\right]^{z+} + ne^- \rightleftharpoons M + yL$$

$$with\ E_{\left(\frac{[ML_y]^{z+}}{M}\right)} = E°_{\left(\frac{[ML_y]^{z+}}{M}\right)} - \frac{RT}{nF}\ln\left(\frac{[L]^y}{\left[\left[ML_y\right]^{z+}\right]}\right) \qquad (Eq.2.5)$$

$$\Leftrightarrow$$

$$E°_{\left(\frac{[ML_y]^{z+}}{M}\right)} = E°_{\left(\frac{M^{z+}}{M}\right)} - \left(\frac{RT}{nF}\right)\ln(K_f) \qquad (Eq.2.6)$$

Table 2.6: Redox reactions between HNO_2 or NO_2^- species and $(NH_4)_2PtCl_4$

$(NH_4)_2PtCl_4$ [91]: **Where $K_f = 10^{16}$; $E°_{\frac{Pt^{2+}}{Pt}} = 1.2V$** $[PtCl_4]^{2-} + 2e^- \rightleftharpoons Pt + 4Cl^-$ $E° = 0.73 + 0.0295log\left(\frac{C_{[PtCl_4]^{2-}}}{(C_{[Cl^-]})^4}\right) = 0.924\ V$		
NO_2/NO_2^- (Eq. 1.19) $E° = 0.9$ V	$[PtCl_4]^{2-} + 2NO_2^- \rightleftharpoons Pt + 2NO_2 + 4Cl^-$	$\Delta E =$ 0.02 V
NO_2/HNO_2 (Eq. 1.20) $E° = 1.09$ V	$[PtCl_4]^{2-} + 2HNO_2 \rightleftharpoons Pt + 2NO_2 + 2H^+ + 4Cl^-$	$\Delta E =$ -0.17 V

We can therefore see that considering the actual ions present in solution upon dissolution of the precursor is important to anticipate its potential reaction with plasma species and, consequently, its possible precipitation. In the case of the $(NH_4)_2PtCl_4$ precursor, precipitation is not possible because the ΔE for the redox reaction of $[PtCl_4]^{2-}$ with HNO_2 or NO_2^- is either very close to 0 or less than 0.

3.1.4. Solubility of the precipitate:

In addition to the precursors mentioned above, there are other precursors that did not precipitate and were not previously discussed. These include compounds that do not require a change of oxidation state (OS) to form the corresponding solid (Al^{3+}, Fe^{3+}, Ti^{4+}) (Table 2.2). For these precursors, a redox reaction is not the phenomenon required to initiate the precipitation. Instead, the formation of the precipitate depends solely on the concentration of ions present in the solution that participate in the formation of the solid. It is governed by the solubility of the precipitate that can be formed.

In fact, a solid in solution exists in a chemical state known as solubility equilibrium. Each solubility equilibrium is defined by a temperature-dependent equilibrium constant (K_s). In a dynamic equilibrium as such, certain individual molecules migrate between the solid and solution phases at equal rates of dissolution and precipitation. When equilibrium is reached and the solid has not been completely dissolved, the solution is considered saturated. The concentration of a solute in saturated solution is known as the solubility (s), which is temperature dependent. A solution containing a higher concentration of solute than the solubility is said to be supersaturated, and it is under these conditions that a precipitate can form [93]. This occurs when the so-called solubility quotient (Q_s) (that has the same expression as K_s but with the concentrations at a specific point in time) is higher than the solubility constant K_s [94].

When the precipitate is a hydroxide of a metal ion (which can later be transformed into an oxide either through thermal treatment or spontaneously if the hydroxide form is unstable), K_s is usually defined as follows [91]:

$$M(OH)_{n(s)} \rightleftharpoons M^{n+}_{(aq)} + nOH^{-}_{(aq)} \qquad (Eq.\,2.7)$$

$$K_s = [M^{n+}][OH^{-}]^n \qquad (Eq.\,2.8)$$

To determine whether a hydroxide can form in our plasma-exposed solution, we need to have $Q_s > K_s$, which is thus function of the amount of metallic ion M^{n+} and OH^- present in the medium. By considering this, we can calculate the Q_s of the precursors mentioned above since we know the concentration of M^{n+} introduced into the solution (from the initial concentration of the precursor (Table 2.1)) and the concentration of OH^- determined from the final pH measurement (Table 2.2, Eq.2.9) (Table 2.7) [91]. By doing that, we observe that, for all of these precursors, $Q_s < K_s$, which is coherent with the fact that no precipitate was observed.

$$pOH = 14 - pH \quad and \quad pOH = -\log[OH^-] \qquad (Eq.2.9)$$

Table 2.7: Initial concentration, final pH after plasma exposure, precipitate that is supposed to form, Ks and Qs of precursors that do not necessitate a change of OS to form a precipitate in the final pH range obtained after plasma-exposure

Metal	**Precursor**	**C_i (mol/L)**	**Final pH**	**Precipitate that can be formed** [86]	**Ks** [86]	**Qs**
Al	$AlCl_3$	$2*10^{-2}$	3.2	$Al(OH)_3/Al_2O_3$	10^{-34}	10^{-35}
Fe	$Fe(NO_3)_3$	10^{-2}	2.3	$Fe(OH)_3/Fe_2O_3$	$[10^{-37}; 10^{-42}]$	10^{-38}
	$FeCl_3$		2.4			10^{-37}
Ti	$Ti(SO_4)_2$	10^{-2}	1.6	$Ti(OH)_4/TiO_2$	$[10^{-40}; 10^{-43}]$	10^{-52}

The solubility constant explains why these precursors did not form a precipitate by exposure to the GP. Indeed, the initial concentration of the precursor used, and therefore of the metallic ions, was not high enough to fulfil the condition $Q_s > K_s$ and initiate precipitation. To confirm this, we attempted to expose a precursor containing Fe^{3+} and Al^{3+} ions at a higher concentration (0.03 mol/L) to the plasma, ensuring $Q_s > Ks$. Under these conditions, a precipitate formed. However, it is worth noting that precursors that do not require a change in OS to form the corresponding hydroxide do not necessitate plasma to precipitate. On the contrary, since hydroxides are the primary species involved in the precipitation, exposing the precursor to plasma, which generates H^+ species, tends to prevent the precipitation. Indeed, when we compared the precipitate formed from the $Fe(NO_3)_3$ precursor with or without exposure to the plasma, we obtained the same solid, confirming the lack of interest of plasma for these types of precursors (Figure 2.6) (NB: To see the formation of a precipitate from a precursor containing Fe^{3+} ion at higher concentration, heating the solution was necessary either after plasma exposure for the GP synthesis or during the stirring for the non-GP synthesis).

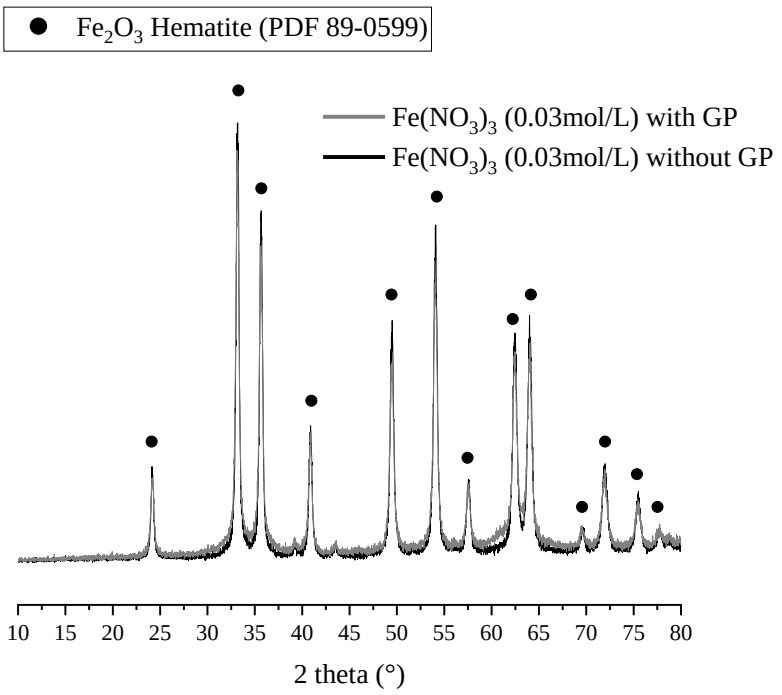


Figure 2.6: XRD data of solids formed after calcination, in the case of $Fe(NO_3)_3$ (0.03 mol/L) exposed to the GP or not

This reveals another important parameter to consider before exposing any type of precursor, namely that the initial precursor concentration is high enough to allow the formation of a precipitate provided that a redox reaction can occur. Indeed, if we calculate the Q_s for all precursors that react by plasma (if possible), we observe that in every case, $Q_s > K_s$ (Table 2.8), in line with the formation of precipitates following the redox reaction in all these cases.

Table 2.8: Initial concentration, final pH after plasma exposure, precipitate that is supposed to form, Ks and Qs of precursors reacting by GP to form a precipitate

Metal	Precursor	C_i (mol/L)	Final pH	Precipitate	K_s [86,95]	Qs
Fe	$FeSO_4$	10^{-2}	3	$Fe(OH)_3/Fe_2O_3$	$[10^{-37}; 10^{-42}]$	10^{-35}
	$(NH_4)_2Fe(SO_4)_2$		3			10^{-35}
Mn	$Mn(CH_3COO)_3$		4.8	MnO_2	Insoluble	
	$KMnO_4$		3.2			
	$NaMnO_4$		3.2			
Sn	$SnCl_2$		1.6	$Sn(OH)_4/SnO_2$	$[10^{-58}; 10^{-64}]$	10^{-51}
	$SnSO_4$					10^{-50}
Ti	$TiCl_3$		3.7	TiO_2	Insoluble	

In conclusion to this part, the solubility of the precipitate formed is not a determining factor in whether a precursor will react by GP. However, it is important to consider this aspect to be able to observe the precipitate resulting from the redox reaction of the precursors with the plasma species. Therefore, solubility should be considered, as is the case for any usual precipitation process, after confirming that a precursor is expected to react by GP, before exposing it to the GP reactor.

This section also highlights an important issue in the GP catalysts synthesis. Most precipitates initially form as hydroxides before converting to oxides. Consequently, the concentration of OH^- ions is critical to determine their ability to precipitate. However, as mostly acidic species are generated in the medium during GP exposure, the concentration of OH^- decreases over time, which in turn affects the ability of the precursor to precipitate.

3.1.5. Interest of the plasma for precursors that spontaneously form a precipitate in water

It also worth noting that some precursors forming a precipitate after GP exposure, tend to also undergo oxidation or reduction spontaneously in water. As previously discussed in section 3.1.1., species located outside the zone between the lines “a” and “b” on the Pourbaix diagram are not stable in water and tend to spontaneously transform into more stable ones found within this zone [86]. However, MnO_4^-, Sn^{2+} and Ti^{3+} precursors are all present outside this area, indicating that they tend to spontaneously transform into the solids also formed by GP. By employing a similar process to that used with HNO_2 and/or NO_2^- species, but this time using H_2O as a reactant (O_2/H_2O or O_2/O^{2-} if reduction, H_2O/H_2 or H^+/H_2 if oxidation), we observe that the ΔE values of the redox reactions of these three precursors with water indicate spontaneous reaction (Table 2.9) [86,91]. However, we know that plasma makes the formation of these precipitates quicker. For example, while it takes days for $KMnO_4$ to precipitate into MnO_2 in water, with GP, a precipitate appears after only 4 minutes of exposure [42,96].

In this context, the question arises as to whether we can anticipate the benefit of exposing a precursor to the GP rather than allowing it to react in water. To answer this, we need to consider the kinetics of the redox reactions. In fact, a redox reaction is more likely to occur if the number of electrons needed is smaller [90]. Furthermore, the greater the ΔE between 2 reacting couples, the quicker the reaction may occur [91]. In fact, for all the precursors that react by GP, we observe that the number of electrons needed is sometimes smaller

and ΔE is always greater when reacting with plasma species (Table 2.9). This theoretically demonstrates the benefit of using plasma over allowing the reaction to occur in water, as calculations indicate that the redox reaction with GP-generated species are quicker than those with water species.

Table 2.9: Redox reactions between HNO_2/NO_2^- species or H_2O/H^+ and precursors exposed to the GP that give a precipitate

Precursor → precipitate	**Reaction with HNO_2 or NO_2^-**		**Reaction with H_2O or H^+** **If metal reduction:** $O_2 + 4H^+ + 4e^- \rightleftharpoons 2H_2O$ $E° = 1.23\ V$ **If metal oxidation:** $2H^+ + 2e^- \rightleftharpoons H_2$ $E° = 0\ V$	
	Number of electrons	**ΔE (V)**	**Number of electrons**	**ΔE (V)**
$KMnO_4$: $MnO_4^- + 4H^+ + 3e^- \rightleftharpoons MnO_2 + 2H_2O$ $E = 1.692 - 0.0788pH + 0.0197log(C_{MnO_4^-}) = 1.41\ V$	3	0.51 ; 0.32	12	0.18
$SnSO_4$; $SnCl_2$: $SnO_2 + 4H^+ + 2e^- \rightleftharpoons Sn^{2+} + H_2O$ $E = -0.077 - 0.1182pH - 0.0295log(C_{Sn^{2+}}) = -0.26\ V$	2	1.46 ; 1.26	2	0.26
$TiCl_3$ [86]**:** $TiO_2 + 4H^+ + e^- \rightleftharpoons Ti^{3+} + 2H_2O$ $E = -0.666 - 0.2364pH - 0.0591log(C_{Ti^{3+}}) = -1.11\ V$	1	2.31 ; 2.11	2	1.11

3.2. Application of the identified factors to predict precursors that may react by GP:

With the parameters we have identified, it is now possible to anticipate which precursors will react by GP to give a precipitate and which will not. To facilitate this approach, we have created a dichotomous key. This key allows to determine, step by step, whether a precursor may or may not fit the identified parameters identified crucial for its ability to react and form a precipitate by GP (Figure 2.7).If we examine this dichotomous key in detail and explain how to use it, we can see that the first step is to choose a precursor that is soluble in water as, currently, only aqueous solutions of a precursors are used and studied when exposed to the GP. Next, we need to identify which species are present upon the dissolution of the precursor, as mentioned in section 3.1.3 “Nature of the precursor”. If the precursor forms a complex ion upon dissolution, it is preferable to use a Pourbaix diagram that accounts this possibility for the next steps. However, if such diagram is unavailable, the Pourbaix diagram of the simple metal ion can be considered, keeping in mind that this might overlook important information on whether a precipitate can form. If a Pourbaix diagram of the formed metal ions is available, this tool allows us to quickly anticipate whether a precipitate can form at the type of pH we will have upon exposure, typically around 2-3 if the precursor does not act as a buffer, or around the pKa of the precursor. In fact, if no precipitate can be formed at such pH, there is no interest in exposing this precursor to the GP. If a precipitate can form, we still need to determine whether the metal ions present in solution would react with the plasma species by calculating the ΔE of the redox reaction between the precursor and the HNO_2/NO_2^- species, as mentioned in section 3.1.2 “Potential of the redox reaction”. For better prediction, it is preferable to calculate this ΔE using the actual E of the metal redox couple, considering the concentration of the precursor we will use and the final pH we expect to have at the end of the exposure. If the ΔE indicates that no redox reaction with plasma species will occur, the precipitate is unlikely to form. On the other hand, if the ΔE suggests that the reaction will occur, it is still possible to assess the benefit of exposing the precursor to the GP rather than allowing it to react spontaneously in water. This assessment involves examining the number of electrons and the ΔE of the redox reaction between the precursor and water, as explained in section 3.1.5 “Interest of the plasma for precursors that spontaneously form a precipitate in water”. Finally, before exposing the chosen precursor, we need to ensure that the initial concentration selected guarantees a Qs > Ks at the final pH we expect, as

mentioned in section 3.1.4 “Solubility of the precipitate”. This ensures that a precipitate will indeed form upon reaction, allowing us to recover it effectively.

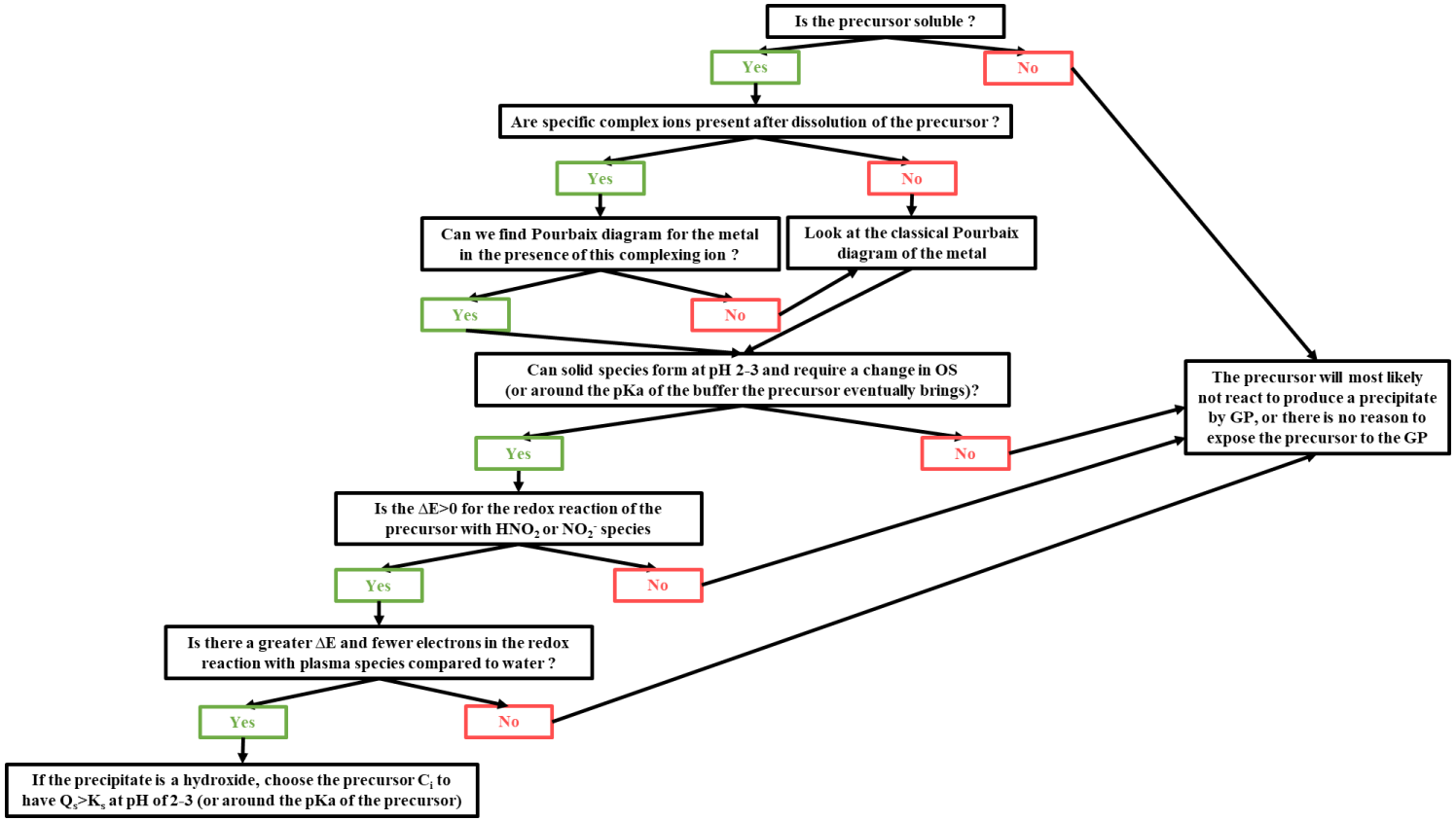


Figure 2.7: Dichotomous key to determine whether a precursor may or may not to react and form a precipitate by GP

By using this tool, two new precursors were identified as potentially reacting by GP: $HAuCl_4$ and $KRuO_4$.

For $KRuO_4$, the first parameter is respected as this precursor is soluble. In solution, it dissolves to release RuO_4^- and K^+, the latter being a spectator ion. As seen in this chapter 2, section 3.1.1, RuO_2, $Ru(OH)_3$ and Ru can all be formed under acidic pH conditions (Figure 2.8) [86]. However, referring to the position of these solids with respect to RuO_4^- in the Pourbaix diagram, we observe that the formation of RuO_2 must precede the formation of $Ru(OH)_3$ or Ru species. Therefore, it is only interesting to determine if RuO_2 can be formed as, if not, other ruthenium-based solids will also not be able to form. To ascertain this, we calculated the ΔE for the redox reaction of RuO_4^- with HNO_2 or NO_2^- species to form RuO_2, which indicates that the reaction is feasible (Table 2.10). We can also confirm the interest of exposing this precursor to the GP rather than allowing it to simply react with water. By calculating the ΔE and the number of electrons involved in the redox reaction, it is evident that both values are respectively higher and smaller, when reacting with GP than with water species (Table 2.10). Finally, before exposing this precursor to the GP, we need to ensure that the initial concentration of $KRuO_4$ is high enough to have $Q_s > K_s$. However, as RuO_2 is considered completely insoluble, the initial concentration does not really matter [97]. To validate the theory that tells us that this reaction will work, we exposed a solution of 10^{-3} mol/L of $KRuO_4$ to the GP for 30 min and observed indeed the formation of a black precipitate after 1 min, corresponding to RuO_2 (Figure 2.9, Figure 2.10).

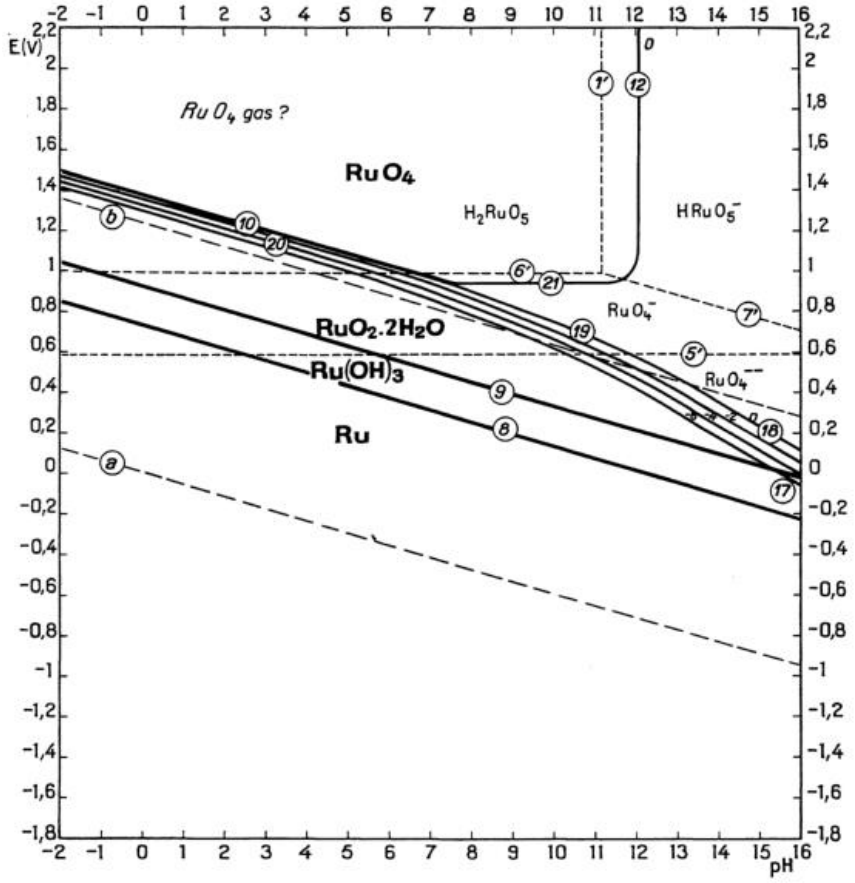


Figure 2.8: Pourbaix diagram of Ru-water at 25°C [86]

Table 2.10: Redox reactions between HNO_2 or NO_2^- species and $KRuO_4$ precursor

<u>$KRuO_4$</u> [86]<u>:</u> $\boldsymbol{RuO_4^- + 4H^+ + 3e^- \rightleftharpoons RuO_2 + 2H_2O}$ $\boldsymbol{E_0 = 1.533 - 0.0788pH + 0.0197log(C_{RuO_4^-}) = 1.238\ V}$ (if pH=3 and C_i $KRuO_4^-$= 1*10^{-3} mol/L)		
NO_2/NO_2^- (Eq. 1.19) $E° = 0.9$ V	$RuO_4^- + 4H^+ + 3NO_2^-$ $\rightleftharpoons RuO_2 + 3NO + 2H_2O$	ΔE $= 0.338\ V$ $; 3e^-$
NO_2/HNO_2 (Eq. 1.20) $E° = 1.09$ V	$RuO_4^- + H^+ + 3HNO_2$ $\rightleftharpoons RuO_2 + 3NO_2 + 2H_2O$	ΔE $= 0.148\ V$ $; 3e^-$
$O_2 + 4H^+ + 4e^-$ $\rightleftharpoons 2H_2O$ $E_0 = 1.23$ V	$4RuO_4^- + 4H^+ \rightleftharpoons 4RuO_2 + 3O_2 + 2H_2O$	ΔE $= 0.008\ V$ $; 12e^-$



Figure 2.9: Pictures of solids formed, in the case of $KRuO_4$ exposed to the GP

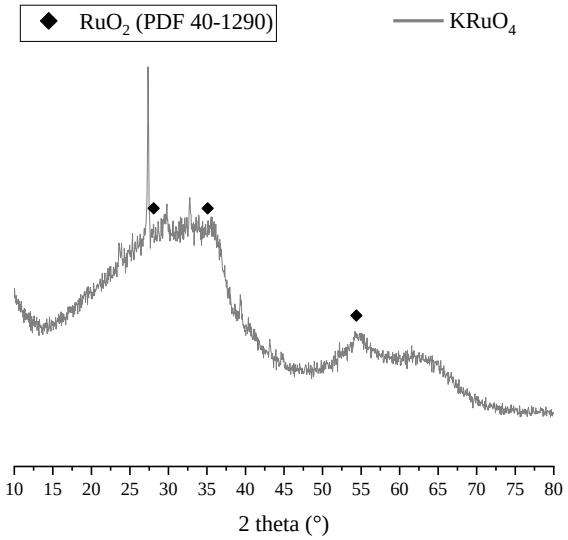


Figure 2.10: XRD data of solids formed, in the case of $KRuO_4$ exposed to the GP

In the case of $HAuCl_4$, the system is more complicated. This precursor is soluble and can potentially form the Au precipitate under acidic pH conditions (Figure 2.11 (a)) [86]. However, when $HAuCl_4$ dissolves in water, it behaves as a strong Brönsted acid and dissociates into H^+ and $AuCl_4^-$ ions (Figure 2.11 (b)) [98]. Furthermore, in aqueous solution, $AuCl_4^-$ undergoes spontaneous hydrolysis with different levels of hydroxylation depending on the pH (Eq.2.10) [99,100]. According to the literature, at pH around 2-3, the predominant species present in solution are $AuCl_4^-$, $[AuCl_3(OH)]^-$, and $[AuCl_2(OH)_2]^-$ [100,101].

$$AuCl_4^- + jH_2O \rightleftharpoons AuCl_{4-j}(OH)_j^- + jCl^- + jH^+ \qquad (Eq.2.10)$$

(a)

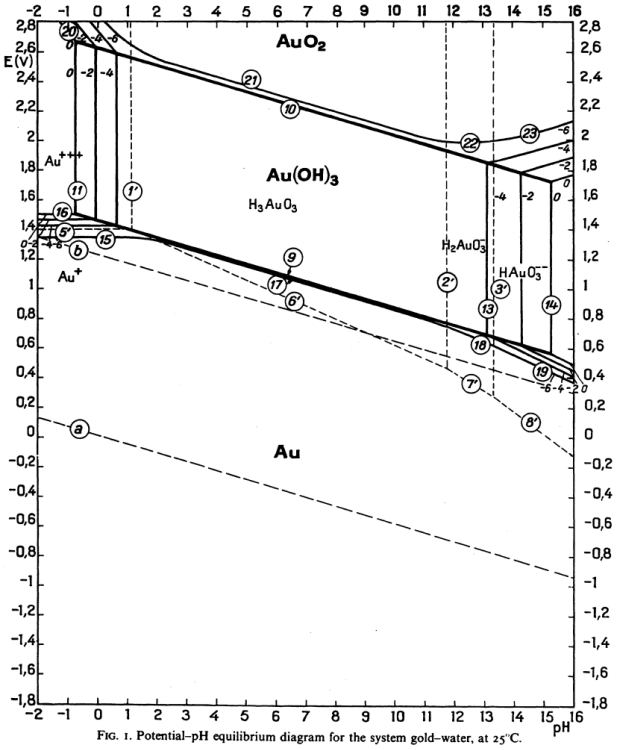


FIG. 1. Potential–pH equilibrium diagram for the system gold–water, at 25°C.

(b)

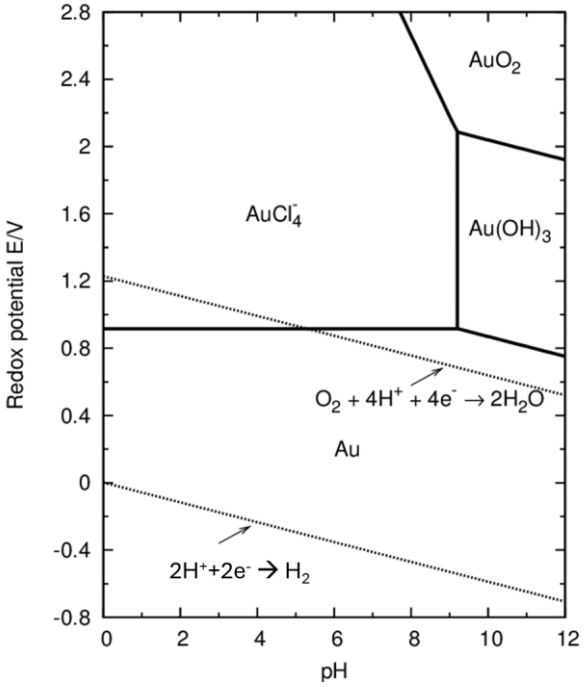


Figure 2.11: Pourbaix diagram of (a) Au-water at 25°C, (b) Au-water-Cl⁻ at 25°C [86,98]

Therefore, to determine if $HAuCl_4$ is able to react with HNO_2 or NO_2^- species to form Au^0, we first need to calculate the $E_{\left(\frac{[ML_y]^{z+}}{M}\right)}$ of these complexes using their formation constant K_f and the $E_{\left(\frac{M^{z+}}{M}\right)}$ of the redox couple $Au^{3+/}Au$ (Eq.2.11-2.14, Table 2.11) [86,102]. By calculating the ΔE of the redox reaction of these complexes with HNO_2 or NO_2^- species, we observe that all of them could achieve a redox reaction with at least NO_2^-.

Before testing this precursor, we selected a concentration in $HAuCl_4$ of 10^{-3} mol/L, as Au is considered as completely insoluble. Finally, when $HAuCl_4$ is exposed to the GP, we do obtain a precipitate, which is pure metallic Au (Figure 2.12, Figure 2.13).

$$Au^{3+} + 3e^- \rightleftharpoons Au \quad E_1^\circ = 1.5 + 0.0197\log(C_{Au^{3+}}) = 1.44V \quad (\text{if } C_{Au^{3+}} = 10^{-3}\ \text{mol/L}) \qquad (\text{Eq. 2.11})$$

$$Au^{3+} + 4Cl^- \rightleftharpoons [AuCl_4]^- \quad K_f = 1 * 10^{24} \qquad (Eq. 2.12)$$

$$Au^{3+} + 3Cl^- + OH^- \rightleftharpoons [AuCl_3(OH)]^- \quad K_f = 1 * 10^{19} \qquad (Eq. 2.13)$$

$$Au^{3+} + 2Cl^- + 2OH^- \rightleftharpoons [AuCl_2(OH)_2]^- \quad K_f = 1 * 10^{13} \qquad (Eq. 2.14)$$

Table 2.11: Redox reactions between HNO_2 or NO_2^- species and $HAuCl_4$ precursor

$HAuCl_4$: $AuCl_4^-$: $\boldsymbol{AuCl_4^- + 3e^- \rightleftharpoons Au + 4Cl^-}$ $\boldsymbol{E° = 0.97\ V}$		
NO_2/NO_2^- (Eq. 1.19) $E° = 0.9$ V	$AuCl_4^- + 3NO_2^- \rightleftharpoons Au + 3NO_2 + 4Cl^-$	$\Delta E = 0.07\ V\ ; 3e^-$
NO_2/HNO_2 (Eq. 1.20) $E° = 1.09$ V	$AuCl_4^- + 3HNO_2 \rightleftharpoons Au + 3NO_2 + 3H^+ + 4Cl^-$	$\Delta E = -0.12\ V\ ; 3e^-$
$HAuCl_4$: $[AuCl_3(OH)]^-$: $\boldsymbol{[AuCl_3(OH)]^- + H^+ + 3e^- \rightleftharpoons Au + 3Cl^- + H_2O}$ $\boldsymbol{E° = 1.07\ V}$		
NO_2/NO_2^- (Eq. 1.19) $E° = 0.9$ V	$[AuCl_3(OH)]^- + H^+ + 3NO_2^- \rightleftharpoons Au + 3NO_2 + 3Cl^- + H_2O$	$\Delta E = 0.17\ V\ ; 3e^-$
NO_2/HNO_2 (Eq. 1.20) $E° = 1.09$ V	$[AuCl_3(OH)]^- + H^+ + 3HNO_2 \rightleftharpoons Au + 3NO_2 + 3Cl^- + H_2O$	$\Delta E = -0.02\ V\ ; 3e^-$
$HAuCl_4$: $[AuCl_2(OH)_2]^-$: $\boldsymbol{[AuCl_2(OH)_2]^- + 2H^+ + 3e^- \rightleftharpoons Au + 2Cl^- + 2H_2O}$ $\boldsymbol{E° = 1.18\ V}$		
NO_2/NO_2^- (Eq. 1.19) $E° = 0.9$ V	$[AuCl_2(OH)_2]^- + 2H^+ + 3NO_2^- \rightleftharpoons Au + 3NO_2 + 2Cl^- + 2H_2O$	$\Delta E = 0.28\ V\ ; 3e^-$
NO_2/HNO_2 (Eq. 1.20) $E° = 1.09$ V	$[AuCl_2(OH)_2]^- + 2H^+ + 3HNO_2 \rightleftharpoons Au + 3NO_2 + 2Cl^- + 2H_2O$	$\Delta E = 0.09\ V\ ; 3e^-$



Figure 2.12: Pictures of solids formed, in the case of $HAuCl_4$ exposed to the GP, before drying

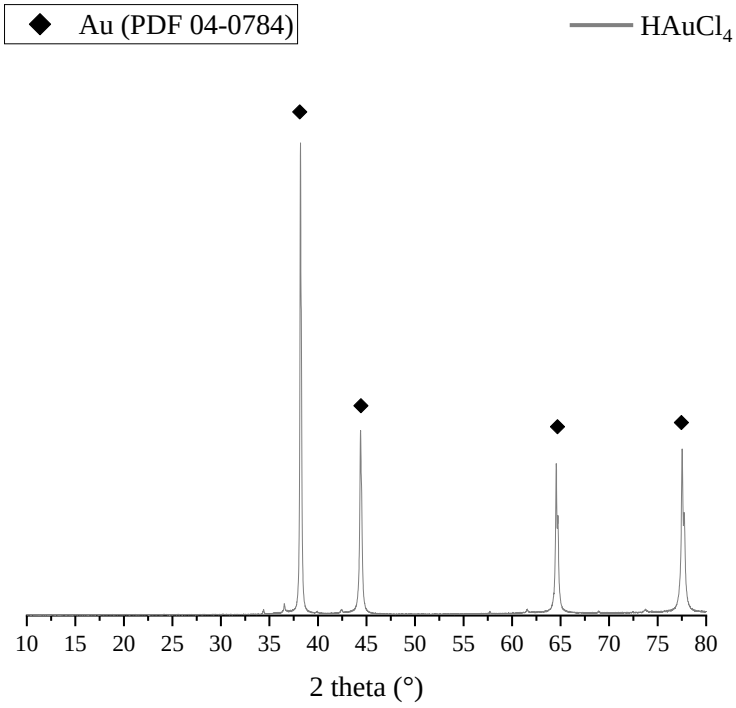


Figure 2.13: XRD data of solids formed, in the case of $HAuCl_4$ exposed to the GP

The formation of these two new precipitates suggests that the dichotomous key created to predict the formation of a solid upon exposure of a metal precursor to the GP is effective, at least in providing an indication of whether a precursor might react to form a precipitate upon GP exposure.

4. Conclusion

The objective of this chapter was to investigate the parameters influencing the ability of specific precursors to react via humid air GP, leading to the formation of a precipitate. The aim was to enhance understanding of the method, ultimately enabling the synthesis of a wider range of catalysts and increasing the interest of GP as an innovative method for catalyst synthesis.

To achieve this objective, we adopted a strategy to identify commonalities between precursors that do form a precipitate via GP and those that do not react. The purpose was to determine the factors influencing the ability of a precursor to react. Since our method shares commonalities with the precipitation process, we sought to draw inspiration from this technique.

Several factors were identified as predominant in the ability of a precursor to react, including medium pH, potential of redox reactions, nature of the metal precursor and precursor and precipitate's solubility. Precisely, now we know that for a precursor to react by GP and form a precipitate, it is needed to:

1) Ensure that the precursor is soluble in aqueous medium.
2) Identify the actual species resulting from the dissociation of the precursors.
3) Identify if the metal can form a solid at acidic pH around 3
4) Ascertain that the precipitation of the precursor necessitates a change of oxidation state of the metal.
5) Calculate whether the ΔE of the redox reaction between the precursor and HNO_2 and/or NO_2^- plasma species to form the solid are > 0.
6) Choose an initial concentration of precursor high enough to ensure that $Q_s > K_s$ for the precipitate.
7) Check the potential interest of GP exposure over a simple water reaction by calculating the ΔE and the number of electrons needed for the precursor to undergo a redox reaction with water species. If the ΔE and number of electrons required are respectively higher and smaller with plasma species compared to water species, this indicates that GP exposure is advantageous.

These identified factors have enabled us to create a dichotomous key that can be used for any type of precursors that could be intended to expose to the GP, allowing to anticipate its potential reaction and precipitation. By utilizing this key, we have identified 2 new precursors that react by GP, forming new types of solids never before synthesized by this method: Au and Ru-based solids. This demonstrates that GP may be a promising method for developing new

types of catalysts, such as metal-supported catalysts. However, it is important to note that this dichotomous key also indicates that only a limited number of precursors may react by plasma, at least without changing the conventional synthesis parameters we are currently employing. Therefore, this chapter not only highlights the new possibilities that the GP catalysts synthesis may offer, but also underlines its limitations.

Part II - Optimization of the humid air GP catalysts synthesis

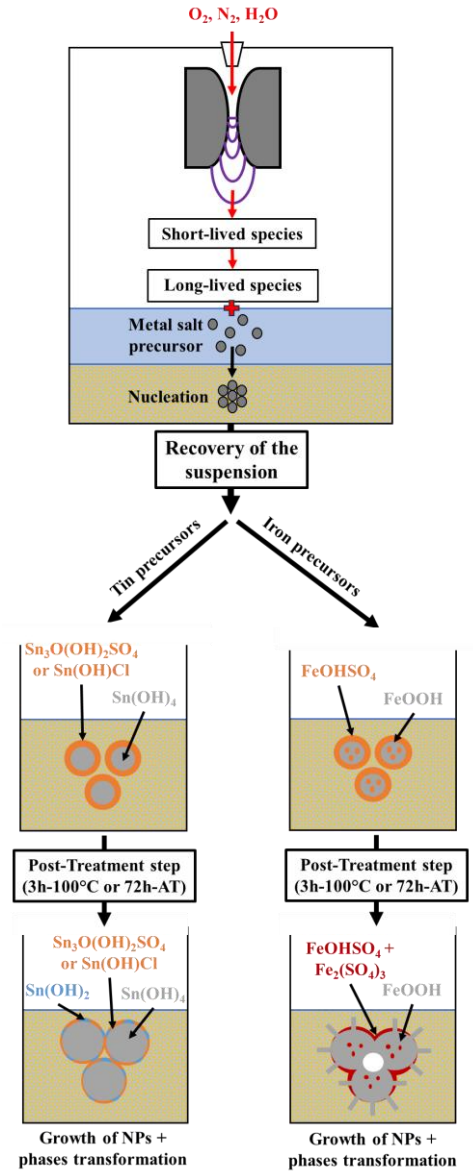
Abstract

In previous Part I, we have improved the understanding of the GP catalysts synthesis method by identifying the main plasma species responsible for the precipitation of the precursors. Furthermore, we identified the factors dictating the ability of a metal precursor to react and precipitate by GP. Consequently, we now have a better grasp of the types of precursors that react by GP and the types of precipitates that can be formed after exposure. Additionally, we have demonstrated that the GP catalysts synthesis offers the possibility to synthesize various types of catalysts under interesting synthesis conditions.

However, the method can still be improved. Although the catalysts formed have been shown to possess interesting characteristics in the literature, there is still room for improvement by modifying some synthesis conditions. Furthermore, despite the already favourable synthesis conditions, such as the use of non-chemical reagents other than air and water and the rapid reaction time, further enhancements can be made to improve the method from both environmental and economical perspective.

Therefore, the part 2 presented here aims to enhance the GP catalysts synthesis by either improving the characteristic of the synthesized solids or optimizing the synthesis conditions. This section is divided in 3 chapters: the first focuses on optimizing the catalysts through the use of a Post-Treatment step, and the other 2 others primarily discuss improving the method by employing a “no-cooling system” and a “Glidarc Plasma Activated Water” approach.

Chapter 3 - Post-Treatment: an interesting step to improve heterogeneous catalysts synthesized by glidarc plasma?



Abstract

Gliding arc plasma (GP) is an interesting method for synthesizing heterogeneous catalysts. In this process, metal salts precursors react with plasma species to form a precipitate. Research has shown that adding a Post-Treatment (PT) step in the synthesis of catalysts (FeO_x and MnO_x derived from $(NH_4)_2Fe(SO_4)_2$ and $KMnO_4$) can enhance properties like phase transformation, specific surface area and catalytic activity. Hypotheses have been proposed, suggesting that the long-lived species created in PT affect the solids transformation, but this has not been conclusively proven. Therefore, this chapter aims to explore the influence of PT on various types of solids GP-synthesized and understand the mechanisms of this step. Iron and tin precursors were exposed to the plasma and submitted to two types of PT. The synthesis conditions did not consistently impact the characteristics of the plasma-synthesized solids for the different metals, but a consistent pattern was observed for different salts of a same metal. Specifically, solids obtained from different precursors of the same metal, identically exhibit superior catalytic activity when synthesized under similar conditions. To investigate further, iron and tin precursors were exposed to a PT where no plasma species were present. To do so, the plasma-synthesized solids were recovered and placed into pure distilled water before performing the PT step. By comparing solids obtained through classical PT, we understood that, although long-lived plasma species can still trigger the reaction of metal ions remaining in solution during the PT, they do not impact the way the solid is transformed during this stage.

The results presented in this chapter have been published in:

F. Hanon, E.M. Gaigneaux, Post-discharge: An interesting step to improve heterogeneous catalysts synthesized by glidarc plasma?, Chemical Engineering Journal, Volume 489, 2024, 151088

https://doi.org/10.1016/j.cej.2024.151088

1. Introduction

As already mentioned in the General Introduction, section 3.3.2, GP has demonstrated its potential for synthesizing metal (hydr)oxides (TiO_2, FeO_x, MnO_2, SnO_2) and supported catalysts (FeO_x/Kaolinite, TiO_2/SnO_2) with interesting properties and catalytic activity when used for pollutant degradation in both gaseous and liquid phases (Table I.3) [42,56,57,59–61,64]. For some previously synthesized catalysts documented in the literature, such as FeO_x and MnO_x derived from $(NH_4)_2Fe(SO_4)_2$ and $KMnO_4$ through GP exposure, it has been observed that implementing a post-discharge (PD) step in their synthesis can impart valuable new properties such as phase transformation, increased specific surface area, and enhanced catalytic activity (Figure 3.1, Table 3.1) [61,65]. This step has historically been referred to as such in the literature. However, given that the term "Post-Discharge" in plasma terminology differs from its usage in the context of GP catalysts synthesis, this step will be referred to as the "Post-Treatment" (PT) step throughout of this thesis.

The PT step consists of, after exposing the precursor solution to GP and turning off the discharge, allowing the solution to stand outside the reactor for a defined duration and at a fixed temperature (Figure 3.1). Hypotheses have been proposed to explain the changes that the solid undergoes during this step, suggesting that the long-lived species created in PT might influence the solid's transformation. However, no conclusive evidence supporting these hypotheses has been provided. At this stage, this step is clearly not fully understood. Therefore, it remains challenging to determine *a priori* whether it is beneficial to incorporate the PT step in the GP synthesis of various catalysts.

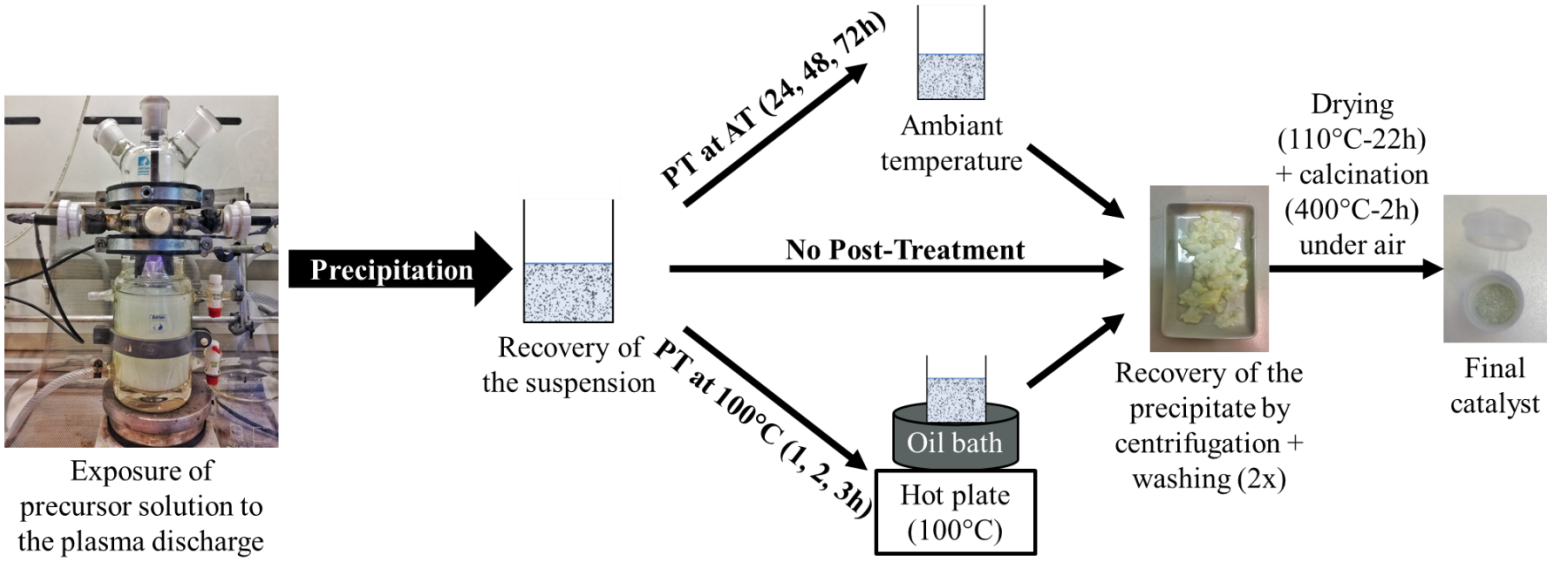


Figure 3.1: Scheme of catalysts synthesis with and without a post-discharge step

Table 3.1: Effect of the post-treatment step at 100°C and/or AT on solids synthesized from $(NH_4)_2Fe(SO_4)_2$ and $KMnO_4$ (compilation of [61,65])

	$(NH_4)_2Fe(SO_4)_2$	**$KMnO_4$**	
	PT at 100°C (1,2,3h)	**PT at 100°C (1,2,3h)**	**PT at AT (24,48,72h)**
Change of phase	Amorphous solid → crystalline α-FeOOH	α-MnO_2 → γ-MnO_2	
Specific surface area	↗	↘	↗
Pore volume	↗	↘	↗
Catalytic activity	↗	↘	↗

Given this context, the aim of the research presented here was to explore the influence of PT on various types of solids synthesized by GP and to understand the underlying mechanisms of this step. This investigation was undertaken with the purpose of gaining a more comprehensive understanding of the synthesis of catalysts by GP, aiming to refine and improve the process. This goal aligns with the broader objective of developing interesting catalysts through this innovative, economically viable, and environmentally friendly approach. Here, we particularly focus on the synthesis of catalysts dedicated to air depollution by the total oxidation of pollutants.

2. Experimental methods

2.1. Materials

Iron(II) sulfate heptahydrate ($FeSO_4.7H_2O$; ≥ 99%), tin(II) sulfate ($SnSO_4$; ≥ 95%) and tin(II) chloride ($SnCl_2$; ≥ 99%) were purchased from Sigma Aldrich and ammonium-iron(II) sulfate hexahydrate ($(NH_4)_2Fe(SO_4)_2.6H_2O$; ≥ 99%) from Roth.

All the solutions were prepared with demineralized water as solvent.

2.2. Method

2.2.1. Synthesis device: the GP reactor

The gliding arc plasma system used in this study is the same as the one presented in Experimental, section 1.

2.2.2. Materials synthesis

The precursor solutions were prepared by dissolving 10^{-2} mol/L of these compounds in deionized water. Subsequently, 450 mL of the respective

solutions were introduced into the reactor, stirred magnetically (1 rotation/s), and exposed to the plasma discharge for 45 min for $(NH_4)_2Fe(SO_4)_2.6H_2O$, 60 min for $FeSO_4.7H_2O$ and 120 min (1h of exposure, 15 min break, 1h of exposure) for $SnSO_4.7H_2O$ and $SnCl_2$. These four precursors were chosen because, among those that react with GP, they produce the largest amount of precipitate, which facilitates analysis of the synthesized solids. Based on previous studies, either from literature or in the lab, these exposure times were chosen to synthesize the catalysts with the best catalytic activity and/or the highest yield of recovered precipitate [25,56]. The optimal exposure time varies depending on the type of precursor used.

To investigate the impact of the PT on different types of solids, 2 recovery methods were performed:

- For catalysts produced without PT (named "precursor"), the solid formed when the solution is exposed to the plasma discharge was recovered by centrifugation (24490 G, 30 min) and subjected to two washing cycles with distilled water (Figure 3.1).
- For catalysts produced with PT, the suspension obtained after plasma exposure was collected and placed in a berlin before undergoing the PT step, without agitation. The PT was conducted in 2 different ways: by allowing the berlin to stand at ambient temperature (≈ 20°C) for 72 hours (named "precursor + PT (72h-AT)") or by immersing it in an oil bath at 100°C for 3 hours (named "precursor + PT (3h-100°C)"). The resulting solid was then recovered through centrifugation (24490 G, 30 min) and subjected to two washing cycles with distilled water (Figure 3.1).

Blanks samples were prepared for each precursor to assess the influence of plasma on their precipitation. For the samples intended for comparison with synthesis without PT, the precursor solution was stirred at AT for the same duration as the typical GP. For samples meant to compare with synthesis subjected to a PT step, the solution/suspension was transferred into a beaker after stirring at AT, then underwent PT at AT for 72h or at 100°C for 3h. If a precipitate formed, it was recovered, washed, and dried, as for the solids formed by GP.

For the iron precursors, the quantity of precursors transformed into a precipitate was quantified by UV-visible spectroscopy (in the same conditions as explained in Part I, Chapter 1, section 2.2.3).

To understand the mechanism underlying the PT step, a comparative analysis was conducted between the solids derived from $(NH_4)_2Fe(SO_4)_2$ and $SnSO_4$ when subjected to a classical PT and a PT performed without plasma species present in the system (named "precursor + PT (72h-AT) new water" or "precursor + PT (3h-100°C) new water"). The process involved recovering the precipitate after the plasma discharge through centrifugation at 24490 G for 30 min. Subsequently, a new suspension was created by placing the precipitate in 450 mL of pure distilled water. This suspension was then transferred to a berlin undergoing the PT either at room temperature (≈ AT) for 72 hours or in an oil bath at 100°C for 3 hours.

All the solids obtained after centrifugation were dried in an oven under air at 110°C for 22h ± 2h and then calcined in a muffle furnace under air at 400°C for 2h.

The amount of precipitate formed for iron and tin precursors was measured by weighing the mass of the solid after drying at 110°C.

2.3. Characterization of the solids formed

All the instrumental characterizations used here (XRD, XPS, SEM, EDX, N_2-physisorption) were done after calcination of the solids formed.

All the characterizations performed in this chapter were carried out as presented in Experimental, section 2.

All the synthesized solids were also tested catalytically in the total oxidation of benzene, as presented in Experimental, section 2.

3. Results and discussion

3.1. Investigation of the impact of the PT

3.1.1. Iron precursors

Table 3.2 shows the amount of solid recovered after iron precursors were exposed to the plasma, without and with a PT under different conditions. The plasma indeed influences the reaction of iron precursors, as without plasma-generated species, the precursors do not spontaneously precipitate. This implies that the species formed through GP have the ability to react with the precursors, leading to a subsequent precipitate. Moreover, the increased amount of recovered solid for both types of PT (3h-100°C and 72h-AT) shows that this step enables the species created during the plasma discharge to persist in their reactivity, allowing further precipitation. Furthermore, as the duration of the PT time increases (between 3h and

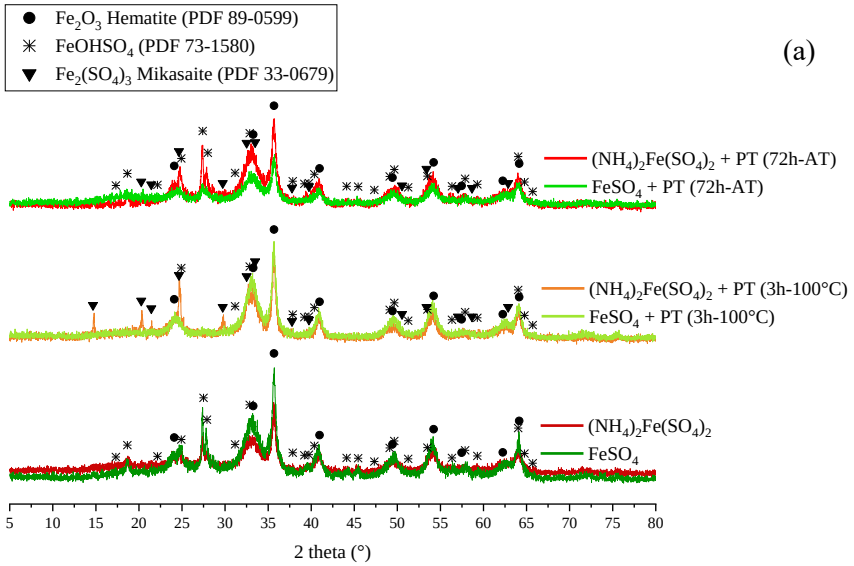
72h), the quantity of solid recovered also increases (Table 3.2). The quantification analysis, by UV-visible spectroscopy, confirmed a progressive increase in the formation of solids during the PT step (Table 3.2).

As a result of the formation of H^+ species by plasma, the medium gets acidified during the exposure process (Table 3.2). Throughout the PT, the pH continues to decrease due to the ongoing formation of H^+ species, originating from the transformation of plasma-generated nitrogen species into more stable forms, such as HNO_3 and HNO_2 [33].

Table 3.2: Mass of solid produced and pH of the solution when iron precursors are exposed to the GP without PT, with PT (3h-100°C and 72h-AT) and without plasma

	Formed precipitate			**pH**		
	Mass after exposure/PT (g)	**Yield after exposure/PT (%)**	**After no plasma exposure (g and %)**	**Precursor solution**	**After exposure**	**After PT**
$(NH_4)_2Fe(SO_4)_2$	0.050	5	0	4	3	/
$(NH_4)_2Fe(SO_4)_2$ + PT (3h-100°C)	0.119	14	0			1.9
$(NH_4)_2Fe(SO_4)_2$+ PT (72h-AT)	0.177	78	0			2.6
$FeSO_4$	0.131	28	0			/
$FeSO_4$+ PT (3h-100°C)	0.152	31	0			2.7
$FeSO_4$+ PT (72h-AT)	0.242	91	0			2.6

XRD diffractograms of the solids generated from the iron precursors reveal that the phases developed, whatever the synthesis type, are approximately the same (Figure 3.2). Both $(NH_4)_2Fe(SO_4)_2$ and $FeSO_4$ without PT consist in a mixture of hematite (Fe_2O_3) and $FeOHSO_4$. When PT is performed using $(NH_4)_2Fe(SO_4)_2$, the $FeOHSO_4$ phase tends to disappear in favor of Fe_2O_3 and mikasaite ($Fe_2(SO_4)_3$), especially for the PT conducted at 100°C. This transformation can be explained by the influence of heat, which promotes the conversion of $Fe(OH)SO_4$ into $Fe_2(SO_4)_3$, subsequently transforming into Fe_2O_3 (Eq. 3.5) [103,104]. Knowing this, it is worth noting that although the $Fe_2(SO_4)_3$ phase is not observed on the X-ray diffractograms of $FeSO_4$ + PT (3h-100°C) and + PT (72h-AT) samples, it could still be formed through the transformation of $FeOHSO_4$ but in an amorphous state.



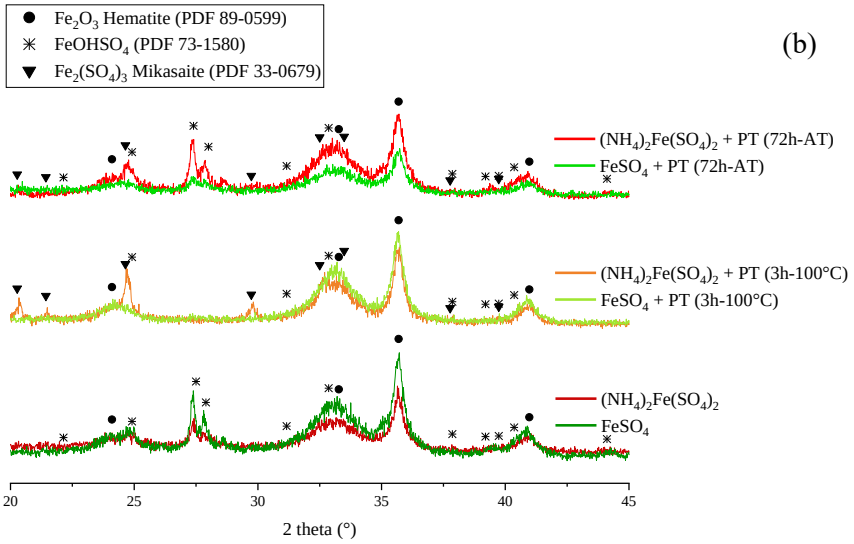


Figure 3.2: XRD data (a) complete range of 2 theta angles measured, (b) zoom on the 20-45° 2 theta range, for solids obtained after calcination with iron precursors without and with PT (3h-100°C and 72h-AT)

EDX and XPS data confirm the presence of iron sulfate phases in each solid, as indicated by the presence of sulfur and the position of the S2p peak around 169 eV (Table 3.3) [105]. Additionally, the data reveals the presence of nitrogen in the solids derived from $(NH_4)_2Fe(SO_4)_2$, suggesting the likely formation of another phase containing NH_4^+ (as indicated by the position of the N1s peak around 402 eV (Table 3.3)), which was not observed by XRD (Figure 3.2) [105]. Moreover, the at % of each element at the surface and in bulk significantly differs, indicating the heterogeneous composition of the precipitates. Furthermore, the at % of S at the surface is higher than in the bulk, implying that iron sulfate phases predominantly exist on the outer layer of the solids (Table 3.3). Furthermore, since there is no significant variation in the binding energy of Fe and O elements, it can be concluded that the valence of these elements remains the same across varying synthesis conditions (Table 3.3).

For catalytic purposes, our primary interest lies in promoting the formation of more iron oxide and fewer iron sulfate phases since sulfur is known to act as a poison in reactions like total oxidation for depollution purposes [106]. An ideal solid for depollution catalysis should have a reduced S content and a Fe/O ratio increasing towards 0.67. A solid containing a higher proportion of Fe_2O_3 (Fe/O=0.67) in comparison to $FeOHSO_4$ (Fe/O=0.2) and/or $Fe_2(SO_4)_3$ (Fe/O=0.17) achieves a Fe/O ratio

closer to 0.67. For both types of PT (3h-100°C and 72h-AT), the at % of S decreases, and the Fe/O ratio at the surface increases toward 0.67 (Table 3.3). This shows that the development of Fe_2O_3 occurs at the expense of iron sulfate. The at % of S and Fe/O ratio after the PT at AT for 72h is close to those after the PT at 100°C for 3h, especially with $(NH_4)_2Fe(SO_4)_2$ (Table 3.3). This suggests that the application of heat during PT accelerates the transformation.

Table 3.3: XPS and EDX data of solids obtained with iron precursors without and with PT (3h-100°C and 72h-AT)

	Fe			O			S			N		Fe/O
	XPS (Fe2p)		EDX	XPS (O1s)		EDX *	XPS (S2p)		EDX	XPS (N1s)		XPS
	BE (eV)	(% at)		BE (eV)	(% at)		BE (eV)	(% at)		BE (eV)	(% at)	
$(NH_4)_2Fe(SO_4)_2$	710.9	23.9	26	530.1	66.5	72	169.0	6.5	2	401.7	3.1	0.36
$(NH_4)_2Fe(SO_4)_2$ + PT (3h-100°C)	711.3	27.7	30	530.3	65.6	67	169.1	5.3	2	401.9	1.3	0.42
$(NH_4)_2Fe(SO_4)_2$ + PT (72h-AT)	711.0	28.1	31	530.5	65.8	67	169.0	4.9	3	401.8	1.2	0.42
$FeSO_4$	710.9	26.5	28	530.4	66.6	69	169.5	6.8	3	/	/	0.40
$FeSO_4$ + PT (3h-100°C)	710.8	30.2	22	530.0	65.7	77	169.0	4.1	1	/	/	0.46
$FeSO_4$ + PT (72h-AT)	710.8	26.0	22	530.0	67.4	76	168.8	6.6	2	/	/	0.39

** The at % of O obtained by EDX is likely overestimated due to the underlying adhesive carbon tape used to fix the sample.*

The provided information allows for imagining a reaction mechanism involving iron precursors during plasma discharge and during the subsequent PT steps. A. Tiya Djowe *et al*. previously proposed a 2-step solid formation mechanism for $(NH_4)_2Fe(SO_4)_2$ involving OH radicals [61]. However, our findings differ from their results, as we previously demonstrated that the primary plasma species driving the oxidoreduction leading to precipitation are instead the HNO_2/NO_2^- species (Part I, Chapter 1) [88]. Considering this, we proposed an alternative hypothetical mechanism. Given our understanding that, during the plasma discharge, a solid composed of FeOOH and $FeOHSO_4$ is formed, with the sulfate phase primarily located at the solid's surface, it is likely that a 3-step formation process of these 2 phases takes place [88]:

1) Firstly, it is probable that the Fe^{2+} ions originating from the precursor undergo oxidation by plasma species, resulting in the formation of Fe^{3+} (Eq.3.1):

$$Fe^{2+} + NO_2^- + 2H^+ \rightarrow Fe^{3+} + NO° + H_2O$$

or

$$Fe^{2+} + HNO_2 + H^+ \rightarrow Fe^{3+} + NO° + H_2O \qquad (Eq.3.1)$$

2) In an aqueous environment, Fe^{3+} ions are unstable, prompting their spontaneous hydrolysis into FeOOH if the medium is not sufficiently acidic (which subsequently transforms into Fe_2O_3 through calcination) [86] (Eq.3.2):

$$Fe^{3+} + 2H_2O \rightarrow FeOOH + 3H^+ \qquad (Eq.3.2)$$

3) Additionally, Fe^{3+} can also react with other ions present in the medium, such as SO_4^2 ions originating from the precursor (Eq.3.3):

$$Fe^{3+} + SO_4^{2-} + H_2O \rightarrow FeOHSO_4 + H^+ \qquad (Eq.3.3)$$

Given that the concentration of SO_4^{2-} is lower than that of H_2O, the likelihood of this last reaction taking place is lower. Consequently, a reduced formation of the $FeOHSO_4$ phase occurs. Furthermore, since Fe^{3+} formed ions initially react with H_2O molecules, the availability of SO_4^{2-} ions probably increases with exposure time, which means that the likelihood of $FeOHSO_4$ formation increases with time, leading to its formation mostly at the surface of the already formed FeOOH. Imagining a formation process like this could provide a plausible explanation for the type of solid we observe, wherein a core primarily composed of FeOOH and a shell predominantly composed of $FeOHSO_4$ are formed (Figure 3.4).

During the PT step, various mechanisms can still occur. Firstly, HNO_2/NO_2^- has been identified as the primary species responsible for the oxidation of the precursors exposed to the GP (Part I, Chapter 1) [88]. This species has a sufficiently long lifetime to remain present during the PT [33]. However, to be sure this is the case, we observed and quantify the amount of long-lived species (NO_3^- and NO_2^-) that are still formed during the PT step. To achieve this, we subjected distilled water to plasma exposure for 45 min then to a PT at 100°C for 1, 2 and 3h and to a PT at AT for 24, 48 and 72h. We performed an UV-visible spectroscopic analysis of the solutions as already mentioned in the Part I, Chapter 1, section 2.2.3. The amount of NO_2^- formed decreases with PT time while, on the contrary, the formation of NO_3^- increases. The larger the PT time is, the greater will be the amount of NO_3^- formed. The decrease of NO_2^- is more pronounced when the PT is performed at 100°C (Figure 3.3). Indeed, we know that NO_2^- tends to be oxidized to form NO_3^- and since oxidizing species are probably present in the medium, they can therefore eventually carry out this reaction [86]. However, even after 3h at 100°C and 72h at AT, some NO_2^- species still remain in the solution, indicating that they can still participate in reactions during both PT steps.

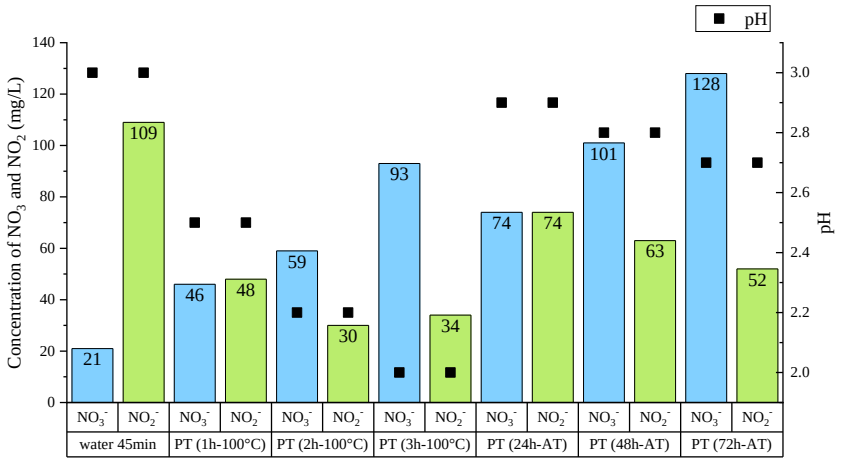


Figure 3.3: pH and concentration of NO_2^- and NO_3^- of distilled water exposed to the GP for 45 min then to PT of 1, 2 and 3h at 100°C and of 24, 48 and 72h at AT

Consequently, Fe^{2+} from the precursor that was not oxidized during the discharge may have enough time to be transformed into Fe^{3+} by these HNO_2/NO_2^- species during the PT step. This could explain the increased amount of precipitate recovered when a PT step is performed (Table 3.2). Additionally, the Fe^{3+} ions formed both during the discharge and the PT step can still react with the remaining H_2O and SO_4^{2-} in the solution.

Thereby, FeOOH and iron sulfate phases can further be created. This can occur either at the surface of previously formed particles or lead to the formation of new particles.

However, other phenomena can take place during this stage without being influenced by the plasma species generated. As suggested by the XPS results, this primarily occurs at the surface of particles already formed during the discharge. $FeOHSO_4$ can indeed react with water to form FeOOH, but it can also decompose into $Fe_2(SO_4)_3$ and FeOOH (Eq.3.4, Eq.3.5). This can explain the increased amount of Fe_2O_3 present in the solid and at its surface, as well as the appearance of $Fe_2(SO_4)_3$. However, since the transformation of $FeOHSO_4$ is more efficient under heat, it can explain why solids formed from a PT performed at 100°C have a reduced presence of this phase (Figure 3.4) [103].

$$FeOHSO_4 + H_2O \rightarrow FeOOH + H_2SO_4 \qquad (Eq.3.4)$$

$$3FeOHSO_4 \rightarrow Fe_2(SO_4)_3 + FeOOH + H_2O \qquad (Eq.3.5)$$

At this stage, it is understood that both types of PT facilitate the gradual transformation of the iron sulfate phase into iron oxide. Nevertheless, the supply of energy to the system seems to help accelerate this transformation (Figure 3.4).

However, it is worth noting that the hypothesis proposed here regarding the distribution of phases within the solid and their transformations under different synthesis conditions is based on the phases identified by XRD. Although they are not accounted in the suggested process, we can however not disregard the possibility that other phases may be present.

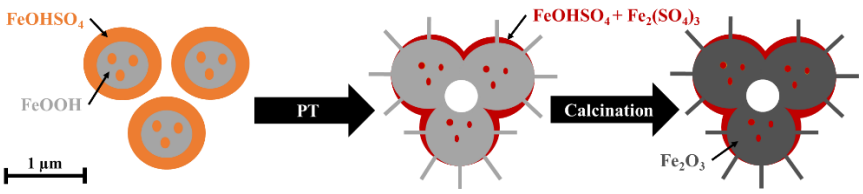
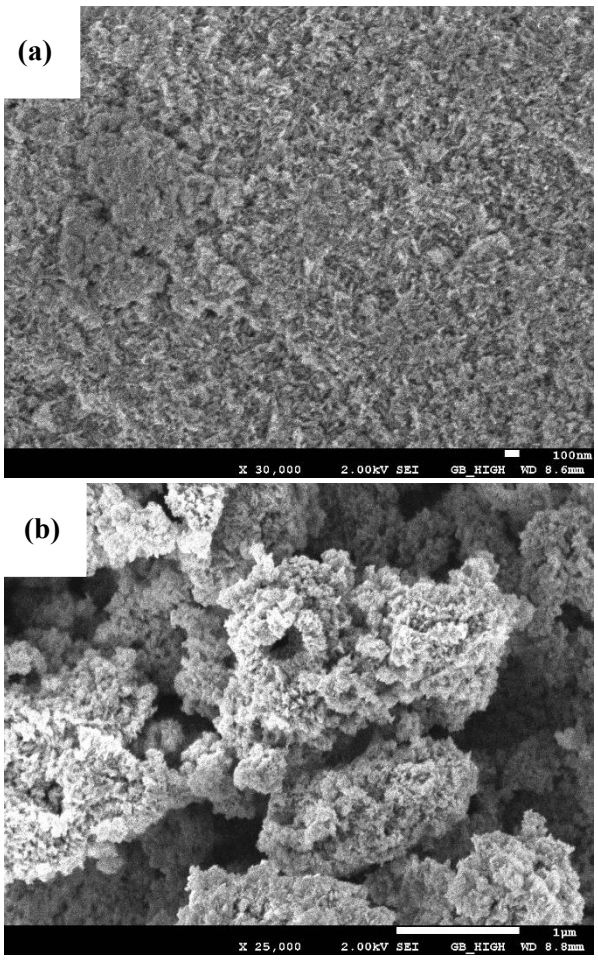
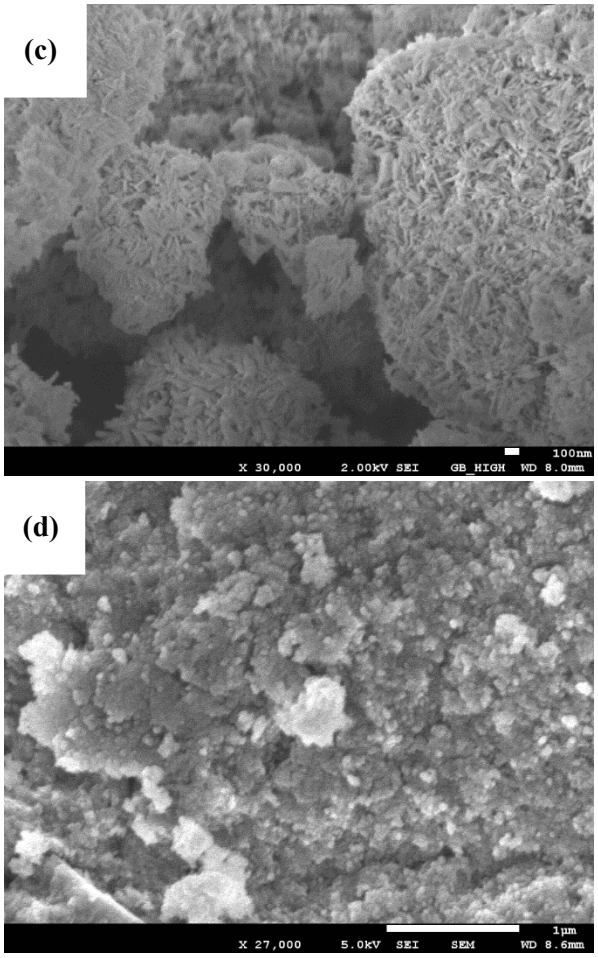


Figure 3.4: Mechanism of formation of solids obtained with iron precursors without and with PT

Regarding the change in solid morphology during the PT process, the growth of FeOOH crystals has previously been investigated by A. Tiya Dowe with $(NH_4)_2Fe(SO_4)_2$ as a precursor [25]. It was observed that during the PT, the particles agglomerate and develop into sea-urchin like hollow spheres, thereby enhancing their specific surface area and pore volume (Figure 3.4). In the literature, the formation of such structures for FeOOH synthesized by precipitation has already been achieved, but in

most cases, it requires the addition of a template during the synthesis or specific conditions (such as temperature, time and pressure) during precipitation, or a post-treatment step, as in our approach [107–109]. In our study, comparable findings were noted for the solid formed using both iron precursors. When PT is performed at 100°C for 3h and at AT for 72h, solids develop cavities and form crystals with more spikes on their surface, thereby increasing the specific surface area of the solid (Figure 3.5). When performing the PT at 100°C, alongside the emergence of spikes, we observe the formation of the "sea-urchin like" crystals for both precursors (Figure 3.5 (b) ; (e)). This observation indicates that applying heat during the PT step facilitates the advancement of crystal development. Consequently, conducting PT results in solids with a larger specific surface area and pore volume for both precursors, especially when done at 100°C for 3h (Table 3.4).




(c)
X 30,000 2.00kV SEI GB_HIGH WD 8.0mm
100nm
(d)
X 27,000 5.0kV SEI SEM WD 8.6mm
1µm

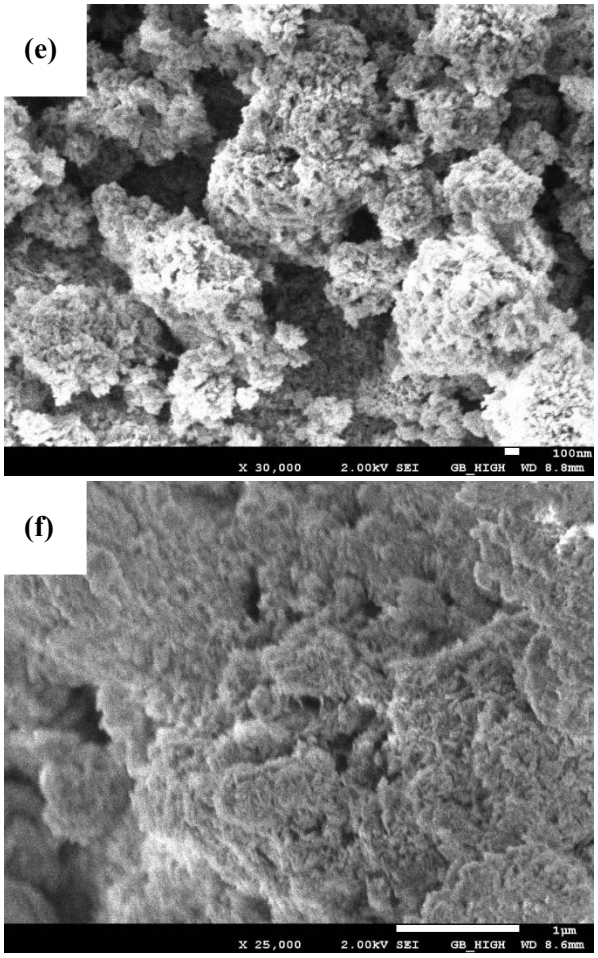


Figure 3.5: SEM images of solids formed from $(NH_4)_2Fe(SO_4)_2$ (a) without PT ; (b) + PT (3h-100°C) ; (c) + PT (72h-AT) and from $FeSO_4$ (d) without PT ; (e) + PT (3h-100°C) ; (f) + PT (72h-AT)

Table 3.4: Textural properties obtained by N_2-physisorption with iron precursors without and with PT (3h-100°C and 72h-AT) (isotherms Supplementary information SI.6)

	Specific surface area (m^2/g)	**Pore volume (cm^3/g)**
$(NH_4)_2Fe(SO_4)_2$	69	0.18
$(NH_4)_2Fe(SO_4)_2$ + PT (3h-100°C)	112	0.30
$(NH_4)_2Fe(SO_4)_2$+ PT (72h-AT)	80	0.22
$FeSO_4$	95	0.33
$FeSO_4$+ PT (3h-100°C)	133	0.34
$FeSO_4$+ PT (72h-AT)	63	0.17

In terms of catalytic activity of the solids derived from iron precursors, it is slightly enhanced when a PT is performed at 100°C for 3h for both precursors. However, the PT (72h-AT) is only beneficial for catalyst produced from $(NH_4)_2Fe(SO_4)_2$ (Figure 3.6). These results align with previously identified characteristics. As the PT process increases the presence of the catalytically active phase (Fe_2O_3) in the solid and slightly augments its specific surface area and pore volume, it accordingly enhances the catalytic activity of the resulting material. In the case of solids formed from iron precursors, the application of heat promotes the gradual transformation of the iron sulfate phase into iron oxide and improves the formation of crystals with a higher specific surface area and pore volume. Consequently, conducting the PT at 100°C for 3h has a more significant impact on the catalytic activity of the solid obtained from both precursors. Furthermore, the iron-based catalysts synthesized by GP either already resemble to or are better than commercial Fe_2O_3 (iron(III) oxide, Alfa Aesar, 30-60 m^2/g) even without the addition of a PT. However, their catalytic activity becomes even more competitive with the addition of a PT (Figure 3.6).

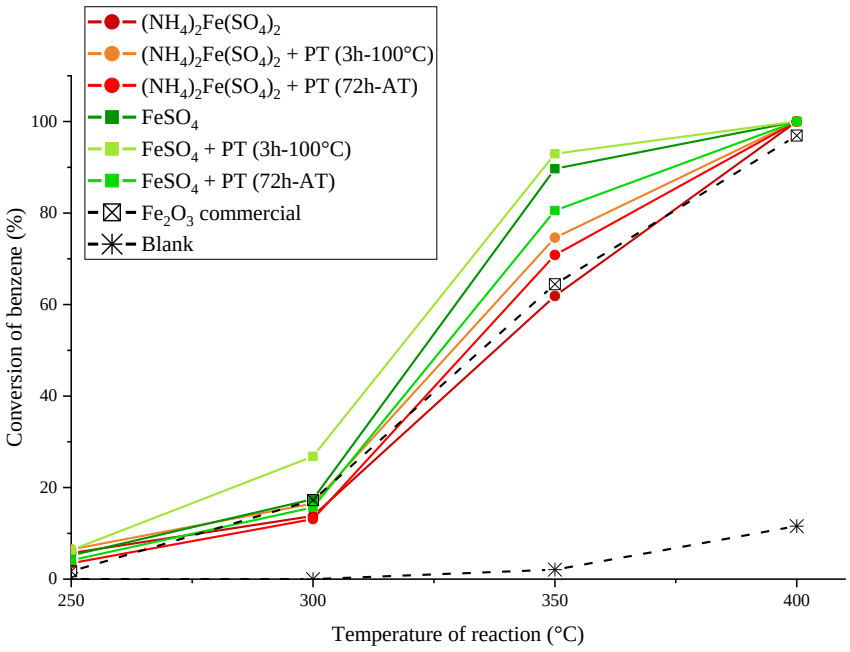


Figure 3.6: Catalytic performances of solids formed from iron precursors without and with PT (3h-100°C and 72h-AT) for the total oxidation of benzene (conversion of benzene as function of reaction temperature)

3.1.2. Tin precursors

The first observation is that the presence of plasma-generated species is not necessary for the reaction and precipitation of tin precursors, as even without plasma, a solid is formed (Table 3.5). This phenomenon arises from the instability of Sn^{2+} ions in a not acidic enough aqueous solution, causing them to spontaneously react and form $Sn(OH)_4$ [86]. Additionally, $SnSO_4$ and $SnCl_2$ in water tend to undergo hydrolysis, transforming into $Sn_3O(OH)_2SO_4$ and Sn(OH)Cl respectively [86,110–113]. However, through plasma synthesis, the quantity of recovered precipitate significantly surpasses that obtained without plasma (Table 3.5). This heightened yield is likely attributed to the oxidizing species generated by plasma. These species accelerate the oxidation of Sn^{2+} to Sn^{4+} and potentially also convert the intermediates $Sn_3O(OH)_2SO_4$ and Sn(OH)Cl into $Sn(OH)_4$. Moreover, the increased amount of recovered solid for both types of PT (3h-100°C and 72h-AT) for the $SnCl_2$ precursor shows that this step enables the species created during the plasma discharge to persist in their reactivity, facilitating further precipitation.

The precursor solution is already acidic before plasma exposure, owing to the spontaneous formation of $Sn(OH)_4$, $Sn_3O(OH)_2SO_4$ and Sn(OH)Cl, which release H^+ ions in the medium when $SnSO_4$ and $SnCl_2$ are dissolved in water [86,111,113]. The exposure to plasma further acidifies the solution by generating H^+. Throughout the PT, the pH level remains relatively stable because the solution is already at a very low pH, where the HNO_2/NO_2^- couple present in the medium (pKa = 3.3) acts as a buffer. (Table 3.5) [114].

Table 3.5: Mass of solid produced and pH of the solution when tin precursors are exposed to the GP without PT, with PT (3h-100°C and 72h-AT) and without plasma

	Mass of solid produced (g)		**pH**		
	After exposure/PT	**After no plasma exposure**	**Precursor solution**	**After exposure**	**After PT**
$SnSO_4$	0.686	0.156	2.5	2	/
$SnSO_4$ + PT (3h-100°C)	0.681	0.356			1.9
$SnSO_4$ + PT (72h-AT)	0.677	0.336			1.8
$SnCl_2$	0.674	0.069			/
$SnCl_2$ + PT (3h-100°C)	0.723	0.406			1.8
$SnCl_2$ + PT (72h-AT)	0.705	0.023			1.7

The XRD diffractograms of the solids derived from tin precursors reveal that the phases developed before and after both PT (3h-100°C and 72h-AT) remain unchanged. In both precursors, the phase developed is cassiterite (SnO_2), resulting from the dehydration of the $Sn(OH)_4$ formed in solution during the solid's drying steps (Figure 3.7). However, the presence of S and Cl detected by XPS and EDX for solids obtained from $SnSO_4$ and $SnCl_2$ respectively, suggests the possible development of another amorphous phase (Table 3.6). These phases could be Sn(OH)Cl and $Sn_3O(OH)_2SO_4$, formed through the hydrolysis of $SnSO_4$ and $SnCl_2$ respectively, as previously explained [86,111,113]. This speculation gains support from the binding energy measured by XPS, as the Cl1s peak position around 199 eV corresponds to that of chlorine atoms linked with a transition metal, and the S1s peak position around 169 eV aligns with that of a sulfate element (Table 3.6) [56,113]. Concerning the binding energy of the other elements (Sn and O), no significant variation is observed. Therefore, it can be concluded that the valence of these elements remains the same across varying synthesis conditions (Table 3.6).

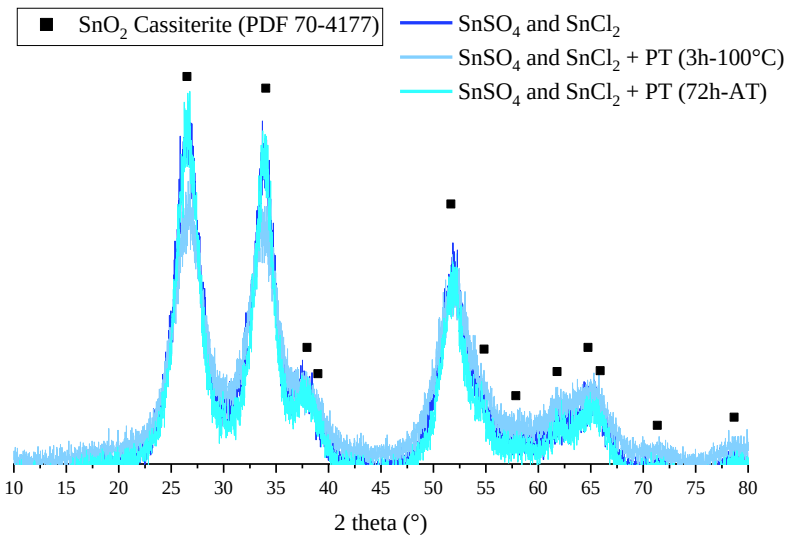


Figure 3.7: XRD patterns of solids obtained after calcination with tin precursors without and with PT (3h-100°C and 72h-AT)

XPS and EDX data highlight that the at % of each element at the surface and in bulk significantly differs, indicating the heterogeneous composition of the precipitates. Furthermore, the at % of S and Cl at the surface is higher than in bulk, implying that iron sulfate or iron chloride phases predominantly exist on the outer layer of the solids (Table 3.6).

For catalytic purposes, our primary interest lies in promoting the formation of more tin oxide and less tin sulfate or tin chloride phases since sulfur and chloride are known to act as poisons in reactions like total oxidation for depollution purposes [115–117]. Therefore, an ideal solid for depollution catalysis should have a reduced S and Cl content and a Sn/O ratio closer to 0.5. A solid containing a higher proportion of SnO_2 (Sn/O=0.5) than $Sn_3O(OH)_2SO_4$ (Sn/O=0.43) or Sn(OH)Cl (Sn/O=1) achieves a Sn/O ratio closer to 0.5. For both types of PT, the at % of S and Cl decreases at the surface, but the PT performed at AT for 72h has the most effective impact. Consequently, the development of tin oxide occurs at the expense of tin sulfate or tin chloride, at the surface of the solid. In bulk, the at % of S and Cl is already close to 0, so no big change is observed (Table 3.6).

However, regarding the Sn/O ratio, even before the PT, the value exceeds 0.5 and becomes even larger afterward (Table 3.6). This scenario is not feasible if only SnO_2, as tin oxide, is formed during the transformation of tin sulfate or tin chloride. Our observations therefore imply the presence

of another unidentified phase with a Sn/O ratio >0.5 in the solid. This could be SnO (Sn/O=1) from $Sn_3O(OH)_2SO_4$ or Sn(OH)Cl that has not had the opportunity to oxidize and subsequently transforms into tin(II) oxide. This might explain the observed increased Sn/O ratio after PT.

Table 3.6: XPS and EDX data of solids obtained with tin precursors without and with PT (3h-100°C and 72h-AT)

	Sn			O			S or Cl			Sn/O
	XPS (Sn3d)		EDX	XPS (O1s)		EDX *	XPS (S2p or Cl1s)		EDX	XPS
	BE (eV)	(at %)		BE (eV)	(at %)		BE (eV)	(at %)		
$SnSO_4$	487.1	33.5	14	530.6	63.5	85	169.4	2.9	1	0.53
$SnSO_4$ + PT (3h-100°C)	487.0	35.2	17	530.3	62.4	81	169.3	2.5	1	0.56
$SnSO_4$ + PT (72h-AT)	486.9	36.5	21	530.9	61.3	79	169.8	2.2	1	0.58
$SnCl_2$	486.6	35.2	29	530.7	63.4	71	199.1	1.4	0	0.56
$SnCl_2$ + PT (3h-100°C)	486.7	36.7	25	530.6	62.4	75	198.9	0.9	0	0.59
$SnCl_2$ + PT (72h-AT)	486.6	38.7	25	530.5	60.7	74	199.3	0.5	0	0.64

** The at % of O obtained by EDX is likely overestimated due to the underlying adhesive carbon tape used to fix the sample.*

With the above information, we propose a hypothetical reaction mechanism for $SnSO_4$ and $SnCl_2$ exposed to plasma discharge as follows:

1) Firstly, either Sn^{2+} ions resulting from the dissolution of $SnSO_4$ and $SnCl_2$ precursors spontaneously oxidize to form $Sn(OH)_4$ (Eq.3.6), or the precursors undergo hydrolysis in water to produce tin hydroxy sulfate or tin hydroxy chloride (Eq.3.7 ; Eq.3.8). In fact, in solution with Cl^- or SO_4^{2-} ions at pH = 2.5, Sn^{2+} does not form the tin hydroxide $Sn(OH)_2$ but instead prefers to transform into these components, which are more stable [86,110–113]:

$$Sn^{2+} + 4H_2O \rightarrow Sn(OH)_4 + 4H^+ + 2e^- \qquad (Eq.3.6)$$

$$3SnSO_4 + 3H_2O \rightarrow Sn_3O(OH)_2SO_4 + 4H^+ + 2SO_4^{2-} \qquad (Eq.3.7)$$

$$SnCl_2 + H_2O \rightarrow Sn(OH)Cl + HCl \qquad (Eq.3.8)$$

2) Subsequently, Sn^{2+} ions that have not had sufficient time to react spontaneously with water and tin sulfate or tin chloride intermediates formed previously can be oxidized by the plasma species into $Sn(OH)_4$ [88] (Eq.3.9):

$$Sn^{2+} + 2NO_2^- + 2H_2O \rightleftharpoons Sn(OH)_4 + 2NO°$$

or

$$Sn^{2+} + 2HNO_2 + 2H_2O \rightleftharpoons Sn(OH)_4 + 2NO° + 2H^+ \qquad (Eq.3.9)$$

In the process of transforming $Sn_3O(OH)_2SO_4$ or Sn(OH)Cl particles into $Sn(OH)_4$, it is conceivable that upon their transformation, these particles undergo rapid oxidation by plasma species, preventing them from being "trapped" within the particle core. Consequently, when plasma exposure ceases, the unoxidized portion of the precipitate predominantly resides on the solid's surface. This phenomenon could explain the absence of S or Cl in the material's bulk (Figure 3.8).

Afterward, as $Sn(OH)_4$ is less stable than Sn(IV) oxide, the application of heat during the drying steps leads to the spontaneous dehydration of $Sn(OH)_4$, resulting in SnO_2, which is the phase observed by XRD (Eq.3.10, Figure 3.7, Figure 3.8).

$$Sn(OH)_4 \rightarrow SnO_2 + 2H_2O \qquad (Eq.3.10)$$

Throughout the PT step, NO_2^- is still present due to its extended lifespan, allowing it to probably continue oxidizing some $Sn_3O(OH)_2SO_4$ or Sn(OH)Cl particles into $Sn(OH)_4$. However, NO_2^-, which is no longer generated during this step, tends to transform into NO_3^-, thus hindering its ability to completely oxidize these phases (Figure 3.3) [86]. Consequently,

some $Sn_3O(OH)_2SO_4$ or Sn(OH)Cl may simply decompose into $Sn(OH)_2$, which is later transformed to SnO during the drying step (Eq.3.11, Eq.3.12, Eq.3.13; Figure 3.8). This hypothesis fits with the observed increased Sn/O ratio during the PT step. Furthermore, even though the PT at AT for 72h has a more significant impact on transforming sulfate and chloride phases, the PT performed at 100°C for 3h already effectively transforms these phases. It appears that applying heat to the system seems to accelerate the transformation, which would probably occur anyway under ambient temperature conditions if given sufficient time.

$$Sn_3O(OH)_2SO_4 + 3H_2O \rightarrow 3Sn(OH)_2 + SO_4^{2-} + 2H^+ \quad (Eq.3.11)$$

$$Sn(OH)Cl + H_2O \rightarrow Sn(OH)_2 + Cl^- + H^+ \quad (Eq.3.12)$$

$$Sn(OH)_2 \rightarrow SnO + H_2O \quad (Eq.3.13)$$

However, it is worth noting that the hypothesis proposed here regarding the distribution of phases within the solid and their transformations under different synthesis conditions is based on the phases identified by XRD, the Sn/O ratio calculated by XPS, and information from the literature suggesting hydrolysis of the tin precursors upon dissolution into water. Although they are not accounted in the suggested process, we can however not disregard the possibility that other phases may be present.

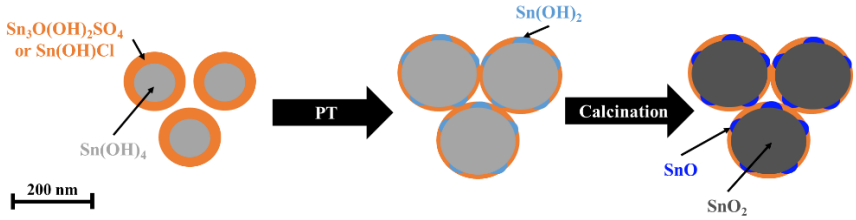


Figure 3.8: Mechanism of formation of solids obtained with tin precursors without and with PT

Regarding the change in solid morphology during the PT process, for both precursors, the specific surface area of the solid decreases without changing the pore volume (Table 3.7). This is likely a result of particle agglomeration due to heat and time. However, this hypothesis is difficult to confirm with SEM images (Supplementary information SI.8).

Table 3.7: Textural properties obtained by N_2-physisorption with tin precursors without and with PT (isotherms supplementary information SI.7)

	Specific surface area (m^2/g)	**Pore volume (cm^3/g)**
$SnSO_4$	162	0.13
$SnSO_4$ + PT (3h-100°C)	140	0.15
$SnSO_4$ + PT (72h-AT)	132	0.14
$SnCl_2$	146	0.11
$SnCl_2$ + PT (3h-100°C)	110	0.11
$SnCl_2$ + PT (72h-AT)	89	0.11

Regarding the catalytic activity of solids derived from tin precursors, it is enhanced when a PT is performed at 100°C and AT for both, but the 72h PT demonstrates a superior effect, especially for $SnSO_4$ (Figure 3.9). These results align with previously identified characteristics. As the PT process leads to an increased presence of the catalytically active phase (tin (IV and II) oxide) at the surface of the solid, particularly when conducted at AT, it thereby enhances its catalytic activity. However, in both cases, the specific surface area of the solids diminishes when a PT step is performed, especially when done at AT for 72h. This implies that augmenting the quantity of the catalytically active phase has a more significant impact than the decrease in specific surface area. Consequently, conducting the PT at AT has a more significant impact on the catalytic activity of the solid in both cases. Furthermore, compared to SnO_2 synthesized by classical with base (NH_3) addition precipitation (following the protocol proposed in the article [118], XR diffractogram of this solid in Supplementary Information SI.9), the tin-based catalysts synthesized by GP are already more catalytically active when no PT is added. However, their catalytic activity becomes even more competitive with the addition of a PT.

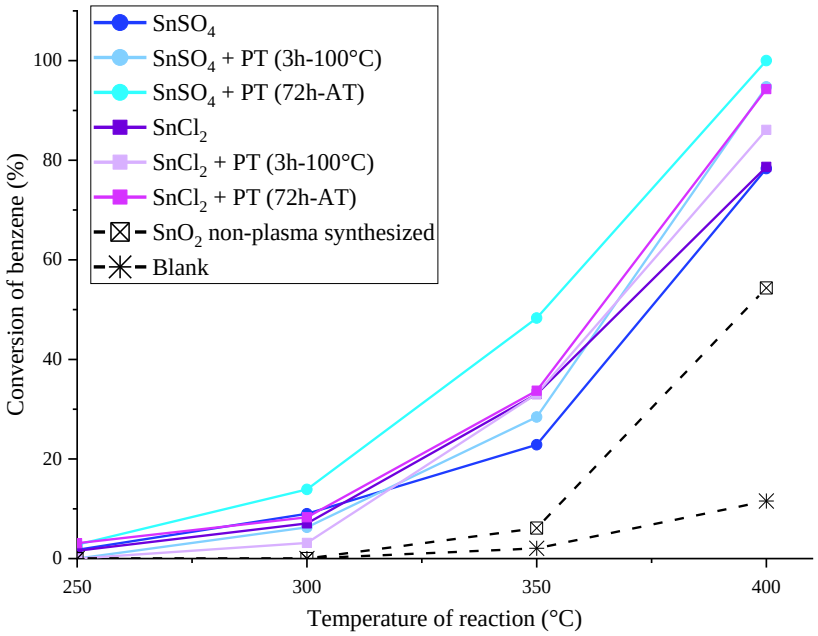


Figure 3.9: Catalytic performances of solids formed from tin precursors without and with PT for the total oxidation of benzene (conversion of benzene as function of reaction temperature)

3.1.3. What are the similar impacts of the PT on precursors exposed to the GP?

At this stage, we cannot assert that a particular type of PT consistently yields superior results by developing more interesting characteristics for all types of plasma-synthesized solids. However, when considering the influence of the PT step on precursor salts of the same metal, a discernible pattern emerges. Specifically, solids obtained from different precursors of the same metal exhibit identically superior catalytic activity when synthesized under similar conditions. Precisely, in the case of iron precursors, the PT at 100°C yields the most interesting properties, while for tin precursors, the PT at AT proves most promising. This suggests that we may be able to anticipate in advance the preferable type of PT to conduct when using a new precursor of a metal previously studied with a different precursor.

Although the impact of each PT type varies for different metal precursors, a global effect can still be observed. Firstly, the PTs do not fundamentally alter the type of solid formed. Instead, a phase formed during the plasma discharge is more or less present after the PT due to the transformation from one phase to another. Consequently, the same atoms remain in the

solid after the PT, but not in the same atomic percentage. Additionally, all tested precursors tend to form a sulfate or chloride phase, primarily located at the solid surface during the plasma discharge. Throughout each PT type, this intermediate appears to transform into a metal oxide. Furthermore, the PT invariably influences the textural properties of the solid. While the pore volume may not always change, the specific surface area does. Due to factors like time and temperature, particles formed during plasma discharge tend to agglomerate. However, this does not consistently result in a decrease in a specific surface area. Depending on crystal growth patterns, some roughness and porosity can be created, thereby increasing the solid's specific surface area. Certainly, the fact that PT affects various solid characteristics leads to changes in its catalytic activity. The activity improves when the amount of catalytically active phase increases and/or the specific area increases, but it worsens if the opposite occurs.

However, in nearly all cases, conducting a PT at either 100°C or AT enhances catalytic performance, with the exception of $FeSO_4$ + PT(72h-AT). This suggests that incorporating a PT step is almost always beneficial. If a quicker synthesis is preferred, the PT at 100°C is the more compelling choice. Alternatively, if a synthesis method requiring less energy input and resulting in a higher yield of recovered solids is desired, the PT at AT is more suitable. These results indicate that, depending on the synthesis parameters of preference, one PT may outperform another, but the addition of a PT step consistently proves to be a constructive way to enhance the performance of a plasma-synthesized catalyst.

Furthermore, it has been observed that the amount of solid recovered is impacted when a PT is performed. For most precursors, allowing more time for the solid to develop increases the quantity of recovered solid. Hence, although there are instances where the catalytic performance of the catalysts does not exhibit a significant change, questioning the necessity of adding a PT step, it consistently enhances the yield of solid formation. Therefore, incorporating a PT step is an effective way to enhance the overall plasma synthesis for two reasons: by augmenting the yield of solid formation while increasing its catalytic activity.

3.2. Elucidation of the mechanism underlying the PT

We have demonstrated that PT is an interesting step to apply in the GP synthesis, enhancing the yield of recovered solids and enabling the development of catalysts with more interesting properties. However, the exact mechanism behind this step remains unclear. Some hypotheses

proposed in the literature suggest that the species generated during the PT (H_2O_2, HNO_3, HNO_2, etc) influence the modification of the solid. Actually, these hypotheses were never proven before. Therefore, our objective is to comprehend the functioning of the PT step and determine whether the plasma species present during the PT indeed impact the modification of GP-synthesized solids. To address this, we compared solids obtained from $(NH_4)_2Fe(SO_4)_2$ and $SnSO_4$ subjected to a classical PT step with solids developed when a PT is conducted without the presence of plasma species.

The diffractograms obtained for these solids reveal that the phases developed when the PT is performed with or without the presence of plasma species are identical for $(NH_4)_2Fe(SO_4)_2$ and $SnSO_4$ in both types of PT (Figure 3.10, Figure 3.11).

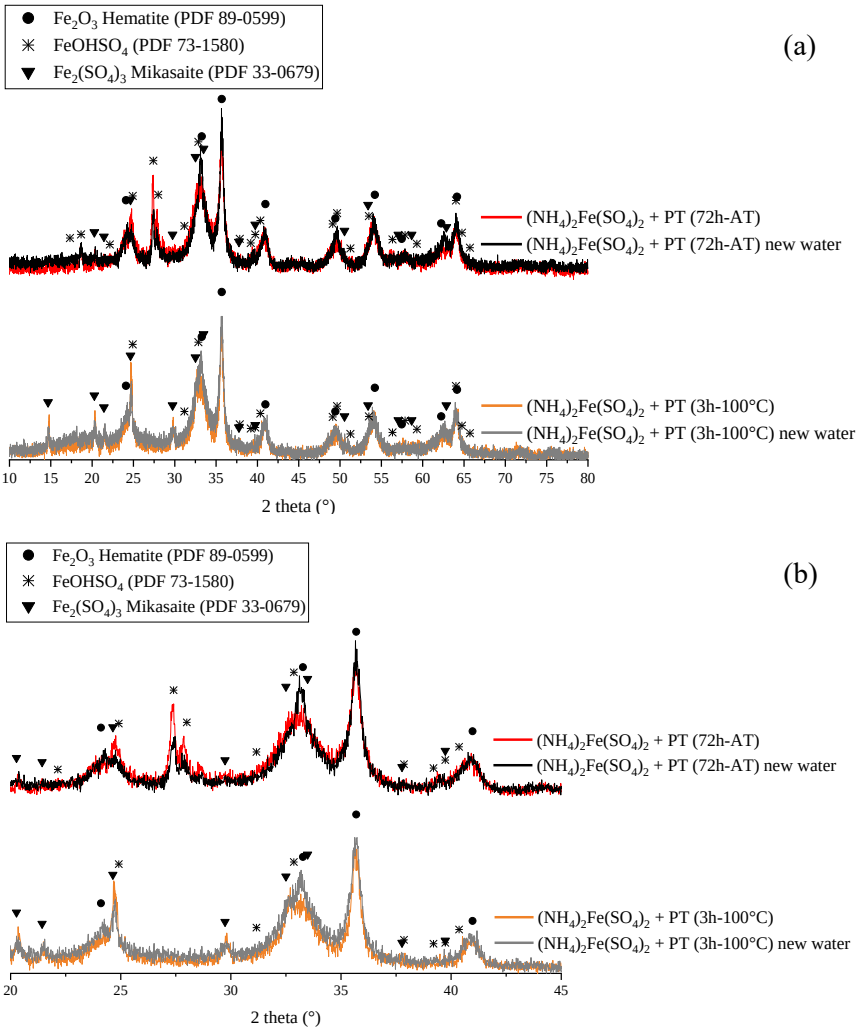


Figure 3.10: XRD data (a) complete range of 2 theta angles measured, (b) zoom on the 20-45° 2 theta range, of solids obtained after calcination with $(NH_4)_2Fe(SO_4)_2$ with PT with and without plasma species

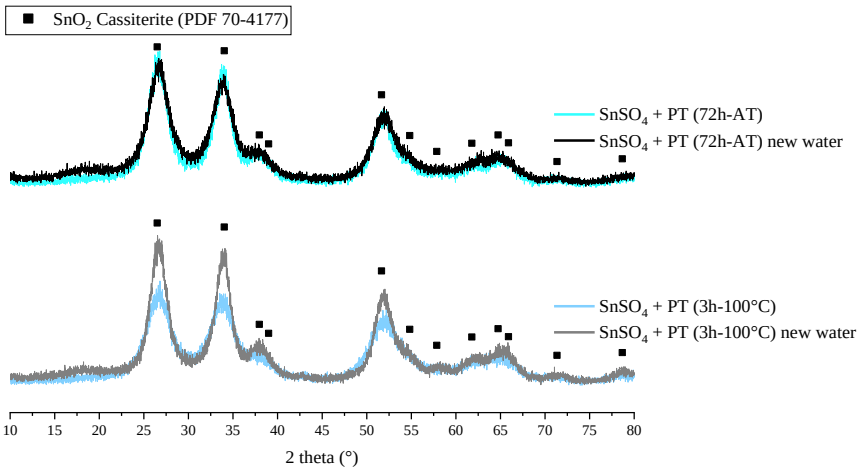


Figure 3.11: XRD patterns of solids obtained after calcination with $SnSO_4$ with PT with and without plasma species

By comparing the at % of elements present in solids synthesized with and without plasma species during the PT step, it is evident that they rarely exhibit really close similarities (Table 3.8). Notably, the only samples demonstrating a relatively similar elemental composition are the solids formed from $(NH_4)_2Fe(SO_4)_2$ with a PT (3h-100°C). However, certain commonalities are observable. Firstly, the binding energy of S2p around 169 eV as determined by XPS, constantly corresponds to SO_4^{2-}, as previously observed (Table 3.8). Furthermore, the changes occurring within the solid during the PT step remain consistent, regardless of the presence of plasma species. Specifically, the at % of S decreases, while the at % of Sn or Fe increases (Table 3.8). This suggests that the plasma-generated species present during the PT are not essential for triggering the observed transformation that typically occurs during this step, which is the conversion of iron or tin sulfates into iron or tin oxides.

The at % of S is similar or smaller, while the at % of Fe or Sn is similar or higher in almost all cases when the PT is done without plasma species (Table 3.8). This can be attributed to the "washing step" conducted by recovering the synthesized solid after the discharge and immersing it in fresh distilled water. This step not only removes the plasma-generated species but also eliminates other ions, including SO_4^{2-}. Consequently, these species can no longer interact with the synthesized solid and, therefore, cannot be deposited on its surface, diminishing the formation of the sulfates during this step.

Table 3.8: XPS and EDX data of solids obtained with $(NH_4)_2Fe(SO_4)_2$ and $SnSO_4$ with PT without plasma species

	Fe or Sn			O			S			Fe/O or Sn/O
	XPS Fe2p or Sn3d		EDX	XPS (O1s)		EDX *	XPS (S2p)		EDX	XPS
	BE (eV)	(at %)		BE (eV)	(at %)		BE (eV)	(at %)		
$(NH_4)_2Fe(SO_4)_2$ + PT (3h-100°C)	711.3	27.7	30	530.3	65.6	67	169.1	5.3	2	0.42
$(NH_4)_2Fe(SO_4)_2$ + PT (3h-100°C) new water	710.8	28.1	31	530.3	65.6	66	169.1	5.2	3	0.43
$(NH_4)_2Fe(SO_4)_2$ + PT (72h-AT)	711.0	28.1	31	530.5	65.8	67	169.0	4.9	3	0.42
$(NH_4)_2Fe(SO_4)_2$ + PT (72h-AT) new water	710.6	31.6	31	530.1	64.7	67	169.2	3	3	0.49
$SnSO_4$ + PT (3h-100°C)	487.0	35.2	17	530.3	62.4	81	169.3	2.5	1	0.56
$SnSO_4$ + PT (3h-100°C) new water	486.6	35.8	21	530.6	63.3	79	168.4	1	0	0.57
$SnSO_4$ + PT (72h-AT)	486.9	36.5	21	530.9	61.3	79	169.8	2.2	1	0.58
$SnSO_4$ + PT (72h-AT) new water	487.0	34.9	20	531.0	62.9	80	169.1	2.3	1	0.55

***** *The at % of O obtained by EDX is likely overestimated due to the underlying adhesive carbon tape used to fix the sample.*

Regarding their texture, it is evident that the changes in the solid are consistent, regardless of the presence of plasma species during the PT step (Table 3.9). When the PT is performed at 100°C for $(NH_4)_2Fe(SO_4)_2$, the specific surface area and pore volume increase. However, these features decrease when the PT is carried out at AT for the $(NH_4)_2Fe(SO_4)_2$ and for both PT involving $SnSO_4$.

Table 3.9: Textural properties obtained by N_2-physisorption of solids obtained with (a) $(NH_4)_2Fe(SO_4)_2$ and (b) $SnSO_4$ with PT with and without plasma species

	Specific surface area (m^2/g)	**Pore volume (cm^3/g)**
$(NH_4)_2Fe(SO_4)_2$ + PT (3h-100°C)	112	0.30
$(NH_4)_2Fe(SO_4)_2$ + PT (3h-100°C) new water	105	0.30
$(NH_4)_2Fe(SO_4)_2$+ PT (72h-AT)	80	0.22
$(NH_4)_2Fe(SO_4)_2$ + PT (72h-AT) new water	74	0.28
$SnSO_4$ + PT (3h-100°C)	140	0.15
$SnSO_4$ + PT (3h-100°C) new water	107	0.14
$SnSO_4$ + PT (72h-AT)	132	0.14
$SnSO_4$ + PT (72h-AT) new water	120	0.14

Finally, regarding their catalytic activity, both precursors, irrespective of plasma species presence during PT, yield solids with higher catalytic activity (Figure 3.12). This is attributed to the consistency in solid transformation, whether plasma species are present or not. In fact, although the catalytic activities of solids synthesized with or without plasma species present in the PT may not be identical, we have observed a consistent pattern of solid transformation that tends to enhance catalytic activity. Therefore, these modifications result in a similar impact on the catalytic test, regardless of the presence of plasma species during the PT, ultimately improving it compared to when no PT is performed.

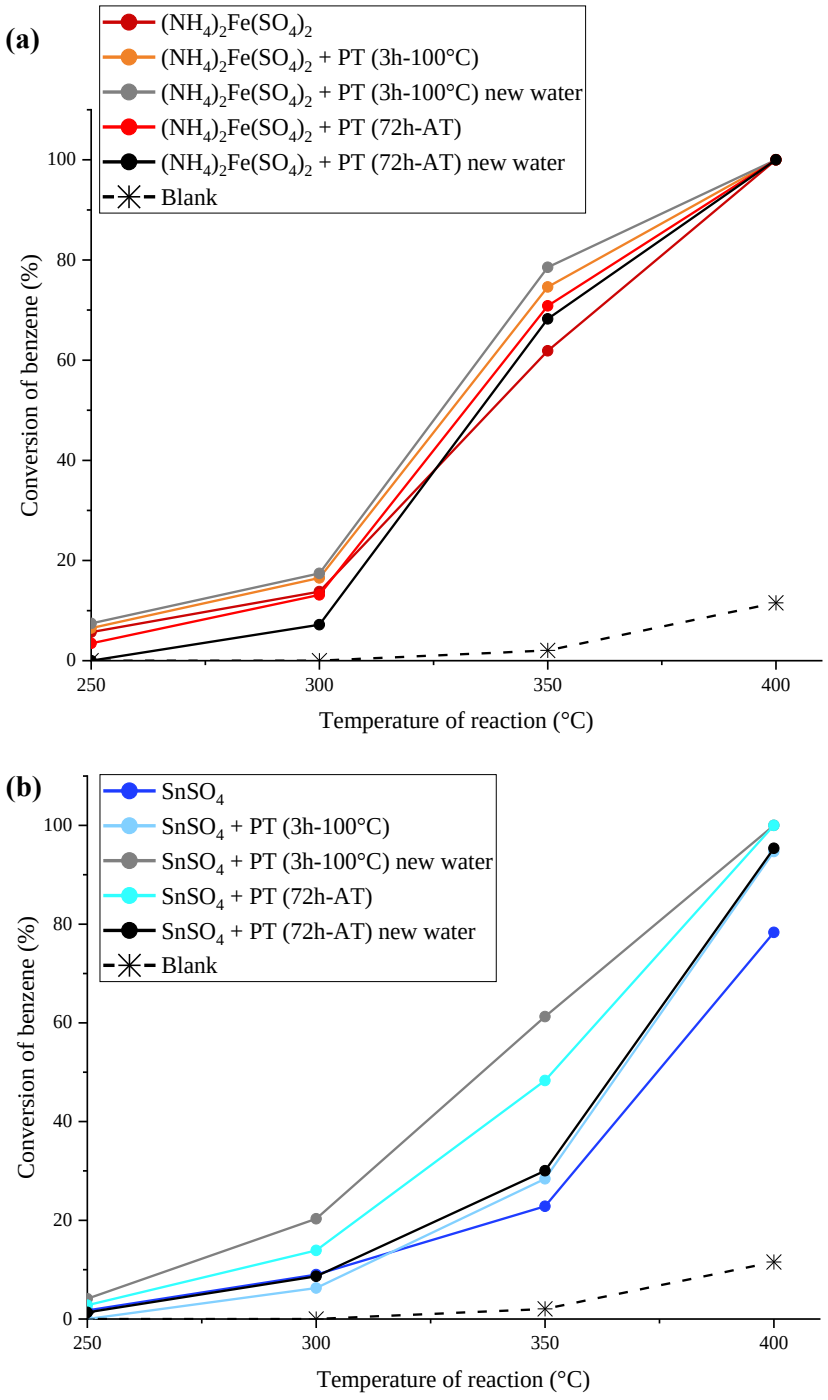


Figure 3.12: Catalytic performances of solids formed with (a) $(NH_4)_2Fe(SO_4)_2$ and (b) $SnSO_4$ with PT with and without plasma species for total oxidation of benzene (conversion of benzene as function of reaction temperature)

With the above information, in contrast to earlier suggestions in the literature, we can conclude that species generated by plasma do not play a role in the solid transformations occurring during the PT step. The phases conversion and crystal growth observed in this process primarily reflect a maturation step that involves the solid in a specific manner, contingent upon the applied heat and the duration of the step.

In classical plasma applications, the term "post-discharge" holds a different meaning than in GP. It is defined as "the area downstream of the discharge, where the species produced by the discharge are entrained by a gaseous or liquid flow but are no longer influenced by the electric field" [119]. In the gold nanoparticles (NPs) synthesis described by Mariotti et al., it is explained that within the "plasma zone", where reactive species formed by the plasma discharge are concentrated, the precursor undergoes transformation into gold NPs, constituting the "nucleation step". Subsequently, when these particles exit this zone, they enter the "post-discharge zone" where the solid grows, leading to the development of larger particles (Figure 3.13) [120]. Knowing this, we can draw a parallel between the PT step of GP and classical plasma PD. In both cases, when the precursor is exposed to the plasma discharge, it interacts with the plasma species to form a precipitate. Subsequently, when the solid is placed in PD, it undergoes a "maturation step", influenced by the duration and temperature of the PD process.

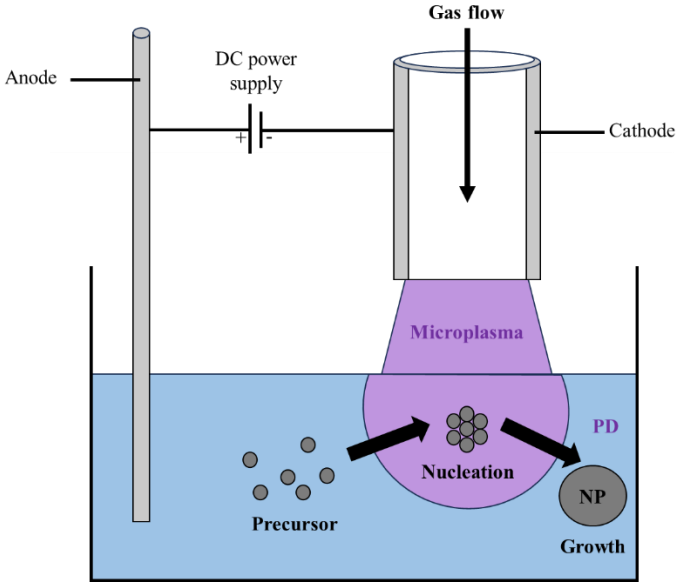


Figure 3.13: Schematic diagrams depicting the microplasma set-up used for NPs synthesis adapted from [120]

Nevertheless, although it can be concluded that plasma species do not contribute to the transformation during the PT of already precipitated solids, it can be asserted that they do influence the reaction of metal ions from the precursor that have not had sufficient time to react during the discharge. This is evidenced by the increased amount of recovered precipitate when iron and tin precursors undergo the PT step (Table 3.2, Table 3.5). In fact, we have previously established that NO_2^- is the main species responsible for the precipitation process and that it persists long enough to be present during the PT step (Figure 3.3) [33,88]. Therefore, these species do still initiate the transformation of metal ion precursors remaining in solution. However, once the discharge is shut down, no more NO_2^- species are generated, and they tend to decompose into NO_3^- (which has been identified as not triggering the reaction) (Figure 3.3) [86,88]. Consequently, they cannot remain present in sufficient amounts to facilitate the reaction of all the remaining metal ion precursors in solution.

4. Conclusion

GP catalyst synthesis offers interesting conditions when compared to alternative synthesis methods, such as mild conditions and short processing time. Additionally, this approach can be considered eco-friendly and cost-effective, as the only chemical used to generate these reactive species is water-saturated air, which is non-polluting, available, and renewable. Nonetheless, while catalysts synthesized through this method already exhibit promising characteristics and catalytic activity, enhancing the method by introducing a new synthesis step while preserving its advantage presents an opportunity to further improve its interest.

As previously suggested in the literature for FeO_x and MnO_x derived from $(NH_4)_2Fe(SO_4)_2$ and $KMnO_4$ synthesized through GP exposure, we confirm that the PT step is valuable to all types of solids synthesized from various precursors. Regardless of the precursor type, conducting a PT either at 100°C or AT proves to be an interesting process to increase the quantity of recovered solids and/or bring interesting new characteristics to the catalyst. Moreover, we observed similar transformations occurring during the PT, whatever the nature of the precursor salts used for a given metal. Specifically, solids with superior catalytic activity are consistently synthesized under comparable conditions for each metal. In our study, solids synthesized from iron precursors exhibit enhanced catalytic activity when the PT is performed at 100°C, whereas for tin precursors, the PT at AT shows the most promising results.

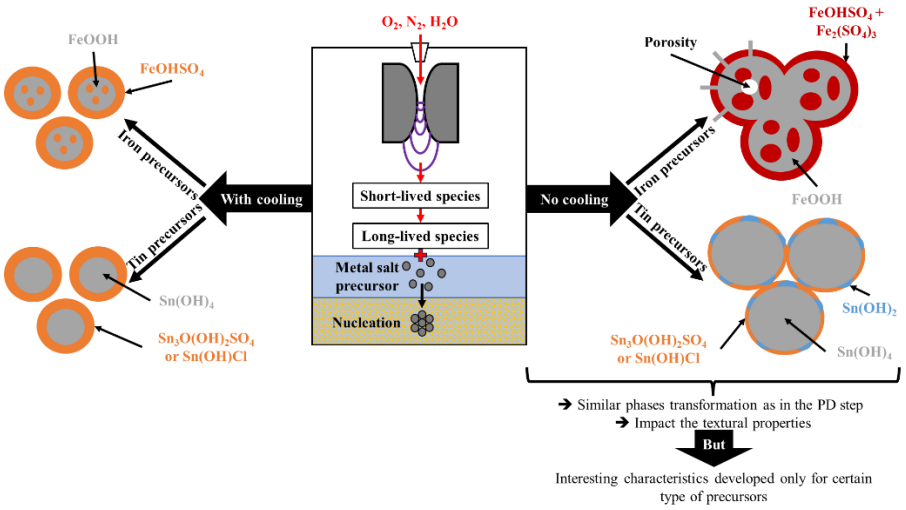
Although the impact of each PT type varies from precursors of one metal to another, a global effect is still apparent. That englobes the transformation of sulfate or chloride phases into metal oxides, the modification of the solid's textural properties, the increase in the amount of recovered solid, and the corresponding modification of its catalytic activity.

However, in nearly all cases, conducting a PT at either 100°C or AT enhances the catalytic performance of GP-synthesized solids. This means that, depending on the synthesis parameters of preference, such as a lower synthesis time, less energy input, or a higher yield of recovered solid, one PT may outperform another.

Consequently, the PT step has proven to be a crucial stage to implement in plasma-synthesized catalysts. However, contrary to what was stated before, our experiments show that species generated by plasma do not play the most important role in the solid transformations occurring during the PT step. In fact, we demonstrate that, whether plasma species are present during the PT step or not, the transformations occurring in the solid remain consistent. The phases conversion and crystal growth observed in this process primarily reflect a maturation step that involves the solid in a specific manner, contingent upon the applied heat and the duration of the step.

However, this does not imply that plasma species present during the PT step are irrelevant to the process. On the contrary, the NO_2^- remaining in solution during this stage does still facilitate the reaction of ion precursors remaining in solution when the discharge is switched off, transforming them into precipitates and thereby increasing the amount of solid formed.

Chapter 4 - Improving the synthesis of heterogeneous catalysts by gliding arc plasma using the “no-cooling system”



Abstract

Glidarc plasma (GP) is a promising method for preparing heterogeneous catalysts thanks to its mild conditions and short processing time. This technique has been used to synthesize various catalysts like FeO_x and MnO_x. Adding a Post-Treatment (PT) step during synthesis has been shown to impart valuable new properties, such as phase transformation, increased specific surface area, and enhanced catalytic activity. Knowing that the PT step mostly impacts the plasma-synthesized solids maturation and can be accelerated if heat is introduced into the system (see Part II, Chapter 3), we now contemplate the possibility of accelerating the GP catalysts synthesis by allowing the precursors solution to be heated by the energy spontaneously provided by the plasma without the necessity to add a PT. To challenge this approach, we subjected $FeSO_4$ and $SnSO_4$ precursors to plasma exposure without employing the cooling system usually integrated in the GP set-up, and compared the resulting solids with those obtained via conventional GP synthesis involving a PT step. The findings show that for iron precursors, the absence of cooling accelerates the formation of non-catalytically active phases and causes particle agglomeration, which is undesirable. However, for tin precursors, the absence of a cooling system introduces features that further improve the catalytic activity of the solids. Precisely, tin oxide phases developed better than other less-catalytically active ones without affecting the textural properties of the solid. This suggests that in some cases, eliminating the PT step can simplify the GP catalyst synthesis process and reduce its environmental and economic impact.

The results presented in this chapter have been published in:

Fanny Hanon, Eric M. Gaigneaux, Improving the synthesis of heterogeneous catalysts by gliding arc plasma using the "no-cooling system", Applied Materials Today, Volume 40, 2024, 102408

https://doi.org/10.1016/j.apmt.2024.102408

1. Introduction

In chapter 3, it has been observed that including a Post-Treatment (PT) step in GP synthesis can impart valuable new properties, such as phase transformation, increased specific surface area, and enhanced catalytic activity, to the catalysts synthesized by GP (Table 4.1) [61,65]. As a reminder, the PT step consists of exposing the precursor solution to GP, turning off the discharge, and allowing the suspension to stand outside the reactor for a defined duration at a fixed temperature (Figure 3.1). While this procedure is intriguing for the development of more valuable catalysts, it comes with the drawback of prolonging the synthesis duration and potentially requiring additional energy input into the system.

Table 4.1 : Effect of the post-discharge step at 100°C and 25°C on solids synthesized from iron precursors ($(NH_4)_2Fe(SO_4)_2$ and $FeSO_4$) and tin precursors ($SnSO_4$ and $SnCl_2$) [121]

	Iron precursors ($(NH_4)_2Fe(SO_4)_2$ and $FeSO_4$)		**Tin precursors ($SnSO_4$ and $SnCl_2$)**	
	PT at 100°C for 3h	**PT at 25°C for 72h**	**PT at 100°C for 3h**	**PT at 25°C for 72h**
Mass of solid produced	↗*	↗↗	= for $SnSO_4$; ↗↗ for $SnCl_2$	= for $SnSO_4$; ↗ for $SnCl_2$
Phases developed	↗↗ of Fe_2O_3, ↗↗ of $Fe_2(SO_4)_3$, ↘↘ of $FeOHSO_4$	↗ of Fe_2O_3, ↗of $Fe_2(SO_4)_3$, ↘ of $FeOHSO_4$	SnO_2	
% of S or Cl presents in the solid	↘**	↘	↘	↘↘
Specific surface area	↗↗	↗	↘	↘↘
Pore volume	↗↗	↗	=	
Catalytic activity	↗↗	↗ for $(NH_4)_2Fe(SO_4)_2$; ↘ for $FeSO_4$	↗	↗↗

**↗: increase ; **↘: decrease*

As suggested in the previous chapter, the PT step actually mostly consists of transforming the plasma-synthesized solid by allowing its maturation. Furthermore, accelerating this growing process often goes with introducing

heating to the system during this step [121]. Therefore, to further optimize the approach, we contemplated the possibility of accelerating the maturation of GP-synthesized solids by applying heat directly during the plasma exposure. In conventional plasma synthesis, the GP reactor and the exposed solution are cooled down using a double jacket with circulating cold water. Consequently, we explored the idea of omitting this cooling system, i.e. allowing the solution to get heated by the energy spontaneously provided by the plasma, and checked whether this is enough to induce rapid maturation.

To challenge this hypothesis, we exposed various types of iron and tin precursors to the plasma without using the cooling system and compared the resulting solids with those obtained from conventional GP synthesis, in which the cooling system was employed during the exposure, and in which a PT step at 100°C or 25°C was involved afterward. If successful, the "no-cooling system" would considerably reduce both the synthesis time and energy provided to the system, while still producing solids with characteristics closely resembling those obtained by incorporating a PT step. This would align with the broader objective of developing interesting catalysts through this innovative, economically viable, and environmentally friendly GP approach.

Since this approach has never been used before, our research, has been structured as follows. (i) First, we have determined how intense was the heating naturally occurring from the plasma discharge, and whether it could cause the exposed solution to evaporate too quickly, thereby altering the conditions during exposure. (ii) Then the impact of using (or not) the cooling system during the plasma exposure of the metals precursors solutions has been investigated via the characterization of the surface (probed by XPS), the bulk (probed by DRX, EDX, SEM) and the catalytic performance of respectively recovered solids. (iii) Finally, as the no-cooling approach has not been tested before in GP-catalysts synthesis, we have sought at investigating the difference between letting the precursor solution heat during exposure along the no cooling approach, *vs* using the cooling system during exposure but heating the precipitating solids after the GP, applying the post-discharge approach presented as in Part II, Chapter 3.

2. Materials and methods

2.1. Materials

Iron(II) sulfate heptahydrate ($FeSO_4.7H_2O$; ≥ 99%), tin(II) sulfate ($SnSO_4$; ≥ 95%) and tin(II) chloride ($SnCl_2$; ≥ 99%) were purchased from Sigma Aldrich and ammonium-iron(II) sulfate hexahydrate ($(NH_4)_2Fe(SO_4)_2.6H_2O$; ≥ 99%) from Roth.

All the solutions were prepared with demineralized water as solvent.

2.2. Methods

2.2.1. Synthesis device: the GP reactor

The gliding arc plasma system used in this study is the same as the one presented in Experimental, section 1.

2.2.2. Materials synthesis

In the initial step, demineralized water was exposed to the GP without employing the cooling system for 1 h, and the temperature of the solution was monitored every 5 min. This was done to investigate the influence of not utilizing the cooling system on the heating of the solution.

The precursor solutions were prepared by dissolving 10^{-2} mol/L of these compounds in deionized water. Subsequently, 450 mL of the respective solutions were introduced into the reactor, stirred magnetically (1 rotation/s) and exposed to the plasma discharge for 45 min for $(NH_4)_2Fe(SO_4)_2.6H_2O$, 60 min for $FeSO_4.7H_2O$ and 120 min (1h of exposure, 15 min break, 1h of exposure) for $SnSO_4.7H_2O$ and $SnCl_2$. Based on previous studies, either from literature or in the lab, these exposure times were chosen to synthesize the catalysts with the best catalytic activity and/or the highest yield of recovered precipitate [25,56]. The optimal exposure time varies depending on the type of precursor used.

To assess the influence of the cooling system, solids were synthesized by either cooling the solution with tap water circulating in the double-jacket during the exposure (samples named “precursor”) or not using the cooling system and allowing the solution to heat up during the exposure (samples named “precursor no cooling”). The solid formed was subsequently recovered by centrifugation (24490 G, 30 min) and subjected to two washing cycles with distilled water. All the solids obtained after centrifugation were dried in an oven under air at 110°C for 22h ± 2h and then calcined in a muffle furnace under air at 400°C for 2h.

The amount of precipitate formed for iron and tin precursors was measured by weighing the mass of the solid after drying at 110°C.

The resulting solids were compared with those obtained from classical synthesis involving a PT step at 100°C for 3 h or at 25°C for 72 h, where the cooling system was employed during the exposure (see complete synthesis protocol in Part II, Chapter 3, section 2.2.2 [121]).

2.3. Characterization of the solids formed

All the instrumental characterizations used here (XRD, XPS, SEM, EDX, N_2-physisorption) were done after calcination of the solids formed.

All the characterizations performed in this chapter were carried out as presented in Experimental, section 2.

All the synthesized solids were also tested catalytically in the total oxidation of benzene, as presented in Experimental, section 2.

3. Results and discussion

3.1. Impact of the no-cooling system on the temperature of the exposed solution

When demineralized water is exposed to the GP without using the cooling system, the temperature of the solution gradually rises and stabilizes around 60°C after 1 h of exposure (Figure 4.1). This indicates that, although the solution warms up during the exposure, it does not go above the boiling point of water. Consequently, it remains feasible to expose metal solution precursors without significantly changing the volume of the exposed solution, thereby maintaining a consistent distance between the electrodes and the liquid surface.

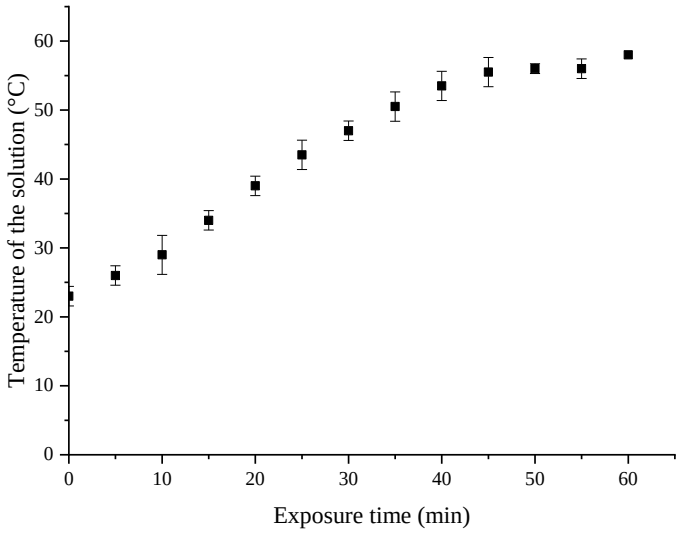


Figure 4.1: Temperature of demineralized water exposed to the GP without using the cooling system

3.2. Impact of the no-cooling system on solids GP-synthesized

3.2.1. Iron precursors

Regarding the mass of solids formed from iron precursors, it remains relatively constant with or without the cooling system (Table 4.2). For the $(NH_4)_2Fe(SO_4)_2$ precursor, the small difference observed between the samples with and without cooling is considered insignificant as the recovered mass is already small, and that some solid is always lost during the washing steps. Therefore, contrary to observations made with the addition of a PT step, the yield of recovered solids does not increase when the no cooling system is used instead [121]. This is likely due to the fact that the exposure time remains identical in both systems, with or without the cooling system. Consequently, the reactive species (HNO_2/NO_2^- [88]) do not have additional time to react with the precursor, as is the case when a PT step is introduced.

Table 4.2: Mass of solid produced with iron precursors by GP with and without cooling system

	Mass of solid produced (g)
$(NH_4)_2Fe(SO_4)_2$	0.050
$(NH_4)_2Fe(SO_4)_2$ no cooling	0.040
$FeSO_4$	0.131
$FeSO_4$ no cooling	0.136

XRD reveals that for both iron precursors, with or without the cooling system, the resulting solid contains a mixture of hematite (Fe_2O_3) and $FeOHSO_4$. However, the mikasaite ($Fe_2(SO_4)_3$) phase tends to emerge when the cooling system is not utilized, especially in the solid formed from the $(NH_4)_2Fe(SO_4)_2$ precursor (Figure 4.2). The appearance of mikasaite can be attributed to the tendency of $FeOHSO_4$ to decompose, particularly under heat, into FeOOH (which transforms into Fe_2O_3 upon calcination) and $Fe_2(SO_4)_3$ (Eq.4.1) [103]. This observation aligns with previous findings in classical GP synthesis, where the addition of a PT step led to similar results (Part I, Chater 3, section 3.1.1). In fact, although the $Fe_2(SO_4)_3$ phase develops in both types of PT (3 h at 100°C and 72 h at 25°C), its presence is notably higher in the diffractograms of the solids formed when heat is introduced to this step [121].

$$3FeOHSO_4 \rightarrow Fe_2(SO_4)_3 + FeOOH + H_2O \qquad (Eq.4.1)$$

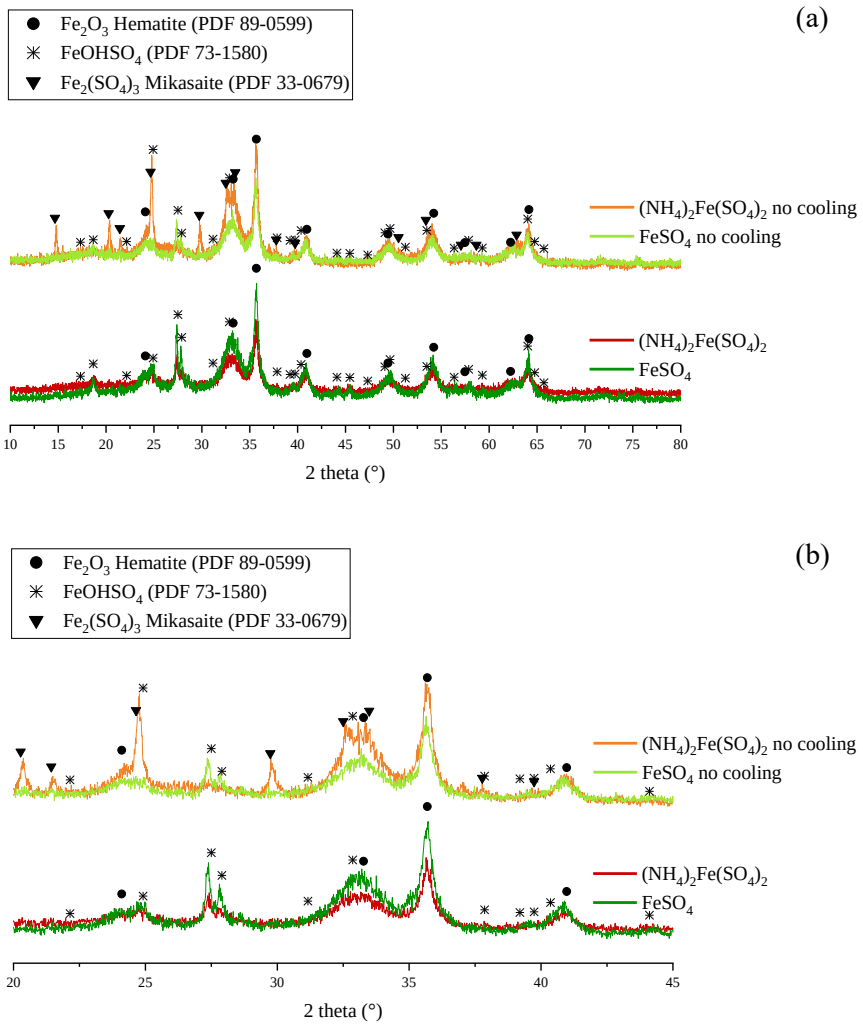


Figure 4.2: XRD data (a) complete range of 2 theta angles measured, (b) zoom on the 20-45° 2 theta range, of solids obtained after calcination with iron precursors with and without cooling system

For the $(NH_4)_2Fe(SO_4)_2$ precursor, XPS reveals the presence of nitrogen as NH_4^+ ions (as indicated by the position of N1s peak around 402 eV), suggesting the likely formation of another phase that was not observed by XRD (Table 4.3). From the at % of N, we understand that this phase is less present when the cooling system is not used. Moreover, similarly with observations made in classical GP synthesis where the cooling system is used and when a PT step is added, the at % of each element at the surface and in bulk also differs without the cooling system. Therefore, it can be deduced that

the absence or presence of the cooling system does not improve the development of a more or less homogeneous (bulk *vs* surface) solid.

Additionally, the binding energy around 169 eV of the S2p peak acquired through XPS confirms the presence of iron sulfate phases in each solid (Table 4.3). However, although the at % of S measured by XPS is higher than when measured by EDX, suggesting that iron sulfate phases predominantly reside on the outer layer of the solids, the difference between the S at % at the surface and in bulk is less pronounced than in other GP synthesis method. The higher at % of S obtained by EDX for the no-cooling samples indicates that the development of a sulfate phase in bulk is higher in the absence of the cooling system, corroborating findings from XRD analysis (Table 4.3). These observations can be elucidated through the hypothetical mechanism of formation proposed in the Part I, Chapter 3, section 3.1.1 [121]. Upon exposure to the GP, iron precursors undergo oxidation, where Fe^{2+} ions are transformed into Fe^{3+} ions by plasma species (Eq.4.2). Subsequently, these Fe^{3+} ions can interact either with water to form FeOOH or with SO_4^{2-} from the precursor to form $FeOHSO_4$ (Eq.4.3, Eq.4.4). Typically, in systems with the cooling system, there is a higher probability for Fe^{3+} to engage with H_2O molecules due to their higher concentration compared to SO_4^{2-}. However, in systems where heat is introduced, it is possible that the probability of collision between SO_4^{2-} and Fe^{3+} is heightened, consequently leading to the formation of a higher quantity of $FeOHSO_4$ phase. Since the rate of formation of FeOHSO4 and FeOOH is less disparate when heat is applied, the likelihood of formation of one phase over the other becomes more similar. Consequently, this can result in a solid with a more homogeneous composition of phases, which is indeed what we observe, evidenced by the less pronounced difference in at % of S in the solid formed without the cooling system.

$$Fe^{2+} + NO_2^- + 2H^+ \rightarrow Fe^{3+} + NO° + H_2O \qquad (Eq.4.2)$$

$$Fe^{3+} + 2H_2O \rightarrow FeOOH + 3H^+ \qquad (Eq.4.3)$$

$$Fe^{3+} + SO_4^{2-} + H_2O \rightarrow FeOHSO_4 + H^+ \qquad (Eq.4.4)$$

Furthermore, as already suggested before and also observed when the PT step is used, in the no cooling system, the $FeOHSO_4$ phase undergoes more decomposition due to the heating effect (Eq.4.1) [121]. As it partially decomposes into $Fe_2(SO_4)_3$, the at % of S increases, given that the S/Fe ratio in the $Fe_2(SO_4)_3$ phase (S/Fe =1.5) is higher than in $FeOHSO_4$ (S/Fe =1). This rise in the at % of S likely reflects the tendency of $FeOHSO_4$ to preferentially decompose into $Fe_2(SO_4)_3$ rather than into FeOOH under heating conditions.

Notably, if the FeOOH phase (which subsequently decomposes into Fe_2O_3 through calcination) had preferentially developed instead of the $FeOHSO_4$ (Fe/O=0.2) and $Fe_2(SO_4)_3$ (Fe/O=0.17) phases, the Fe/O ratio would increase towards 0.67. However, observations of the Fe/O ratio in the solids developed without the cooling system reveal no change. This indicates that the Fe_2O_3 phase does not seem to develop better without the cooling system, at least at the surface of the solid (Table 4.3).

Table 4.3: XPS and EDX data of solids obtained with iron precursors with and without cooling system

	Fe			O			S			N		Fe/O
	XPS (Fe2p)		EDX	XPS (O1s)		EDX *	XPS (S2p)		EDX	XPS (N1s)		XPS
	BE (eV)	(% at)		BE (eV)	(% at)		BE (eV)	(% at)		BE (eV)	(% at)	
$(NH_4)_2Fe(SO_4)_2$	710.8	23.8	26	530.0	66.6	72	168.9	6.5	2	399.5	3.1	0.36
$(NH_4)_2Fe(SO_4)_2$ no cooling	711.0	23.6	26	530.3	67.6	72	169.1	7.1	5	401.8	1.7	0.35
$FeSO_4$	710.9	26.4	28	530.4	66.8	69	169.5	6.8	3	/	/	0.40
$FeSO_4$ no cooling	710.6	26.7	19	529.8	67.4	76	168.7	5.9	6	/	/	0.40

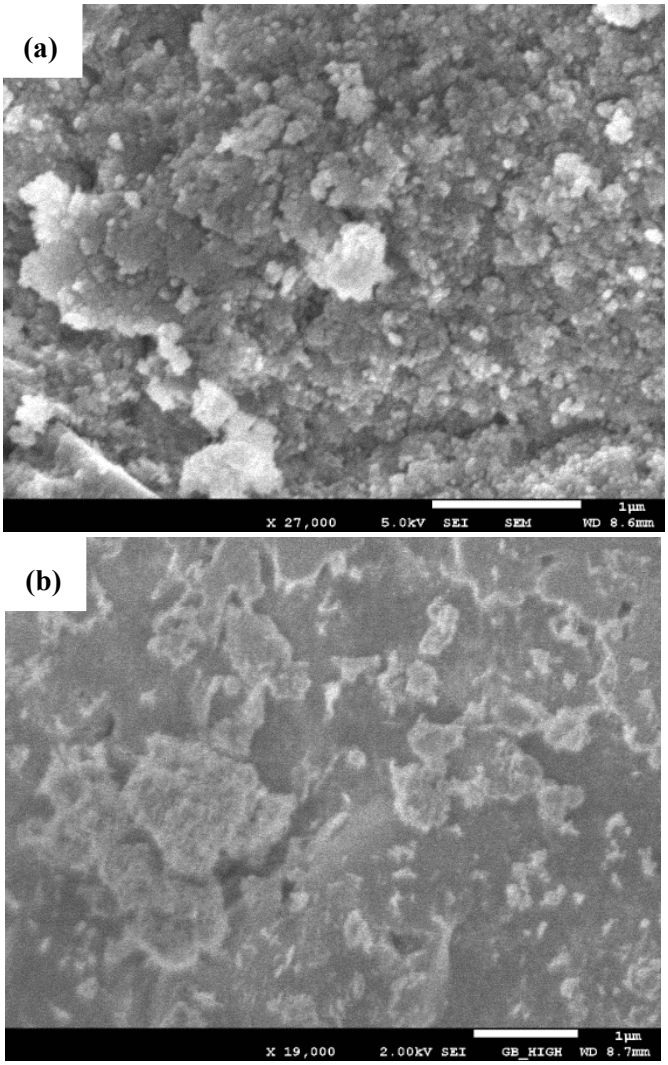
***** *The at % of O obtained by EDX is likely overestimated due to the underlying adhesive tape used to fix the sample.*

Regarding the morphology of the solids, unlike the observations made with the PT, it is evident that the no cooling system tends to result in solids with less specific surface area and pore volume (Table 4.4) [121].

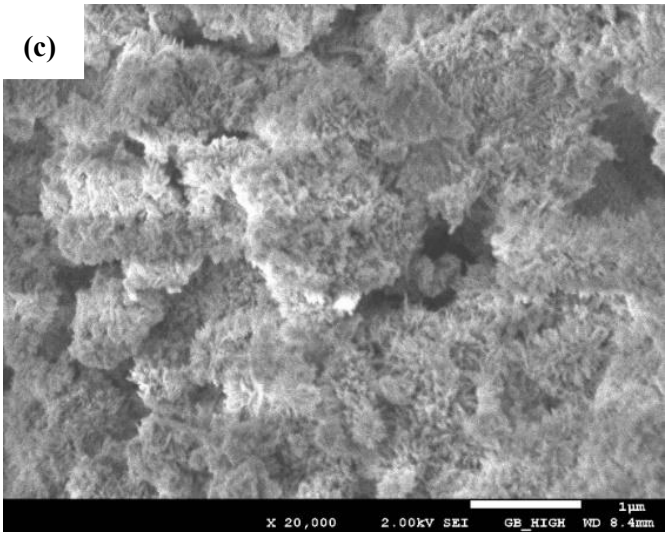
Table 4.4: Textural properties obtained by N_2-physisorption with iron precursors with and without cooling system (isotherms Supplementary information SI.10)

	Specific surface area (m^2/g)	**Pore volume (cm^3/g)**
$(NH_4)_2Fe(SO_4)_2$	69	0.18
$(NH_4)_2Fe(SO_4)_2$ no cooling	32	0.13
$FeSO_4$	95	0.33
$FeSO_4$ no cooling	23	0.11

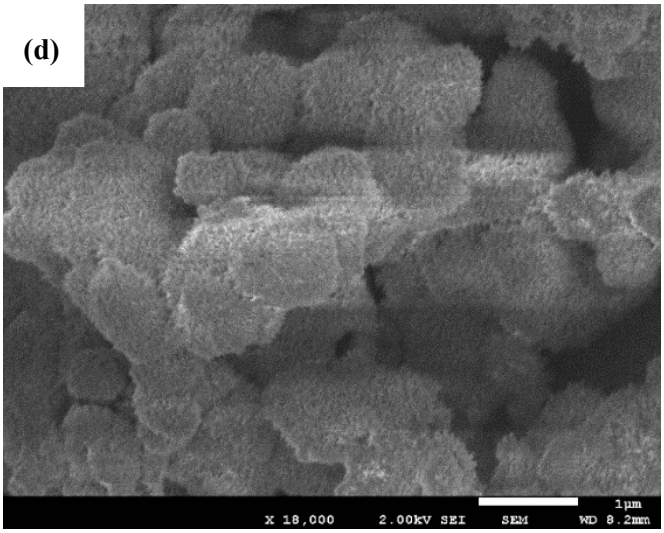
Additionally, the SEM images for $FeSO_4$ precursor indicate that solids produced without the cooling system seem to have less texture on their surface. This may result from the agglomeration of the "flakes-like" particles typically observed when the cooling system is used (Figure 4.3: (a) and (b)). However, it is difficult to conclude that this explains the decrease in specific surface area, as some particles appear to develop "sea-urchin like" crystals, which would normally increase the specific surface area of the solid (Figure 4.3: (c)). In fact, it is noteworthy that these "sea-urchin like" crystals that are formed when the cooling system is omitted during the synthesis for $FeSO_4$ and $(NH_4)_2Fe(SO_4)_2$ precursors, are a characteristic structure not typically observed in conventional GP synthesis utilizing the cooling system (Figure 4.3: (c), (d)). Nevertheless, these "sea-urchin like" crystals are not uniformly developed throughout the synthesized solids. In fact, certain particles resemble large, shapeless crystals that agglomerate together (Figure 4.3: (b), (e)).


(a)
X 27,000 5.0kV SEI SEM WD 8.6mm
1µm
(b)
X 19,000 2.00kV SEI GB_HIGH WD 8.7mm
1µm

(c)


X 20,000 2.00kV SEI GB_HIGH WD 8.4mm
1µm

(d)


X 18,000 2.00kV SEI SEM WD 8.2mm
1µm

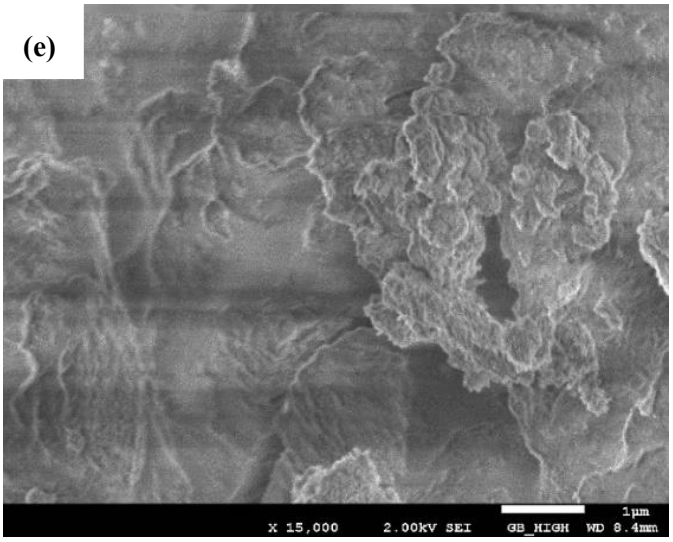


Figure 4.3: SEM images of solids obtained with $FeSO_4$ (a) with cooling and (b), (c) without cooling system and obtained with $(NH_4)_2Fe(SO_4)_2$ (d), (e) without cooling system

As previously explained in Part II, Chapter 3, section 3.2, the PT step primarily involves a maturation process that facilitates crystal growth into the shape of a "sea-urchin like" structure, resulting in particles with a higher specific surface area in the case of solids derived from iron precursors [61,121]. In the absence of the cooling system, although the heat introduced during the synthesis seems to initiate the maturation of the crystals formed during the discharge, it does not afford sufficient time for the complete formation of these distinctive crystals. Consequently, direct application of heat during particles formation predominantly induces their agglomeration, thereby reducing the specific surface area of the catalyst.

With the information obtained from XRD, XPS, EDX, N_2-physisorption and SEM images, we can propose a mechanism of formation of the solids when iron precursors are exposed to the GP as illustrated in Figure 4.4.

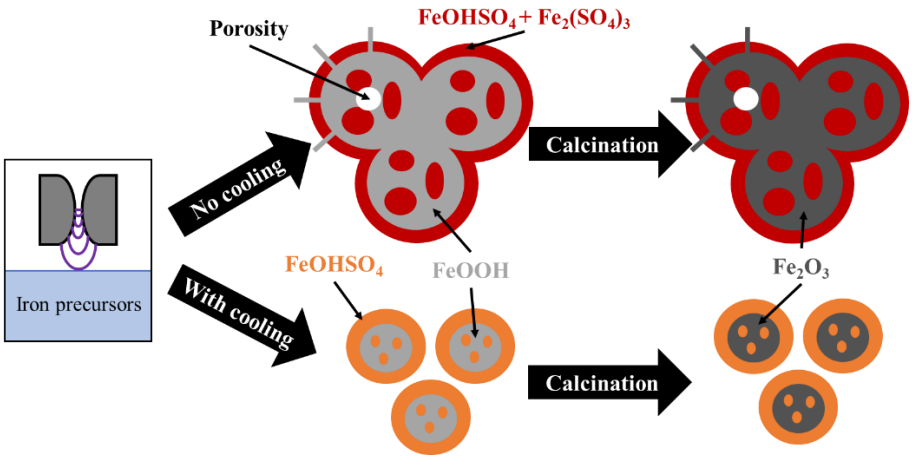


Figure 4.4: Mechanism of formation of solids obtained with iron precursors with and without cooling system

Concerning the catalytic activity of plasma-synthesized solids, a decline is observed when the cooling system is not used for both precursors (Figure 4.5). This observation was expected as the absence of cooling system tends to result in the development of solids with a higher proportion of non-catalytically active phase ($Fe_2(SO_4)_3$) compared to the active phase (Fe_2O_3) and reduce their specific surface area and pore volume. In fact, compared to commercial Fe_2O_3 (iron(III) oxide, Alfa Aesar, 30-60 m^2/g), the catalytic activity of the developed solid is only comparable or better if the cooling system is used in the GP catalysts synthesis (Figure 4.5). Consequently, in the case of solids derived from iron precursors, the no cooling system fails to impart beneficial characteristics able to compete those achieved with the cooling system and the PT step.

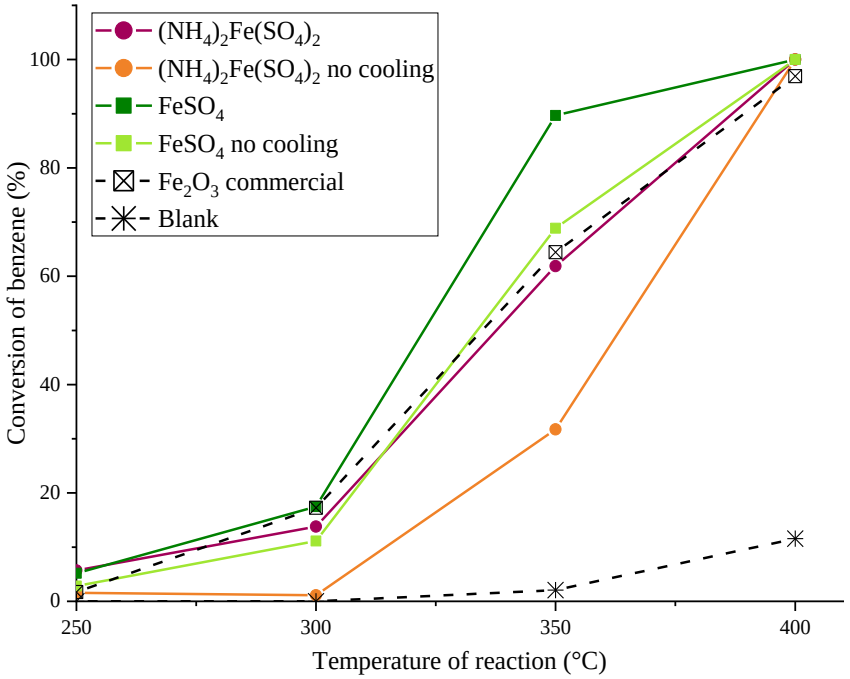


Figure 4.5: Catalytic performances of solids formed from iron precursors with and without cooling system for the total oxidation of benzene (conversion of benzene as function of reaction temperature)

3.2.2. Tin precursors

Regarding the mass of the solid formed from tin precursors, it remains largely unchanged regardless of the presence or absence of the cooling system (Table 4.5). As explained before, contrary to what was observed when a PT step was applied, as the exposure time is identical in both systems, the reactive species (HNO_2/NO_2^- [88]) do not have additional time to react with the precursor, resulting in an unchanged yield of precipitate solid.

Table 4.5: Mass of solid produced with tin precursors by GP with and without cooling system

	Mass of solid produced (g)
$SnSO_4$	0.686
$SnSO_4$ no cooling	0.622
$SnCl_2$	0.674
$SnCl_2$ no cooling	0.704

The XRD diffractograms of the solids derived from tin precursors reveal that the phases developed with or without cooling system are the same. In both

precursors, the phase developed is cassiterite (SnO_2), resulting from the dehydration of the $Sn(OH)_4$ formed in solution during the solid's drying steps (Figure 4.6).

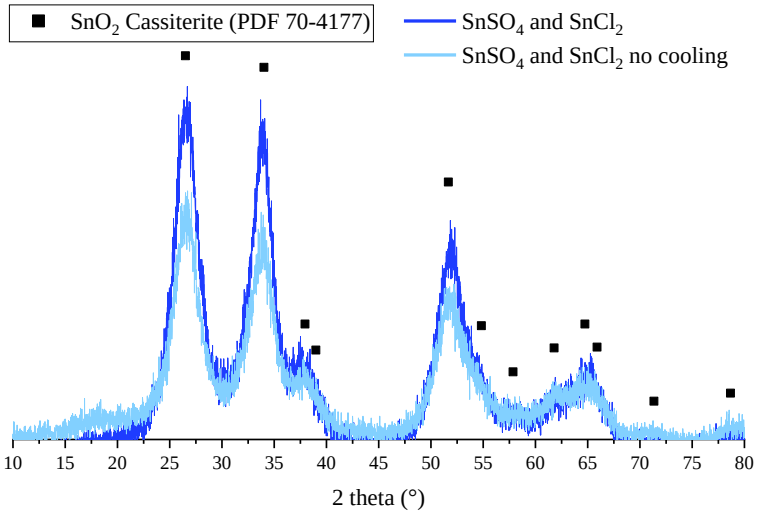


Figure 4.6: XRD data of solids obtained after calcination with tin precursors with and without cooling system

As observed for iron precursors, XPS and EDX data highlight that the at % of each element at the surface and in bulk consistently differs with or without cooling system, indicating the heterogeneous (bulk *vs* surface) composition of the precipitates (Table 4.6).

XPS data reveal the presence of sulfur (as SO_4^{2-}) for solids formed from $SnSO_4$ and Cl (as Cl^-) for $SnCl_2$, as indicated by the positions of S2p and Cl1s (Table 4.6), suggesting the likely formation of another phase that was not observed by XRD. Furthermore, the at % of S and Cl at the surface is consistently higher than in bulk, where they are almost negligible, implying that tin sulfate or tin chloride phases predominantly exist on the outer layer of the solids (Table 4.6).

XPS analysis also indicates that the at % of S or Cl is lower when the cooling system is absent, suggesting a diminished presence of sulfate or chloride phases at the surface (Table 4.6). Referring back to the proposed mechanism of solid formation from tin precursors outlined in the Part II, Chapter 3, section 3.1.2, it is known that $SnCl_2$ and $SnSO_4$ undergo spontaneous hydrolysis to form hydroxychloride (SnOHCl) or hydroxysulfate ($Sn_3O(OH)_2SO_4$) intermediates [121]. These intermediates are subsequently quickly oxidized by plasma species, resulting in the formation of tin hydroxide, $Sn(OH)_4$, which

ultimately transforms into the more stable phase, SnO_2 (Eq.4.5, Eq.4.6, Eq.4.7). Consequently, with the reduced presence of S or Cl at the surface of the solid in the absence of the cooling system, it can be inferred that the transformation of the intermediate phases occurs more efficiently under elevated temperatures. This inference is supported by the well-established tendency of Sn^{2+} ions to oxidize to Sn^{4+} at high temperatures, offering a plausible explanation for these observations [122,123].

$$3SnSO_4 + 3H_2O \rightarrow Sn_3O(OH)_2SO_4 + 4H^+ + 2SO_4^{2-} \quad (Eq.4.5)$$

$$SnCl_2 + H_2O \rightarrow Sn(OH)Cl + HCl \quad (Eq.4.6)$$

$$Sn^{2+} + 2NO_2^- \rightarrow Sn(OH)_4 + 2NO^\circ + H_2O \quad (Eq.4.7)$$

However, looking at the Sn/O ratio of these solids, we cannot tell that the chloride and sulfate intermediates only undergo oxidation to form $Sn(OH)_4$, but they seem to also form another tin (hydr)oxide phase under heat (Table 4.6). If the $Sn_3O(OH)_2SO_4$ (Sn/O=0.43) or Sn(OH)Cl (Sn/O=1) intermediates were exclusively oxidized into SnO_2 (Sn/O=0.5), the Sn/O ratio of the resulting solid would be closer to 0.5. However, even with the cooling system, the value already exceeds 0.5 and is even higher without the cooling system (Table 4.6). Furthermore, as the at % of S or Cl indeed decreases, it means than another tin oxide phase with a higher Sn/O ratio is likely to form. It is conceivable that this phase corresponds to SnO (Sn/O=1) originating from $Sn_3O(OH)_2SO_4$ or Sn(OH)Cl, which were not oxidized but rather transformed into tin(II) oxide, namely an observation that was already made when a PT step was applied to a classical GP synthesis. Consequently, without the cooling system, it is plausible that a solid containing a mixture of SnO_2 and SnO phases is generated, wherein less tin sulfate or tin chloride phases remain compared to the solid obtained when the cooling system is utilized in its preparation.

Table 4.6: XPS and EDX data of solids obtained with tin precursors with and without cooling system

	Sn			O			S or Cl			Sn/O
	XPS (Sn3d)		EDX	XPS (O1s)		EDX *	XPS (S2p or Cl1s)		EDX	XPS
	BE (eV)	(at %)		BE (eV)	(at %)		BE (eV)	(at %)		
$SnSO_4$	487.0	33.4	14	531.2	63.7	85	169.3	2.9	1	0.52
$SnSO_4$ no cooling	486.9	34.6	17	530.8	63.6	82	169.4	1.8	1	0.54
$SnCl_2$	486.6	35.2	29	530.7	63.4	71	199.1	1.4	0	0.56
$SnCl_2$ no cooling	486.7	36.6	28	530.7	62.8	72	198.5	0.7	0	0.58

* *The at % of O obtained by EDX is likely overestimated due to the underlying adhesive carbon tape used to fix the sample.*

Regarding the texture of the solids, whether the cooling system is used or not, there is no substantial difference in the specific surface area or pore volume (Table 4.7). In contrast to observations made with the PT, applying heat to the system does not notably decrease the specific surface area. This is likely attributed to the fact that in the absence of the cooling system, the particles have less time to agglomerate compared to when a PT step is included in the synthesis protocol.

Table 4.7: Textural properties obtained by N_2-physisorption with tin precursors with and without cooling system (isotherms Supplementary information SI.11)

	Specific surface area (m^2/g)	**Pore volume (cm^3/g)**
$SnSO_4$	162	0.13
$SnSO_4$ no cooling	142	0.14
$SnCl_2$	146	0.11
$SnCl_2$ no cooling	164	0.10

With the information obtained from XRD, XPS, EDX and N_2-physisorption, we propose a mechanism of formation of the solids when tin precursors are exposed to the GP as illustrated in Figure 4.7.

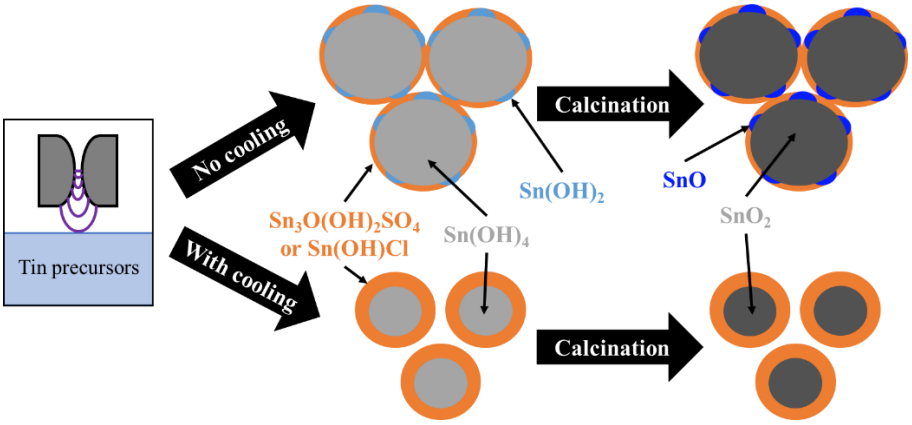


Figure 4.7: Mechanism of formation of solids obtained with tin precursors with and without cooling system

Regarding the catalytic activity of solids derived from tin precursors, it is enhanced when the cooling system is not used. (Figure 4.8). These results align with the previously discussed characteristics. As the no cooling system facilitates the transformation of tin sulfate or chloride phases into more catalytically active phases (tin (IV and II) oxides) at the surface of the solid without altering the texture of the solids, it thereby enhances the catalytic

activity of the obtained solids. Furthermore, compared to SnO_2 synthesized by classical precipitation with base (NH_3) addition precipitation, the tin-based catalysts synthesized by GP are already more catalytically active when the cooling system is used. However, their catalytic activity becomes even more competitive when the cooling system is not used [118].

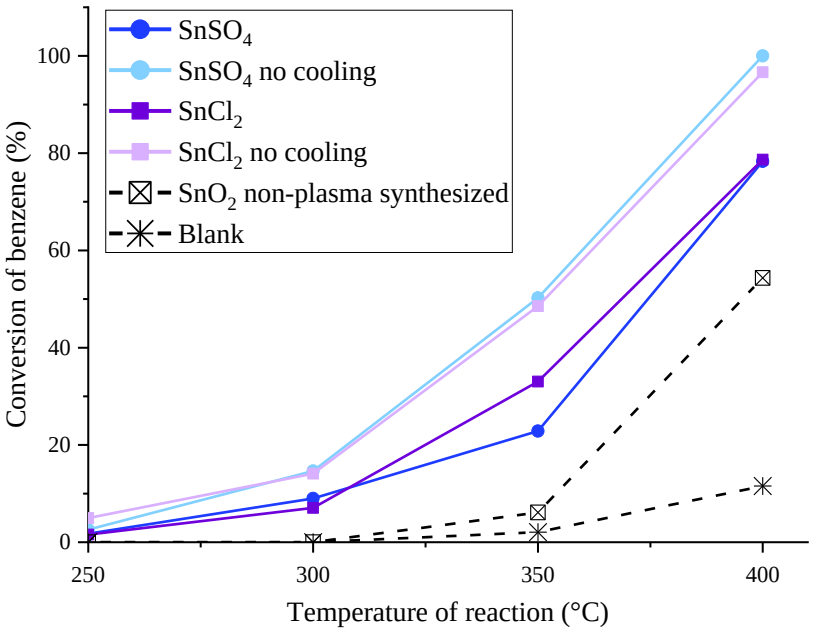


Figure 4.8: Catalytic performances of solids formed from tin precursors with and without cooling system for the total oxidation of benzene (conversion of benzene as function of reaction temperature)

3.3. Can the no-cooling system replace the PT step in the GP catalysts synthesis?

We have previously shown that conducting a PT step either at 100°C for 3 h or at 25°C for 72 h irrespective of the precursor type, is an interesting process to increase the quantity of recovered solids and/or introduce intriguing new characteristics to the catalyst [121]. In fact, the PT effectively transforms the sulfate or chloride phases, which may have formed during the discharge, into metal oxides. Furthermore, it influences the textural properties of the solid, increases the amount of recovered solids and, in most cases, enhances its catalytic activity.

On the contrary, the no cooling system does not consistently improve the properties of solids generated by GP. For iron precursors, synthesis without cooling system results in a higher proportion of $Fe_2(SO_4)_3$ and less of the

catalytically active phase Fe_2O_3. Furthermore, the direct application of heat during particles formation predominantly promotes their agglomeration, reducing specific surface area, pore volume, and thus overall catalytic activity. However, for tin precursors, synthesis without cooling system increases the amount of catalytically active phase (tin (II and IV) oxides), reduces tin sulfate or chloride phases remaining at the surface, and maintains a high specific surface area, yielding a more active catalyst compared to synthesis with cooling.

This finding is intriguing, particularly considering that conducting a PT at 100°C for 3h proved to be more beneficial for iron precursors than for tin precursors. It suggests that heat applied during the PT step (maturation), is advantageous for iron precursors, whereas heat applied directly during the discharge (nucleation) is not. Several factors may explain these differences. Firstly, for iron precursors, exposure to discharge initially produces phases such as $FeOHSO_4$ and FeOOH. However, the formation of these phases is influenced by the introduction of heat, altering the rate at which one phase develops preferentially to another. Moreover, as observed when incorporating a PT step, the $FeOHSO_4$ tends to decompose into $Fe_2(SO_4)_3$ and FeOOH, a transformation that heat accelerates. Therefore, without cooling system, heat applied directly during the discharge already triggers the transformation of $FeOHSO_4$ that seems to preferentially decompose into $Fe_2(SO_4)_3$ rather than FeOOH, bypassing the desired phase evolution. Additionally, while elevated temperatures during PT encourage the maturation of solids into "sea-urchin-like" crystals, heat applied during particle formation primarily promotes agglomeration, reducing the specific surface area and pore volume of the catalyst. Consequently, for iron-based solids, it is less favorable to introduce heat directly during the nucleation step rather than during the maturation step.

On the other hand, the no cooling system for tin precursors leads to catalysts with more intriguing characteristics and even more active than those synthesized with a PT step. Interestingly, as observed with PT step, heat introduced into the system seems to improve either the oxidation of tin sulfate and tin chloride intermediates into SnO_2 or accelerate their decomposition into SnO, thus promoting the formation of more catalytically active phases. Furthermore, unlike PT step, where extended synthesis time and heat often lead to particle agglomeration and reduce specific surface area, the no cooling system avoids these drawbacks by limiting the process to the duration of the discharge exposure. As a result, the specific surface area remains relatively unaffected, achieving the benefits off the PT without its negative effects.

Ultimately, this approach enables the creation of more catalytically active solids by significantly reducing the synthesis time that would normally be required if a PT step were to be included.

4. Conclusion

In the aim of exploring the possibility of accelerating the maturation of GP-synthesized solids by directly applying heat during plasma exposure, we subjected various iron and tin precursors to plasma exposure without employing the cooling system and compared the resulting solids with those obtained through conventional synthesis involving a PT step at either 100°C for 3 h or at 25°C for 72 h.

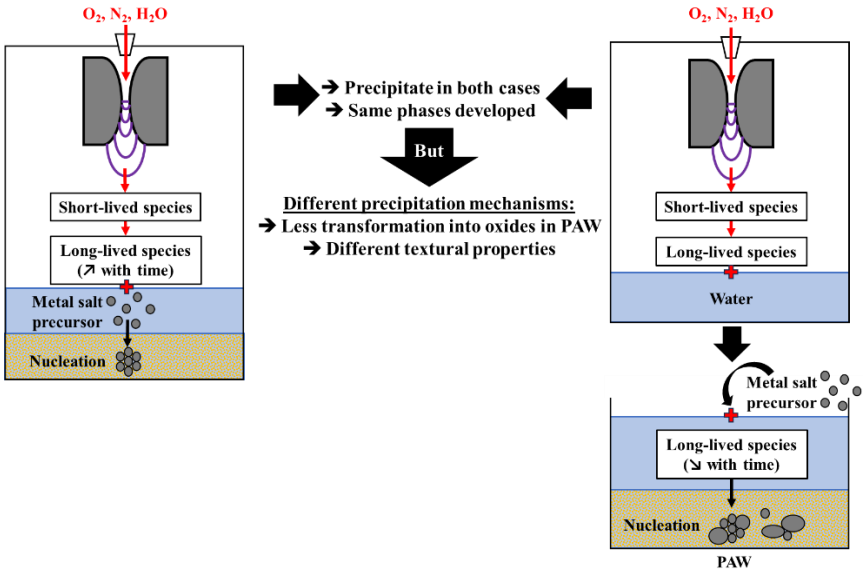
Our findings showed that for iron precursors, the absence of cooling led to more less catalytically active phases ($FeOHSO_4$ and $Fe_2(SO_4)_3$) and fewer catalytically active phases (Fe_2O_3) compared to when the cooling system was employed during the synthesis. Moreover, the direct application of heat during particles formation induced their agglomeration, resulting in a reduction of specific surface area and pore volume, consequently diminishing the catalytic activity of the formed solids.

In contrast, for tin precursors, solids developed without the cooling system had more catalytically active phases (tin (II and IV) oxides) and fewer less active tin sulfate or chloride phases on the surface. Additionally, the specific surface area was relatively unaffected by the heat. Therefore, this yielded a catalyst that was more active compared to that synthesized with the cooling system.

Therefore, we can conclude that, much like with the PT step, the results obtained vary from one precursor to another, while following a common pattern for precursor salts of the same metal. For certain precursors, the absence of a cooling system cannot replicate the interesting characteristics developed with the PT step, while for others, it appears to introduce even more intriguing features. When favourable, the no cooling system becomes notably interesting, as it can potentially replace the PT step. In fact, in the no cooling approach, no additional heat is introduced, as we allow the solution to be heated by the energy naturally provided by the plasma discharge. Consequently, this drastically reduces the energy cost of the synthesis. Additionally, we can significantly decrease the synthesis time, thereby reducing both the energy and economic impacts of the synthesis. This system could, therefore, represent an interesting approach to improving the overall

GP catalyst synthesis process, by reducing its environmental and economic footprint.

Chapter 5 - Using "Glidarc Plasma Activated Water" as a new way to synthesize heterogeneous catalysts



Abstract

This chapter investigates the feasibility of synthesizing solid materials by introducing a metal precursor into plasma-activated water (PAW) rather than directly exposing it to the GP discharge. This alternative approach aims to enhance the economic and ecological benefits of GP catalyst synthesis by eliminating the need for reactor cleaning between exposures of different precursor solutions. The study builds on some of our previous discovers, that long-lived reactive species, particularly HNO_2 and NO_2^-, were identified as key agents in the precipitation of metal precursors during GP exposure (Part I, Chapter 1). The primary objective was to assess whether these long-lived species could be generated in PAW in sufficient quantities and with enough stability to initiate the precipitation of various metal precursors added afterward. Experiments with different precursors ($FeSO_4$, $KMnO_4$, $SnSO_4$) demonstrated that the long-lived species in PAW were indeed capable of inducing solid formation with some similar characteristics to those obtained through direct GP exposure. However, the study revealed differences in precipitation mechanisms between the two methods, leading to some variations in the solids' characteristics, such as a limited oxide transformation in PAW synthesis, resulting in solids with different textural properties. Furthermore, the long-lived species in PAW were found to be stable long enough to trigger precipitation of the $FeSO_4$ even after a delay before precursor addition, even though the reproducibility of the resulting solids were variable. The findings confirm the viability of using PAW to synthesize solids, although differences in nucleation and maturation processes between PAW and direct GP methods result in distinct material properties**.**

1. Introduction

As suggested in the General Introduction, section 3.3.2, the GP catalysts synthesis offers interesting conditions when compared to alternative synthesis methods. One of the most significant advantages is the mild conditions and short processing time it requires. Additionally, this approach can be considered eco-friendly and cost-effective, as the only chemical used to generate these reactive species is water-saturated air, which is non-polluting, available, and renewable [61]. However, the synthesis conditions can still be improved. For example, while no other chemical than air and water are necessary for the reaction, this is not the case for the washing steps of the reactor. Currently, the GP reactor used for catalyst synthesis is a batch reactor. Therefore, it requires a washing step between each type of precursor exposure to prevent any contamination between samples. In our case, diluted HCl is used, followed by several rinsing steps with a large volume of water. This process takes time and generates waste water containing chemicals that need to be collected and treated as chemical waste. This diminishes the ecological and time-saving advantages of GP synthesis.

In Part I, Chapter 1, we discovered that long-lived species are the main plasma species responsible for the precipitation of precursors exposed to the GP plasma. Therefore, we wondered if it might be possible to perform the precipitation reaction of the precursors by first exposing water to the GP, recovering it, and then adding different precursors in this water, yielding to similar precipitates to those obtained when exposed directly to the discharge. This process is comparable to what is already known in the literature as “plasma activated water” (PAW) [52,85,124]. In fact, reactive oxygen and nitrogen species (RONS) created in the exposed water have been highlighted as essential players in many applications. Among these RONS, some have a long enough lifetime to remain present in the exposed medium after for some time, such as HNO_2/NO_2^-, NO_3^-, H_2O_2 and O_3. The concentration and type of the reactive species present in PAW depend on the way their generation is achieved, including the plasma type, plasma exposure time, input voltage, storage time, water source (distilled or demineralized), and plasma gas. In addition to creating species, the interaction between water and plasma affects the physicochemical properties of PAW, such as decreasing the pH, increasing the electrical conductivity and the oxidation-reduction potential. The use of PAW instead of directly exposing the medium to the plasma has already been

investigated in biomedical, food, and agricultural technologies [52,85,124].

The interest of this method lies in not directly exposing a medium containing the material to the discharge but instead utilizing a medium pre-exposed to the discharge and adding the material to it. This is possible when long-lived species created are the species of interest. In our case, it was previously discovered that the plasma species responsible for the redox reaction followed by the precipitation process of the precursors exposed to the GP are mainly these long-lived species, specifically HNO_2 and/or NO_2^- species.

Therefore, the aim of this chapter is to determine if it is possible to precipitate similar solids using PAW as those obtained when precursors are directly exposed to the GP discharge. This could be achieved by simply exposing demineralized water to the GP and recovering the PAW, where the precursor can be added afterward. If successful, this method might result in potentially eliminate the need for the reactor washing step, thus decreasing the synthesis time and reducing the chemical waste created by the process. The purpose would be to decrease the economic and ecologic impact of GP catalysts synthesis, thereby enhancing its appeal.

2. Materials and methods

2.1. Materials

Iron(II) sulfate heptahydrate ($FeSO_4.7H_2O$; ≥ 99%) and tin(II) sulfate ($SnSO_4$; ≥ 95%) were purchased from Sigma Aldrich and potassium permanganate ($KMnO_4$; ≥ 99%) from Thermo Scientific.

All the solutions were prepared with demineralized water as solvent.

2.2. Methods

2.2.1. Synthesis device: the GP reactor

The gliding arc plasma system used in this study is the same as the one presented in Experimental, section 1.

2.2.2. Materials synthesis

For the solids not synthesized from PAW, the precursor solutions were prepared by dissolving 10^{-2} mol/L of these compounds in demineralized water. Subsequently, 450 mL of the respective solutions were introduced into the reactor, stirred magnetically (1 rotation/s), and exposed to the plasma discharge for 30 min for $KMnO_4$, 60 min for $FeSO_4.7H_2O$ and 120

min (1h of exposure, 15 min break, 1h of exposure) for $SnSO_4.7H_2O$. Based on previous studies, either from literature or in the lab, these exposure times were chosen to synthesize the catalysts with the best catalytic activity and/or the highest yield of recovered precipitate [25,56]. The optimal exposure time varies depending on the type of precursor used.

For the solids synthesized from PAW, 450 mL of demineralized water was stirred magnetically (1 rotation/s) and exposed for 30 min for $KMnO_4$, 60 min for $FeSO_4.7H_2O$ and 120 min (1h of exposure, 15 min break, 1h of exposure) for $SnSO_4.7H_2O$ precursors. After exposure, the PAW was recovered, and each type of precursor was directly solubilized in it. Since some water evaporated during the plasma exposure, the recovered PAW was weighed to determine its remaining volume, and therefrom adjust the exact amount of precursor needed to achieve a concentration of 10^{-2} mol/L for each of them. After adding the precursor, the solution was stirred at ambient temperature for 30 min for $KMnO_4$, 60 min for $FeSO_4.7H_2O$ and 120 min for $SnSO_4.7H_2O$.

We also investigated the effect of letting the PAW rest before adding the precursor $FeSO_4.7H_2O$. To do so, 450 mL of deionized water was stirred magnetically (1 rotation/s) and exposed for 60 min to the GP. After exposure, the PAW was recovered and allowed to rest at ambient temperature while being stirred magnetically (3 rotations/s) for 30, 60 and 90 min before adding the required amount of precursor to reach a 10^{-2} mol/L solution. After adding the precursor, the solution was stirred (3 rotations/s) at ambient temperature for 60 min.

The solid formed was subsequently recovered by centrifugation (24490 G, 30 min) and subjected to two washing cycles with distilled water. All the solids obtained after centrifugation were dried in an oven under air at 110°C for 22 h ± 2 h and then calcined in a muffle furnace under air at 400°C for 2 h.

For your information, some of the solids presented here have identical synthesis conditions as in previous chapters but do not have identical properties and features. In fact, because we have realized that synthesis conditions (such as air humidity, temperature, etc) may impact the reproducibility of the synthesis, all the materials discussed in this chapter have been resynthesized in a same short period of time. Consequently, the reader should not be surprised that some solids presented here do not exactly match the characteristics described in previous chapters.

2.2.3. Stability of reactive species created in PAW

To quantify the amount and stability of some long-lived species generated in our medium, 450 mL of demineralized water was exposed to the discharge for 60 min. Subsequently, the solution was stirred (3 rotations/s) at ambient temperature for 120 min and analysed by UV-visible spectroscopy (Shimadzu UV-3600 PLus) at 15, 30, 45, 60, 90 and 120 min. The conditions used were the same as in the Part I, Chapter 1, section 2.2.3. The samples were contained in a quartz cuvette (100-QS, Hellma Analytics) of a standard optical path of 10 mm. The transmission spectrum is recorded from 200 to 300 nm with photomultiplier tube (PMT) detector since the absorption spectrum of long-lived species extends below 300 nm and that no absorption occurs in the visible and near infrared ranges (400–900 nm) [77].

The long-lived species quantified in this activated water were NO_3^- and NO_2^- species. The quantifications of these species was performed as presented in the Part I, Chapter 1, section 2.2.3. Calibration curves using $NaNO_2$ and $NaNO_3$ were established (Supplementary Information SI.1). The matrix used to measure the blank is pure demineralized water. The measurement of NO_2^- intensity absorbance was performed at 240 nm, as it exclusively absorbs at this wavelength. Quantification of NO_3^- was performed by measuring the absorbance at 210 nm, with the contribution from previously calculated NO_2^- absorbance subtracted (Supplementary Information SI.2). Along the experiment, the pH of the solution was measured at 15 min intervals. The impact of pH on this quantification was previously reported in the literature and taken into account here to select the appropriate wavelengths for our analysis [77].

2.2.4. Yield of formed solid

The quantity of precursors transformed into a precipitate was quantified by UV-visible spectroscopy for $KMnO_4$ and $FeSO_4$ using the same conditions as in Part I, Chapter 1, section 2.2.3. MnO_4^- ions absorb within the wavelength range of 425 to 625 nm, with a maximum absorbance at 525 nm. Therefore, it is possible to determine the quantity of $KMnO_4$ that has reacted by analyzing the solution before and after the solid synthesis. To avoid an absorbance saturation, all $KMnO_4$ solutions were diluted 8 times. On the other hand, to distinguish the presence of Fe^{2+} ions from the $FeSO_4$ precursor, the introduction of a complexing agent is imperative. When combined, Fe^{2+} and 1,10-phenanthroline (phen) interact in a 1:3 ratio, forming an orange-red coloured complex $[Fe(phen)_3]$ when in

aqueous medium (Eq.5.1). To quantify this complex, the absorbance is gauged at 510 nm via UV-visible spectroscopy. As for $KMnO_4$ quantification, the evaluation of reacted Fe^{2+} necessitates an analysis of the solution before and after the solid synthesis. To perform this experiment, a solution containing 66 µL of the sample is mixed with 5 mL of a phen solution (100 mg of phen in 100 mL of demineralized water) within a 100 mL flask. After a mixing period of 15 min to allow a full colour development, the flask is then filled to the mark with deionized water.

$$Fe^{2+} + 3phen \rightarrow [Fe(phen)_3]^{2+} \qquad (Eq.5.1)$$

The final yield of formed precipitate for each experiment was computed using Eq.5.2.

$$Yield(\%) = \left(\frac{[precursor]_i - [precursor]_f}{[precursor]_i}\right) * 100 \qquad (Eq.5.2)$$

A calibration curve was established for both precursors in order to determine the quantity of MnO_4^- and Fe^{2+} within the solutions (Supplementary Information SI.3).

For $SnSO_4$, the amount of solid formed was quantified by weighing of solid recovered after the drying step, assuming that only SnO_2 was produced. This approach was used with tin precursors because the larger quantity of solid formed allowed for more accurate measurement by weighing the recovered material. In contrast, iron and manganese precursors produced only a small amount of solid (around 100 mg), increasing the potential for error in weight measurements.

2.3. Characterization of the solids formed

All the instrumental characterizations used here (XRD, XPS, SEM, EDX, N_2-physisorption) were done after calcination of the solids formed.

All the characterizations performed in this chapter were carried out as presented in Experimental, section 2.

All the synthesized solids were also tested catalytically in the total oxidation of benzene, as presented in Experimental, section 2.

3. Results and discussion

3.1. Lifetime of long-lived species present in PAW

As explained in the introduction, it was previously discovered that the plasma species identified as mainly responsible of the redox reaction

followed by the precipitation of metal precursors exposed to the GP are the HNO_2 and/or NO_2^- species. The interest in these species lies in their classification as long-lived species, allowing them to persist in the aqueous phase exposed to the discharge for a certain period. However, before determining if PAW can be used as a medium with sufficient reactive species to trigger the reaction of metal precursors that would be dissolved in it after its "activation", we need to confirm that these active HNO_2 and/ or NO_2^- species are indeed present in the PAW and determine their stability over time.

By looking at the amount of some long-lived created in distilled water exposed to the GP discharge and then left at AT for 2h, we observe that the amount of NO_2^- decreases over time, while the amount of NO_3^- increases (Figure 5.1). This can be explained by the fact that HNO_2 is not thermodynamically stable at low pH (< 2.6) and tends to slowly disproportionate to NO and NO_3^-. Previous literature has reported that the nitrite concentration increases with the time of plasma exposure, reaches a plateau, and then slowly decreases, while the nitrate concentration continuously increases [31,33,49]. It is also possible that NO_2^- ions react with H_2O_2 to transform into NO_3^- [85]. However, this hypothesis is not considered here as H_2O_2 was never observed as a species formed under our plasma conditions.

The maximum amount of NO_2^- present in the medium is immediately after exposure and immediately decreases over time (Figure 5.1). This indicates that the species identified as the main active agents are not stable enough to conclude that the PAW created in our conditions can be used as reactive medium for the precipitation of precursors for an undefined period of time. However, it is worth noting that after 2h of resting, more than 50% of the initially created nitrite species remain in the solution. Therefore, it is possible that this amount is still sufficient to trigger the precipitation of some precursors. Furthermore, we previously stated that although HNO_2 and/or NO_2^- were identified as active species in the precipitation, they may not be the only species triggering the process. Thus, the study performed here is not comprehensive enough to determine the stability of other long-lived species that may also impact the precipitation process. To complete the analysis of using PAW for GP catalysts synthesis, it would have been valuable to identify other long-lived species generated in our medium and study their effects on the precipitation of the precursors exposed to the GP.

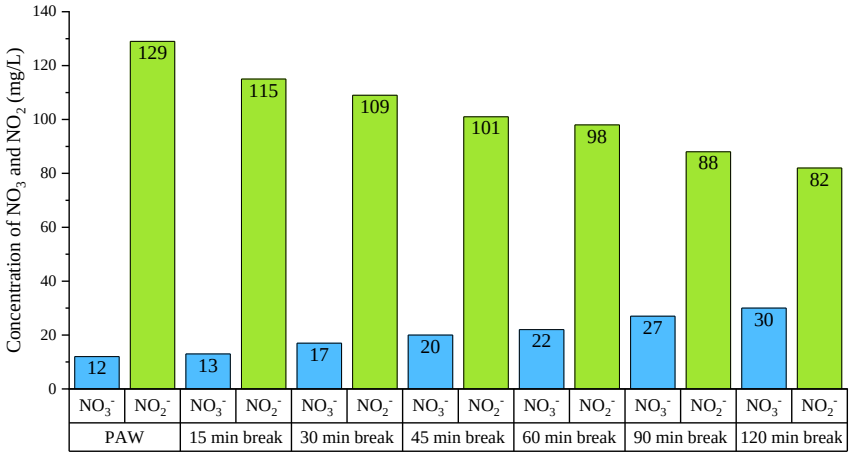


Figure 5.1 : Concentration of NO_2^- and NO_3^- in demineralized water exposed to the GP for 1h before resting at AT for 120 min

3.2. Investigation of the impact of PAW for catalysts synthesis

By comparing the yield of formed precipitate for $KMnO_4$ and $SnSO_4$, it is slightly smaller when these precursors are added to PAW than when they are directly exposed to plasma discharge (Table 5.1). This might be expected because, in the PAW formation of solid process, precursors are added to the PAW then left for the same duration that they are normally exposed to the discharge. However, as discussed in the previous point, HNO_2 and/or NO_2^- species, identified as the mean reactive species in the previous Part I, Chapter 1, tend to transform over time into NO_3^-, which was identified as non-active species. Yet, this shows that, HNO_2 and/or NO_2^- species can react in a delayed manner with the metal precursors, although getting simultaneously degraded over time. Additionally, compared with the direct exposure, where HNO_2 and/or NO_2^- are continuously generated, in the PAW, HNO_2 and/or NO_2^- are consumed by the precipitation process. Consequently, at the end, a smaller amount of HNO_2 and/or NO_2^- is there to react with the precursor in PAW, making it logical that the amount of recovered precipitates is smaller in the latter approach.

However, this hypothesis is not confirmed with $FeSO_4$, as for this precursor, the yield of recovered precipitate is higher when added to PAW (Table 5.1). In previous Part I, Chapter 1, section 3.3, we discovered that using O_2 as the plasma gas instead of humid air increased significantly more the yield of the precipitate formed from $FeSO_4$ than for $KMnO_4$. Therefore, it is possible that other long-lived species, not identified and

with a longer lifetime than HNO_2 and/or NO_2^- species, are still present in PAW, potentially explaining the high yield of precipitate with $FeSO_4$.

Table 5.1: Yield of formed precipitate for $FeSO_4$, $KMnO_4$ and $SnSO_4$ exposed to GP or added to PAW

	Yield of formed precipitate (%)
$FeSO_4$	44
$FeSO_4$ PAW	68
$KMnO_4$	20
$KMnO_4$ PAW	15
$SnSO_4$	100
$SnSO_4$ PAW	68

Concerning the phases developed, XRD diffractograms of the solids formed show that they are the same if we directly exposed the precursor to the discharge or just added it in a PAW (Figure 5.2). In the case of $FeSO_4$, the resulting solid is identified as the FeOOH phase before calcination and a mixture of Fe_2O_3 and $FeOHSO_4$ after calcination, while for $KMnO_4$, the formed solid corresponds to the $KMnO_2$ phase and for $SnSO_4$, to the SnO_2 cassiterite, before and after calcination (Figure 5.2, Supplementary Information SI.12). Noted that the $KMnO_2$ phase is actually a polymorph of MnO_2 (birnessite) that is non-stoichiometrically composed. In this structure, K^+ ions are inserted into the channel of the

materials, and some Mn^{4+} ions are either missing, or replaced by Mn^{3+} ions [24].

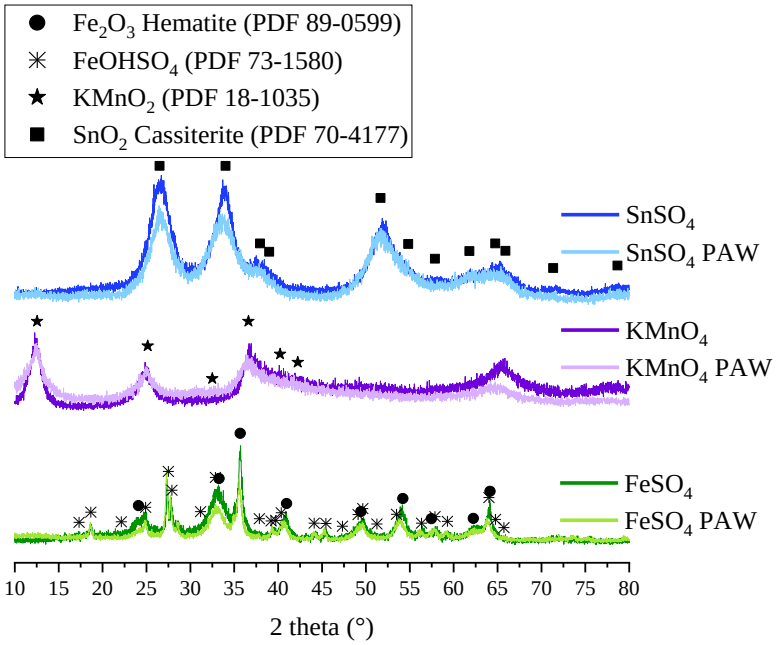


Figure 5.2: XRD data of solids obtained after calcination with $FeSO_4$, $KMnO_4$ and $SnSO_4$ exposed to GP or added to PAW

For all the solids formed by PAW, more S or K is present both at their surface and in the bulk (Table 5.2). The binding energy of the XPS peaks of S 2p corresponds to SO_4^{2-} groups (168.9 eV). This could indicate that the sulfate precursors are less transformed into oxides when added to PAW than when directly exposed to the GP.

For $SnSO_4$, this is plausible because, as seen in Part II, Chapter 3, section 3.1.2, when dissolved in water, it releases Sn^{2+} ions that spontaneously oxidized to form $Sn(OH)_4$ or undergo hydrolysis to produce tin hydroxysulfate. Plasma species can either oxidize Sn^{2+} ions that have not had sufficient time to react spontaneously with water or oxidize $Sn_3O(OH)_2SO_4$ into $Sn(OH)_4$. In PAW, it is possible that less oxidation occurs, resulting in more $Sn_3O(OH)_2SO_4$ remaining.

For $FeSO_4$, under dissolution, Fe^{2+} are released and oxidized by plasma species into Fe^{3+}. In an aqueous environment, Fe^{3+} ions are unstable, prompting their spontaneous hydrolysis into FeOOH if the medium is not sufficiently acidic. Additionally, Fe^{3+} can also react with other ions present in the medium, such as SO_4^2 ions originating from the precursor,

forming $FeOHSO_4$. It appears that slightly more of this hydroxysulfate phase is present for the solid synthesized in PAW.

For $KMnO_4$, it is more challenging to interpret the amount of K remaining in bulk or at the surface. However, this may be due to the washing step. In fact, this solid consists of very small particles that do not adhere well on the surface of the centrifuge tube. Therefore, to avoid losing too many particles during the washing step, less liquid was removed between each washing stage. As a result, each washing used less clean distilled water compared to other precursors. Consequently, the remaining K in the solid may primarily come from the precursor that did not react and was not washed away completely before drying.

Table 5.2: XPS and EDX data of solids obtained with $FeSO_4$, $KMnO_4$ and $SnSO_4$ exposed to GP or added into PAW

	Fe or Mn or Sn			**O**			**S or K**		
	XPS (Fe2p ; Mn2p ; Sn3d)		**EDX**	**XPS (O1s)**		**EDX ***	**XPS (S2p ; K2p)**		**EDX**
	BE (eV)	**(% at)**		**BE (eV)**	**(% at)**		**BE (eV)**	**(% at)**	
$FeSO_4$	710.9	26.5	28	530.4	66.6	69	169.5	6.8	3
$FeSO_4$ PAW	711.3	21.3	24	532.0	70.7	73	169.1	8.0	3
$KMnO_4$	642.0	19.8	25	529.5	63.8	67	292.4	16.4	7
$KMnO_4$ PAW	642.1	20.9	27	529.6	60.3	64	292.5	18.8	9
$SnSO_4$	487.1	33.5	23	530.6	63.5	75	169.4	2.9	2
$SnSO_4$ PAW	487.6	33.5	20	531.9	61.7	78	169.5	4.7	2

** The at % of O obtained by EDX is likely overestimated due to the underlying adhesive carbon tape used to fix the sample.*

Regarding the texture of the solids, the specific area and/or pore volume vary depending on whether the precursors were directly exposed to the discharge or added in PAW (Table 5.3). For $FeSO_4$ the specific surface area and pore volume are approximately the same. For $KMnO_4$, the specific surface area is the same, but the pore volume is slightly higher for solids obtained by PAW. This increase in pore volume may be due to greater agglomeration in PAW, leading to increased interparticle porosity and pores size. In the case of $SnSO_4$, both the specific surface area and pore volume are significantly smaller when the solid is synthesized by PAW.

This highlight that the precipitation process and maturation of the particles likely differ when exposing the precursor directly to the discharge compared to adding it to PAW. This can be understood by examining the parameters influencing the precipitation process. As described in the General Introduction, section 2.1.2, the process of forming a solid from a solution involves several steps: supersaturation, nucleation, growth, and eventually maturation [13]. Supersaturation, the prerequisite for nucleation, can be achieved through chemical methods, by adding a coprecipitating agent [13], which is what occurs in our case. Exposure to GP creates reactive species, such as long-lived species previously identified as precipitating agent, which trigger the oxido-reduction of the precursor followed by the precipitation process.

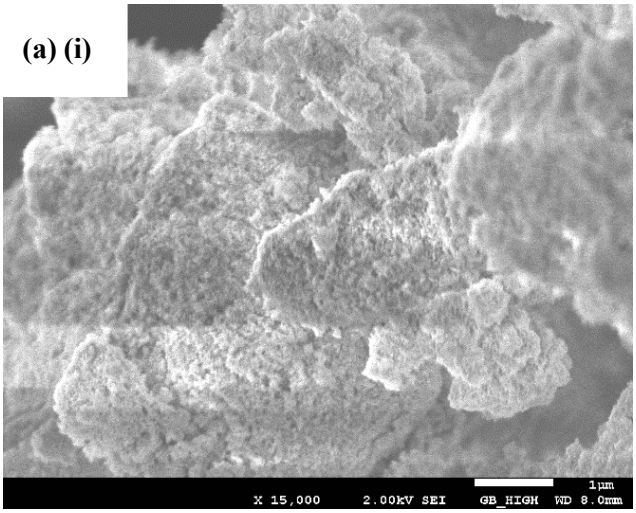
In our system, when the precursor is exposed to the discharge, the precipitating agent, HNO_2 and/or NO_2^-, is slowly added to the solution as it forms during the discharge. Consequently, the reaction between these species and the precursor occurs slowly, while the concentration of the precipitating agent remains likely relatively constant since it is continuously created during exposure. Conversely, in PAW, all the precipitating agents are already present in the solution when the precursor is added. Therefore, the reaction between the plasma species and the precursor happens quicker, decreasing the concentration of the precipitating agent, which is no longer created in the medium. Under these conditions, we can expect that the nucleation regime criteria become more stringent as the precursor concentration decreases rapidly, compared to when the chemical coprecipitating agent is added slowly. This may result in the formation of larger particles in PAW synthesis.

Table 5.3 : Textural properties obtained by N_2-physisorption of solids obtained with $FeSO_4$, $KMnO_4$ and $SnSO_4$ exposed to GP or added to a PAW (isotherms Supplementary information SI.13)

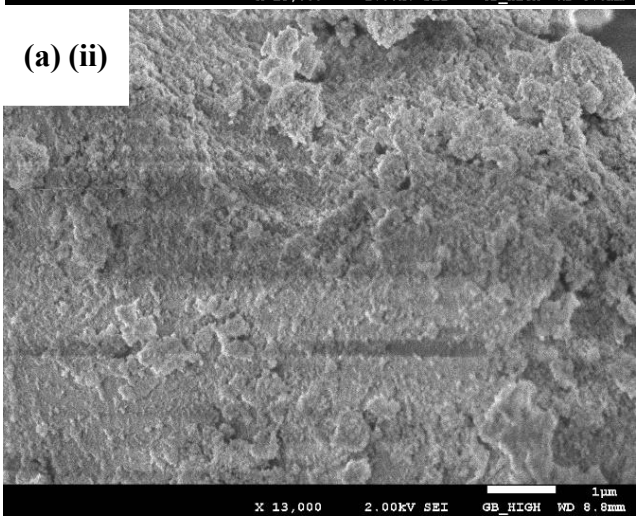
	Specific surface area (m^2/g)	**Pore volume (cm^3/g)**
$FeSO_4$	95	0.33
$FeSO_4$ PAW	95	0.29
$KMnO_4$	29	0.12
$KMnO_4$ PAW	30	0.17
$SnSO_4$	162	0.13
$SnSO_4$ PAW	15	0.03

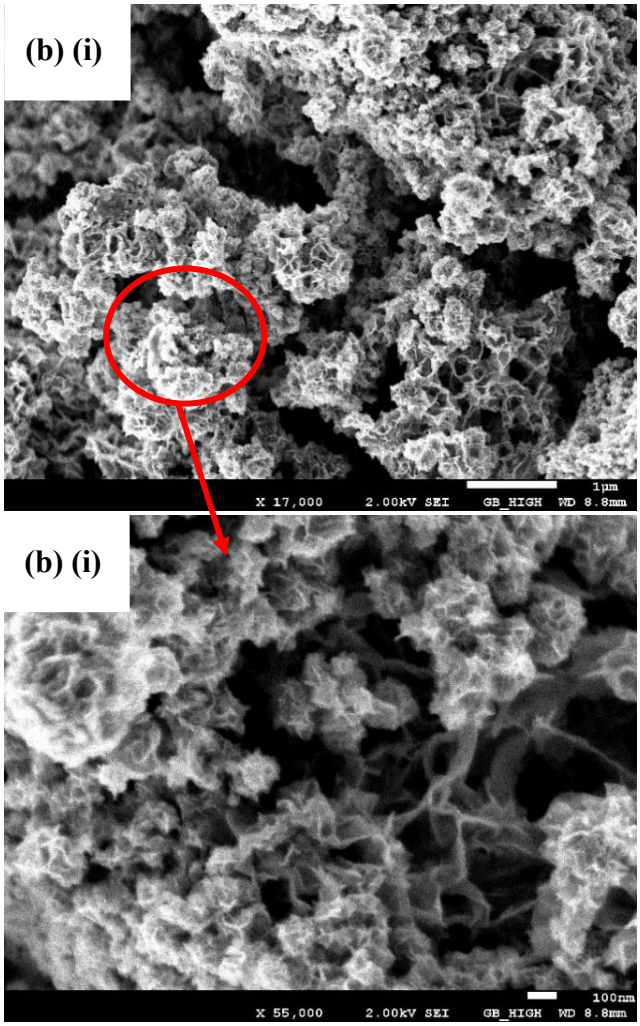
Regarding the morphology of the solids, no significant difference is observed between samples synthesized by direct exposure of the precursor or by adding it to PAW for $FeSO_4$ and $SnSO_4$ (Figure 5.3: (a) and (c)). This is surprising for $SnSO_4$, as the textural properties between the two solids are so different that we expected to observe some difference of morphology between them. However, even in PAW, the spherical particles that we normally observe were able to develop. For $KMnO_4$, although the particles developed seem to have the same shapes, in PAW, they appear to be an agglomeration of particles forming more spherical shape in the end (Figure 5.3: (b)). This agglomeration may be the reason why the interparticular volume increases in N_2-physisorption.

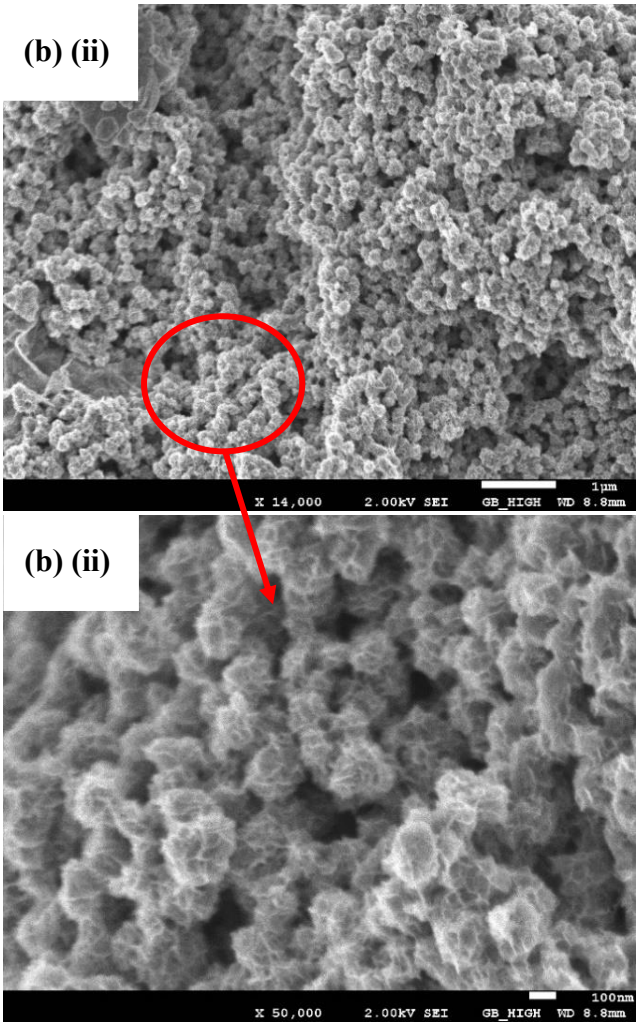
(a) (i)


X 15,000 2.00kV SEI GB_HIGH WD 8.0mm
1µm

(a) (ii)


X 13,000 2.00kV SEI GB_HIGH WD 8.8mm
1µm


(b) (i)
X 17,000 2.00kV SEI GB_HIGH WD 8.8mm 1μm
(b) (i)
X 55,000 2.00kV SEI GB_HIGH WD 8.8mm 100nm


(b) (ii)
X 14,000 2.00kV SEI GB_HIGH WD 8.8mm 1μm
(b) (ii)
X 50,000 2.00kV SEI GB_HIGH WD 8.8mm 100nm

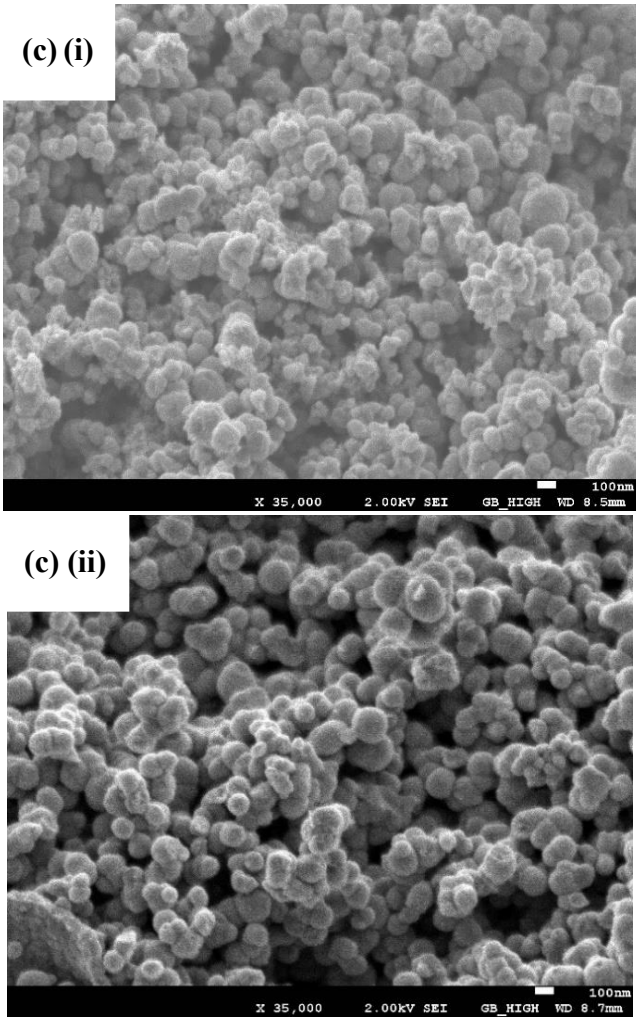


Figure 5.3: SEM images of solids formed with (a) $FeSO_4$ (i) exposed to GP or (ii) added to a PAW; (b) $KMnO_4$ (i) exposed to GP or (ii) added to a PAW ; and (c) $SnSO_4$ (i) exposed to GP or (ii) added to a PAW

All these observations suggest that although the long-lived species created in PAW are present in sufficient amounts and for a sufficient duration to develop solids with some characteristics similar to those obtained by directly exposing the precursor to the discharge, they also highlight that the precipitation mechanism differs between the two types of synthesis, resulting in solids with also distinct characteristics.

3.3. How long after the exposure PAW can be used for the catalysts precipitation ?

To investigate the effect of waiting before adding the precursor to a PAW, we focus on using the $FeSO_4$ precursor. As already evoked, the yield of

precipitate formed for this precursor is higher for solids synthesized by PAW than by direct exposure of the precursor. However, if we wait before adding the precursor to the PAW, the yield decreases (Table 5.4). We could expect that, as we observed in this Chapter 5, section 3.1, the quantity of reactive species, in this case HNO_2 and/or NO_2^-, decreases over time, resulting in fewer reactive species available to react with the precursor to form less precipitate (Figure 5.1). However, even after waiting 90 min before adding the precursor to the PAW, the yield remains significantly high compared to by direct exposure. This is notable, especially considering the reaction discussed in Part I, Chapter 2, section 3.1.2 (Eq.5.3). After 1 h of exposure, the 129 mg/L ($2.8*10^{-3}$ mol/L) of NO_2^- generated is insufficient to precipitate all the Fe^{2+} in solution ($1*10^{-2}$ mol/L). Therefore, since waiting before adding the precursor in PAW reduces the NO_2^- concentration, a lower yield was excepted.

$$Fe^{2+} + H_2O + NO_2^- \rightleftharpoons FeOOH + H^+ + NO \qquad (Eq.5.3)$$

This can be explained by the hypothesis we stated earlier, suggesting that other long-lived unidentified species with a longer lifetime than HNO_2 and/or NO_2^- may be responsible for the precipitation of this precursor.

Table 5.4: Yield of formed precipitate for $FeSO_4$ added to PAW after 0, 30, 60 and 90 min

	Yield of formed precipitate (%)
$FeSO_4$	44
$FeSO_4$ PAW	68
$FeSO_4$ PAW break 30 min	45
$FeSO_4$ PAW break 60 min	38
$FeSO_4$ PAW break 90 min	36

Regarding the phases developed, XRD diffractograms of the formed solids show that the $FeOHSO_4$ phase tends to disappear when the precursor is

added to PAW after waiting 30 and 60 min, but reappears after 90 min (Figure 5.4).

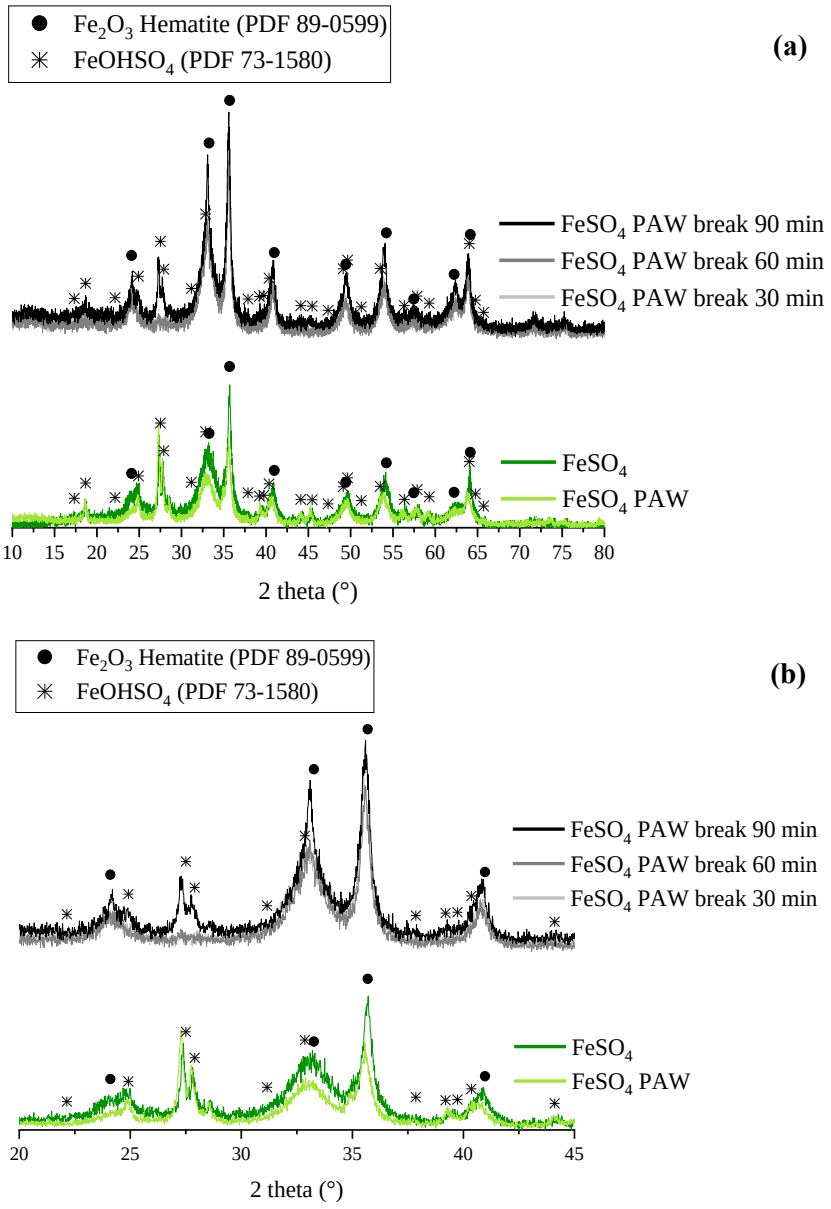


Figure 5.4: XRD data (a) complete range of 2 theta angles measured, (b) zoom on the 20-45° 2 theta range, of solids obtained after calcination with $FeSO_4$ added to PAW after 0, 30, 60 and 90 min

Based on XPS and EDX results, we observe that waiting before adding the precursor to PAW results in solids with less sulfate phase on the

surface (Table 5.5). However, after 90 min, this phase appears to increase again, consistent with the XRD observations (Table 5.5).

As previously mentioned, $FeSO_4$ precursor seems to have a unique way of reacting in PAW, possibly due to its capacity to interact with other plasma species besides HNO_2 and/or NO_2^-, which may have a longer lifetime. Therefore, it is possible that after 60 min, these species tend to disappear, explaining the difference between a 60 min and 90 min break. Since these species were not identified, it is challenging to predict their stability and how they react with the precursor. However, these results might also indicate less reproducibility in the PAW synthesis method.

Table 5.5: XPS and EDX data of solids obtained with $FeSO_4$ added to PAW after 0, 30, 60 and 90 min

	Fe (at %)		**O (at %)**		**S (% at)**		
	XPS (Fe2p)	**EDX**	**XPS (O1s)**	**EDX ***	**Eb (eV)**	**XPS (S2p)**	**EDX**
$FeSO_4$	26.5	28	66.6	69	169.2	6.8	3
$FeSO_4$ PAW	21.3	20	70.7	77	169.1	8.0	3
FeSO4 PAW break 30 min	29.5	21	65.1	76	169.0	5.4	2
FeSO4 PAW break 60 min	28.3	27	66.8	71	168.9	4.9	2
FeSO4 PAW break 90 min	27.4	36	65.5	61	168.6	7.1	3

** The at % of O obtained by EDX is likely overestimated due to the underlying adhesive carbon tape used to fix the sample.*

Regarding the textural properties of the developed solids, the specific surface area and pore volume are sometimes higher, identical or lower compared to the solid obtained when the precursor is directly exposed to the discharge (Table 5.6). As previously explained, the nucleation and maturation process are likely different in PAW compared to direct exposure to the discharge. Additionally, there seems to be no clear correlation between the waiting time before adding the precursor in PAW and the textural properties of the resulting solids. This again suggests potential issues with the reproducibility of the PAW synthesis method.

Table 5.6: Textural properties obtained by N_2-physisorption of solids obtained with $FeSO_4$ added to PAW after 0, 30, 60 and 90 min (isotherms Supplementary information SI.14)

	Specific surface area (m^2/g)	**Pore volume (cm^3/g)**
$FeSO_4$	95	0.33
$FeSO_4$ PAW	57	0.23
$FeSO_4$ PAW break 30 min	168	0.66
$FeSO_4$ PAW break 60 min	94	0.63
$FeSO_4$ PAW break 90 min	66	0.22

4. Conclusion

The purpose of this chapter was to explore the possibility of synthesizing solids by adding a metal precursor to plasma activated water (PAW) instead of directly exposing it to the GP discharge. This approach was thought as a way to enhance the economic and ecological impact of the GP catalysts synthesis by eliminating the washing step of the reactor required between the exposure of different precursors solutions to prevent any contamination between samples.

This idea emerged from the understanding gained from previous Part I, Chapter 1, that long-lived species are the primary species responsible for the redox reaction and subsequent precipitation of metal precursors exposed to the GP. Among these species, HNO_2 and/or NO_2^- were found to be the main triggers of the reaction. We thus wondered whether these long-lived species could be generated in sufficient quantities in PAW to initiate the precipitation of various precursors, typically reactive to GP, that would be added afterwards in the PAW. Furthermore, we investigated whether these species were stable enough over time to still trigger the precipitation process even after a delay before adding the precursor to PAW.

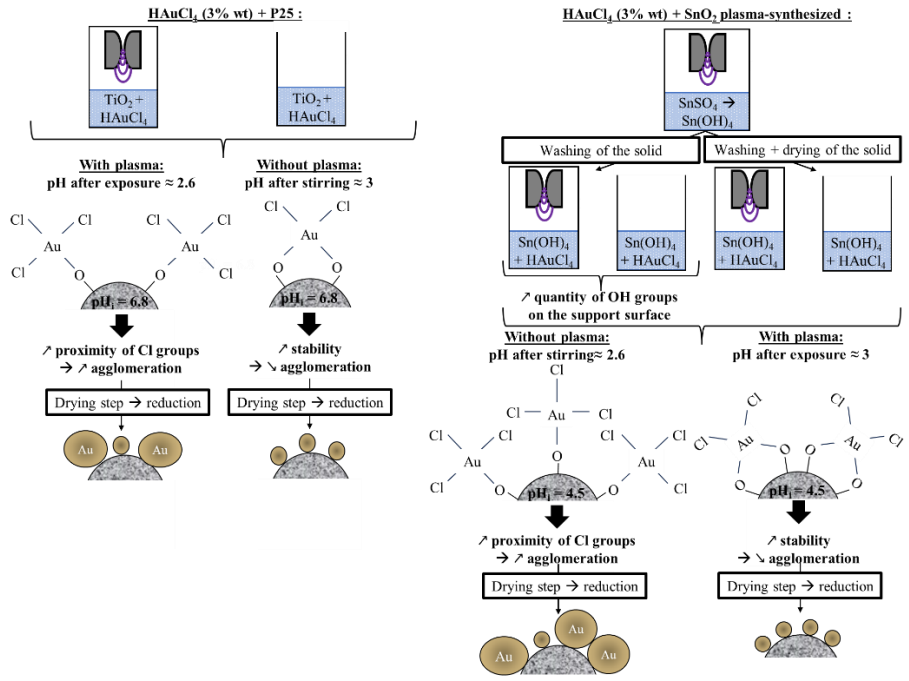
By adding different types of precursors to PAW ($FeSO_4$, $KMnO_4$ and $SnSO_4$), it was observed that the long-lived species present in PAW were sufficient in both quantity and lifetime to form solids with some characteristics similar that those obtained by exposing the same precursors directly to the discharge. For instance, the same types of phases developed in both synthesis methods. However, we also noted that the precipitation mechanism differed between the two methods, resulting in solids with sometimes distinct characteristics. Precisely, the precursor undergoes less transformation into oxides when added to PAW compared to direct GP exposure, and the resulting solids may exhibit different textural properties.

Furthermore, we have also understood that the long-lived species present in PAW are stable for a sufficiently long time to still trigger the precipitation process of the precursor even after waiting a certain period before adding it, at least for the $FeSO_4$ precursor. However, the characteristics obtained for the solids in this section are slightly random, making them difficult to interpret. This might, be due to the capacity of $FeSO_4$ to interact with other unidentified plasma species besides HNO_2 and/or NO_2^-, which may have a longer lifetime. However, it may also highlight the lack of reproducibility in the PAW synthesis method when a delay is introduced before adding the precursor.

In conclusion, we proved that it is indeed possible to trigger the precipitation of a metal precursor both by directly exposing it to the GP discharge and by adding it to PAW. However, we cannot deny that the nucleation and maturation processes differ between these synthesis methods, resulting in solids with some distinct characteristics in each case.

Part III - Synthesis of supported metal/metal oxide catalysts through GP

Chapter 6 - Synthesis of Au/metal oxides catalysts by humid air GP



Abstract

The GP method, previously identified as a promising technique for synthesizing bulk metal oxides and metal oxide/metal oxide catalysts, had not been explored yet for metal/metal oxide catalysts. This chapter investigates the synthesis of Au/TiO_2 and Au/SnO_2 catalysts using GP, with the goal of broadening the application of this method. We evaluated the effectiveness of GP in depositing Au NPs on both commercially available TiO_2 (P25) and plasma-synthesized SnO_2 supports. The synthesis parameters explored included the initial mass ratio of gold precursor (1% or 3%), exposure time to GP (7–30 min), and the timing of Au precursor ($HAuCl_4$) addition (post-support synthesis, post-washing of the support, post-washing and drying of the support, or simultaneous exposure of support and gold precursors to GP). We identified that the GP deposition method for TiO_2 faces a significant challenge due to rapid acidification during exposure, which affects gold NPs deposition which requires a pH close to the PZC of the support to maximize OH group availability on the surface. Furthermore, the low pH limits the formation of $[AuCl_2(OH)_2]^-$ species, crucial for stable bidentate bonding, leading to NP agglomeration and reduced catalytic activity. Furthermore, the plasma induced pre-reduction of gold NPs potentially exacerbates this agglomeration issue. To mitigate these challenges, we explored SnO_2 as a support due to its lower PZC. The higher pH closer to the PZC during GP exposure of SnO_2 improved Au deposition by increasing the number and the stability of the bonds between Au and the surface. It was also discovered that effective Au/SnO_2 catalyst formation required washing the pre-synthesized support and avoiding drying the support before gold precursor addition. Despite these improvements, catalysts synthesized without GP during the Au deposition step outperformed those involving GP. Additionally, a one-pot synthesis method was tested but proved unsuitable due to mismatched precipitation times for Au and the SnO_2 support. Therefore, while Au/TiO_2 and Au/SnO_2 catalysts were successfully synthesized, the acidification during GP exposure presents a significant barrier to optimizing Au-supported catalysts. The study highlights the potential and limitations of GP in synthesizing metal/metal oxide catalysts and suggests that further optimization of synthesis conditions is needed.

This chapter has been written based on the results obtained by two Master's students, who were supervised in the context of their Master's theses (Nicolas Van Hecke and Martin Ben Haddou).

1. Introduction

In the previous chapters, we have enhanced the understanding of the GP catalysts synthesis method and explored various synthesis conditions to improve the characteristics of the catalysts themselves or to identify more economical and environmentally friendly synthesis approaches. However, the catalysts we experimented were all consistently of the same type: bulk oxides catalysts. While these catalysts are of significant interest due to their widespread applications, as discussed in the General Introduction, section 3.3.2, other types of catalysts, such as mixed oxides and supported catalysts, are also widely used and valuable for many reactions. The GP has previously been applied in the literature to develop supported catalysts, such as FeO_x/kaolinite and TiO_2/SnO_2, which have demonstrated promising properties. This suggests that the GP method could potentially be employed for synthesizing other types of catalysts as well. However, its application remains somewhat limited in terms of the range of catalysts that can be synthesized using this method.

Another type of catalysts that could be interesting to synthesize, and which has never been attempted before by GP method, is the supported metal/metal oxide catalyst. In the Part I, chapter 2, section 3.2, we identified 2 metals, gold and ruthenium, that can precipitate by GP. This led us to consider whether it would be possible to synthesize Au or Ru supported catalysts by GP, thereby expanding the potential of the method by creating different types of catalysts. There are several approaches to achieve this: using a support synthesized by another method and attempting to deposit the metal onto it, synthesizing the support by GP and then trying to deposit the metal, or directly exposing both the precursor of the support and the metal precursor to see if we can form the metal/metal oxide catalyst.

To begin exploring the possibility of synthesizing metal-supported catalysts by GP, we focused on the synthesis of Au supported catalysts. In the Part I, chapter 2, section 3.2, we observed that the gold precursor $HAuCl_4$ tends to precipitate as pure Au, whereas the Ru precursor $KRuO_4$ seems to form a Ru oxide. This indicates that synthesizing Ru-supported catalyst would require an additional reduction step before they can be used, making the process more complex. Therefore, we initially focus our research on the synthesis of gold-supported catalysts. We experimented also 2 different types of support: P25, as well-known and stable support frequently used in the literature for gold deposition, and SnO_2, which can be synthesized by the GP and offers the

highest specific surface area among metal oxides synthesized by GP, making it an attractive support material.

Au-supported catalysts are extensively used in various catalytic reactions for bulk chemical synthesis, such as producing gluconic acid, vinyl acetate monomer, methyl glycolate, H_2O_2, … They also play a crucial role in hydrogen production system from CO or CO_2, and in pollution and emission control, including the total oxidation of CO or nitrogen-based molecules [125,126]. Previous research has shown that to achieve significant catalytic activity in gold-supported catalysts, it is essential to reduce the size of gold particles to diameters of less than 5 nm and to have a specific shape of hemispherical particles. This presents challenges in depositing these NPs onto a support surface, as the synthesis method must ensure a well-dispersed distribution of the NPs. They must also be sufficiently stable to prevent their sintering, which tends to occur spontaneously during the drying step due to the low fusion point of gold and the weak bonds it typically forms with oxides support. Consequently, the nature of the support material also significantly impact on the stabilization of the gold NPs [127].

Although the impregnation method without interaction, as presented in the General Introduction, section 2.2.1, is commonly used to deposit metal on a support, it is not the most effective technique when using $HAuCl_4$ as the gold NPs precursor. This is because the presence of chlorine cause the gold particles to grow rapidly, increasing their size and consequently decreasing their catalytic activity [128]. Gold NPs can be deposited on the support surface in liquid phase, where both the support and metal precursors are present, using co-precipitation or sol-immobilization techniques. However, deposition-precipitation is one of the most widely used techniques (described in General Introduction, section 2.2). This technique is specifically used for the deposition on basic (or least amphoteric) metal oxide support. In this process, $[Au(OH)_4]^-$ or $[AuCl(OH)_3]^-$ ions, formed by ligand exchange of $[AuCl_4]^-$ ions at a high pH range, interact with the positively charge oxide surface or hydroxyl groups on the surfaces. Subsequently, $Au(OH)_3$ species precipitate onto the support oxide surface. To control the pH of the medium, NaOH or urea is usually added to the system [128].

The major challenge will be to determine whether gold NPs can indeed be deposited on the surface of supports exposed to the GP, and whether these NPs possess desirable characteristics such as small size and high stability. By using different types of supports (P25 and SnO_2), we aim to evaluate the method's effectiveness in depositing gold NPs on both well-known support and plasma-

synthesized support. The synthesis conditions explored in this chapter will include the initial mass ratio of gold precursor (<1% or 3%) and the exposure time of the suspension/solution (ranging from 7 min to 30 min). This will allow us to assess the impact of various synthesis conditions on the deposited NPs. Finally, we will evaluate the effectiveness of these various catalysts in the total oxidation of benzene, as this catalytic test is used throughout the thesis and gold is known to be an effective oxidation catalyst. However, gold-supported catalysts are generally more active in other reactions, such as the total oxidation of CO, which would have been a more suitable test for assessing catalytic performance. Nonetheless, the total oxidation of benzene proved sufficient to distinguish between the solids produced under different synthesis conditions.

2. Materials and methods

2.1. Materials

For the supports, TiO_2 in the form of P25 (79.89 g/mol) form Degussa was used, and SnO_2 was synthesized from tin(II) sulfate ($SnSO_4$; 214.77 g/mol ; ≥ 95%) from Sigma-Aldrich.

The gold precursor used was tetrachloroauric(III) acid trihydrate (393.83 g/mol ; ≥ 99.9%) from Sigma-Aldrich.

All the solutions were prepared with demineralized water as solvent.

2.2. Method

2.2.1. Synthesis device: GP reactor

The GP reactor used in this chapter differs slightly from the one used in previous discussed chapters. While the main characteristics of the reactor remain the same, some differences need to be noted:

- The humid air flow sent between the electrodes is of 7.5 L/min.
- The stirring during the exposure is approximately 120 rpm.
- The maximum liquid volume the reactor can contain is 400 mL.

2.2.2. Materials synthesis

2.2.2.1. Au/TiO_2

Before deposing Au particles on P25, we wanted to observe the effect of the GP discharge on the support alone. To do so, a 10 g/L of P25 suspension in demineralized water was prepared, and 400 mL of it was either exposed to the

GP for 60 min (named "P25 60") or stirred at ambient temperature (AT) for 60 min (named "P25 60 NE") (Table 6.1).

To prepare Au/TiO_2 catalysts, with a 3% mass ratio of Au/TiO_2, 0.1043 g of $HAuCl_4.3H_2O$ was added to 500 mL of a 3.478 g/L suspension of P25. 400 mL of the solution was exposed to the GP for 7, 15 and 30 min (named "TA exposure time"). The remaining 100 mL was used as a blank, by stirring it at ambient temperature for 7, 15 and 30 min, to compare with the solid synthesized by exposure to the glidarc discharge (named "TA exposure time NE") (Table 6.1, Figure 6.1).

The pH of each suspension was measured before and after exposure or after stirring at ambient temperature.

Table 6.1: Synthesis conditions used for the preparation of Au/TiO_2 samples

<table>
<tr><th rowspan="2">Sample name</th><th colspan="4">Before exposure of P25 + $HAuCl_4.3H_2O$</th></tr>
<tr><th>TiO_2 concentration (g/L – mol/L)</th><th>$HAuCl_4.3H_2O$ concentration (g/L – mol/L)</th><th>%mass Au/TiO_2</th><th>(non-)exposure time (min)</th></tr>
<tr><td>P25 60</td><td rowspan="2">10 – $1.25*10^{-1}$</td><td rowspan="2">/</td><td rowspan="2">/</td><td rowspan="2">60</td></tr>
<tr><td>P25 60 NE</td></tr>
<tr><td>TA7</td><td rowspan="6">3.4780 – $4.353*10^{-4}$</td><td rowspan="6">0.2086 – $5.297*10^{-4}$</td><td rowspan="6">3</td><td rowspan="2">7</td></tr>
<tr><td>TA 7 NE</td></tr>
<tr><td>TA15</td><td rowspan="2">15</td></tr>
<tr><td>TA15 NE</td></tr>
<tr><td>TA30</td><td rowspan="2">30</td></tr>
<tr><td>TA30 NE</td></tr>
</table>

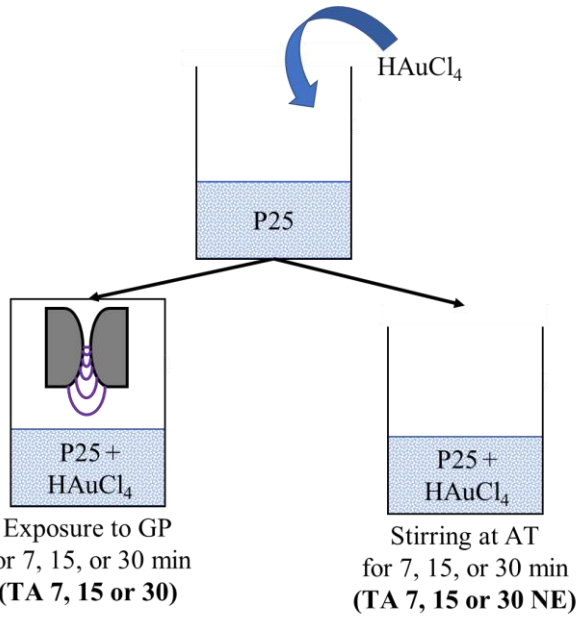


Figure 6.1: Schematic representation of the Au/TiO_2 samples prepared with and without GP

2.2.2.2. Au/SnO_2

a. 2 steps

Unlike the Au/TiO_2 samples, the SnO_2 support was directly synthesized by GP exposure of the $SnSO_4$ precursor.

Before synthesizing Au/SnO_2 precursor, we synthesized the support alone by exposing 400 mL of a 10^{-2} mol/L $SnSO_4$ solution to the GP for 2h (1h of exposure, 15 min break, 1h of exposure) (named "Sn"). This duration was previously determined to achieve 100% conversion of the precursor. Additionally, 100 mL of the solution was used as a blank, by stirring it at AT for 2h, to compare with the solid synthesized by exposure to the glidarc discharge (named "Sn NE") (Table 6.2, Figure 6.2).

To synthesize Au/SnO_2 in 2 steps, 3 different types of synthesis were performed:

i. Direct addition of gold precursor after support synthesis: 400 mL of a 6.196 g/L $SnSO_4$ solution was exposed to the discharge for 2h (1h of exposure, 15 min break, 1h of exposure). Subsequently, 0.03 g of $HAuCl_4.3H_2O$ was added to the suspension to achieve a 0.86% mass ratio of Au/SnO_2. The entire suspension was then exposed to the discharge for 15 and 30 min (named "SA exposure time") (Table 6.2).

ii. Washing and drying of the support before addition of the gold precursor: 400 mL of a 2.1478 g/L $SnSO_4$ solution was exposed to the discharge for 2h (1h of exposure, 15 min break, 1h of exposure). The solid was then recovered by centrifugation (24490 G, 30 min) and subjected to two washing cycles with distilled water. After drying the solid in an oven under air at 110°C for 24h ± 5h, the weight of the recovered solid was measured to determine the amount of gold precursor to add. The solid was resuspended in 500 mL of demineralized water, and $HAuCl_4.3H_2O$ was added to achieve a 3% mass ratio of Au/SnO_2. After adding the gold precursor, 400 mL of the suspension was exposed to the GP for 7 and 15 min (named "SAWD exposure time"). The remaining 100 mL was used as a blank, by stirring it at AT for 7 and 15 min, to compare with the solid synthesized by exposure to the glidarc discharge (named "SAWD exposure time NE") (Table 6.2, Figure 6.2).

iii. Washing of the support before addition of the gold precursor: 400 mL of a 2.1478 g/L $SnSO_4$ solution was exposed to the discharge for 2h (1h of exposure, 15 min break, 1h of exposure). The solid was then recovered by centrifugation (24490 G, 30 min) and subjected to two washing cycles with distilled water. Without drying, the solid was directly resuspended in 500 mL of demineralized water. The average mass of SnO_2 recovered in point b was 0.5673 g, and based on this, 0.034 g of $HAuCl_4.3H_2O$ was added to the suspension to achieve a 3% mass ratio of Au/SnO_2. After adding the gold precursor, 400 mL of the suspension was exposed to the GP for 7 and 15 min (named "SAWH exposure time"). The remaining 100 mL was used as a blank, by stirring it at AT for 7 and 15, to compare with the solid synthesized by exposure to the glidarc discharge (named "SAWH exposure time NE") (Table 6.2, Figure 6.2).

The pH of each suspension was measured before and after exposure or after stirring at AT.

Table 6.2: Synthesis conditions used for the preparation of Au/SnO_2 – 2 steps samples

Sample name	Before exposure of $SnSO_4$		Before adding $HAuI_4.3H_2O$	Before exposure of SnO_2 + $HAuCl_4.3H_2O$			
	C_{SnSO_4} (g/L – mol/L)	(non-) Exposure time (min)		C_{SnO_2} (g/L – mol/L)	$C_{HAuCl_4.3H_2O}$ (g/L – mol/L)	%mass Au/SnO_2	(non-) Exposure time (min)
Sn	2.148 – 10^{-2}	120	/	/	/	/	/
Sn NE							
SA 15	6.196 – $3*10^{-2}$			4.348 – $3*10^{-2}$	0.065 – $1.65*10^{-4}$	0.86	15
SA 30							30
SAWD7	2.148 – 10^{-2}		Centrifugation + 2 washing steps + drying under air at 110°C for 24 h ± 5 h	1.140 – $7.6*10^{-3}$	0.068 – $1.73*10^{-4}$	3	7
SAWD7 NE							
SAWD15				1.213 – $8*10^{-3}$	0.073 – $1.85*10^{-4}$		15
SAWD15 NE							
SAWH7			Centrifugation + 2 washing steps	1.135 – $7.5*10^{-3}$	0.068 – $1.73*10^{-4}$		7
SAWH7 NE							
SAWH15							15
SAWH15 NE							

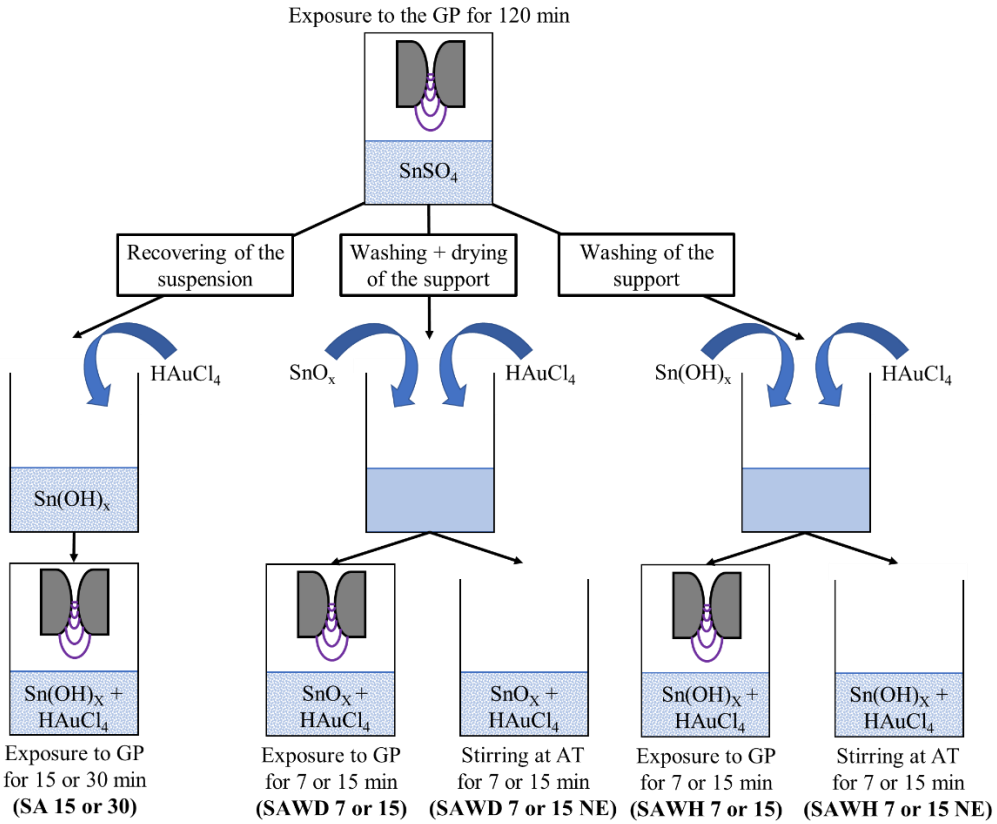


Figure 6.2: Schematic representation of the Au + SnO_2 – 2 steps samples prepared with and without GP

b. 1 step

We also attempted to synthesize Au/SnO_2 catalysts by GP in 1 step, referred as the "one-pot" method. For this, we prepared a solution containing 10^{-2} mol/L of $SnSO_4$ and $2.3*10^{-4}$ mol/L of $HAuCl_4.3H_2O$, aiming for a 3% mass ratio of Au/SnO_2. Subsequently, 400 mL of the solution was exposed to the GP for 7 and 15 min (named "SAOP exposure time"). The remaining 100 mL was used as blank, by stirring it a AT for 7 and 15 min, to compare with the solid synthesized by exposure to the glidarc discharge (named "SAOP exposure time NE") (Table 6.3, Figure 6.3).

It is worth noting that in this synthesis, the $SnSO_4$ precursor is not exposed to the GP for 2h. This likely means that the conversion of $SnSO_4$ into SnO_2 is probably not 100%, and the final % mass ratio of Au/SnO_2 will probably be higher than 3%.

The pH of each suspension was measured before and after exposure or after stirring at AT.

Table 6.3: Synthesis conditions used for the preparation of Au/SnO_2 – 1 step samples

Sample name	Before exposure of SnO_2 + $HAuCl_4.3H_2O$			
	SnO_2 concentration (g/L – mol/L)	**$HAuCl_4.3H_2O$ concentration (g/L – mol/L)**	**%mass Au/SnO_2**	**(non-) Exposure time (min)**
SAOP 7	2.148 – 10^{-2}	0.090 – $2.3*10^{-4}$	> 3	7
SAOP7 NE				
SAOP15				15
SAOP15 NE				

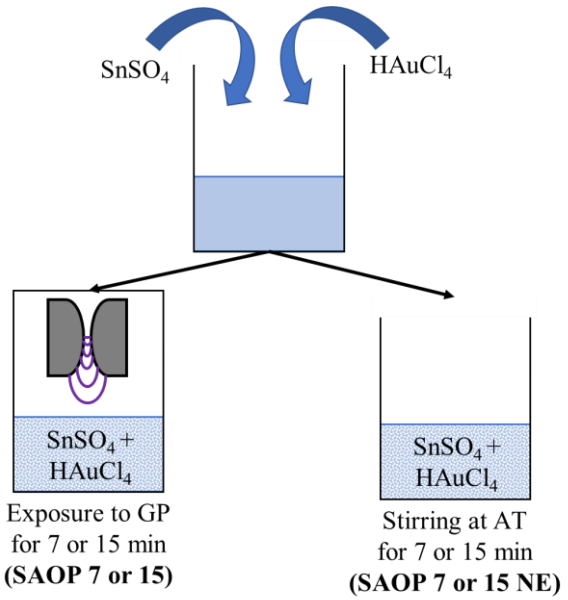


Figure 6.3: Schematic representation of the Au + SnO_2 – 1 step samples prepared with and without GP

2.2.3. Solid recovery

The solid formed in each type of synthesis was subsequently recovered by centrifugation (24490 G, 30 min) and subjected to two washing cycles with distilled water. All the solids obtained after centrifugation were dried in an oven under air at 110°C for 24 h ± 5 h.

After drying, the solid was stored in glass tube wrapped in aluminum fold to avoid contact with light, which is known to have an effect on the sintering of gold NP [129].

2.3. Material characterization

All the instrumental characterizations used here (XRD, XPS, SEM, EDX, N_2-physisorption) were done after drying of the solids formed.

All the characterizations performed in this chapter were carried out as presented in Experimental, section 2.

In addition to these characterizations, Inductively Couple Plasma (ICP) analyses were performed on the synthesized solid. The ICP analyzer used was the ICP-OES (Atomic Emission Spectroscopy) Perkin Elmer, Avio 220 equipped with an automatic sampler Perkin Elmer S23. The conditions of analyses performed are presented in the Table 6.4.

The Au/TiO_2 and Au/SnO_2 samples were dissolved in 50 mL of solution (HNO_3 + HCl (1/1) for Au/TiO_2, HBF_4 + HNO_3 + HCl (1/1/1) for Au/SnO_2). Then, 1 mL of each sample was extracted and added back into a fresh 50 mL solution. It is important to note that SnO_2 could not be dissolved. Therefore, for the Au/SnO_2 samples, only Au was quantified by ICP. The wavelengths used to measure the different elements were: Argon – 420.069 nm, Gold – 267.595 nm and Titanium – 334.940 nm.

Table 6.4: Conditions performed for the ICP analyses of the gold-supported solids synthesized by GP

Instrumental Operating Condition	
Radio-Frequency (RF) Power	1.5 kWatt
Frequency or RF generator	40 MHz
Plasma Argon flow rate	10 L/min
Argon flow rate	0.2 L/min
Nebulizer flow rate	0.6 L/min
Nebulizer type	Concentric Glass
Spray Chamber	Scott type
Sample uptake rate	1.5 mL/min
Integration time	7 s
Integration mode	Peak Area
Replicates	5
Background correction	Manual

All the synthesized solids were also tested catalytically in the total oxidation of benzene, as presented in Experimental, section 2.

3. Results and discussion

3.1. Au/TiO_2

3.1.1. First observations

By looking at the pH of the suspensions, we can see that it decreases with the addition of the $HAuCl_4.3H_2O$, as this precursor is a strong acid. Additionally, the pH drops further when the suspension is exposed to the GP (Table 6.5). This is likely due to the formation of acidic species in solution during the discharge [33,48,49]

Table 6.5: pH of the Au/TiO_2 suspensions before and after (non-)exposure to the GP

	pH before exposure	pH after exposure
P25 60	4.3	3.1
P25 60 NE		4.3
TA7	3.3	2.6
TA7 NE		3.0
TA15	2.8	2.8
TA15 NE		3.0
TA30	3.1	2.8
TA30 NE		3.0

Regarding the aspect of the synthesized powder, it is worth noting the difference in the colors of the samples (Figure 6.4). The P25 powder has a white appearance, which is retained after exposure to GP when exposed alone. However, in the presence of $HAuCl_4$, the powder changed to a purple-blue-grey tint. Interestingly, the color of gold NPs can be used to predict their size, assuming the initial support is white, as it is in this case. Smaller NPs result in a more pink-red-purple color [130]. In our case, there is a significant color difference between exposed and non-exposed samples. The non-exposed powders tend towards a purple-blue color, while the exposed samples shift towards a light blue-grey.

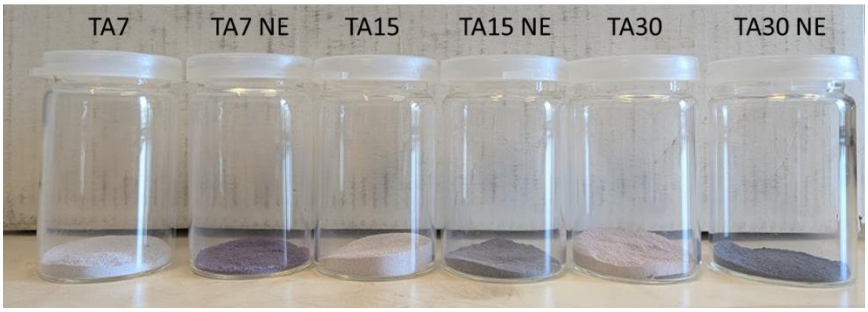


Figure 6.4: Visual aspect of the solids obtained from Au/TiO_2 samples after (non-)exposure to the GP and after drying

The XRD diffractograms of both the exposed and non-exposed P25 reveal two TiO_2 phases: anatase and rutile, which are known to be present in the Degussa P25 (Figure 6.5). This indicates that the phases in P25 do not appear to be altered by plasma exposure. When $HAuCl_4.3H_2O$ is added to the synthesis, in addition to the peaks from the P25 phases, peaks corresponding to Au^0 can sometimes be observed (Figure 6.5, Supplementary information SI.15). By focusing on a range where gold peaks can be seen, we notice that they are present only in the sample exposed to the GP (Figure 6.6).

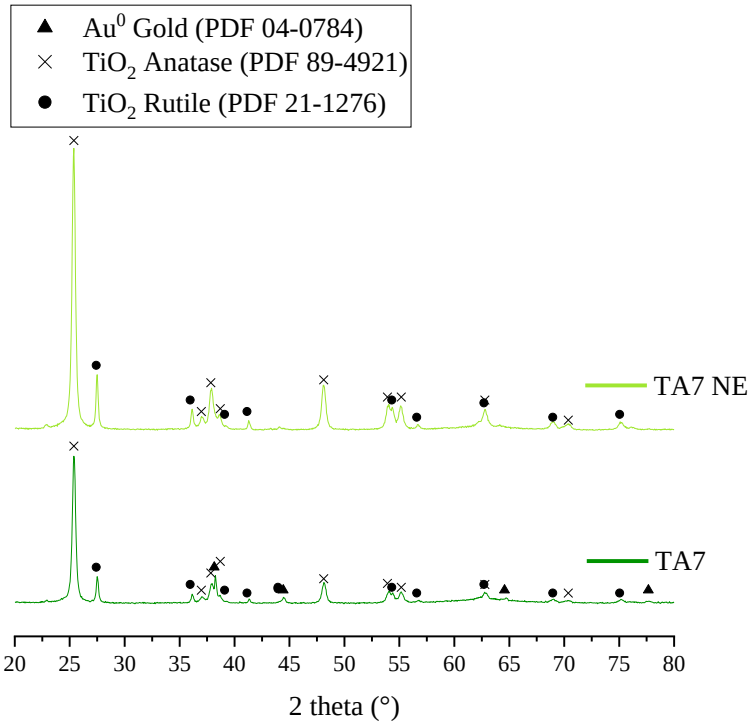


Figure 6.5: XRD data of TA7 and TA7 NE solids

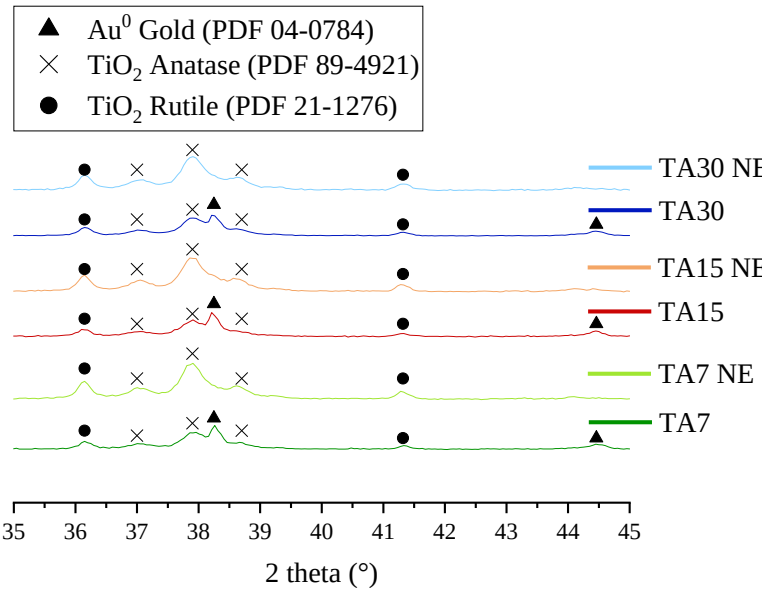


Figure 6.6: Zoom on XRD data of Au/TiO₂ solids obtained after (non-)exposure to the GP (2 theta = [35-45]°)

By examining the surface and bulk composition of the samples using XPS and ICP, we can deduce several points (Table 6.6). First, the composition of the P25 exposed to the GP alone does not change. Second, the at and mass % of Ti and O at the surface do not show significant variation between the samples. However, these % differences are more significant by ICP, therefore in bulk, which is surprising as the support does not appear to be affected by the discharge when exposed alone, and thus is presumably not affected in the presence of the gold precursor either.

Third, there are notable differences in the gold % in the various solids (Table 6.6). According to XPS, the at % of Au is consistently much lower in the samples exposed to the discharge compared to the non-exposed samples, resulting in a significantly lower Au/TiO_2 mass ratio in the exposed samples. In bulk, the difference in gold content between the samples exposed and non-exposed to the discharge appears to be less pronounced for similar exposure times, except for 15 min. However, since the % mass obtained by ICP are approximately the same for all the samples, except for TA15, we might consider the results for this sample somewhat unusual and potentially not indicative of the actual trends in the synthesis conditions. Four and finally, both XPS and ICP indicate a much lower mass ratio than the 3% initially engaged in the suspension before exposure, especially at the surface.

Table 6.6: XPS and ICP data of Au/TiO_2 solids obtained after (non-)exposure to the GP

	Ti		Au				O		Cl	Mass ratio Au/TiO_2 (% mass)	
	XPS (Ti 2p) (% at)	ICP (% mass)	XPS (Au $4f_{7/2}$)			ICP (% mass)	XPS (% at)	ICP (% mass)	XPS (Cl 2p) (% at)	XPS	ICP
			FWHM	E_b (eV)	(% at)						
P25 60	29.8	/	/	/	/	/	70.2	/		/	/
P25 60 NE	29.7	/	/	/	/	/	70.3	/		/	/
TA7	30.0	50	2.01	83.8	0.10	1.5	69.6	48.5	0.3	0.3	1.5
TA7 NE	30.1	47.6	1.82	83.6	0.38	1.4	69.2	51	0.3	0.9	1.4
TA15	30.6	49.8	1.38	82.9	0.03	2.1	69.2	48.1	0.2	0.1	2.1
TA15 NE	30.8	55.0	1.80	83.6	0.48	1.3	68.4	43.7	0.4	1.2	1.3
TA30	31.0	60.1	1.36	83.0	0.03	1.5	68.7	38.4	0.3	0.1	1.5
TA30 NE	30.1	53.7	1.88	83.7	0.41	1.7	69.0	44.6	0.3	1.0	1.7

Regarding the textural properties of the solids, the specific surface area and pore volume of P25 alone are not affected by plasma exposure (Table 6.7). When the gold precursor is added to the suspension, the final solid formed has a specific surface area that decreases slightly but remains approximately the same across different exposure times. However, exposing the suspension to the GP appears to trigger the formation of a solid with a slightly increased pore volume. Based on the position of the hysteresis in the adsorption-desorption curves of all the samples, this porosity seems to consist of large mesopores, likely due to interparticle porosity, as P25 is known to be a non-porous support (Supplementary information SI.16)

Table 6.7: Textural properties obtained by N_2-physisorption of Au/TiO_2 solids obtained after (non-)exposure to the GP (isotherms Supplementary information SI.16)

	Specific surface area (m^2/g)	**Pore volume (cm^3/g)**
P25 60	47	0.30
P25 60 NE	47	0.30
TA7	32	0.36
TA7 NE	37	0.34
TA15	32	0.35
TA15 NE	26	0.27
TA30	24	0.35
TA30 NE	34	0.22

3.1.2. Discussion

3.1.2.1. Hypothesis from the observations

Based on the lack of peaks observed by XRD in the non-exposed samples, we might have assumed that no gold was deposited in these synthesis types. However, XPS and ICP results show that gold is present in all the synthesized solids. Moreover, just considering the XPS results, one might think that more gold was deposited on the non-exposed sample. However, this is not the case, as the Au mass % obtained for TA7 and TA7 NE as well as for TA30 and TA30 NE samples, is the same. In fact, the Au mass % is even higher for the exposed TA15 sample than for the non-exposed TA15 NE sample. These observations highlight that the difference between exposed and non-exposed samples is not in the quantity of gold deposited, but somewhere else.

Indeed, the absence of gold peaks in XRD diffractograms of non-exposed samples, despite higher gold detection by XPS, can be explained by the size, crystallinity, and dispersion of the deposited gold particles. A hypothesis that

can explain these differences is that the gold particles deposited on the non-exposed sample are well dispersed, amorphous and/or composed of small crystals. In fact, in XRD, small, well-dispersed particles are less likely to form diffractogram peaks because they tend to be amorphous and consist of small crystallites, which can be an issue since the crystal size detection limit is 2-2.5 nm [131]. Furthermore, since XPS has a depth detection limit of maximum 10 nm, particles larger than this size will have some Au atoms undetected by the analysis, thereby decreasing the at % of gold detected in comparison to TiO_2 (Figure 6.7). This final hypothesis is further supported by the color of the non-exposed samples, which are more purple-blue compared to the exposed ones. This suggests that the particle size might be smaller for the non-exposed samples.

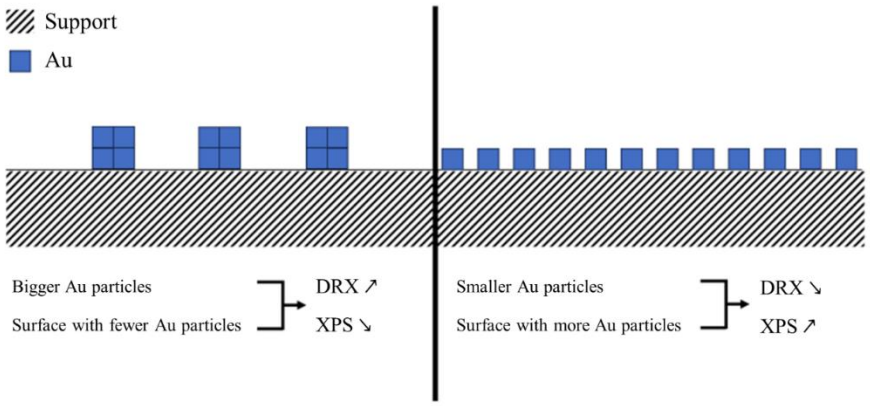


Figure 6.7: Link between the size and dispersion of the gold NPs in their detection by XRD and XPS for a same amount of gold deposited on the surface of a support

Therefore, it seems that the amount of gold deposited on the surface of the support is approximately the same with or without exposure for the same synthesis time, but GP exposure increases the size of the gold particles. Furthermore, it is worth noting that, looking at XPS results for the exposed samples, increasing the plasma exposure time decreases the amount of gold detected. This could mean that, in addition to plasma discharge, the exposure time also impacts on the size of the particles. This can be confirmed by the binding energy and FWHM of Au $4f_{7/2}$. For all the samples without exposure and TA7, the peak position suggests that pure metallic gold is deposited, as this peak is supposed to be between 83.7 and 84.0 eV. However, for TA15 and TA30, the peak position and FWHM are lower. In fact, it has been demonstrated that increasing the size of the gold particles is accompanied by a decrease in the binding energy and of the FWHM of the Au $4f_{7/2}$ peak

(Supplementary Information SI.17) [132]. This confirms that the gold particle size increases with the exposure time as well.

If we only consider the samples exposed 7 and 30 min, these results indicate that the same amount of gold is deposited whether or not it is exposed to the GP, but the size of the deposited gold particles differs. Therefore, 2 things need to be discussed: why the amount of gold deposited is the same in both cases, and why do the particles size and dispersion vary between the 2 synthesis methods.

3.1.2.2. Mechanism of gold deposition

To understand the 2 items just mentioned, we need to discuss the deposition mechanism of gold on the surface of a metal oxide support, specifically on TiO_2.

Firstly, when dissolved in water, $HAuCl_4.3H_2O$ precursor dissociates into H^+ and $AuCl_4^-$. Furthermore, in aqueous solution, $[AuCl_4]^-$ undergoes spontaneous hydrolysis with different levels of hydroxylation depending of the pH (Eq.6.1) [99,100]. According to the literature, at pH<2, the main species present is $[AuCl_4]^-$ (Figure 6.8). By increasing the pH, the ligand Cl^- are replaced by OH^- until $[Au(OH)_4]^-$ is formed at pH of around 6 (Figure 6.8). In our case, at a pH between 2.8 and 3.3, the predominant species present in solution are $[AuCl_3(OH)]^-$, and $[AuCl_2(OH)_2]^-$ (Figure 6.8). However, at the lower recorded pH, it is possible that some $[AuCl_4]^-$ is present, and at the highest pH, that some $[AuCl(OH)_3]^-$ is present [100,101,133].

$$[AuCl_4]^- + jH_2O \rightleftharpoons \left[AuCl_{4-j}(OH)_j\right]^- + jCl^- + jH^+ \qquad (Eq.\,6.1)$$

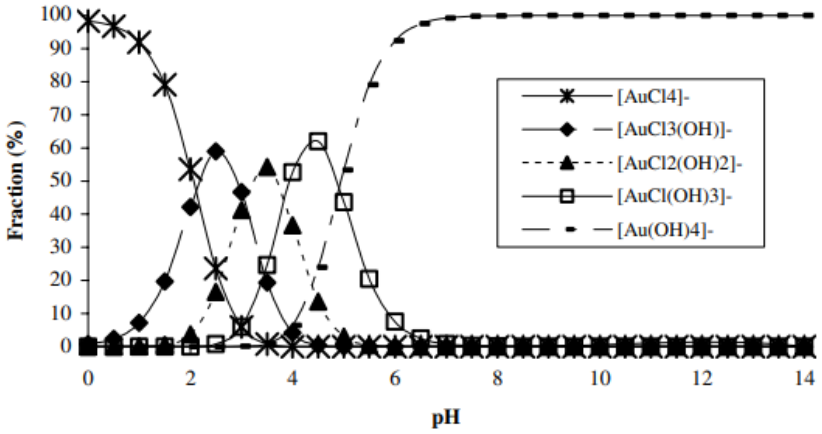


Figure 6.8 : Au(III) speciation as a function of pH (Cl^- and OH^- as ligands) [100]

The other important parameter to consider in order to understand the deposition mechanism is the point of zero charge (PZC) of the support, which is specific for each oxide. In water, the surface of an oxide is covered by a monolayer of hydroxide (noted S-OH) that can be ionized (Eq.6.2). The charge at the oxide surface arises from acid-base equilibrium, which depends on the pH of the medium. Therefore, the PZC is defined as the pH of the medium at which the sum of the surface charges is zero. At pH < PZC, the surface is positively charged, and at pH > PZC, it is negatively charged [17].

$$S - O^- + H_3O^+ \rightleftharpoons S - OH + H_2O \rightleftharpoons S - OH_2^+ + OH^- \qquad (Eq.6.2)$$

In the case of P25 Degussa, the PZC is around 6.8 [134]. This means that at the pH of the medium we are working with, the surface of the support is positively charged. It might be intuitive to think that the negatively charged gold complexes $\left[AuCl_{4-j}(OH)_j\right]^-$ would spontaneously interact with the positively charged surface, forming an ionic bond. However, it has been demonstrated in the literature that increasing the pH toward the PZC of the support also increases the amount of gold deposited on the surface [135]. This indicates that the interaction cannot be purely ionic. Later studies have shown that there is, in fact, a reaction between the hydroxyl groups on the surface of the support and the gold chlorohydrate complexes. This reaction leads to the formation of a surface complex with a covalent bond, predominantly involving grafting deposition (Eq.6.3, Eq.6.4) [135]. Therefore, increasing the number of neutral OH groups on the surface of the support by approaching its PZC lead to an increase in the amount of gold linked to the surface. Additionally, it has been proven that at pH < 2, where the primary gold species

present is $[AuCl_4]^-$, gold deposition does not occur, at least by grafting deposition, due to the lack of hydroxyl groups necessary for linking with the oxide surface [133].

$$TiOH + [AuCl_3(OH)]^- \rightleftharpoons [(TiO)AuCl_3]^- + H_2O \qquad (Eq.\,6.3)$$

$$TiOH + [AuCl_2(OH)_2]^- \rightleftharpoons [TiOAuCl_2(OH)]^- + H_2O \qquad (Eq.\,6.4)$$

Furthermore, the formation of gold complexes on the surface is a rapid mechanism that, after a certain period, becomes independent of time [136]. In fact, since the number of OH groups on the surface of the support is determined by the pH of the medium, this also affects the maximum amount of gold complexes that can be formed. Therefore, once the surface of the support is saturated with gold complexes, increasing the synthesis time or the gold precursor concentration no longer influences the amount of gold linked to the surface.

It was also demonstrated that, as the pH influences both the support and the gold complexes present in the medium, it also influences the way the gold complexes link to the surface. At a pH around 3, the main species present is $[AuCl_3(OH)]^-$, while at pH around 4, it is $[AuCl_2(OH)_2]^-$ (Figure 6.8). These 2 complexes have different numbers of hydroxyl groups that can be removed to interact with the surface. Specifically, $[AuCl_3(OH)]^-$ has only one hydroxyl group, allowing it to form only a single link with the surface, known as monodentate bond. On the other hand, $[AuCl_2(OH)_2]^-$ can lose 2 hydroxyl groups, enabling it to form 2 chemical bonds with the surface, which leads to a stronger interaction (Figure 6.9) [133,136].

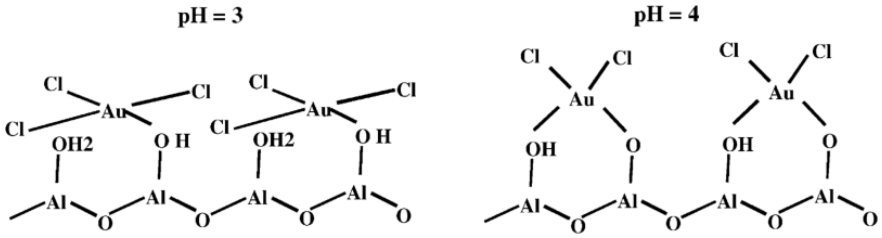


Figure 6.9: Mechanism of interaction of the gold complex with the alumina surface according to the pH [133]

After depositing gold on the surface of the solid, its state and morphology can change due to subsequent synthesis steps, such as drying and/or reducing. Au(III) easily reduces to Au^0 under thermal treatment in air at temperatures above 100°C. This reducibility impacts the tendency to agglomerate because Au^0 has higher mobility on the surface and a strong inherent tendency to attract

other particles. This agglomeration can occur via 2 mechanisms: Ostwald ripening or particle diffusion and coalescence. The process of Ostwald ripening involves larger particles growing at the expense of smaller ones due to differences in surface free energy, which facilitates the transport of mobile species between particles. Conversely, particle migration occurs as nanoparticles move via Brownian motion, potentially leading to coalescence when particles come into close contact. This agglomeration process is commonly understood to occur in three stages: first, Ostwald ripening is the dominant process, and the smallest nanoparticles disappear. Once the smallest particles have vanished, both Ostwald ripening and coalescence contribute to further particle growth until reaching a size at which their mobility significantly reduces. Smaller particles exhibit greater mobility compared to larger ones, and as particles increase in size, sintering decelerates. These phenomena are affected by the environment of the nanoparticles and are initiated by elevated temperatures. In fact, gold particles deposition is particularly challenging due to this agglomeration, forming larger particles with reduced catalytic activity [127,137–142].

The parameters influencing this agglomeration is:

- The interaction between gold and the support. To prevent agglomeration, creating strong bonds that limit the mobility of the atoms is an effective method. This is indeed why covalent bonds with the surface produces more stable gold NP compared to ionic bonds, as for ionic bonds, particle migration is more likely, leading to their agglomeration [127,137–139].
- The proximity of gold particles on the surface. This can be managed by decreasing their surface concentration or creating steric or electrostatic stabilization by adding molecules that adsorb onto the gold particle surface [127,137–140].
- The presence of chloride. Chloride favours NPs aggregation during thermal treatment by promoting the mobilization of gold atoms. Therefore, it is important to ensure chloride removal during catalyst preparation by using multiple washing steps or hydrogen reduction treatment [127,140].

3.1.2.3. Differences and similarities between exposed and non-exposed samples

Understanding the deposition mechanism of gold on the surface of an oxide support allow to comprehend why, for a same exposure time, there is no significant difference in the quantity of deposited gold between exposed and

non-exposed samples. The primary factor influencing gold deposition is the pH of the medium, as it affects the nature of the (dominant) gold complex(es) present and the amount of OH groups at the surface of the support. In our case, the pH difference between exposed and non-exposed sample is small. While this may results in some differences in the nature of the (dominant) gold complex(es) formed, as illustrated in Figure 6.8, it is likely insufficient to significantly affect the quantity of OH groups on the surface of the support. Consequently, the amount of gold complexes that bind to the support surface remains relatively unchanged.

Given that the gold deposition mechanism is fast and the surface rapidly becomes saturated with gold complexes, this explains why, after a certain period of (non-)exposure, the amount of deposited gold no longer increases. Indeed, as shown by ICP analysis, between 7, 15 or 30 min of exposure, the quantity of deposited gold does not increase, and extending the exposure time only have impacted the agglomeration of gold particles.

If we now focus on the reason why GP synthesis seems to produce larger gold particles, several hypotheses can be evoked:

- The pH of the solution, lower after plasma exposure, results in the higher presence of $[AuCl_3(OH)]^-$ species. However, these species cannot achieve 2 chemcial bonds, as mentioned in Part III, Chapter 6, section 3.1.2.2, which are considered more stable due to reduced mobility of gold complexes on the surface of the support. Therefore, the slightly higher pH in non-exposed samples could lead to more 2 chemical bonds and thus more stable particles compared to plasma-exposed samples, increasing the amount of small particles remaining at the surface of the solid.
- The quantity of gold present on the support surface also impacts the particles agglomeration. At lower pH, primarily monodentate bonds form, as fewer $[AuCl_2(OH)_2]^-$ species are present. A monodentate bond involves one OH group from the surface binding to one gold complex, whereas a bidentate bond involves two OH groups binding to one gold complex. This implies that at lower pH, more gold might be deposited on the surface, particularly with more Cl groups, leading to a higher probability of agglomeration, as mentioned in Part III, Chapter 6, section 3.1.2.2.
- The plasma itself could influence particle agglomeration. It has been previously reported that plasma can reduce metallic components grafted on the surface of a support [143]. Furthermore, in previous Part I, Chapter 2, section 3.2, we demonstrated that complexes from

the dissolution of $HAuCl_4$ exposed to the GP can be reduced to form pure Au^0. However, when gold is present as a pure metal rather than in a complex form, its mobility increases, as mentioned in Part III, Chapter 6, section 3.1.2.2, potentially leading to more marked agglomeration. Thus, for exposed samples, the particles may already begin to reduce and agglomerate before the drying step, resulting in larger particles compared to non-exposed samples, for which reduction occurs primarily during the drying step.

3.1.2.4. Catalytic activity

Looking at the catalytic activity of a selection of synthesized solids for the total oxidation of benzene, after more than 7 min of exposure, the catalysts exhibit the same catalytic activity as pure P25. For samples synthesized for 7 min, both show better catalytic activity than pure P25, with the non-exposed sample demonstrating the highest activity (Figure 6.10).

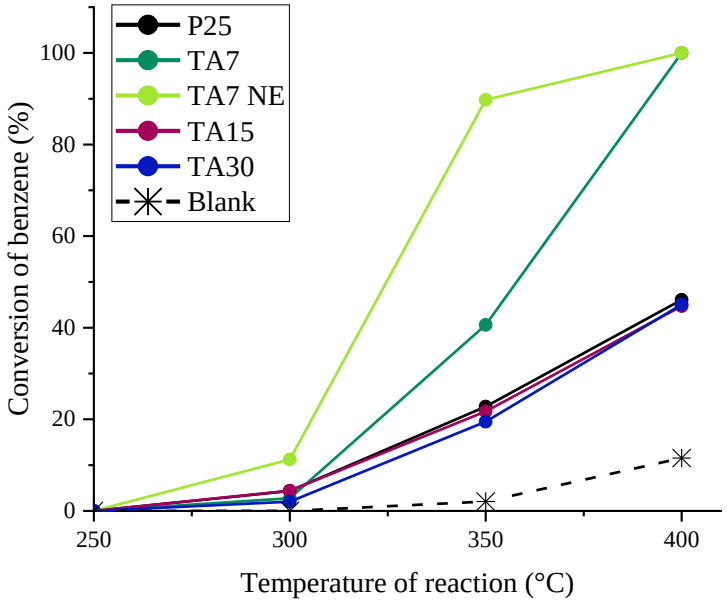


Figure 6.10: Catalytic performances of Au/TiO_2 solids obtained after (non-)exposure to the GP for the total oxidation of benzene (conversion of benzene as function of reaction temperature)

This can be explained by previous observations. The literature indicates that the size of gold NPs on a support influences the catalytic activity of the solid. When the size of gold NPs exceeds 5 nm, their activity becomes mostly negligible [141]. Our characterization and hypotheses suggest that samples exposed for more than 7 min have likely increased the size of their particle

rather than the amount of gold they contain. Additionally, it has been observed that plasma exposure during synthesis tends to agglomerate the gold particles. This explains why TA7 NE is the best catalyst compared to TA7.

3.2. Au/SnO_2 – 2 steps

3.2.1. First observations

The precursor solution is already acidic before plasma exposure due to the spontaneous formation of $Sn(OH)_4$ and $Sn_3O(OH)_2SO_4$ which release H^+ ions in the medium when $SnSO_4$ is dissolved in water (Part II, Chapter 3, section 3.1.2: Eq.3.6, Eq.3.7) (Table 6.8) [86,111,113,121]. Plasma exposure further acidifies the solution by generating acidic species during the discharge [33,48,49]. Adding the gold precursor slightly increases the pH of the suspension, as $HAuCl_4.3H_2O$ has its pKa around 3.3 and acts as a buffer (Table 6.8). Without plasma exposure, the pH remains approximately the same, but it increases slightly after plasma exposure, likely due to the buffering effect of HNO_2/NO_2^- species (pKa=3.3) [114]. For SA suspension, the amount of H^+ produced seems to be too large for the HNO_2/NO_2^- buffer to be effective (Table 6.8). This is likely because the initial concentration of $SnSO_4$ is 3 times higher than in the other solutions, releasing even more H^+ during its transformation.

Table 6.8: pH of the Au + SnO_2 – 2 steps suspensions before and after (non-)exposure to the GP

	pH before 2h (non-) exposure	**pH after 2h (non-) exposure**	**pH before 2th (non-)exposure (after adding $HAuCl_4.3H_2O$)**	**pH after 2th (non-)exposure (after adding $HAuCl_4.3H_2O$)**
Sn	2.7	2.1	/	/
Sn NE		2.5		
SA 15	2.4	/	/	1.7
SA30	2.3	/	/	1.7
SAWD7	2.5	2.2	2.8	3.1
SAWD7 NE				2.8
SAWD15	2.5	2.2	2.6	3.1
SAWD15 NE				2.6
SAWH7	2.6	2.3	2.6	2.8
SAWH7 NE				2.7
SAWH15	2.4	2.2	3.0	3.0
SAWH15 NE				2.9

The XR diffractograms of all the synthesized solid reveal the presence of the cassiterite SnO_2 phase (Figure 6.11, Figure 6.12, Figure 6.13, Figure 6.14). In the case of $SnSO_4$ alone, non-exposed to the plasma, the $SnSO_4$ phase is also identified, likely due to a proportion of the precursor remaining untransformed (Figure 6.11). Furthermore, except for SA15 and SA30, the Au^0 phase is detected in all the solids (both exposed and non-exposed to the plasma) where the gold precursor was incorporated in their synthesis, with more intense peaks observed in the exposed samples (Figure 6.12, Figure 6.13, Figure 6.14).

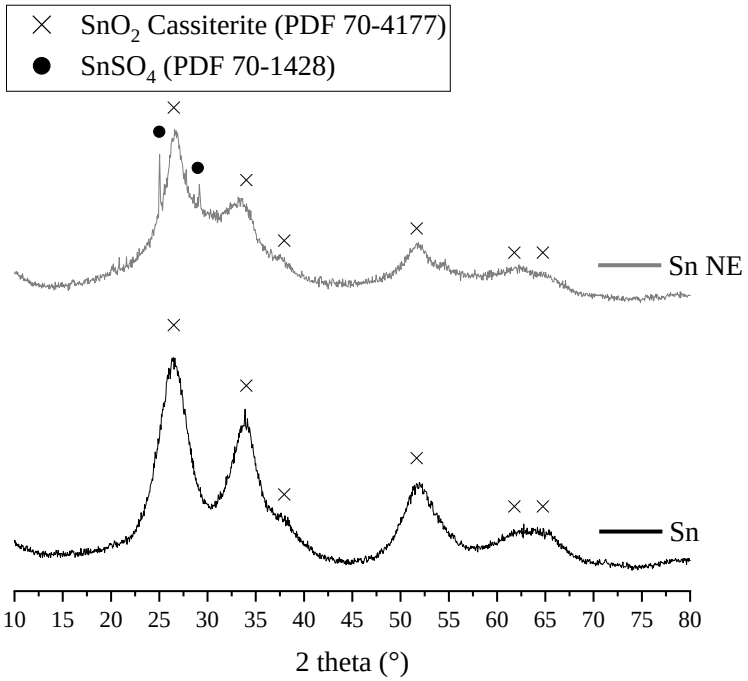


Figure 6.11: XRD data of Sn and Sn NE solids

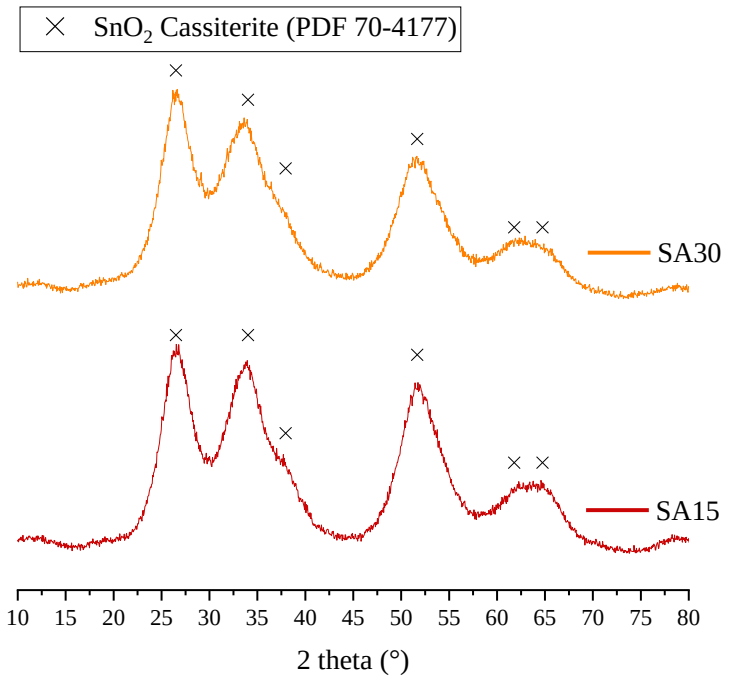


Figure 6.12: XRD data of SA15 and SA30 solids

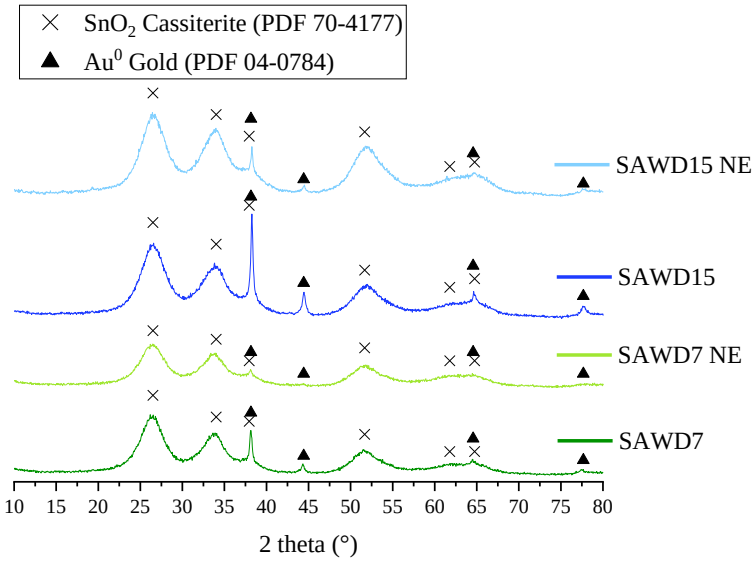


Figure 6.13: XRD data of SAWD solids

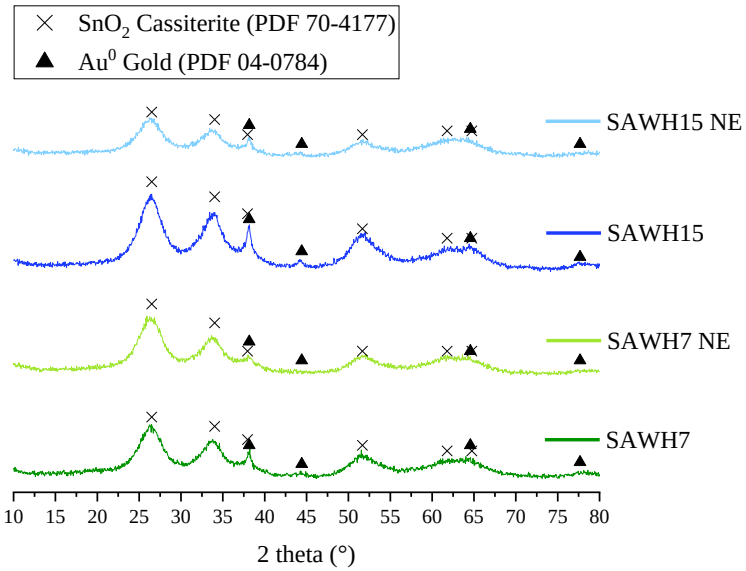


Figure 6.14: XRD data of SAWH solids

By examining the surface and bulk composition of the samples using XPS, we can deduce several things (Table 6.9). First, the composition of the support does not seem to change with the addition of gold precursor, as the at % of Sn and O remain approximately constant whatever the synthesis types. Furthermore, the at % of S is < 1% for all the solids, except for the SA samples. This is likely because the initial concentration of $SnSO_4$ is too high, resulting in a lower conversion compared to the other samples.

However, there are notable differences in the gold content among the various solids (Table 6.9). According to XPS, the at % of Au is much lower for the SA samples, where no washing step was performed before adding the gold precursor. For SAW samples, the at% of gold in XPS increases with the exposure time and is higher when no drying step is performed before adding the gold precursor. Therefore, the Au/SnO_2 mass ratio is higher for SAWH samples but is still < 1%, far from the nominal 3%. However, from ICP results, the mass % does not appear to increase with the exposure time but is also higher for SAWH samples. Finally, slightly more Au is detected on the surface and in bulk of the exposed samples compared to non-exposed ones.

Table 6.9: XPS and ICP data of Au/SnO_2 – 2 steps solids obtained after (non-)exposure to the GP

	Sn*	**Au**				**O***	**S**		**Mass ratio Au/SnO_2 (% mass)**	
	XPS (Sn 3d) (% at)	**XPS (Au $4f_{7/2}$)**			**ICP (% mass)**	**XPS (% at)**	**XPS (S 2p)**		**XPS**	**ICP**
		FWHM	**E_b (eV)**	**(Au 4f) (% at)**			**E_b (eV)**	**(% at)**		
Sn	37.0	/	/	/	/	62.8	169.3	0.3	/	/
SA 15	35.4	1.75	84.4	0.17	/	61.6	169.1	2.9	/	/
SA30	35.8	/	/	0	/	61.6	169.3	2.6	/	/
SAWD7	36.0	1.45	83.4	0.40	2.1	63.1	169.1	0.5	0.5	2.1
SAWD7 NE	37.5	2.06	83.9	0.24	/	61.9	168.9	0.4	0.3	/
SAWD15	38.0	1.41	83.4	0.46	2.1	60.8	168.6	0.7	0.6	2.1
SAWH7	37.6	1.36	83.5	0.55	2.3	61.5	168.8	0.4	0.7	2.3
SAWH7 NE	36.9	1.38	83.5	0.59	1.7	61.6	168.9	1.0	0.8	1.7
SAWH15	37.8	1.35	83.7	0.64	2.3	61.1	169.1	0.5	0.8	2.3
SAWH15 NE	37.2	1.44	83.6	0.58	2.0	61.9	168.3	0.3	0.8	2.0

***** *The % mass of Sn and O were not determined by ICP due to our inability to completely dissolve the SnO_2 before analysis*

Regarding the textural properties of the catalysts, they all exhibit an isotherm corresponding to microporous solids (Supplementary information SI.18). Therefore, the microporous volume was calculated using t-plot method. All of the solids, except for the SA ones, have approximately the same specific surface area, around 170 m^2/g, and microporous volume of about 0.07 cm^3/g (Table 6.10). These values are similar to those of the solid synthesized with only $SnSO_4$, indicating that suspending and re-exposing the material to plasma in presence of gold precursor has no significant effect on its textural properties. However, the solids from SA synthesis, which were prepared without washing before adding the gold precursor have a smaller specific surface area than the others (Table 6.10). We verified through additional experiments that the high concentration of $SnSO_4$ prevents the solid from developing to the extent typically achieved.

Table 6.10: Textural properties obtained by N_2-physisorption of Au/SnO_2 – 2 steps solids obtained after (non-)exposure to the GP (isotherms Supplementary information SI.18)

	Specific surface area (m^2/g)	**Microporous pore volume (cm^3/g)**
Sn	150	0.071
SA 15	76	0
SA30	21	0
SAWD7	154	0.067
SAWD15	174	0.075
SAWH7	167	0.067
SAWH7 NE	196	0.075
SAWH15	174	0.075

3.2.2. Discussion

3.2.2.1. Mechanism of gold deposition

SnO_2 is not a common support used for the deposition of gold, so there is limited information about it in the literature. However, since SnO_2 is a metal oxide and previously discussed deposition mechanism having been shown to be generalized for different types of oxides (such as TiO_2 and Al_2O_3), we can consider using a similar approach with SnO_2.

To understand the deposition mechanism on this support, we need to consider factors that have already been identified as important:

- The PCZ of SnO_2 cassiterite is around 4-4.5, which is lower than TiO_2 [144]. This means that SnO_2 will have more OH group on its surface

than TiO_2 at the pH we are working at. This suggests that more gold complexes would be able to bind at the surface of SnO_2 than TiO_2.

- The initial pH with SnO_2 support is slightly lower than with TiO_2 when gold precursor is added. This means that slightly more $[AuCl_3(OH)]^-$ than $[AuCl_2(OH)_2]^-$ is present in the SnO_2 suspension than in TiO_2 one. As seen in Part III, Chapter 6, section 3.1.2.2, this means that less chemical bonds between a single gold complex and the surface are formed [133,136].

3.2.2.2. Difference between exposed and non-exposed samples

With these 2 previously proposed clues, we can explain some of the observed differences in our samples. Firstly, after plasma exposure, the final pH of the SAW samples is slightly higher and closer to the PZC of SnO_2 than without exposure. This indicates an increase in the number of OH groups on the surface of the support and a higher concentration of $[AuCl_2(OH)_2]^-$ species in the suspension. Intuitively, this would mean plasma exposure both increases the amount of gold deposited on the surface and the number of 2 chemical bonds formed, enhancing the stability of the Au NPs. Consequently, we would expect to observe a higher mass % by ICP and higher at % of Au by XPS for the exposed samples, as the gold particles are more abundant and well-dispersed compared to those without exposure. This is indeed what we observed in most of the samples.

However, this explanation considers only the pH of the medium in the deposition mechanism of gold particles and not the effect of the plasma, which may partially pre-reduce the gold particles and lead to their agglomeration even before the drying step, as previously suggested in the Part III, Chapter 6,section 3.1.2.3. This latter hypothesis might explain why the SAWH7 solid has less gold detected on its surface than SAWH7 NE, suggesting that even though a higher quantity of gold is deposited due to the pH being closer to the PZC, the plasma exposure would cause particles agglomeration, resulting in larger particles in this sample when exposed to the plasma. This may indeed explain why the gold peak detected by XRD is sharper and more intense for all the exposed samples, as such peaks are typically observed when larger particles are present in the solid.

It is worth nothing that for the SAW samples, the differences in the binding energy and FWHM of Au $4f_{7/2}$ peak are not significant enough to conclusively determine the particles size, except for SAWD7 and SAWD7 NE. In these cases, the lower FWHM for the exposed sample could suggest larger particles, but this does not align with the higher at % of gold detected on the surface.

3.2.2.3. Difference between SA, SAWD and SAWH samples

The SA samples exhibit characteristics clearly different from the SAW samples. We previously mentioned that the initial concentration of $SnSO_4$ used, which is 3 times higher in these samples, influences the textural properties of the formed SnO_2. Additionally, the SnO_2 synthesized in these samples is not washed, and the gold precursor is directly added to the pre-exposed solution where untransformed $SnSO_4$ remains. XPS analysis reveals that this impacts the at % of elements present on the surface. Almost no gold is detected when the suspension is exposed for 15 min, and none for 30 min. The hypothesis for this observation is that gold precipitates quickly onto the support when added to the suspension, but the residual $SnSO_4$ in the solution can still precipitate and likely covers the Au particles formed. Consequently, these gold particles become trapped within the bulk of the support, creating an "egg-white" solid. These observations led us to conclude that a washing step was necessary before adding the gold precursor.

Regarding the SAWD and SAWH samples, similar to the Au/TiO_2 samples (Part III, Chapter 6, section 3.1.2.1), increasing the exposure time does not seem to affect the amount of gold deposited, as the mass % remains the same between 7 and 15 min of exposure. We might have expected that, as with Au/TiO_2 samples, increased exposure time would enhance the agglomeration of the particles. However, since the at % measured by XPS is higher with longer exposure time, this does not appear to be the case. However, it is challenging to draw conclusions about the particle size based solely on XPS analyses. To confirm these hypotheses, Transmission Electron Microscopy (TEM) images would have been valuable.

There are some differences between SAWD and SAWH samples. Notably, the amount of gold detected by ICP and XPS is higher for SAWH than in SAWD samples. This could be because there is more gold on the surface and/or because the particles are better dispersed. We have observed that increasing the amount of gold deposited on the surface of a support largely depends on the amount of OH groups present on the surface. Therefore, it is plausible that samples dried before being resuspended with the gold precursor have fewer OH groups than humid samples. In fact, previous studies in literature have examined the impact of prolonged exposure time of a solid to the plasma discharge on the formation of OH groups on its surface. By exposing smectite clay and SnO_2 materials to the discharge for extended periods, it was discovered that the breakdown of the Si-O-Si, Si-O-Al, or Sn-O-Sn bonds leads to the formation of new surface hydroxyl groups Sn-OH (Eq.6.5) [25,56]

$$Sn - O - Sn + OH \rightarrow Sn - OH + Sn - O \qquad (Eq.\,6.5)$$

However, performing a drying step may remove some of these newly formed OH groups, which are useful for depositing more gold particles. Therefore, omitting the drying step before adding the gold particles might be an effective way to preserve the OH groups created by plasma exposure, thus increasing the amount of gold deposited.

3.2.2.4. Catalytic activity

Looking at the catalytic activity of selection of synthesized solids for the total oxidation of benzene, except for the SA samples, they all have a better activity than the solid obtained when $SnSO_4$ is exposed alone (Figure 6.15). This was expected for the SA samples since the gold is completely covered by SnO_2, and the specific surface area developed is much lower than that of the Sn sample. The activity for the samples dried before the addition of the gold precursor (SAWD) is slightly better than Sn, but no difference is observed among the SAWD samples with different exposure times (Figure 6.15). The difference in catalytic activity is most notable for the SAWH7 and SAWH7 NE samples, where the non-exposed solid exhibits the best performance among them (Figure 6.15). As expected, since the SAH samples exhibit a higher quantity of well-dispersed gold at their surface, they have better catalytic activity than the SAWD samples. The washed and humid sample, SAH15, has almost the same activity as the SAWD samples, indicating that increasing the synthesis time for these samples decreases their catalytic activity (Figure 6.15).

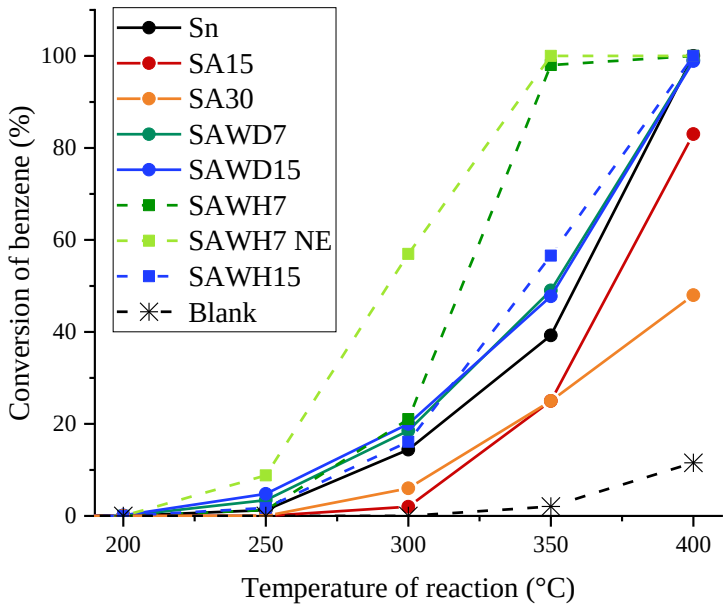


Figure 6.15: Catalytic performances of of Au/SnO_2 – 2 steps solids obtained after (non-) exposure to the GP in the total oxidation of benzene (conversion of benzene as function of reaction temperature)

As previously explained in the introduction of Part III, Chapter 6, the literature indicates that the size of gold NPs on a support influences the catalytic activity of the solid. When the size of gold NPs exceeds 5 nm, their activity becomes mostly negligible [141]. Our characterization and hypotheses with Au/TiO_2 samples suggest that samples exposed for more than 7 min most likely increase the size of their particles rather than the amount of gold they contain (Part III, Chapter 6, section 3.1.2.1). However, for Au/SnO_2 samples, we cannot draw the same conclusion, as the at % of gold detected by XPS increases with the exposure time without changing the amount detected in bulk. This would in principle imply an increase in distribution and, therefore, a decrease in particles size. Normally, we would expect that samples exposed 15 min would have better catalytic activity. However, as mentioned before, it is difficult to conclude something about the size of the gold NPs based solely on XPS results. TEM analyses would have been more helpful in understanding these results.

Additionally, it has been observed for Au/TiO_2 samples that plasma exposure during synthesis tends to agglomerate the gold particles (Part III, Chapter 6, section 3.1.2.1). Again, this does not seem to be the case with Au/SnO_2 samples, as the non-exposed samples have less gold detected on their surface,

reflecting a less well-dispersed particles and, therefore, larger gold particles, which would normally mean less catalytic activity for the non-exposed samples.

Therefore, explaining why the SAWH7 NE sample is more active than SAWH7 sample is difficult with only the characterizations presented here. TEM characterization would have been necessary to determine if their difference comes from the size of the deposited gold NPs or not.

3.3. Au/SnO_2 – 1 step

As observed for Au/SnO_2 – 2 steps, the pH of the solution increases a little bit with and without exposure, probably due to the buffer effect of $HAuCl_4$ and/or the HNO_2/NO_2^- species created by GP (Table 6.11).

Table 6.11: pH of the Au + SnO_2 – 1 step suspensions before and after (non-)exposure to the GP

	pH before exposure	pH after exposure
SAOP7	2.1	2.8
SAOP7 NE		2.4
SAOP15	2.3	2.3
SAOP15 NE		2.5

The XR diffractograms of all the synthesized solid are composed of the cassiterite SnO_2 phase and Au^0 phase. However, the gold peaks are more intense in the non-exposed samples, which is the opposite of the trend observed for the 2-steps samples (Figure 6.16). This may be due to a greater amount of gold precipitate forming without GP exposure or the formation of more crystalline particles. For exposed samples, $SnSO_4$ phase is also identified, likely resulting from a portion of the precursor that did not have enough time to be transformed.

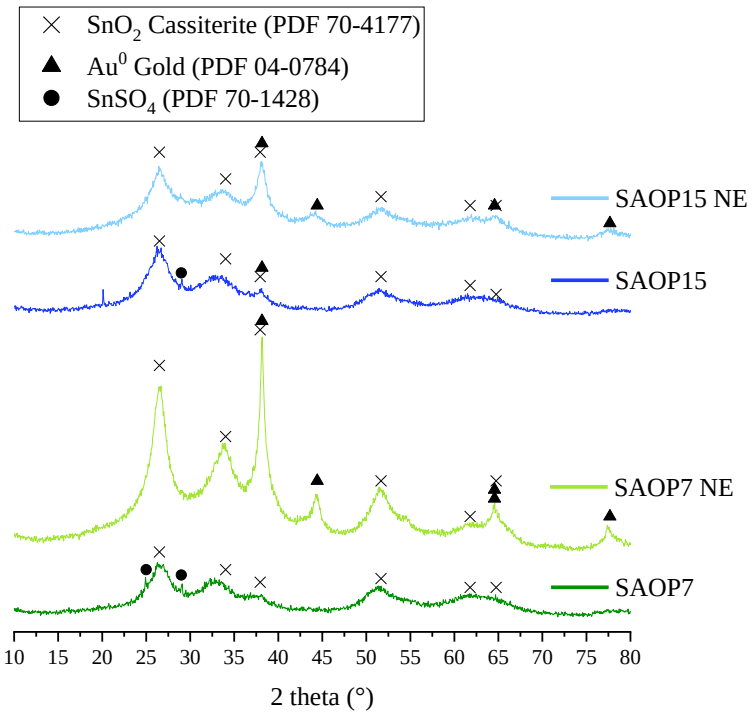


Figure 6.16: XRD data of SAOP solids

By examining the surface composition of the samples using XPS, we can see that the amount of S remaining in the solids is significantly higher than in previous SA samples (Table 6.12). This is likely because the maximum exposure time here is only 15 min, compared to at least 2h for the Au/SnO_2 – 2 steps samples, meaning that $SnSO_4$ has less time to be transformed into tin oxides. This aligns with the position of the S 2p peak, which corresponds to the SO_4^{2-} group. Furthermore, XPS analysis shows an Au at % of 0 for each sample, indicating that no gold is present on the surface of the solid. However, ICP analysis confirms the presence of gold within the sample, with a mass % exceeding the targeted 3%.

In the one pot synthesis, since both gold and tin precursors are added simultaneously and exposed together to the GP, we might have expected such a result (Table 6.12). In fact, in previous observations, Part III, Chapter 6, section 3.1.2.1, we deduced that the precipitation time of the gold precursor is much smaller than that of $SnSO_4$. This suggests that the Au that precipitates during the exposure is gradually covered by SnO_2, which takes longer to be synthesized. Consequently, the resulting solid is primarily composed of SnO_2, with the gold NPs trapped inside.

Table 6.12: XPS data of Au/SnO_2 – 1 step solids obtained after exposure to the GP

	Sn*	Au		O*	S	
	XPS (Sn 3d) (% at)	XPS (Au 4f) (% at)	ICP (% mass)	XPS (% at)	XPS (S 2p)	
					E_b (eV)	(% at)
SAOP 7	38.0	0	4.1	59.9	169.3	5.1
SAOP 15	39.7	0	4.6	55.5	169.3	4.8

** the % mass of Sn and O were not determined by ICP due to our inability to completely dissolve the SnO_2 before analysis*

Regarding the textural properties of the catalysts, they all exhibit an isotherm characteristic of mesoporous solids, with a low specific surface area (Supplementary information SI.19, Table 6.13). This is likely due to the exposure time not being long enough to allow the development of the textural properties previously obtained for SnO_2 solid.

Table 6.13: Textural properties obtained by N_2-physisorption of Au/SnO_2 – 1 step solids obtained after exposure to the GP (isotherms Supplementary information SI.19)

	Specific surface area (m^2/g)	Pore volume (cm^3/g)
SAOP7	50	0.14
SAOP15	34	0.12

Concerning the catalytic activity of these SAOP solids, they are both less catalytically active than SnO_2 synthesized by simply exposing $SnSO_4$ to the plasma discharge (Figure 6.17). This is expected, as the gold particles are trapped inside the SnO_2 and therefore cannot contribute to the catalytic activity of the solid. Furthermore, since the precursors are only exposed for a maximum of 15 min, the final solid obtained has less favorable textural properties than when we exposed $SnSO_4$ to the GP for 2h, resulting in a lower specific surface area and consequently less catalytic activity.

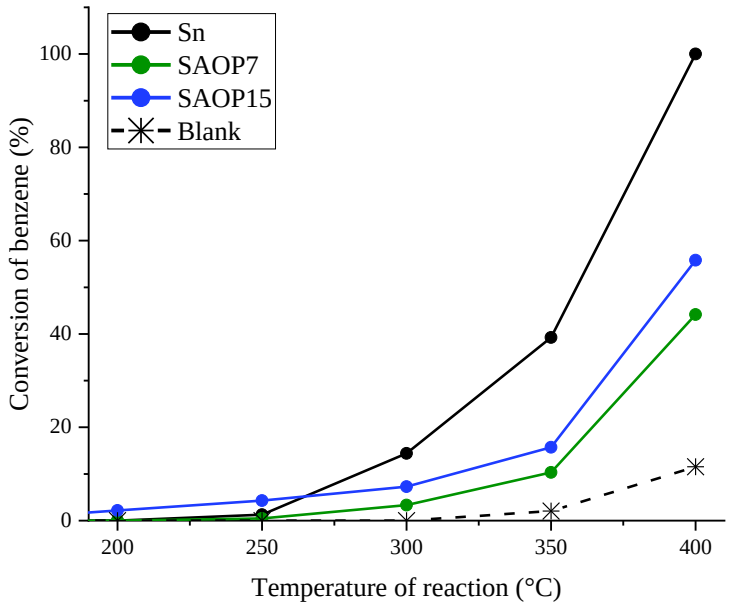


Figure 6.17: Catalytic performances of Au/SnO_2 – 1 step solids obtained after exposure to the GP for the total oxidation of benzene (conversion of benzene as function of reaction temperature)

4. Conclusion

Given that metal-supported catalysts had not been synthesized before by GP in the literature and that we discovered the possibility of synthesizing certain gold-based catalysts by GP (Part I, Chapter 2, section 3.2), we attempted to develop the synthesis of Au/TiO_2 and Au/SnO_2 catalysts by GP.

By understanding the mechanism of gold deposition on the surface of metal oxide, we identified that the GP deposition method of TiO_2 presents a big issue mainly related to the pH of the medium. During the exposure, acidic species are produced, causing the pH of the medium to decrease rapidly to around pH 3, or even lower if an acidic precursor is present, as is the case with $HAuCl_4$. However, the optimal way to deposit a large amount of gold with strong bonds, which increases their stability and decreases the size of the NPs, is to maintain at higher pH, close to the PZC of the support. At this pH level, the number of OH groups on the surface is at its maximum, allowing more gold complexes to bind to the surface. Furthermore, at lower pH, fewer $[AuCl_2(OH)_2]^-$ species are present compared to $[AuCl_3(OH)]^-$, meaning that fewer bidentate bonds can be formed, which are crucial for providing higher stability to the gold NPs. This poses an issue in further steps like drying, which enhances the agglomeration of gold NPs and therefore decreases their catalytic activity.

Additionally, apart from the pH issue, plasma can potentially pre-reduce the gold NPs on the surface of the solid, causing them to agglomerate before the drying step, thereby increasing the issue in the synthesis of Au/TiO_2 catalysts by GP.

Since we currently do not control the pH of the medium during the exposure, the only adjustment we can make in gold-deposition by GP is to use a support with a lower PZC. This would allow for more OH groups on the surface of the support, potentially increasing the amount of gold deposited and enhancing their stability. This is one of the reasons why SnO_2 was considered as a support, in addition to its potential to be synthesized by GP.

Contrary to what was observed with TiO_2 as support, in the case of SnO_2, the pH of the medium is higher and closer to the PZC of the support when exposed to the GP. This is due to the lower PZC of SnO_2 and the lower initial pH of the solution compared to TiO_2, which increases with the exposure due to the buffering effect of HNO_2/NO_2^- species created by GP. Therefore, this seems to influence the deposition of gold on SnO_2 by increasing the amount that can bind to the surface and create more bidentate bonds.

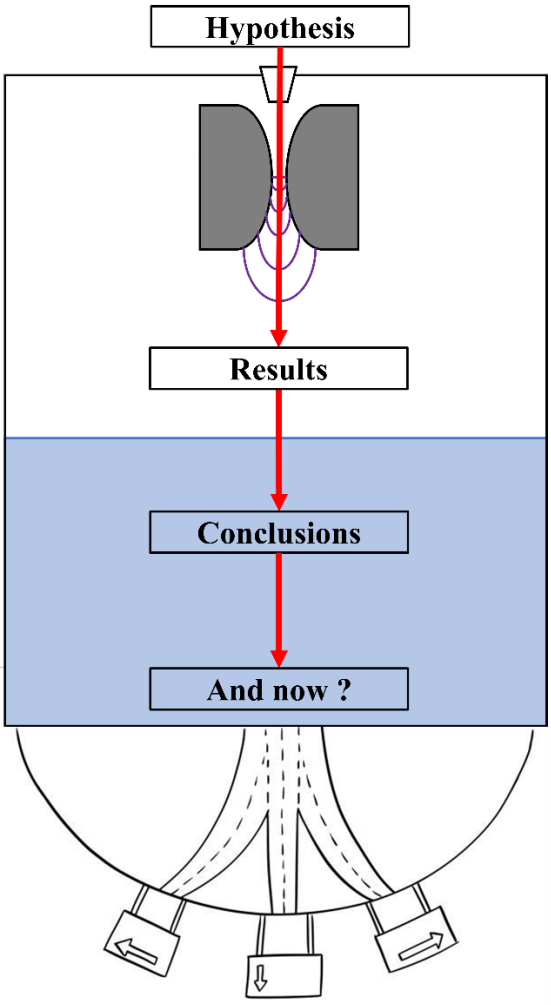
Although the deposition of gold on SnO_2 works better than on TiO_2, we have identified a critical step in creating effective Au/SnO_2 catalysts. This is the washing of the pre-synthesized support before adding the gold precursor, to prevent the covering of the gold by the residual $SnSO_4$ that has not yet reacted. Furthermore, it appears that not drying the pre-synthesized support before adding the gold precursor is also beneficial, as it allows the deposition of more gold thanks to the OH groups developed during the exposure that do not disappear during the (absent) drying step. We would have expected that gold NPs deposited by GP would be more numerous and smaller, thereby providing better catalytic activity than the non-exposed solid, but this is not the case. It is possible that, as previously mentioned for Au/TiO_2 solids, the plasma potentially pre-reduces the gold NPs on the surface of the solid, causing them to agglomerate before the drying step. However, to confirm this hypothesis, TEM characterization would have been necessary.

Finally, we attempted a one-pot synthesis of supported catalysts, but this method is not suitable for Au/SnO_2 solids because the precipitation times for the gold NPs and the SnO_2 support differ too much, particularly because the gold precipitates more quickly than the support. This might have been less an issue if the support formed more rapidly than the metal, as the support would have had the time to develop its beneficial properties before that the metal

begins to precipitate, increasing the likelihood of it being deposited on the surface of the pre-formed support.

In conclusion of this chapter, we have successfully developed supported gold catalysts on 2 types of support: P25 and plasma-synthesized SnO_2. However, the current synthesis conditions in GP synthesis pose challenges in the formation of these catalysts, particularly due to the acidification of the medium during the exposure, which has not yet been controlled. Since gold deposition is highly dependent on this parameter and the number of supports with a low PZC is limited, synthesizing effective gold-supported catalysts by this method seems challenging, at least without changing the existing synthesis conditions. However, we previously discovered in Part I, Chapter 2, section 3.2, that Ru-based catalysts can also be synthesized by GP. Therefore, it might be possible to attempt the formation of some Ru-supported catalysts by GP.

General conclusion and future works



As mentioned in the general introduction, the GP catalysts synthesis has emerged as an intriguing method for producing interesting catalysts while using attractive conditions compared to traditional synthesis approaches. However, until now, the method has been somewhat enigmatic, with limited understanding of the underlying solids formation mechanisms and how the conventional GP synthesis conditions could be modified to enhance catalysts performance, as well as the economic and ecological aspects of the process.

The first goal of this thesis was to improve the more complete understanding of the GP synthesis method. We began to identify the primary plasma species responsible for precipitating the precursors exposed to the discharge. Contrary to what was stated in the literature before, we discovered that OH radicals are not responsible for oxidizing the exposed precursors. Instead, we found that long-lived species, particularly HNO_2 and/or NO_2^-, are the main active agents. Additionally, we observed that oxygen-based species significantly impact the reaction. In fact, when pure O_2 is used instead of humid air as plasma gas, the yield of the solid formed increased.

We also wanted to investigate the parameters influencing the ability of specific precursors to react by humid air GP, leading to the precipitate formation. The aim was to deepen our understanding of the method, ultimately enabling the synthesis of a broader range of catalysts and increasing the interest of GP as an innovative catalyst synthesis method. Several factors were identified as key in determining the ability of a precursor to react, including medium pH, potential of redox reactions, nature of the metal precursor and the solubility of both precursor and precipitate. These identified factors allowed us to create a dichotomous key for anticipating the potential reaction and precipitation of any precursor exposed to the GP. By utilizing this key, we identified 2 new precursors that react by GP, leading to the formation of new types of solids never before synthesized by this method: Au and Ru-based solids. This demonstrates the GP's potential as a promising method for developing new types of catalysts, such as metal-supported catalysts.

The second goal of the thesis was to enhance the economic and ecological viability of the GP synthesis by improving the characteristics of the synthesized solids and/or refining the synthesis conditions. To achieve this, we proposed three approaches: the PT step, the no cooling system, and the PAW. Both the PT step and the no-cooling system proved promising for developing catalysts with desirable characteristics.

Depending on the precursor used, adding a PT step (at AT or 100°C) and/or utilizing the no cooling system helped develop catalysts with improved characteristics, such as more catalytically active phases and increased specific surface area, which in turn boosted their catalytic activity. We discovered that the PT step primarily consists in a maturation step, which can be accelerated by adding heat, leading us to the idea of using the no-cooling system. This system is particularly intriguing as, depending on the precursor, it can sometimes develop similar characteristics to those obtained through the PT step, but with a significant reduction in synthesis time and thus energy consumption. Finally, we introduced the PAW synthesis and utilized the long-lived species generated in PAW, previously identified as triggering the precipitation process. Although we were able to precipitate solids under these conditions, their characteristics differed from those formed by direct exposure to the discharge due to a distinct precipitation mechanism.

In the final part of this thesis, we attempted to develop supported metal catalysts by GP, a task that had not been done before. We successfully developed gold-supported catalysts (Au/TiO_2 and Au/SnO_2). However, the current synthesis conditions in gold supported GP synthesis present challenges, particularly due to the acidification of the medium during the exposure, which remains uncontrolled. Since gold deposition is highly dependent on this parameter and that availability of supports with a low PZC required for depositing a higher amount of gold NPs is limited, synthesizing effective gold-supported catalysts by this method appears challenging, at least without changing the existing synthesis conditions.

So as a general conclusion, this thesis has significantly advanced our understanding of the GP catalysts synthesis method, shedding light on the "magical" aspects previously attributed to this process. We have established that plasma is a complex system, generating a variety of reactive species that can lead to multiple types of reactions. This complexity may introduce unique characteristics that would be impossible to achieve using chemical reagent synthesized through conventional methods, employed as the sole agent for the precipitation reaction of the metal precursor salt. However, along with this improved understanding, we have also identified the limitations of GP catalyst synthesis. Specifically, without altering the conventional synthesis parameters currently employed, it appears challenging to precipitate more solids beyond those already discovered in this research. Nevertheless, the discovery of these precipitates still allows the development in synthesizing

new types of catalysts, such as supported catalysts. Furthermore, although we proposed only three approaches to improve the synthesis conditions and/or the characteristics of the solids formed, there remains other opportunities to further improve the method.

With a deeper understanding of the impact of different aspects of the methods on catalysts synthesis, it is possible to explore various synthesis parameters to enhance our knowledge further, and eventually developing additional types of solids with novel properties.

In the first part of the thesis, we observed that using O_2 as a plasma gas appears to be a more effective way to increase the yield of precipitates formed. This suggests that further investigation into the effect of pure O_2 as plasma gas on the precipitation of solids could be highly beneficial. If another plasma gas source can develop similar catalysts while significantly increasing the yield, it could enhance the economic viability of the method. Additionally, just as we studied the species responsible for triggering the precipitation reaction when using humid air as plasma gas, it would be valuable to examine the species involved when O_2 is used. Preliminary experiments where water was exposed to plasma using O_2, followed by the addition of the precursor, resulted in similar precipitates as direct exposure, indicating that long-lived species are still playing a key role in the reaction, even with O_2. Therefore, identifying these species could help us understand which ones are responsible for triggering the reaction under these conditions. Moreover, as we identified several parameters affecting the precipitation with humid air as plasma gas, it would be interesting to see whether these parameters, such as the pH of the medium and potential of redox reactions between reactive plasma species, also matter when using O_2.

It is evident that forming every desired precipitate by GP is challenging without altering the current synthesis conditions. Based on the parameters we have identified as important in the reaction of the precursors, it would be worthwhile to modify the conditions, such as the medium's pH, the plasma gas, or the medium type, to explore the formation of other types of solids. For example, controlling the medium's pH is crucial, as the acidification that occurs during the exposure presents a significant challenge for precipitating certain oxides and hydroxides. Previous studies have shown that it is possible to control the pH of an aqueous solution exposed to the GP by using buffers stable to the discharge [145]. However, our preliminary work indicates that this is complicated, as it alters the species present in the system and may interfere with the HNO_2/NO_2^-

species formed, which are key to the reaction. We also found that the redox reaction between the precursor and HNO_2 and/or NO_2^- species is an important aspect to consider. If we later find that O_2 is more effective as a plasma gas and that other species are responsible for the reaction, it might be possible to trigger other types of redox reaction, potentially leading to the formation of solids that could not be produced through a redox reaction with HNO_2 and/or NO_2^- species. Finally, using water as medium also imposes limitation, such as the precursor that can be used (which needs to be soluble in water), the precipitate formed (which needs to be insoluble in water), and the species formed. Exploring the use of alternative media exposed to the plasma could expand the range of solids formed. However, this would complicate the system and might reduce the method's ecological benefits, which are more pronounced when using water compared to methods involving organic solvents.

The improvements proposed here have already shown promises in developing better catalysts. For example, the PT step, conducted at ambient temperature for 72 h and at 100°C for 3 h, proved to be effective in developing valuable characteristics in the plasma-synthesized solids. However, now that we understand that this step is a maturation process, we could explore optimizing it for each type of solid synthesized, adjusting conditions such as temperature, time, and atmosphere, to achieve specific desired characteristics. Furthermore, while long-lived species present during the PT step do not affect the phase transformation, they do influence the precipitation of remaining precursor, thereby increasing the yield. Therefore, it would be interesting to study the optimal exposure time for a specific precursor followed by the PT step, aiming to produce the most efficient catalysts while minimizing energy used and/or synthesis time.

Regarding the no cooling system, our studies so far have been conducted without temperature control. However, altering the temperature during the exposure could potentially lead to the development of different characteristics depending on the precursor used. This could be via reducing the temperature with a controlled cooling system or increasing it, tough the latter might pose issues such as solution evaporation and the loss of the "no energy input" benefit.

Other synthesis parameters could also be studied for the known reactive precursors. For example, we noted in the last chapter that the initial concentration of the precursor dictates the final solid formed (observed for $SnSO_4$). It would be interesting to investigate the impact of this parameter

but also others, such as exposure time, discharge voltage, air flow rate sent between the electrodes, etc. All of these factors likely influence the type of solid formed, its formation rate, and its yield, offering valuable insights for further method development. Furthermore, it would be interesting to examine how adding a porogen agent affects the textural properties of the developed solids, as this could enhance the range of properties achievable through GP catalysts synthesis.

Regarding potential improvements in GP catalyst synthesis through varied synthesis conditions, it would also be valuable to enhance our understanding of how these conditions do induce changes in the synthesized solids by using additional characterization methods. For instance, Dynamic Light Scattering (DLS) could be useful for measuring the size of the synthesized particles and assessing the effects of different conditions on their growth and/or agglomeration [146]. Additionally, identifying the phases developed in the solids could be refined by using techniques that provide more detailed structural and compositional information. Mössbauer spectroscopy, for example, is a powerful technique for examining the local atomic environment of elements such as iron and tin in solids, and giving information about electronic structure, phase composition and valence states of the element analyzed [147]. Auger Electron Spectroscopy (AES) can provide an additional detailed surface chemical composition and phase distinction for elements that exhibit overlapping XPS peaks [148]. For example, in materials containing tin, examining the Auger spectra of Sn allows differentiation between SnO and SnO_2 phases [105]. By implementing these advanced techniques, a more comprehensive analysis of GP-synthesized catalysts can be achieved, providing insights into both bulk and surface properties and improving control over synthesis outcomes.

Finally, in Part I, Chapter 2, section 3.2, we discovered that Ru-based catalysts can also be synthesized by GP. This opens the possibility of attempting to form Ru-supported catalysts by GP. Additionally, other supported catalysts could be developed, either entirely through GP (MnO_x/FeO_x, MnO_x/SnO_x, …) or by synthesizing a metal oxide by GP and then achieving a deposition to form a supported catalyst, using another method. However, as the range of solids that can be synthesized by GP is limited, it remains challenging to produce a wide variety of catalysts using only this method. Without changing the conventional synthesis conditions, we are restricted in the types of precipitates, and therefore the types of catalysts, that can be synthesized by GP. Therefore, it would be highly

valuable to investigate the other previously proposed parameters to potentially precipitate new types of solids, which could lead to the development of a wide variety of catalysts types.

From an industrial perspective, if the GP method becomes sufficiently promising for large-scale development, there may be opportunities to improve the reactor itself. Currently, the reactor used is a small volume batch reactor. It might be possible to increase the reactor's volume to synthesize larger amount of catalysts, but this would likely require changes to the electrodes system. Simply increasing the distance between the electrodes to enlarge the plume is not feasible, as it would require a higher voltage to maintain the arc, which could pose an issue. However, it is possible to create larger plume using gliding arc plasma with multiple electrodes, which has already been developed. Additionally, other types of plume, such as rotating arcs, have been developed and have shown promise in generating a greater number of plasma species, which could be advantageous for catalysts synthesis [33,43].

Furthermore, the current reactor used is a batch system, but for industrial-scale applications, a continuous reactor might be preferred. One could envision developing such a reactor for catalysts synthesis by, for example, using fixed electrodes while moving the precursor solution beneath the plume at a controlled rate (preferably slow to allow sufficient time for the species to react with the precursor). Alternatively, the precursor solution could be transported by the plasma gas, passing directly between the electrodes and coming into contact with the arc and the plume, potentially triggering new reactions or increasing the yield of the formed precipitate.

In conclusion, while it may initially seem challenging to scale up GP catalysts synthesis due to limitations in the types of solids that can be synthesized under current conditions, exploring different parameters could significantly enhance the method's potential. By developing new types of catalysts with specific characteristics, all while maintaining advantageous synthesis conditions, the GP method could become a more viable option for large-scale industrial applications.

Supplementary Information

SI.1. Calibration curves of $NaNO_2$ and $NaNO_3$ for NO_2^- and NO_3^- quantification

To quantify the concentration of NO_2^- and NO_3^- generated in demineralized water upon exposure to humid air GP, calibration curves were established using $NaNO_2$ and $NaNO_3$ solutions (Table SI.1). The absorbance spectra of these solutions, measured within the wavelength range of 200 to 260 nm, are illustrated in Figure SI.I.1a for $NaNO_3$ and Figure SI.I.1b for $NaNO_2$. For the determination of NO_2^- concentration, the absorbance intensity measurement was carried out at a wavelength of 240 nm, as it exhibits exclusive absorption at this wavelength. Meanwhile, the absorbance intensity of NO_3^- was recorded at 210 nm. However, given that both NO_2^- and NO_3^- absorb at this wavelength, an additional calibration curve for NO_2^- at 210 nm was established. This allowed for subsequent quantification to account for the contribution of NO_2^- absorption at this wavelength (Figure SI.1c).

Table SI.1: Concentration solutions of NO_2^- and NO_3^- for the calibration curves of NO_2^- and NO_3^-

Solution number	Concentration of $NaNO_2$ (mg/L)	Concentration of $NaNO_3$ (mg/L)
1	6.90	17.00
2	3.45	8.50
3	2.30	4.25
4	1.76	2.13
5	1.20	1.06
6	0.86	/

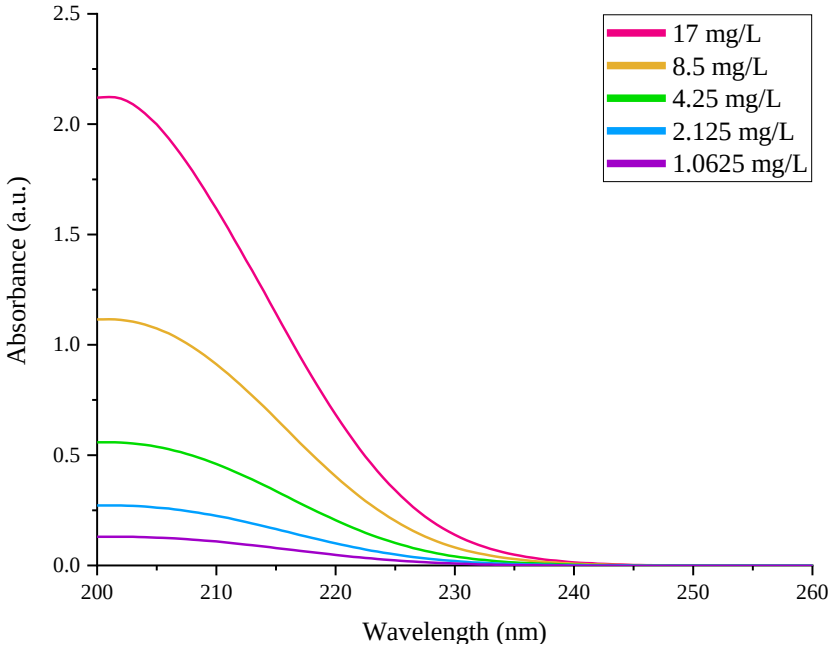


Figure SI.1a: Absorbance spectra of $NaNO_3$ solutions

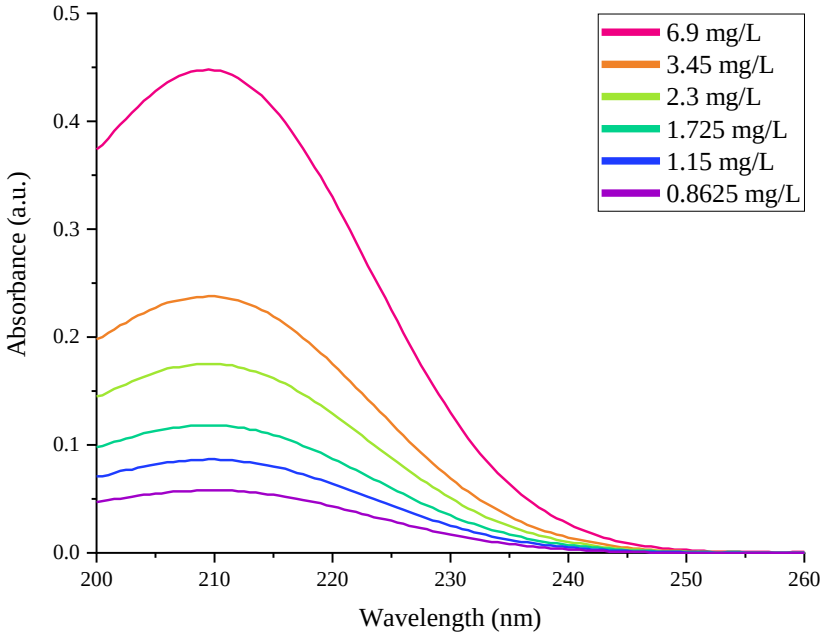


Figure SI.1b: Absorbance spectra of $NaNO_2$ solutions

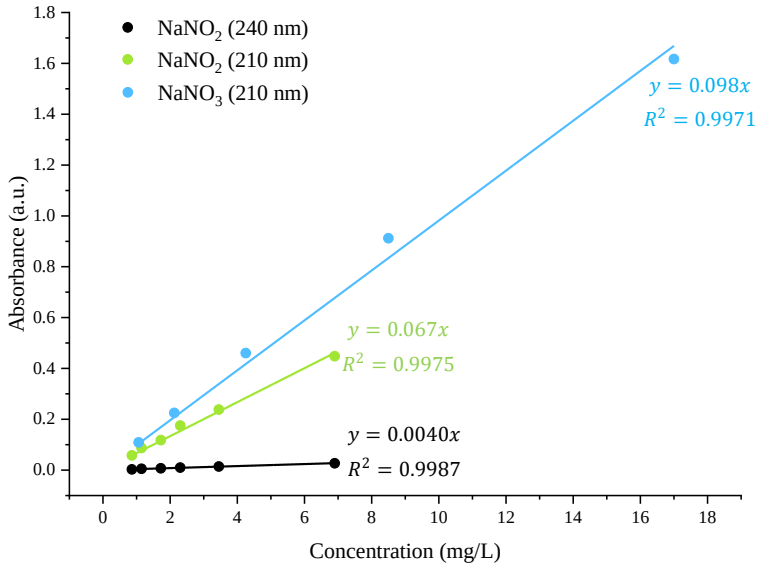


Figure SI.1c: Calibration curves of $NaNO_3$ and $NaNO_2$ solutions at 210 nm and 240 nm

SI.2. NO_2^- and NO_3^- quantification thanks to $NaNO_3$ and $NaNO_2$ calibration curves

We first conducted measurements on demineralized water subjected to GP exposure for 1h, with 15 min intervals. The resulting absorbance values recorded at wavelengths of 240 and 210 nm are presented in Table SI.2a.

Table SI.2a: Absorbance values at wavelengths of 240 and 210 nm of demineralized water subjected to GP exposure for 1h, with 15 min intervals.

Absorbance at	**Water 15 min diluted 8x**	**Water 30 min diluted 8x**	**Water 45 min diluted 8x**	**Water 60 min diluted 8x**
240 nm	0.036	0.059	0.085	0.092
210 nm	0.628	1.195	1.749	1.964

With reference to these measurements and the calibration curve established at 240 nm, as detailed in Supplementary Information SI.1, we are able to determine the quantity of NO_2^- generated as a function of the exposure time (Eq.SI.2a). Subsequently, utilizing this value in conjunction with the calibration curve established at 210 nm, also presented in Supplementary Information SI.I.1, we can compute the quantity of NO_3^- formed as a function of the exposure time (Eq.SI.2b). To obtain the accurate concentrations of both NO_2^- and NO_3^- within the medium, we need to multiply the obtained value by the corresponding dilution factor of 8 (Table SI.2b).

$$A_{240nm} = 0.004 * [NO_2^-]$$
$$\Leftrightarrow [NO_2^-] = \frac{A_{240nm}}{0.004} \qquad (Eq.SI.2a)$$

$$A_{210nm} = (0.0667 * [NO_2^-]) + (0.0982 * [NO_3^-])$$
$$\Leftrightarrow [NO_3^-] = \frac{\left(A_{210nm} - (0.0667 * [NO_2^-])\right)}{0.0982} \qquad (Eq.SI.2b)$$

Table SI.2b: Concentrations of NO_2^- and NO_3^- generated within demineralized water exposed to GP

Concentration (mg/L)	Water 15 min	Water 30 min	Water 45 min	Water 60 min
NO_2^-	72.60	117.00	170.00	184.00
NO_3^-	1.88	17.88	27.00	35.02

SI.3. Calibration curve of MnO_4^- and $Fe(phen)_3^{2+}$ for MnO_4^- and Fe^{2+} quantification

To quantify the concentration of MnO_4^- transformed in demineralized water upon exposure to humid air GP, calibration curves were established using $KMnO_4$ solutions (Table SI.3a). The absorbance spectra of these solutions, measured within the wavelength range of 425 to 625 nm, are illustrated in Figure SI.3a. For the determination of MnO_4^- concentration, the absorbance intensity measurement was carried out at a wavelength of 525 nm, as it exhibits its maximum of intensity (Figure SI.3b).

Table SI.3a: Concentration solutions of MnO_4^- for the calibration curves

Solution number	Concentration of $KMnO_4$	
	(mg/L)	(mol/L)
1	15.63	$9.88*10^{-5}$
2	31.25	$1.2*10^{-4}$
3	62.50	$3.95*10^{-4}$
4	93.75	$5.93*10^{-4}$
5	125.00	$7.91*10^{-4}$

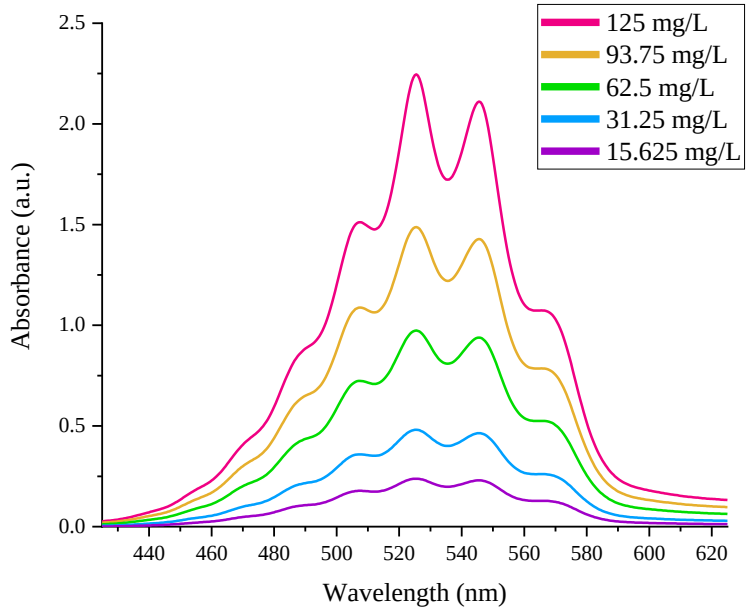


Figure SI.3a: Absorbance spectra of $KMnO_4$ solutions

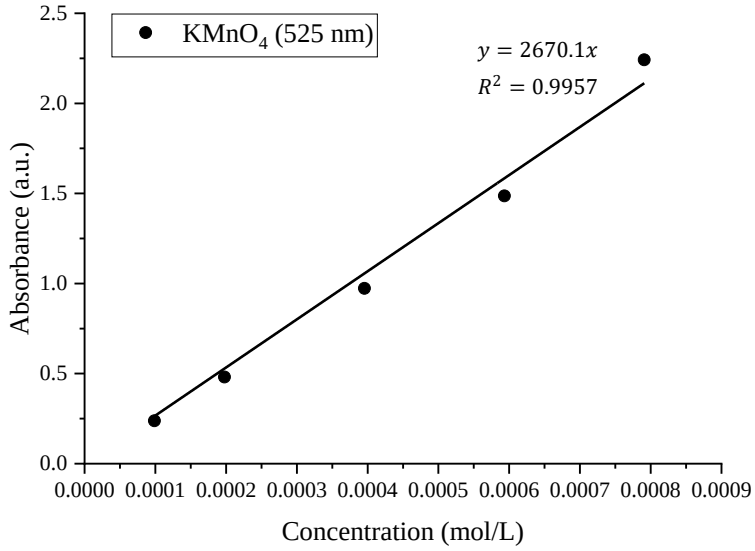


Figure SI.3b: Calibration curves of MnO_4^- solutions at 525 nm

To quantify the concentration of $FeSO_4$ transformed in demineralized water upon exposure to humid air GP, calibration curves were established using $FeSO_4$ and 1,10-phenantroline solutions (Table SI.3b). A blank solution of 1 g/L solution of 1,10-phenantroline in demineralized water served as the reference. The absorbance spectra of these solutions, measured within the wavelength range of 350 to 650 nm, are illustrated in

Figure SI.3c. For the determination of $Fe(phen)_3^{2+}$ concentration, the absorbance intensity measurement was carried out at a wavelength of 510 nm, as it exhibits its maximum of intensity (Figure SI.3d).

Table SI.3b: Composition of Fe^{2+} and phen solutions for the calibration curves of $Fe(phen)_3^{2+}$

Solution number	In a 100 mL flask			Total concentration of $FeSO_4$	
	Volume of a 10^{-2} mol/L $FeSO_4$ solution (mL)	Volume of a 1 g/L solution of 1,10-phenantroline (mL)	Volume of demine-ralized water (mL)	(mg/L)	(mol/L)
1	0.25	5	94.75	7	$2.5*10^{-5}$
2	0.33		94.67	9	$3.3*10^{-5}$
3	0.50		94.50	14	$5*10^{-5}$
4	0.66		94.34	18	$6.6*10^{-5}$
5	1.00		94.00	28	$1*10^{-4}$

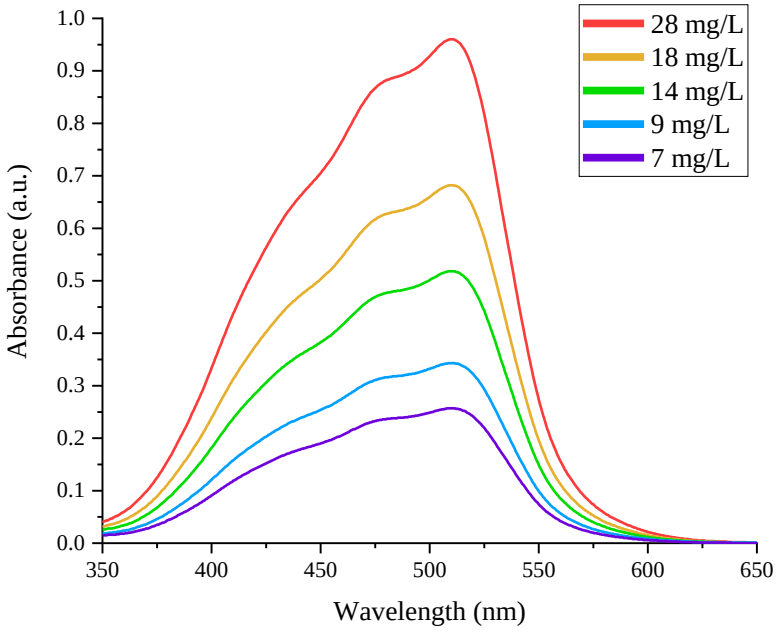


Figure SI.3c: Absorbance spectra of $[Fe(phen)_3]^{2+}$ solutions

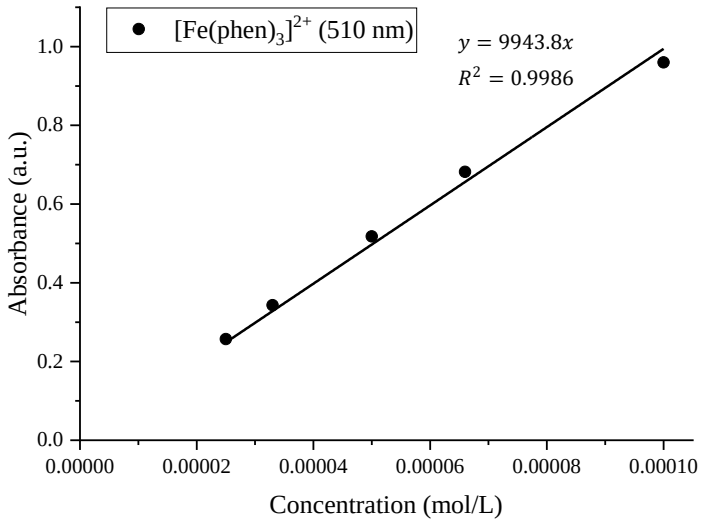


Figure SI.3d: Calibration curves of $[Fe(phen)_3]^{2+}$ solutions at 510 nm

SI.4. Pourbaix diagrams of metal exposed to the GP

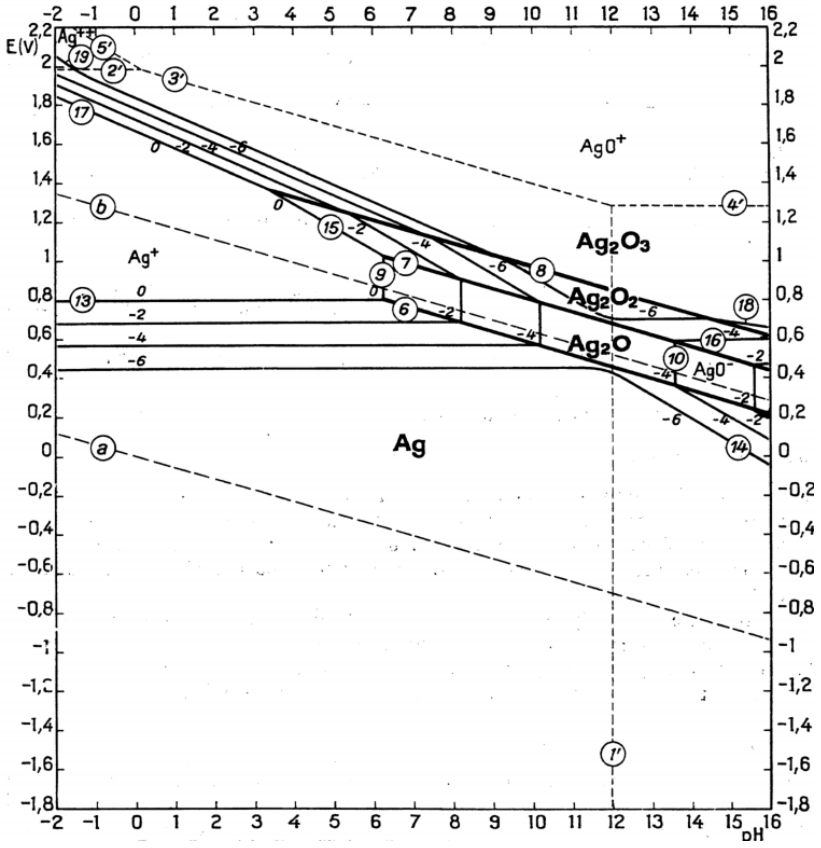


Figure SI.4a: Pourbaix diagram of Ag-water at 25°C [86]

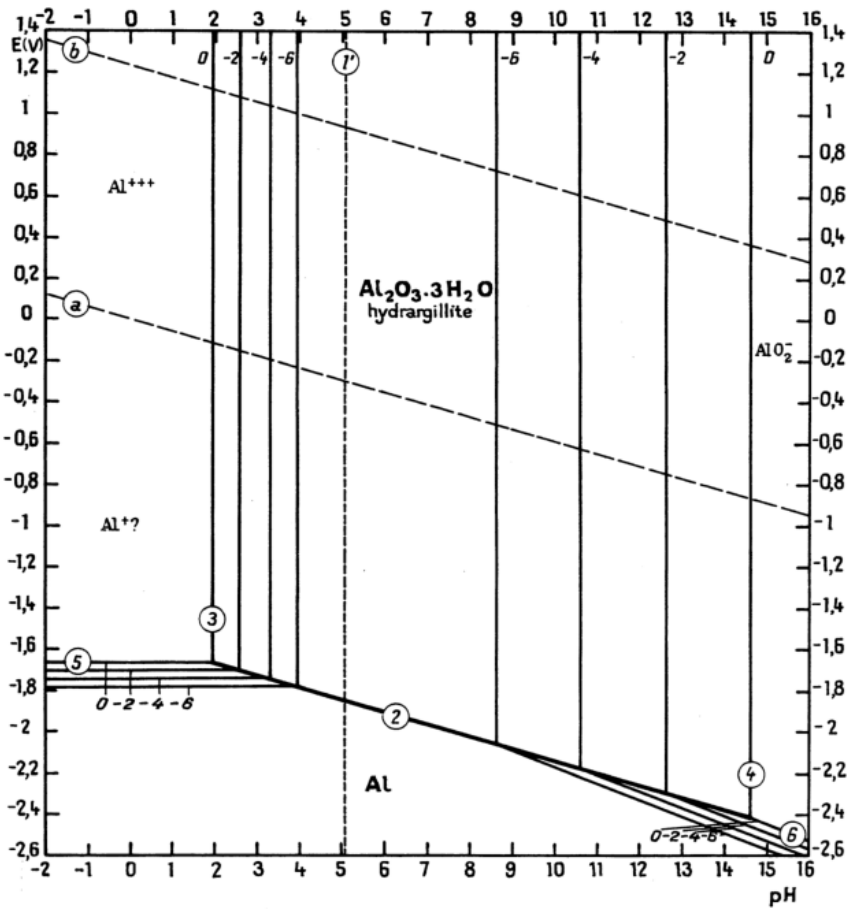


Figure SI.4b: Pourbaix diagram of Al-water at 25°C [86]

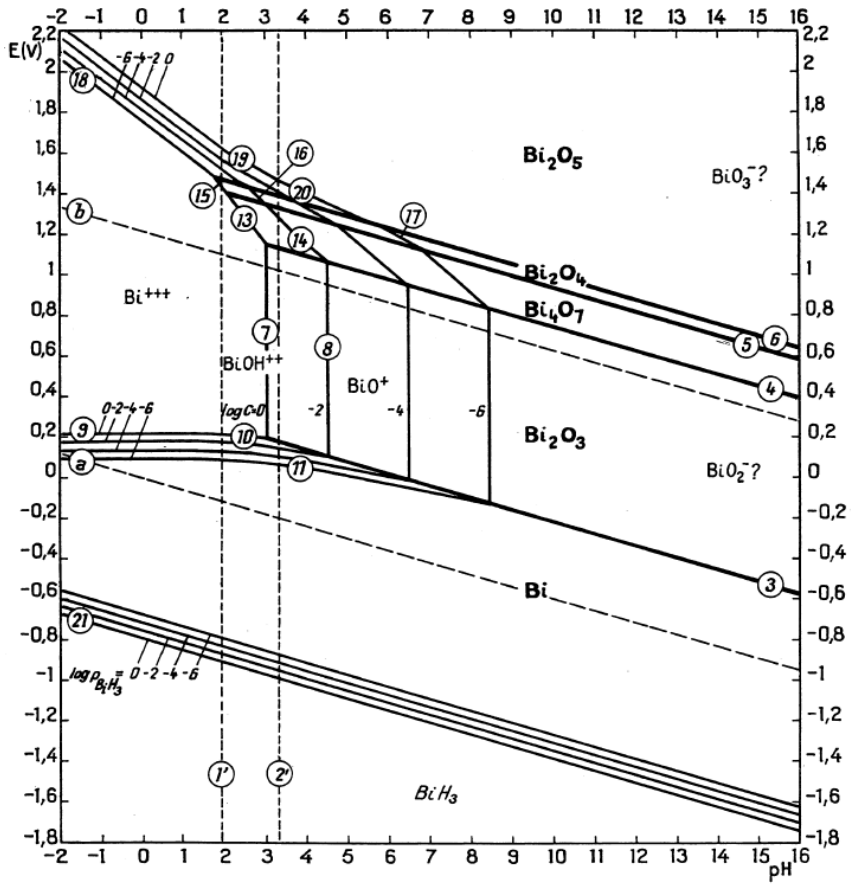


Figure SI.4c: Pourbaix diagram of Bi-water at 25°C [86]

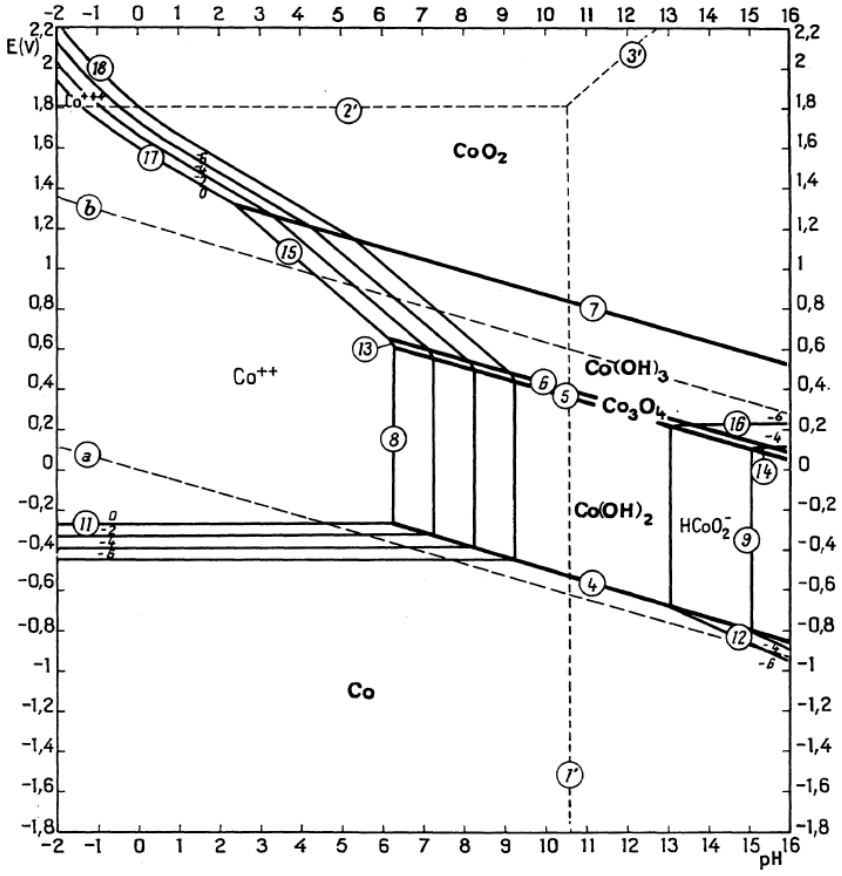


Figure SI.4d: Pourbaix diagram of Co-water at 25°C [86]

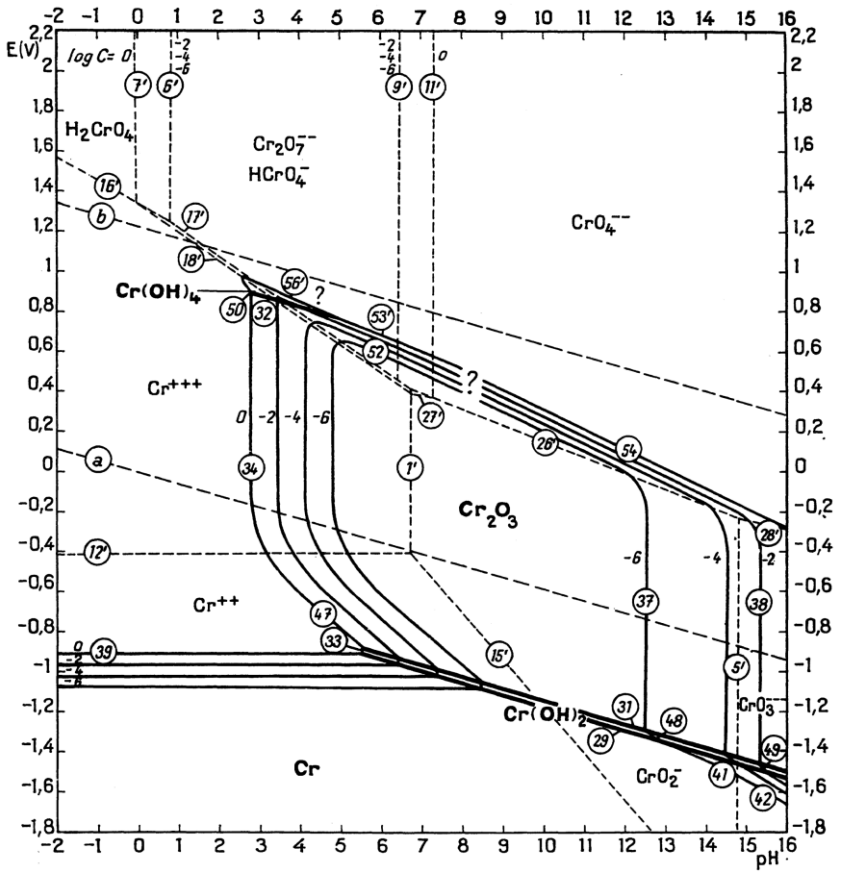


Figure SI.4e: Pourbaix diagram of Cr-water at 25°C, in solution not containing chloride and considering anhydrous Cr_2O_3 [86]

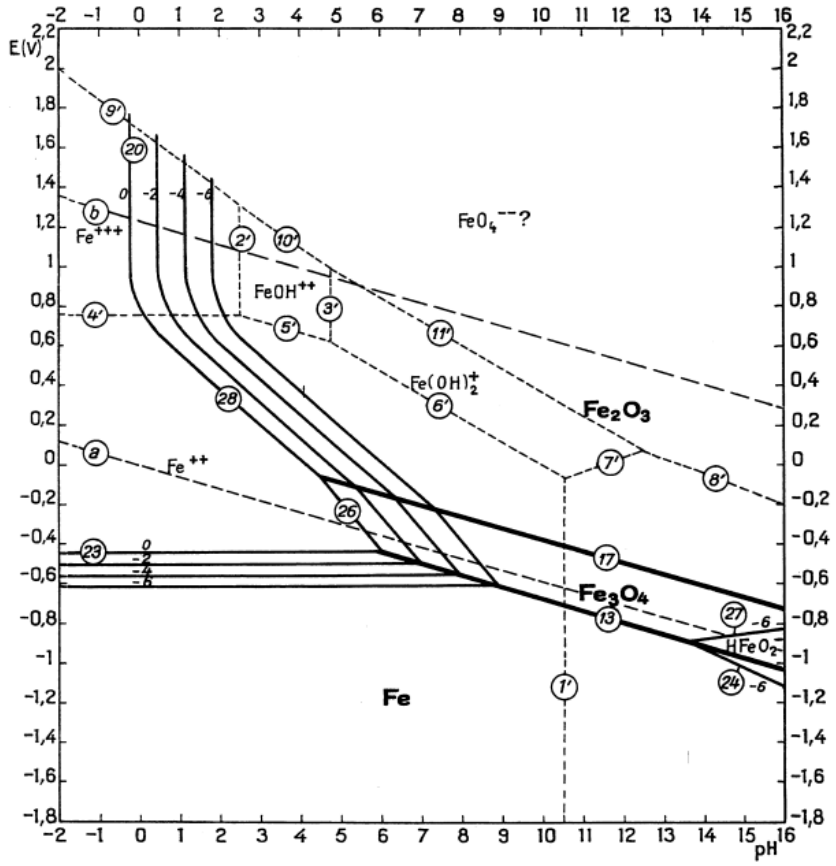


Figure SI.4f: Pourbaix diagram of Fe-water at 25°C, considering as solid substances only Fe, Fe_3O_4 and Fe_2O_3 [86]

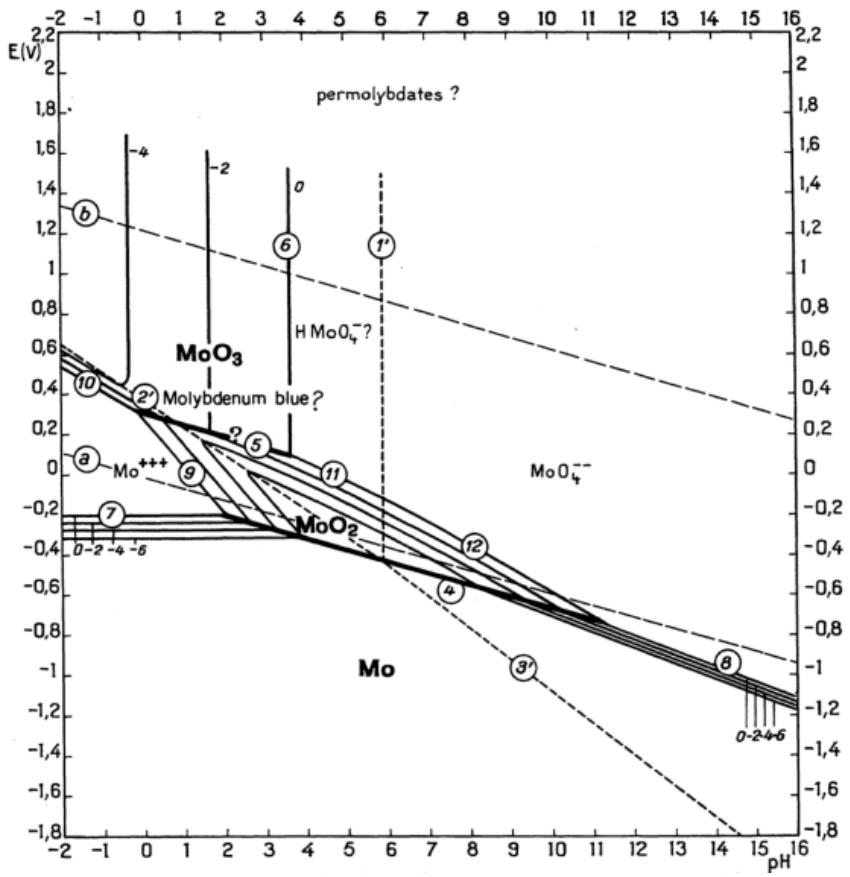


Figure SI.4g: Pourbaix diagram of Mo-water at 25°C [86]

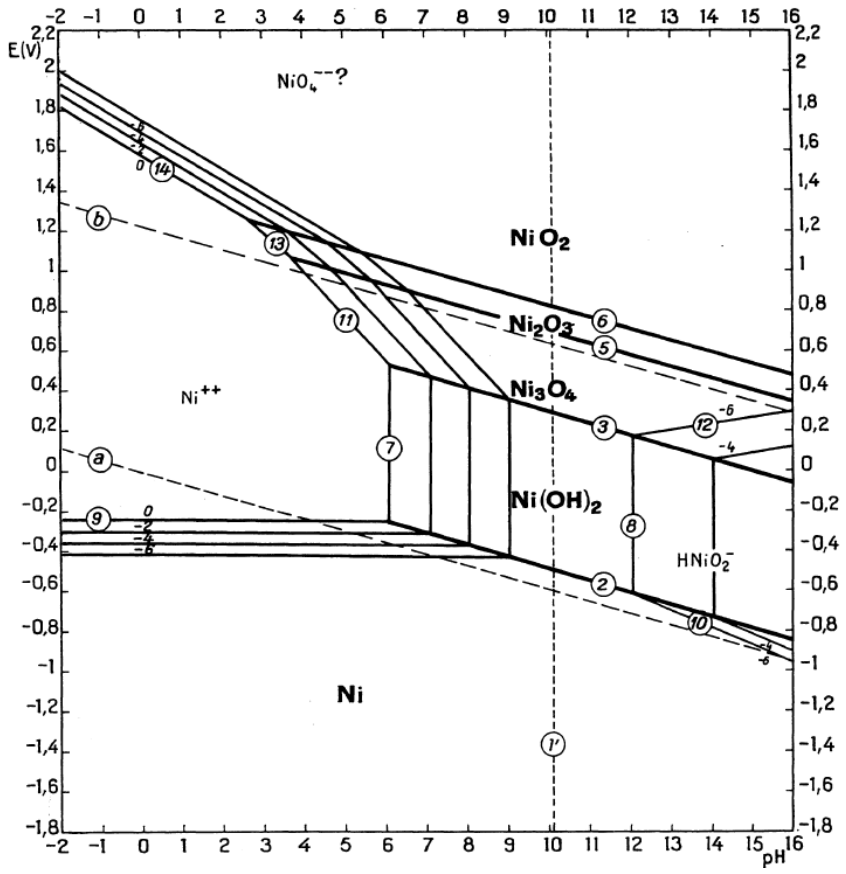


Figure SI.4h: Pourbaix diagram of Ni-water at 25°C [86]

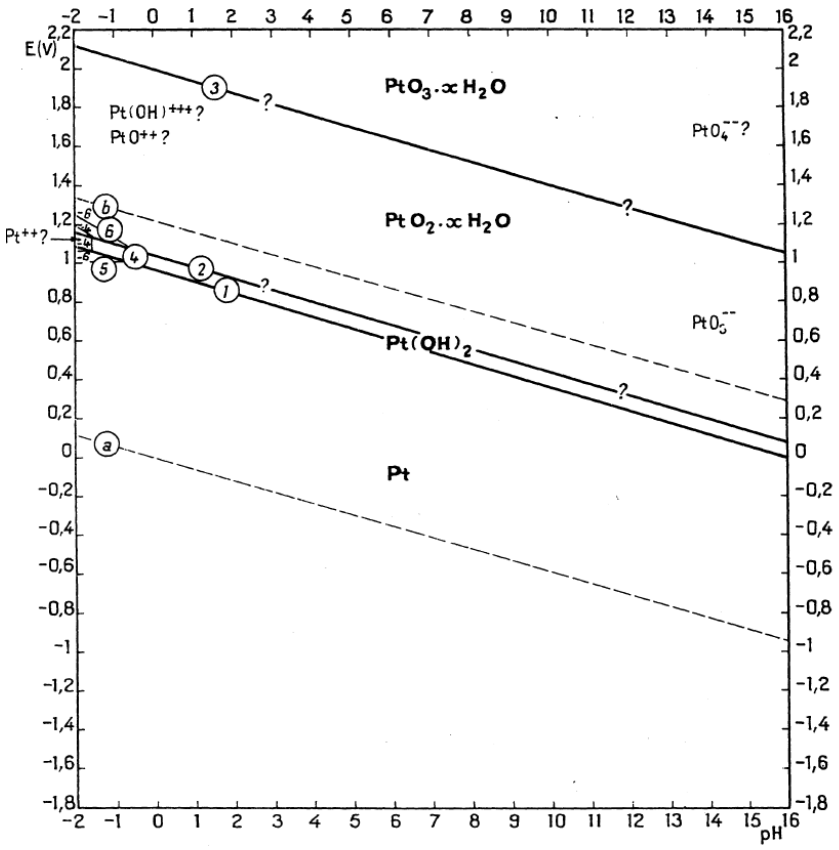


Figure SI.4i: Pourbaix diagram of Pt-water at 25°C [86]

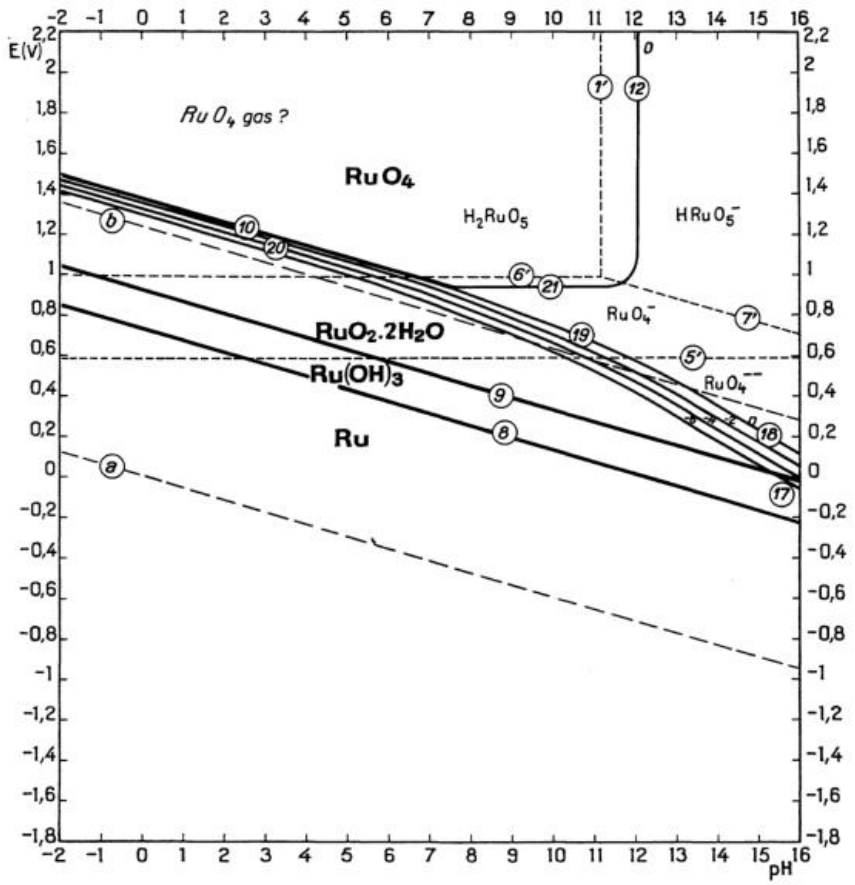


Figure SI.4j: Pourbaix diagram of Ru-water at 25°C (in the presence of solution free from complexing substances) [86]

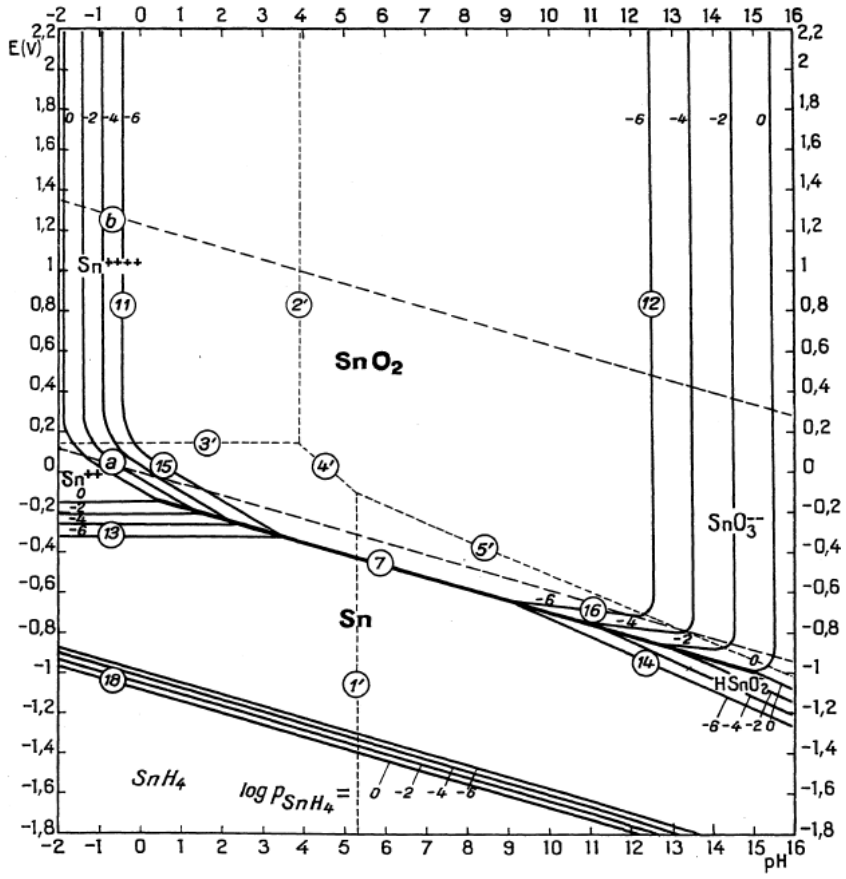


Figure SI.4k: Pourbaix diagram of Sn-water at 25°C (considering the anhydrous oxides SnO and SnO_2) [86]

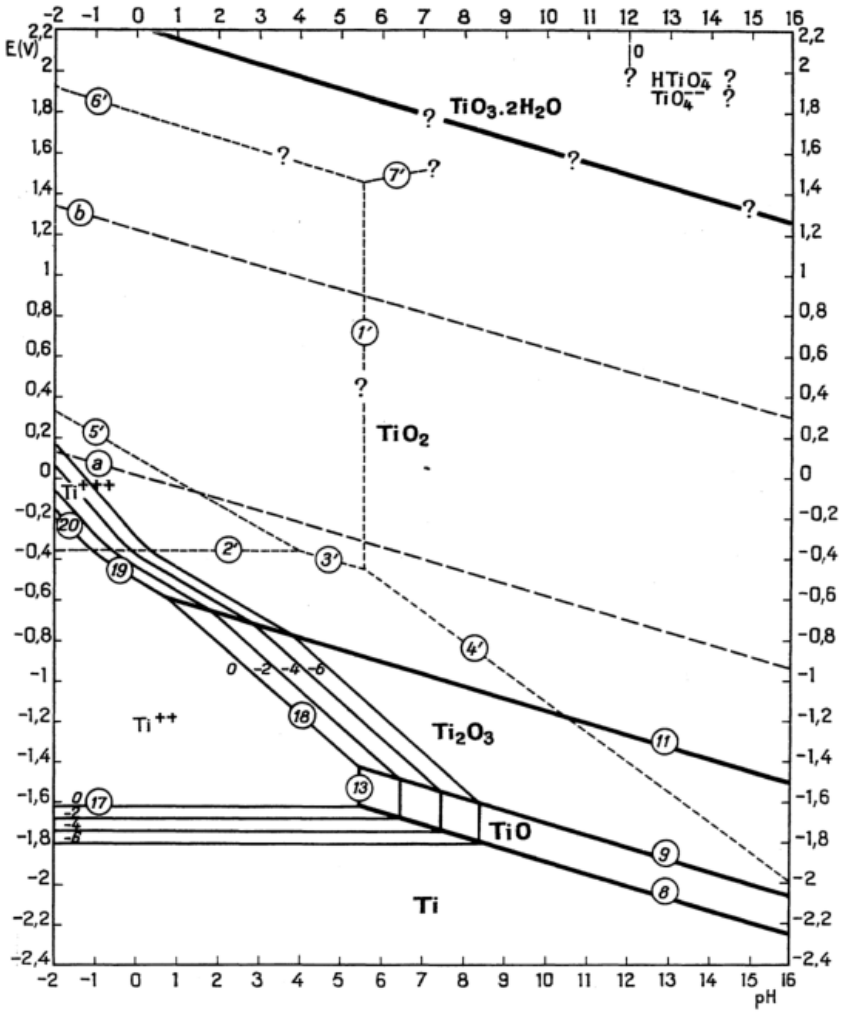


Figure SI.4l: Pourbaix diagram of Ag-water at 25°C (figure established by considering, as derivatives of tri- and tetravalent titanium, the anhydrous oxides Ti_2O_3 and TiO_2 (rutile)) [86]

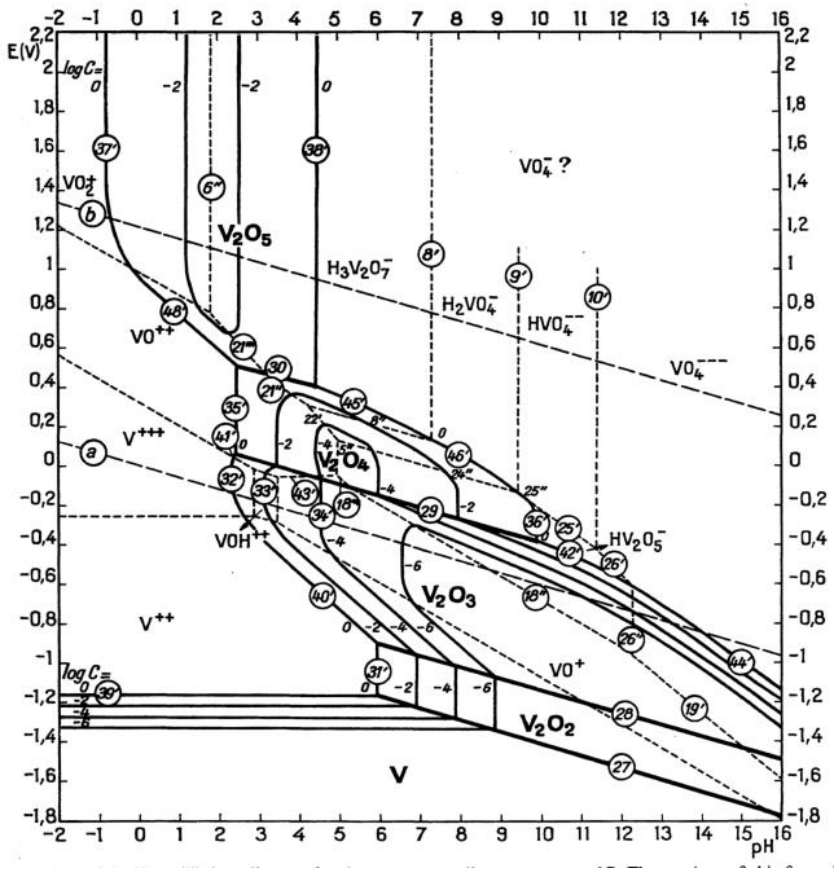


Figure SI.4m: Pourbaix diagram of V-water at 25°C. The portions of this figure lying outside the lines logC = 0 relate to unsaturated solutions (of V, V_2O_2, V_2O_3, V_2O_4 or V_2O_5) containing a total of 1 g-at of dissolved vanadium per litre (51 g/L) in the twelve dissolved forms considered here. The portion of the figure inside the lines logC = 0 relates to solutions saturated with V, V_2O_2, V_2O_3, V_2O_4 or V_2O_5. [86]

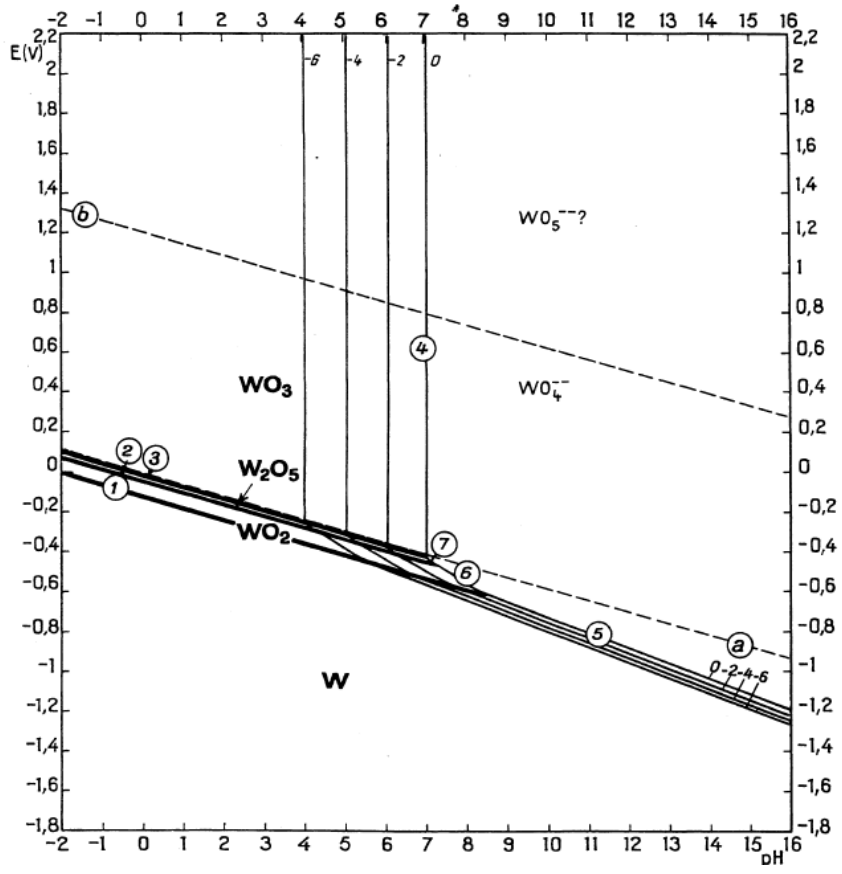


Figure SI.4n: Pourbaix diagram of W-water at 25°C

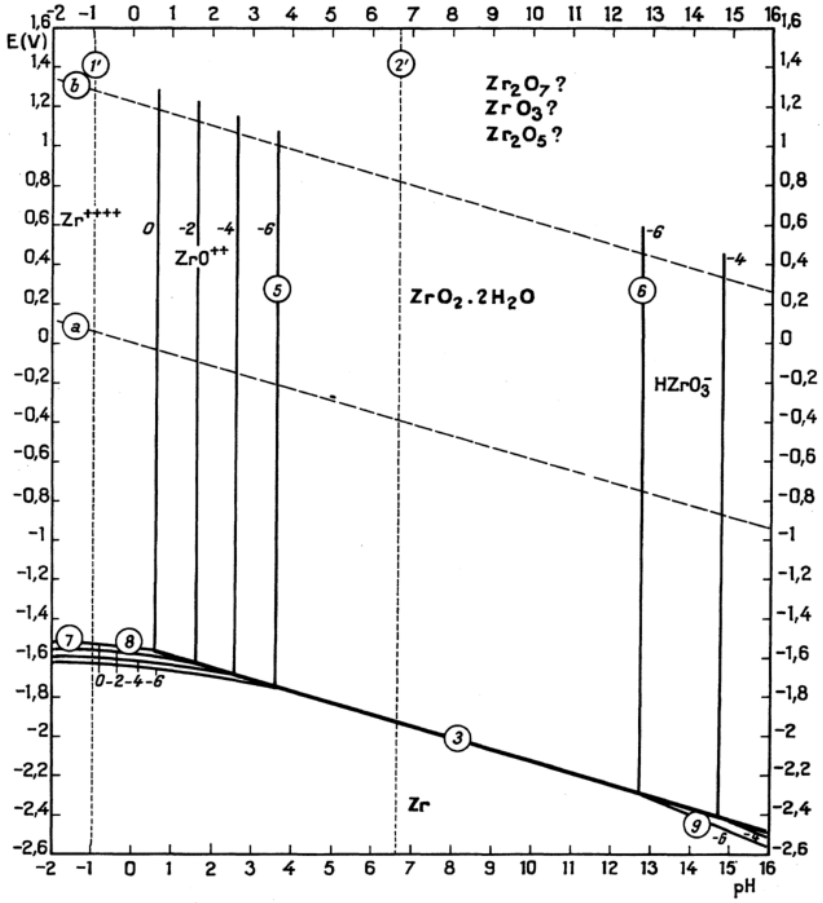


Figure SI.4o: Pourbaix diagram of Zr-water at 25°C (considering $ZrO_2.2H_2O$)

SI.5. Redox reactions between HNO_2 or NO_2^- species and precursors exposed to the GP, considering the actual E of the redox couples

To calculate the actual E of the redox couple involving HNO_2 and NO_2^- species, the concentration of these species, as well as the partial pressure of the gaseous species involved in the reaction (NO or NO_2), need to be considered (Table SI.5a). In Chapter 1, the amount of NO_2^- species generated in demineralized water exposed to the GP over time was measured by UV-visible spectroscopy. Using this value, the pKa of the HNO_2/NO_2^- buffer (pKa = 3.15), and the pH of the solution after the exposure, it is possible to calculate the concentration of HNO_2 formed over time (Eq.SI.5a, Table SI.5b). However, since the partial pressures of the gaseous species generated in the reactor are unknown, we have chosen to set this value at 1.

$$pH = pKa + \log\left(\frac{C_{NO_2^-}}{C_{HNO_2}}\right) \qquad Eq.SI.5a$$

Table SI.5a: Redox couples where HNO_2 or NO_2^- act as oxidants and reducers with only 1 electron involved [86]

	When HNO_2 or NO_2^- act as oxidant	**When HNO_2 or NO_2^- act as reducer**	**E (V)**	**Equation number**
Oxidant	$NO_2^- + 2H^+ + e^-$	$NO_{(g)} + H_2O$	$1.2 - 0.1182pH + 0.0591\log\left(\frac{C_{NO_2^-}}{p_{NO}}\right)$	Eq.SI.5b
	$HNO_2 + H^+ + e^-$	$NO_{(g)} + H_2O$	$1.00 - 0.0591pH + 0.0591\log\left(\frac{C_{HNO_2}}{p_{NO}}\right)$	Eq.SI.5c
Reducer	$NO_2 + e^-$	NO_2^-	$0.90 + 0.0591\log\left(\frac{p_{NO_2}}{C_{NO_2^-}}\right)$	Eq.SI.5d
	$NO_2 + H^+ + e^-$	HNO_2	$1.09 - 0.0591pH + 0.0591\log\left(\frac{p_{NO_2}}{C_{HNO_2}}\right)$	Eq.SI.5e

Table SI.5b: Concentration of HNO_2 and NO_2^- species generated over time in demineralized water exposed to the GP

Exposure time (min)	***pH***	$C_{NO_2^-}$ **(mol/L)**	C_{HNO_2} **(mol/L)**
0	5.4	0	0
15	3.5	$1.59 * 10^{-3}$	$7.10 * 10^{-4}$
30	3.4	$2.25 * 10^{-3}$	$1.27 * 10^{-3}$
45	3.2	$3.70 * 10^{-3}$	$3.30 * 10^{-3}$
60	3	$4.00 * 10^{-3}$	$5.65 * 10^{-3}$

Using the concentration of HNO_2 and NO_2^- generated after 1h of exposure, a partial pressure set to 1, and the pH of the medium after exposure of each precursor, it is possible to calculate a value of E for the redox couple involving HNO_2 and NO_2^- species, for each exposed precursor solution (Table SI.5a). Additionally, as previously performed, knowing the pH of the medium after exposure of each precursor and the concentration used for each, it is possible to calculate the actual E for the redox couples implying the precursor. Finally, by calculating the ΔE for each precursor exposed to the GP, we observe the same conclusions as before, when considering the $E°$ for the redox couple involving HNO_2 and NO_2^-, where $\Delta E > 0$ for the precursors that form a precipitate upon GP exposure (Table SI.5c) and $\Delta E < 0$ for those that do not form a precipitate (Table SI.5d).

Table SI.5c: Redox reactions between HNO_2 or NO_2^- species and precursors exposed to the GP that give a precipitate [88]

Reduction of the precursors		
<u>$KMnO_4$; $NaMnO_4$</u> [86]**<u>:</u>** $\boldsymbol{MnO_4^- + 4H^+ + 3e^- \rightleftharpoons MnO_2 + 2H_2O}$ $\boldsymbol{E = 1.692 - 0.0788pH + 0.0197log\left(C_{MnO_4^-}\right) = 1.41\ V}$		
NO_2/NO_2^- (Eq.SI.5d) $E = 1.06$ V	$MnO_4^- + 4H^+ + 3NO_2^- \rightleftharpoons MnO_2 + 2H_2O + 3NO_2$	$\Delta E = 0.35$ V
NO_2/HNO_2 (Eq.SI.5e) $E = 1.07$ V	$MnO_4^- + H^+ + 3HNO_2 \rightleftharpoons MnO_2 + 2H_2O + 3NO_2$	$\Delta E = 0.34$ V

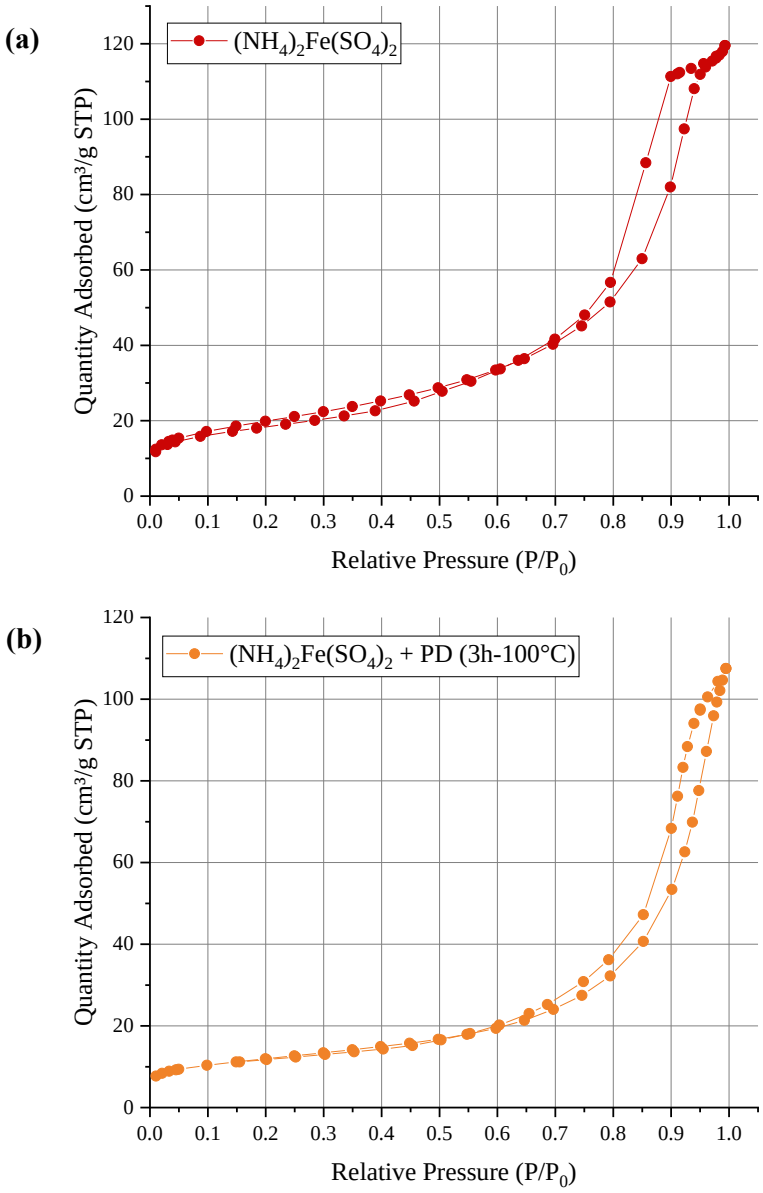
Oxidation of the precursor		
$FeSO_4.7H_2O$; $(NH_4)_2Fe(SO_4)_2.6H_2O$ [86]**:** $\boldsymbol{FeOOH + 3H^+ + e^- \rightleftharpoons Fe^{2+} + 2H_2O}$ $\boldsymbol{E = 0.77 - 0.1773pH - 0.0591log(C_{Fe^{2+}}) = 0.36\ V}$		
NO_2^-/NO (Eq.SI.5b) $E = 0.70$ V	$Fe^{2+} + H_2O + NO_2^- \rightleftharpoons FeOOH + H^+ + NO$	$\Delta E = 0.34$ V
HNO_2/NO (Eq.SI.5c) $E = 0.69$ V	$Fe^{2+} + H_2O + HNO_2 \rightleftharpoons FeOOH + 2H^+ + NO$	$\Delta E = 0.33$ V
$SnSO_4$; $SnCl_2$ [86]**:** $\boldsymbol{SnO_2 + 4H^+ + 2e^- \rightleftharpoons Sn^{2+} + 2H_2O}$ $\boldsymbol{E = -0.077 - 0.1182pH - 0.0295log(C_{Sn^{2+}}) = -0.26\ V}$		
NO_2^-/NO (Eq.SI.5b) $E = 0.81$ V	$Sn^{2+} + 2NO_2^- \rightleftharpoons SnO_2 + 2NO$	$\Delta E = 1.07$ V
HNO_2/NO (Eq.SI.5c) $E = 0.74$ V	$Sn^{2+} + 2HNO_2 \rightleftharpoons SnO_2 + 2NO + 2H^+$	$\Delta E = 1$ V
$TiCl_3$ [86]**:** $\boldsymbol{TiO_2 + 4H^+ + e^- \rightleftharpoons Ti^{3+} + 2H_2O}$ $\boldsymbol{E = -0.666 - 0.2364pH - 0.0591log(C_{Ti^{3+}}) = -1.11\ V}$		
NO_2^-/NO (Eq.SI.5b) $E = 0.85$ V	$Ti^{3+} + H_2O + NO_2^- \rightleftharpoons TiO_2 + 2H^+ + NO$	$\Delta E = 1.96$ V
HNO_2/NO (Eq.SI.5c) $E = 0.76$ V	$Ti^{3+} + H_2O + HNO_2 \rightleftharpoons TiO_2 + 3H^+ + NO$	$\Delta E = 1.87$ V

Table SI.5d: Redox reactions between HNO_2 or NO_2^- species and precursors exposed to the GP that do not give a precipitate

Reduction of the precursors		
<u>$AgNO_3$; $AgCH_3COO$</u> [86]**:** $\boldsymbol{Ag^+ + e^- \rightleftharpoons Ag}$ $\boldsymbol{E_0 = 0.799 + 0.0591 log\left(C_{(Ag^+)}\right) = 0.68\ V}$		
NO_2/NO_2^- (Eq.SI.5d) $E = 1.04$ V	$Ag^+ + NO_2^- \rightleftharpoons Ag + NO_2$	$\Delta E = -0.36$ V
NO_2/HNO_2 (Eq.SI.5e) $E = 1.05$ V	$Ag^+ + HNO_2 \rightleftharpoons Ag + NO_2 + H^+$	$\Delta E = -0.37$ V
<u>$Bi(NO_3)_3$</u> [86]**:** $\boldsymbol{Bi^{3+} + 3e^- \rightleftharpoons Bi}$ $\boldsymbol{E_0 = 0.215 + 0.0197 log\left(C_{Bi^{3+}}\right) = 0.16\ V}$		
NO_2/NO_2^- (Eq.SI.5d) $E = 1.04$ V	$Bi^{3+} + 3NO_2^- \rightleftharpoons Bi + 3NO_2$	$\Delta E = -0.88$ V
NO_2/HNO_2 (Eq.SI.5e) $E = 1.08$ V	$Bi^{3+} + 3HNO_2 \rightleftharpoons Bi + 3NO_2 + 3H^+$	$\Delta E = -0.92$ V

<u>Na_2MoO_4</u> [86]**:** $\boldsymbol{MoO_4^{2-} + 4H^+ + 2e^- \rightleftharpoons MoO_2 + 2H_2O}$ $\boldsymbol{E_0 = 0.606 - 0.1182pH + 0.0295log\left(C_{MoO_4^{2-}}\right) = -0.09\,V}$		
NO_2/NO_2^- (Eq.SI.5d) $E = 1.04$ V	$MoO_4^{2-} + 4H^+ + 2NO_2^- \rightleftharpoons MoO_2 + 2H_2O + 2NO_2$	$\Delta E = -1.13\,V$
NO_2/HNO_2 (Eq.SI.5e) $E = 0.90$ V	$MoO_4^{2-} + 2H^+ + 2HNO_2 \rightleftharpoons MoO_2 + 2H_2O + 2NO_2$	$\Delta E = -0.99\,V$
<u>$Ni(CH_3COO)_2$</u> [86]**:** $\boldsymbol{Ni^{2+} + 2e^- \rightarrow Ni}$ $\boldsymbol{E_0 = -0.250 + 0.0295log\left(C_{Ni^{2+}}\right) = -0.31\,V}$		
NO_2/NO_2^- (Eq.SI.5d) $E = 1.04$ V	$Ni^{2+} + 2NO_2^- \rightarrow Ni + 2NO_2$	$\Delta E = -1.35$ V
NO_2/HNO_2 (Eq.SI.5e) $E = 0.89$ V	$Ni^{2+} + 2HNO_2 \rightarrow Ni + 2NO_2 + 2H^+$	$\Delta E = -1.2$ V
Oxidation of the precursor		
<u>$Ni(CH_3COO)_2$</u> [86]**:** $\boldsymbol{Ni_3O_4 + 8H^+ + 2e^- \rightleftharpoons 3Ni^{2+} + 4H_2O}$ $\boldsymbol{E_0 = 1.977 - 0.2364pH - 0.0886log\left(C_{Ni^{2+}}\right) = 1.40\,V}$		
NO_2^-/NO (Eq.SI.5b) $E = 0.38$ V	$3Ni^{2+} + 2H_2O + 2NO_2^- \rightleftharpoons Ni_3O_4 + 4H^+ + 2NO$	$\Delta E = -1.02\,V$
HNO_2/NO (Eq.SI.5c) $E = 0.53$ V	$3Ni^{2+} + 2H_2O + 2HNO_2 \rightleftharpoons Ni_3O_4 + 6H^+ + 2NO$	$\Delta E = -0.87\,V$

SI.6 Isotherms obtained by N_2-physisorption for solid developed with iron precursors without and with PT



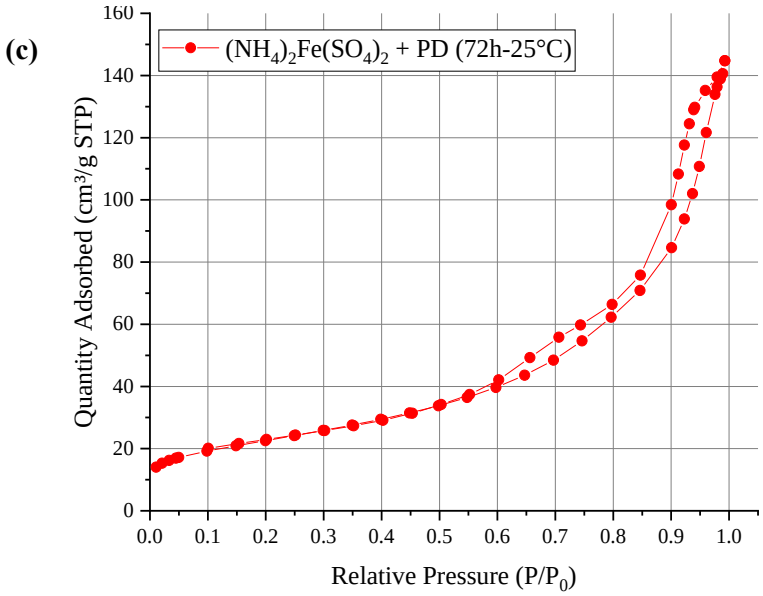
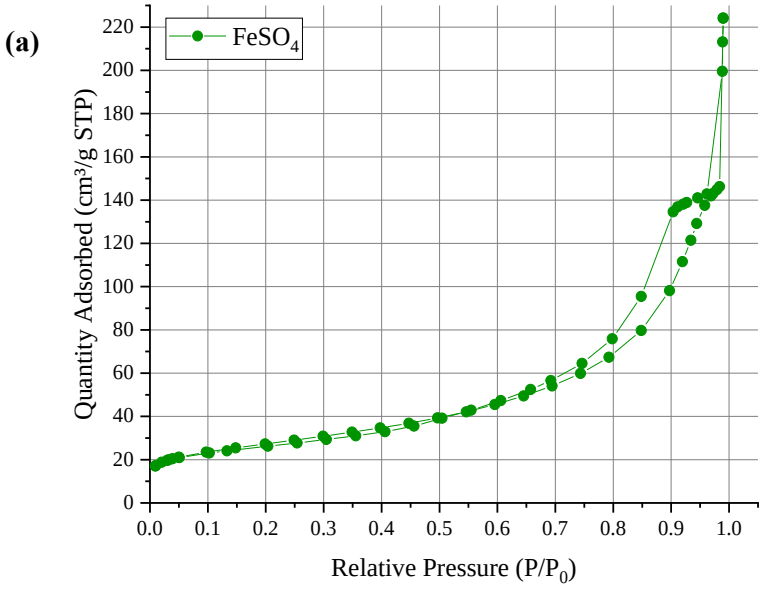


Figure SI.6a: Isotherms obtained by N_2-physisorption for solids obtained from $(NH_4)_2Fe(SO_4)_2$ (a) without and with PT (b) (3h-100°C) and (c) (72h-25°C)



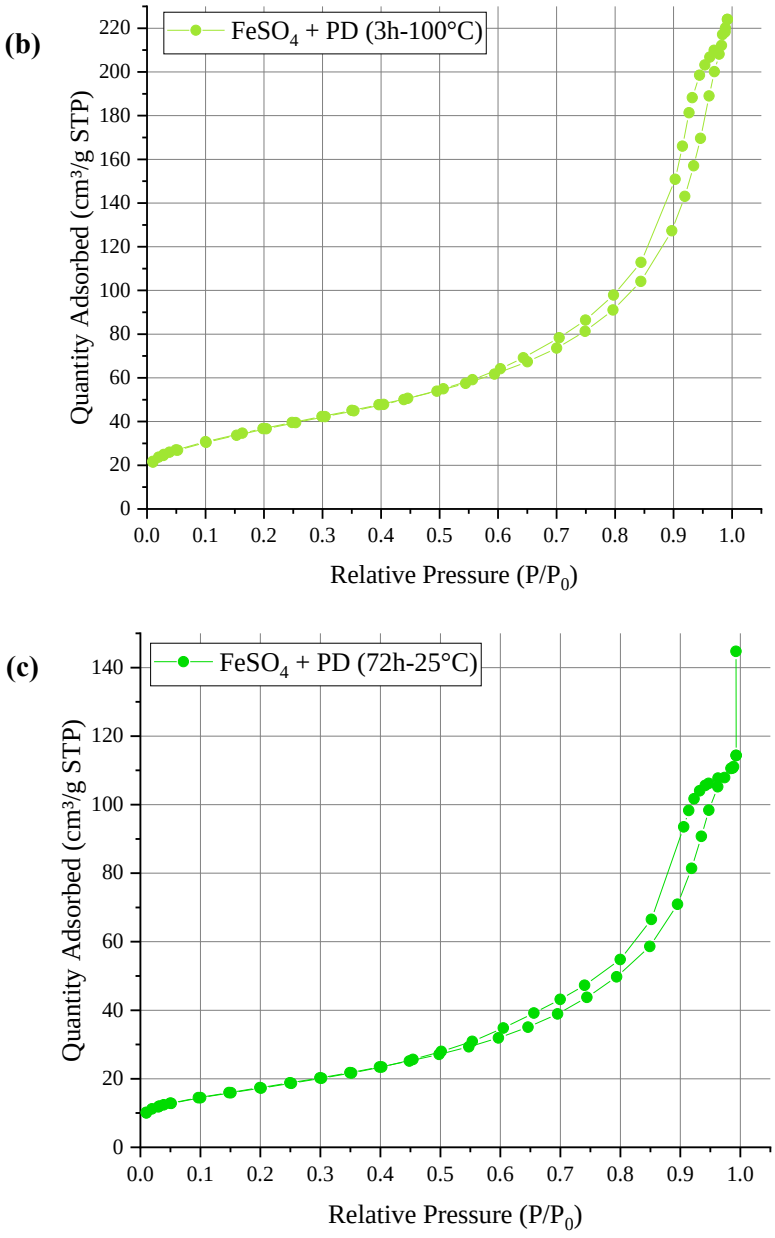
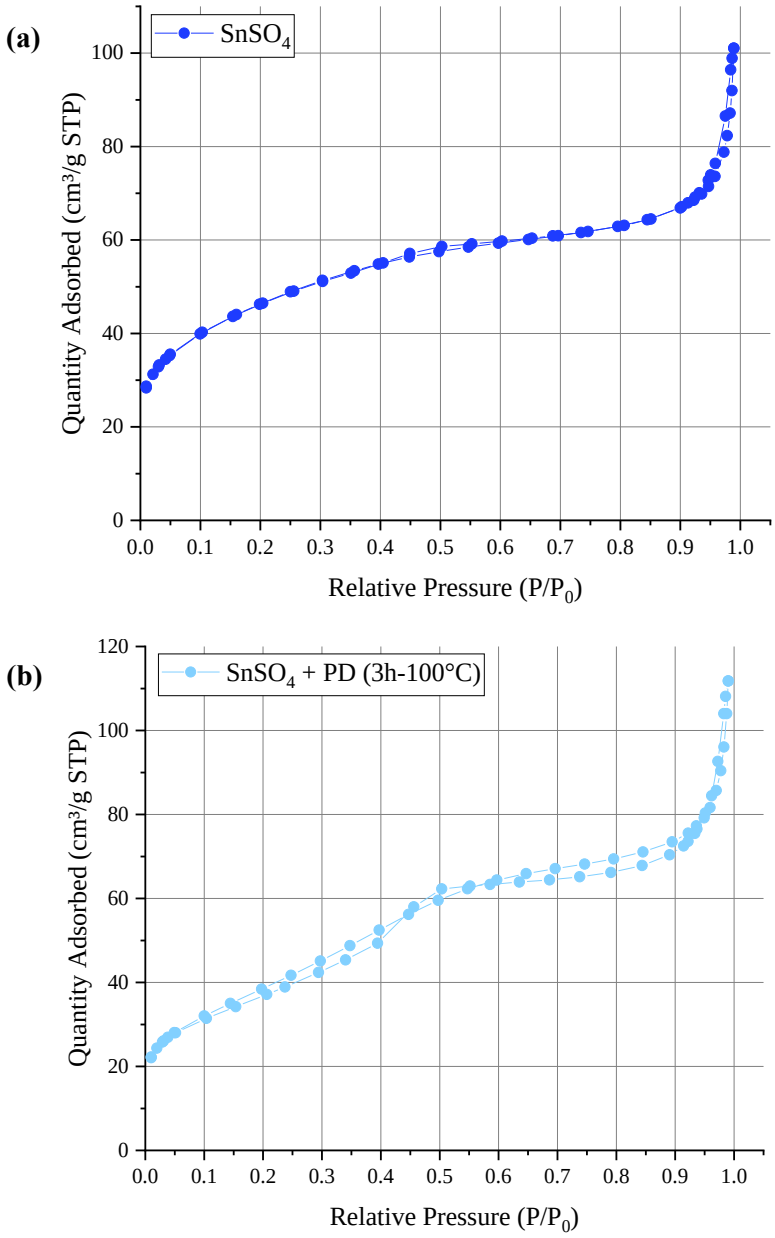


Figure SI.6b: Isotherms obtained by N_2-physisorption for solids obtained from $FeSO_4$ (a) without and with PT (b) (3h-100°C) and (c) (72h-25°C)

SI.7. Isotherms obtained by N_2-physisorption for solid developed with tin precursors without and with PT



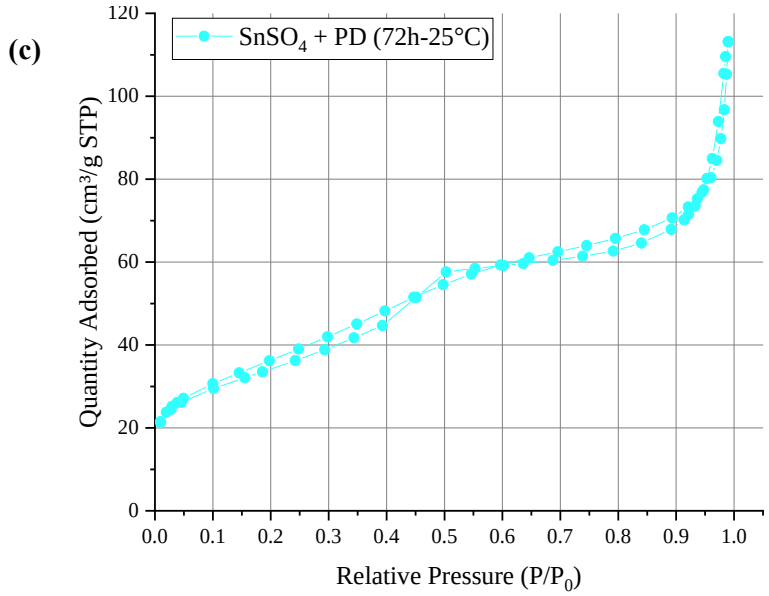
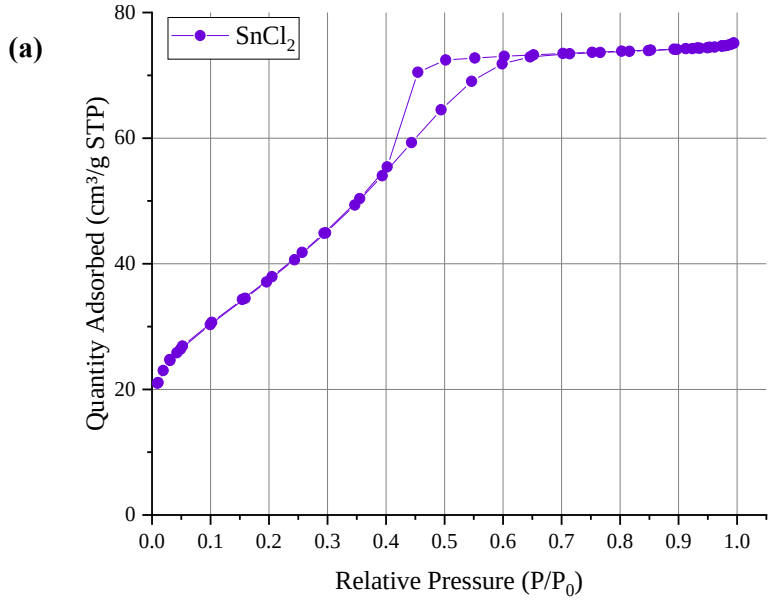


Figure SI.7a: Isotherms obtained by N_2-physisorption for solids obtained from $SnSO_4$ (a) without and with PT (b) (3h-100°C) and (c) (72h-25°C)



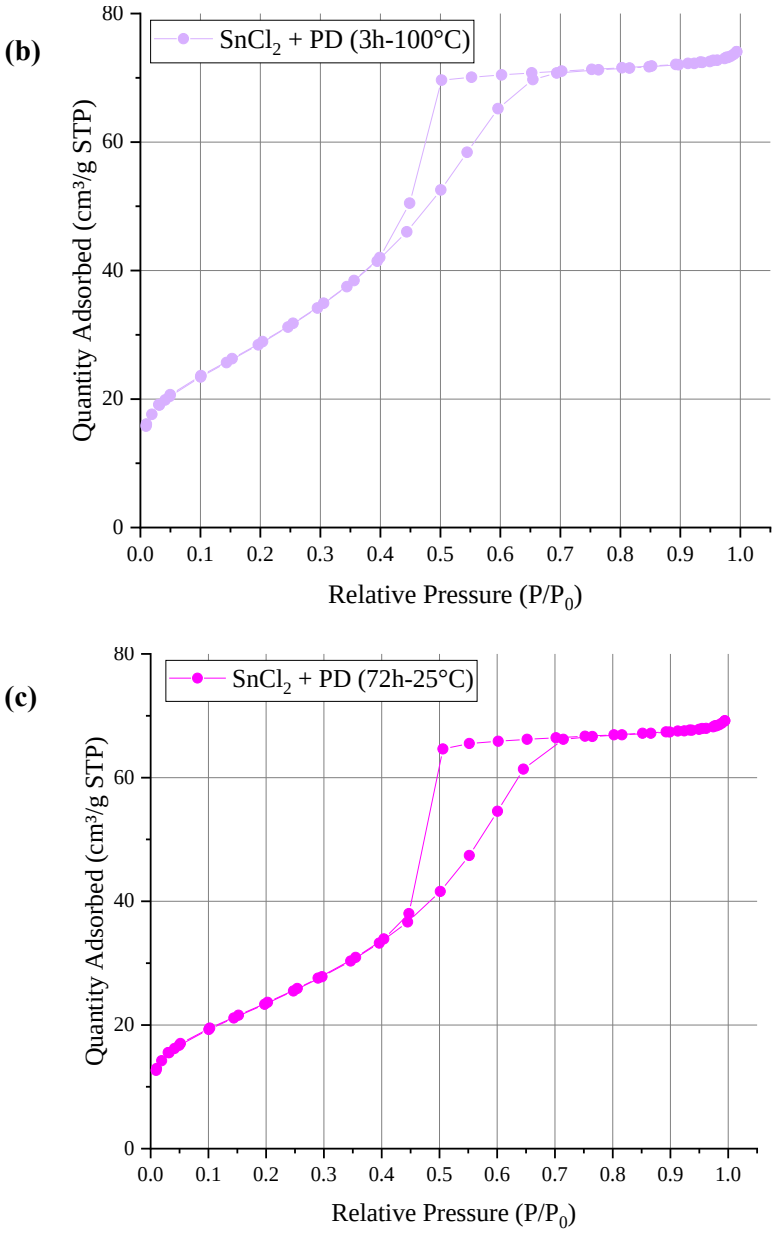
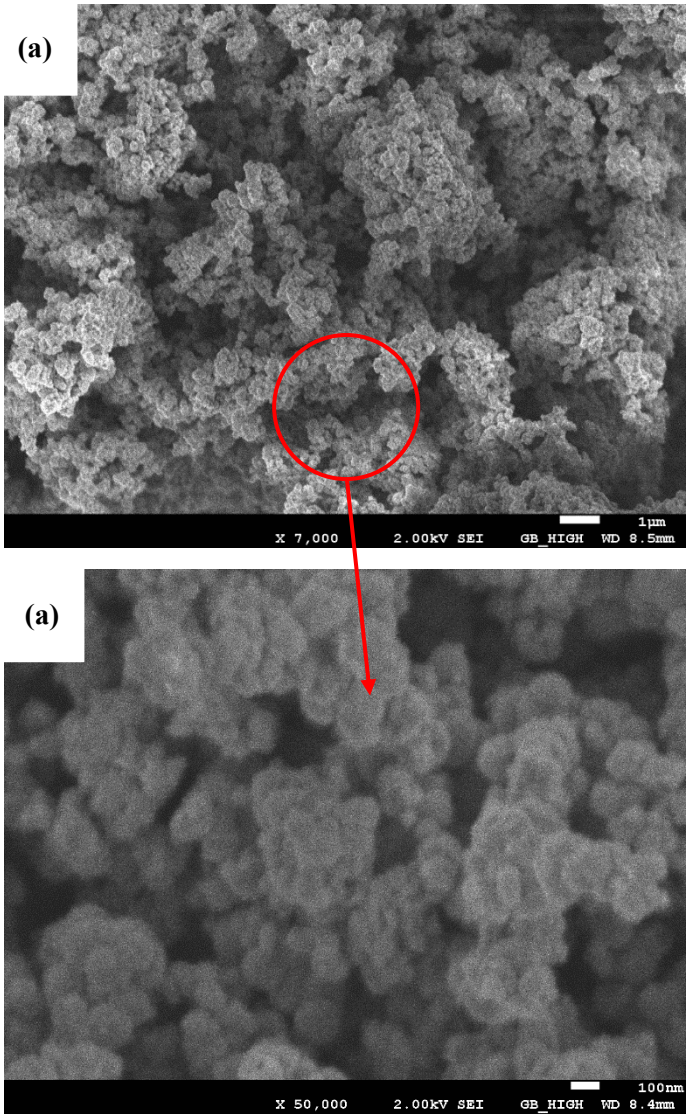
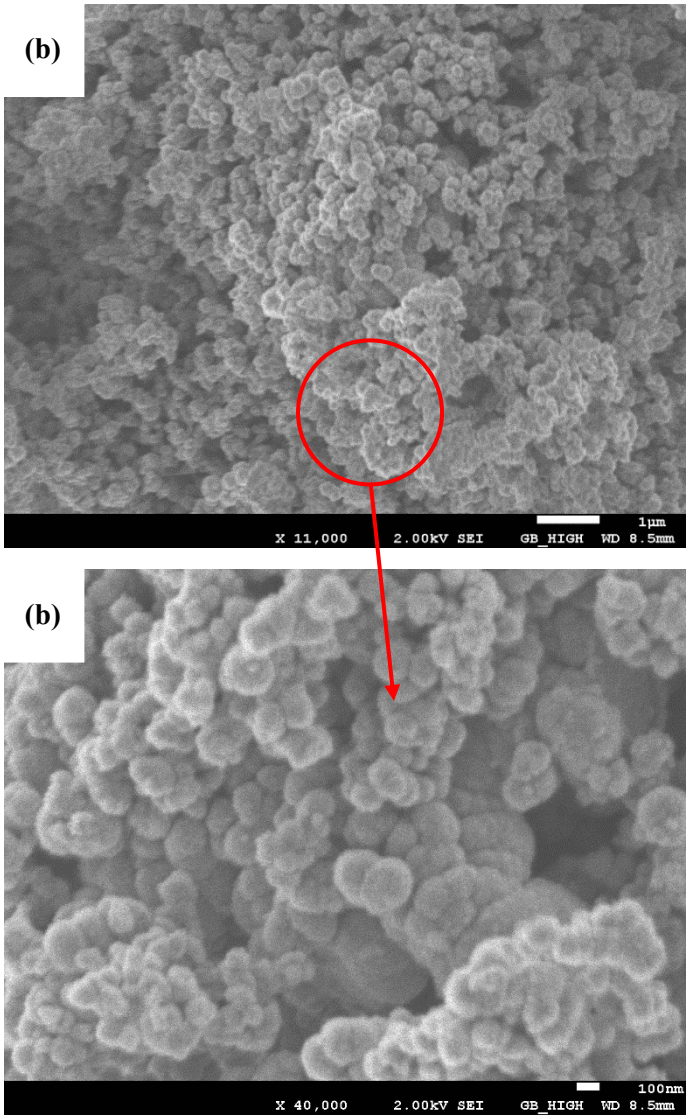


Figure SI.7b: Isotherms obtained by N_2-physisorption for solids obtained from $SnCl_2$ (a) without and with PT (b) (3h-100°C) and (c) (72h-25°C)

SI.8. SEM images of solids formed from $SnSO_4$ with and without PT




(b)
X 11,000 2.00kV SEI GB_HIGH WD 8.5mm
1µm
(b)
X 40,000 2.00kV SEI GB_HIGH WD 8.5mm
100nm

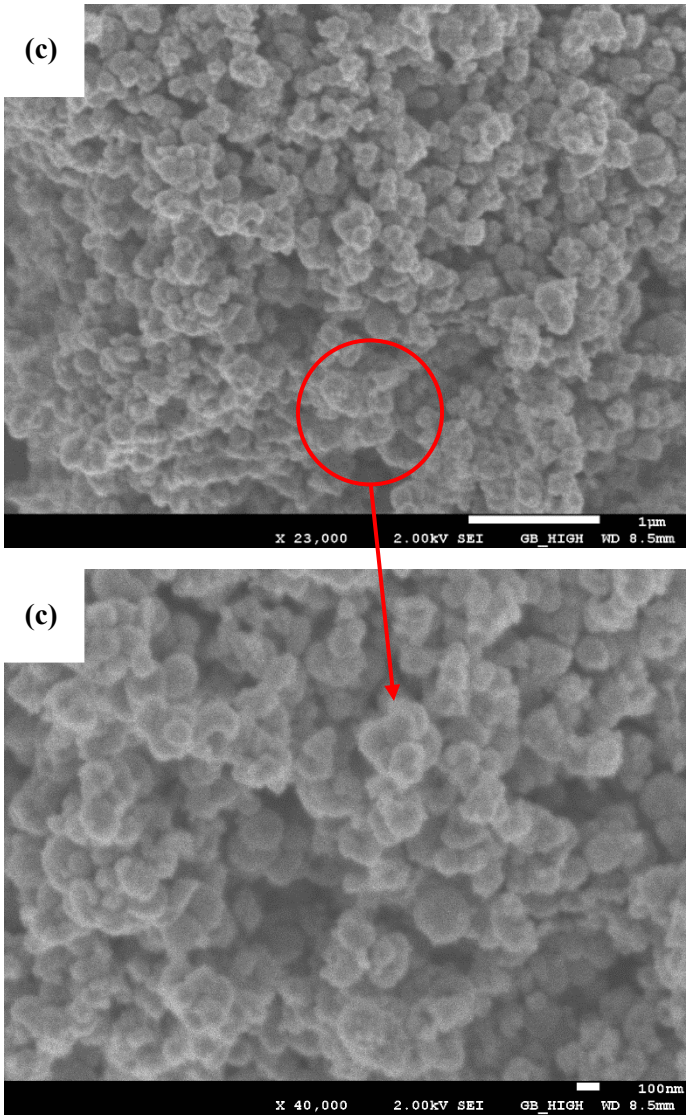


Figure SI.8. SEM images of solids formed from $SnSO_4$ (a) without PT ; (b) + PT (3h-100°C) ; (c) + PT (72h-AT)

SI.9. Diffractograms of SnO_2 synthesized by classical with base (NH_3) addition precipitation

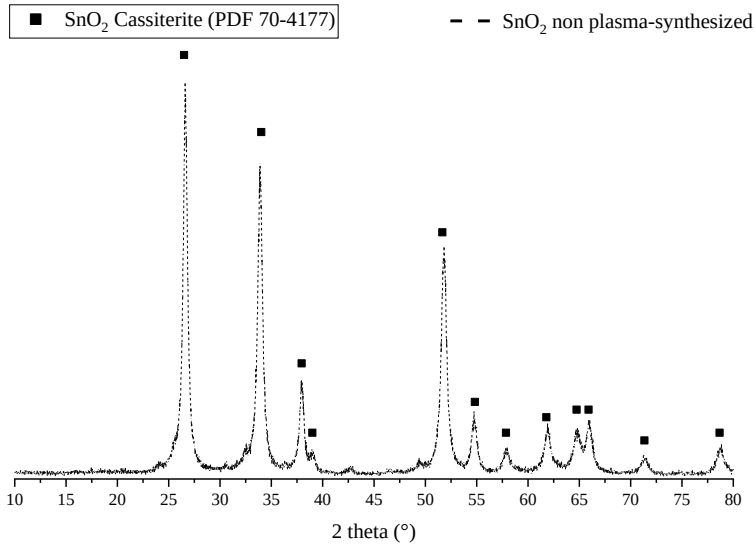
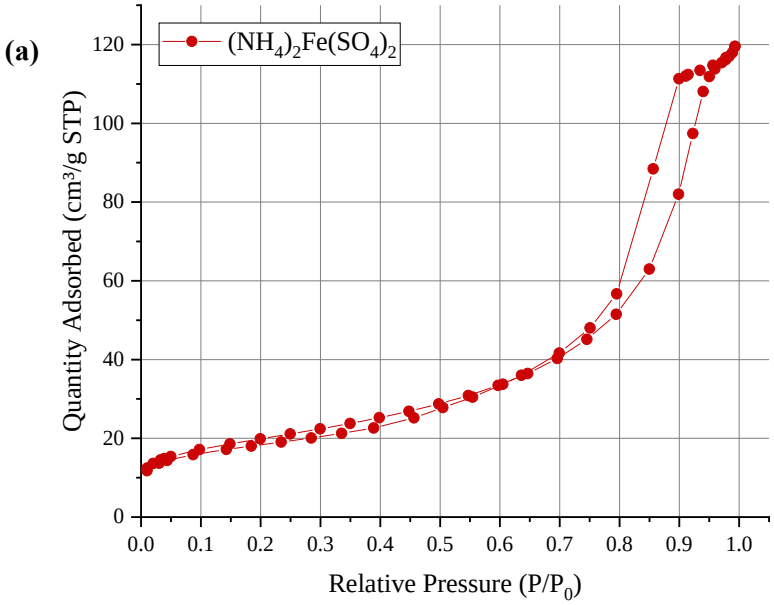


Figure SI.9: XRD data of SnO_2 synthesized by classical with base (NH_3) addition precipitation

SI.10. Isotherms obtained by N_2-physisorption for solid developed with iron precursors with and without the cooling system



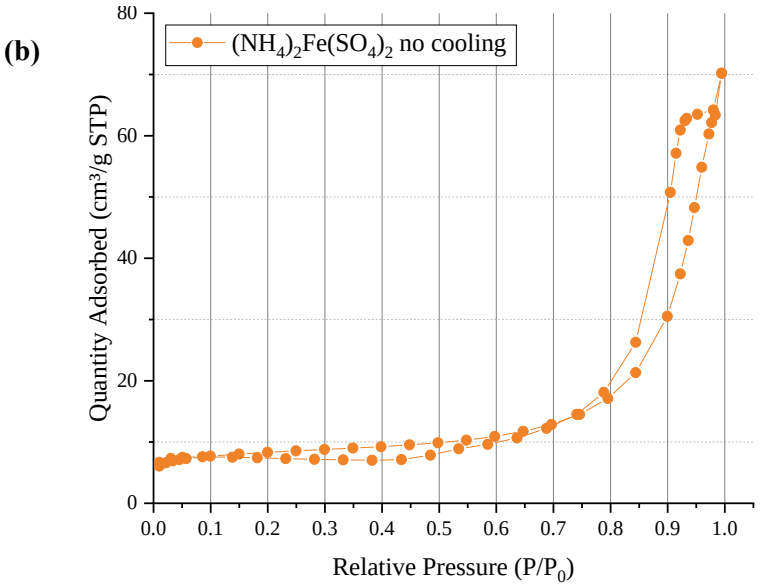
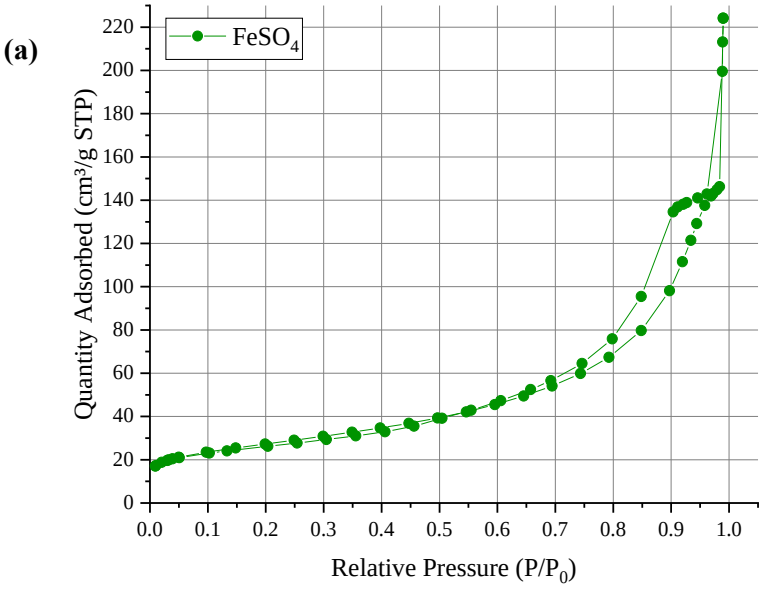


Figure SI.10a: Isotherm obtained by N_2-physisorption for solids obtained from $(NH_4)_2Fe(SO_4)_2$ (a) with and (b) without cooling system



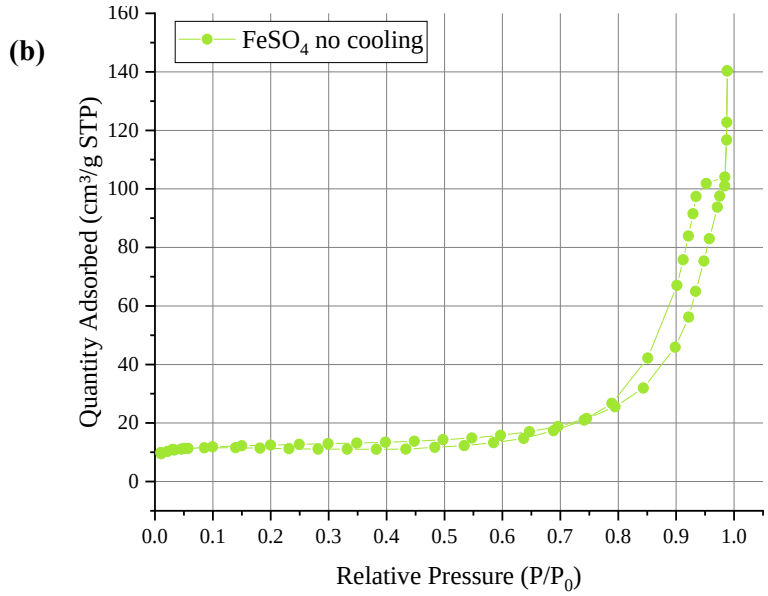
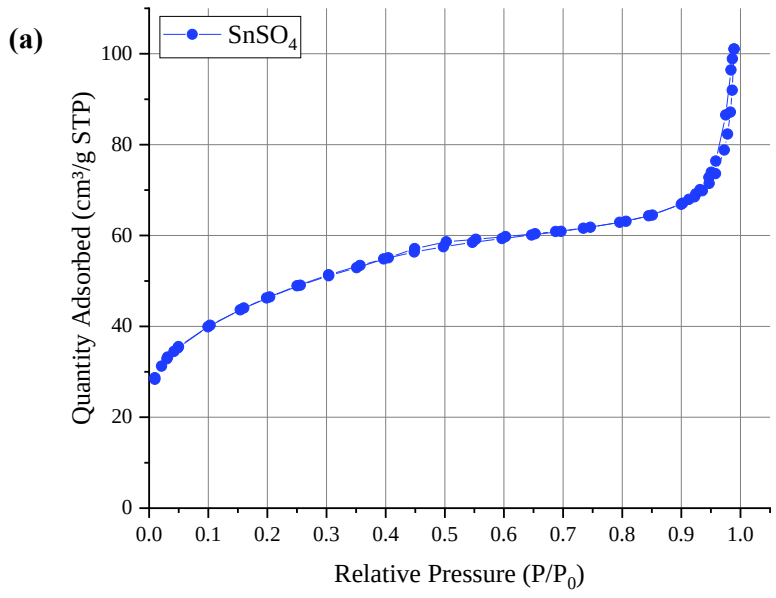


Figure SI.10b: Isotherm obtained by N_2-physisorption for solids obtained from $FeSO_4$ (a) with and (b) without cooling system

SI.11. Isotherms obtained by N_2-physisorption for solid developed with tin precursors with and without cooling system



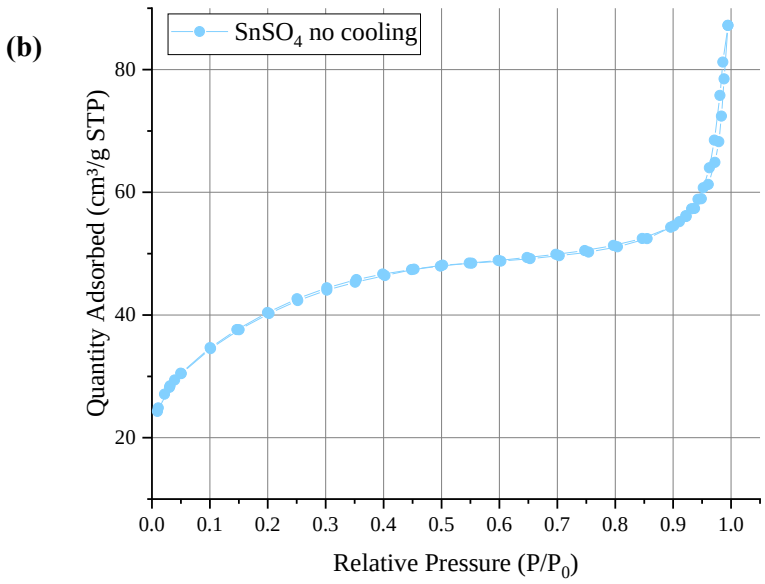
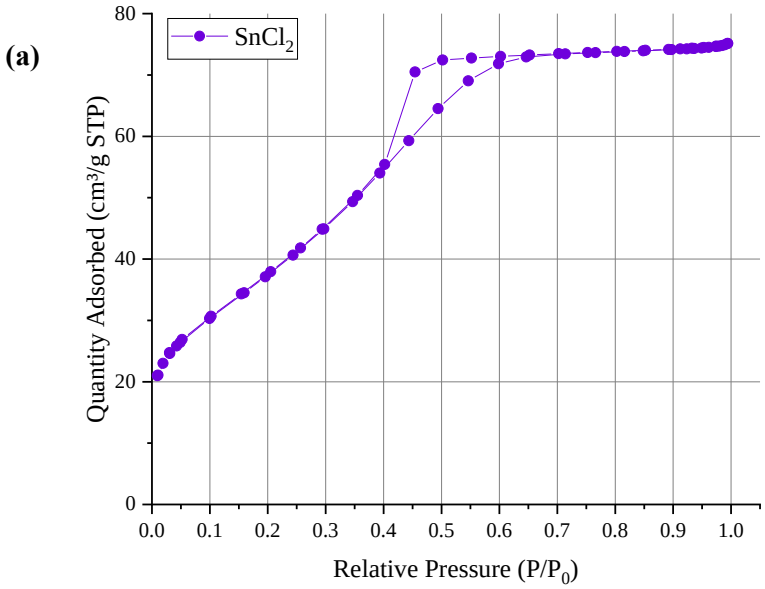


Figure SI.11a: Isotherm obtained by N_2-physisorption for solids obtained from $SnSO_4$ (a) with cooling and (b) without cooling



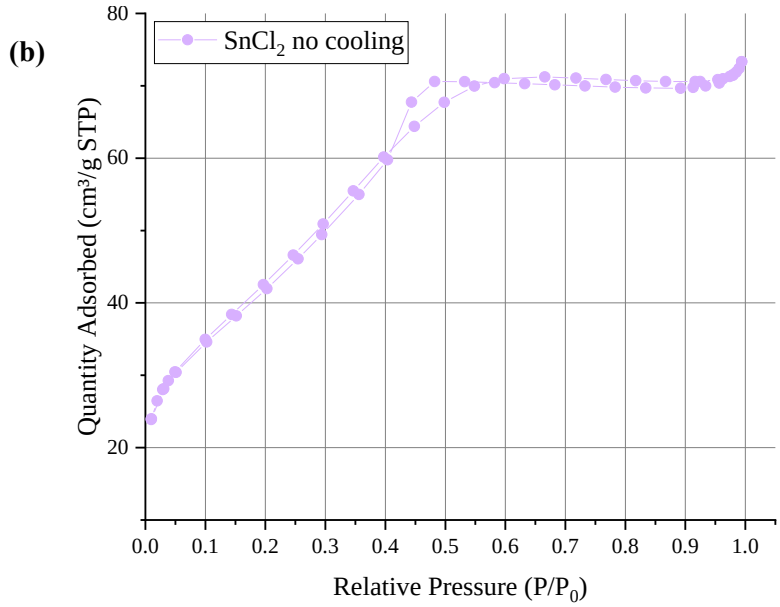


Figure SI.11b: Isotherm obtained by N_2-physisorption for solids obtained from $SnCl_2$ (a) with cooling and (b) without cooling

SI.12. XRD data of solids obtained with FeSO4, KMnO4 and SnSO4 added to PAW before calcination

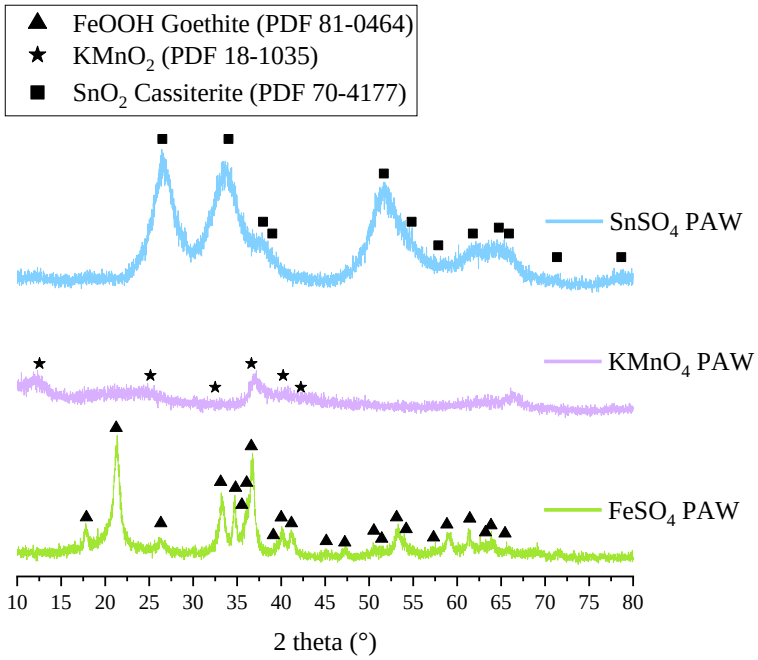


Figure SI.12: XRD data of solids obtained with FeSO4, KMnO4 and SnSO4 added to PAW before calcination

SI.13. Isotherms obtained by N_2-physisorption for solid developed with $FeSO_4$, $KMnO_4$ and $SnSO_4$ by direct exposure and by PAW

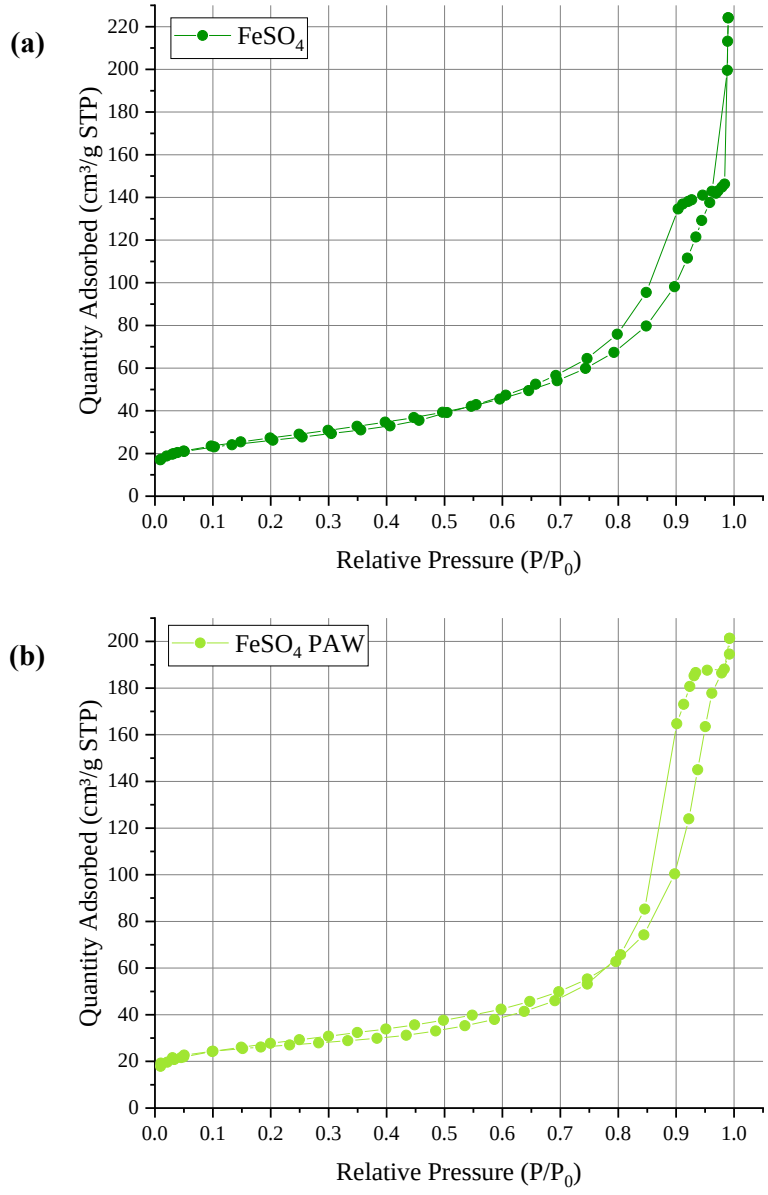


Figure SI.13a: Isotherm obtained by N_2-physisorption for solids obtained from $FeSO_4$ (a) by direct exposure and (b) by PAW

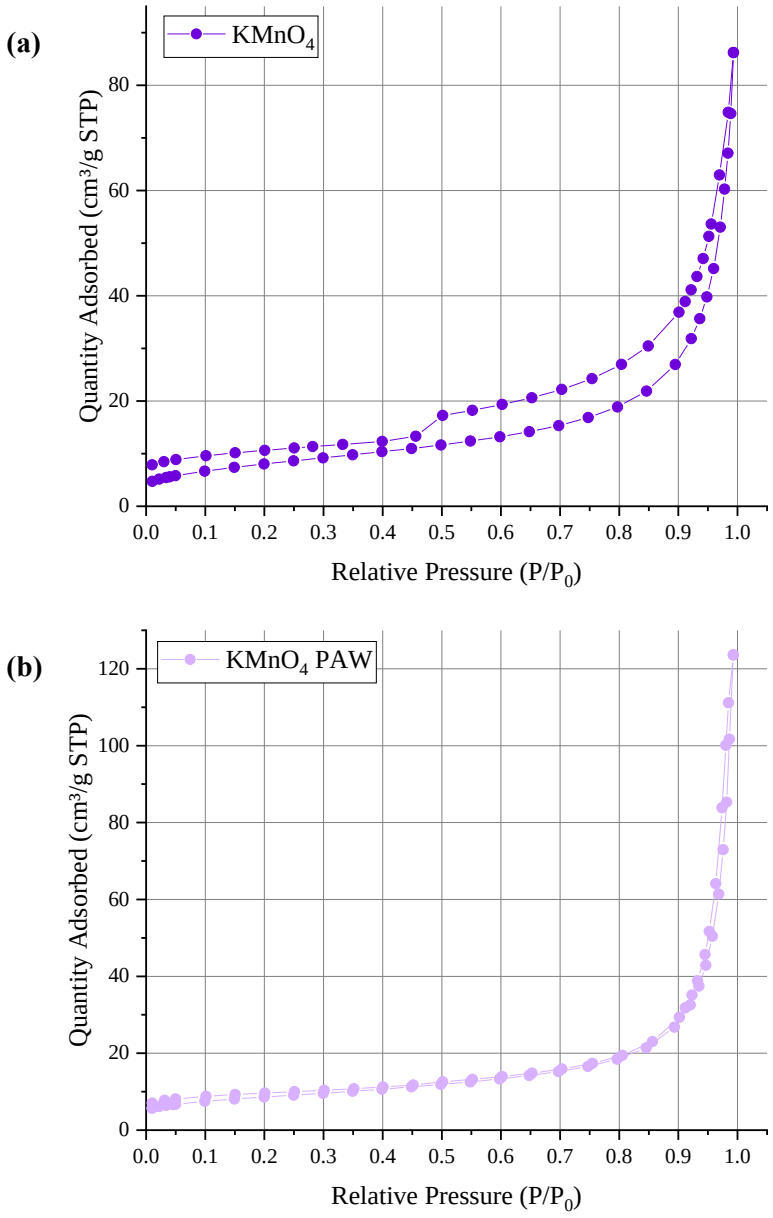


Figure SI.13b: Isotherm obtained by N_2-physisorption for solids obtained from $KMnO_4$ (a) by direct exposure and (b) by PAW

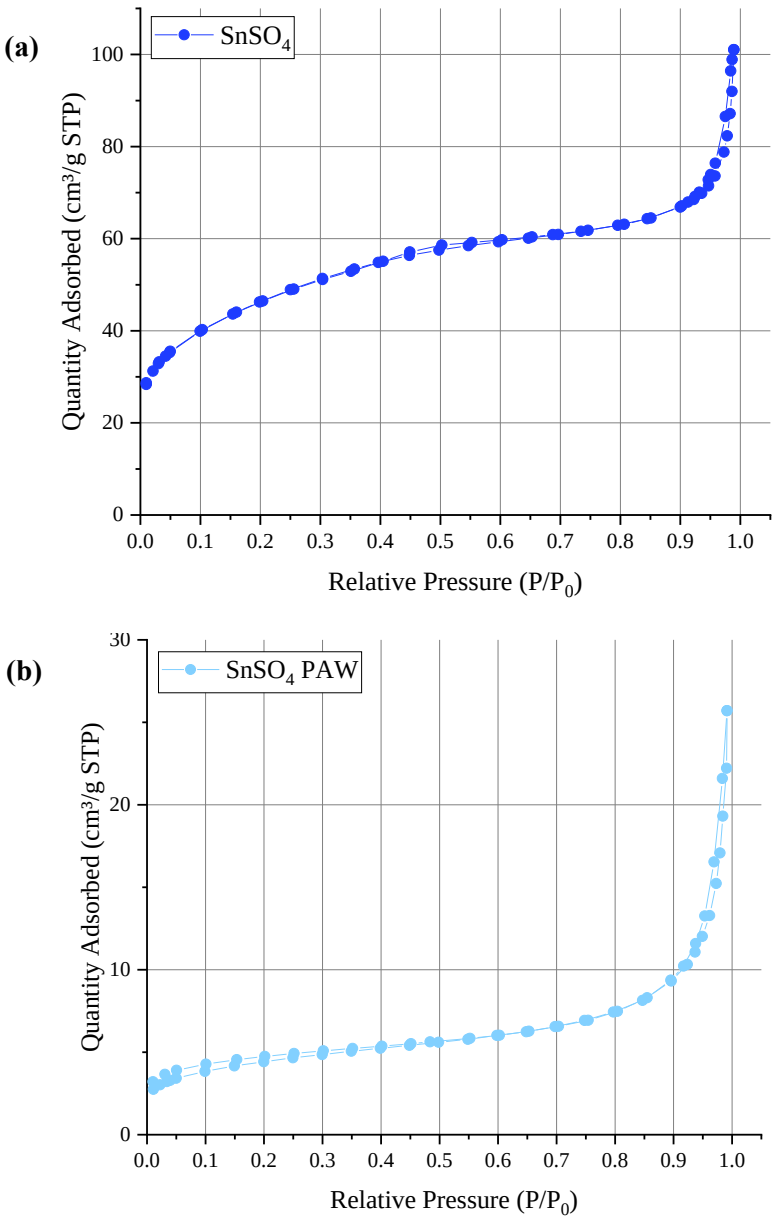
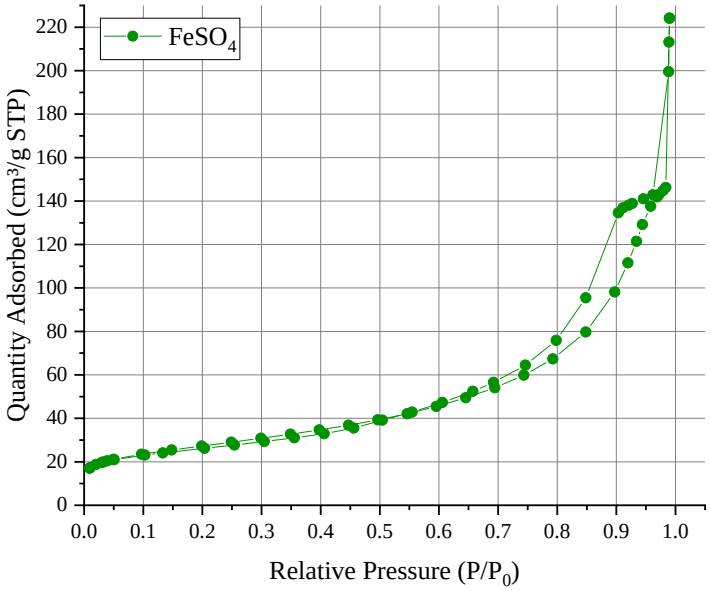


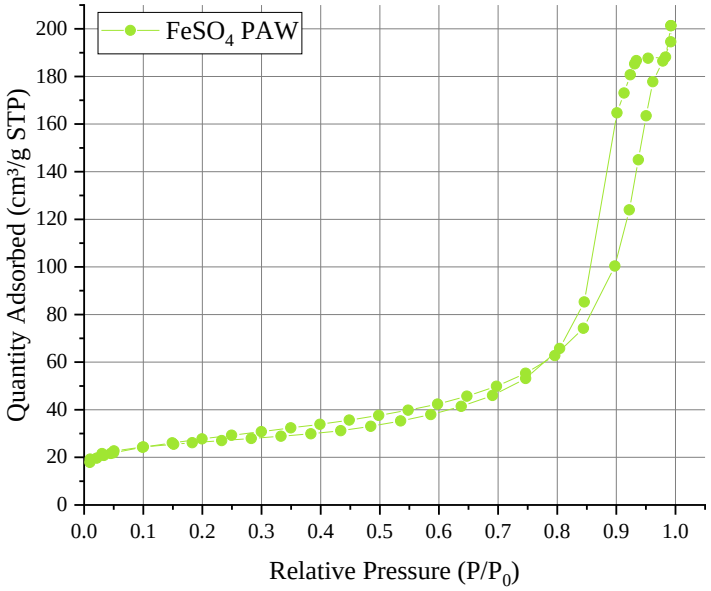
Figure SI.13c: Isotherm obtained by N_2-physisorption for solids obtained from $SnSO_4$ (a) by direct exposure and (b) by PAW

SI.14. Isotherms obtained by N_2-physisorption for solid developed with $FeSO_4$ by direct exposure and by PAW with a break of 30, 60 and 90 min

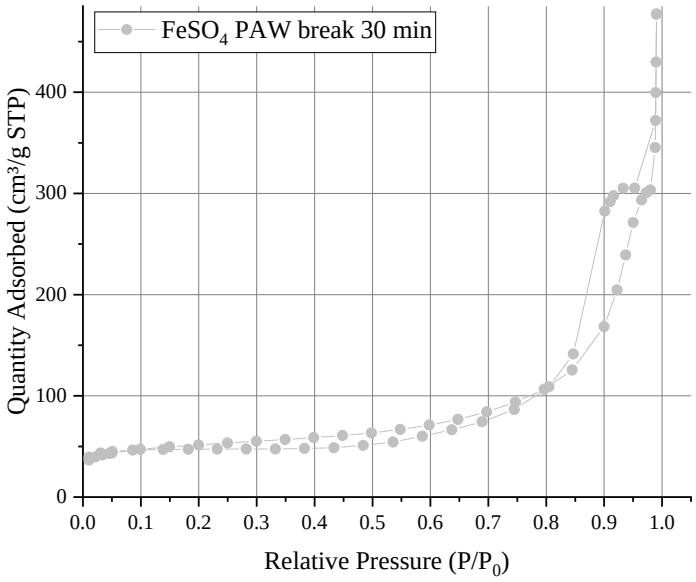
(a)



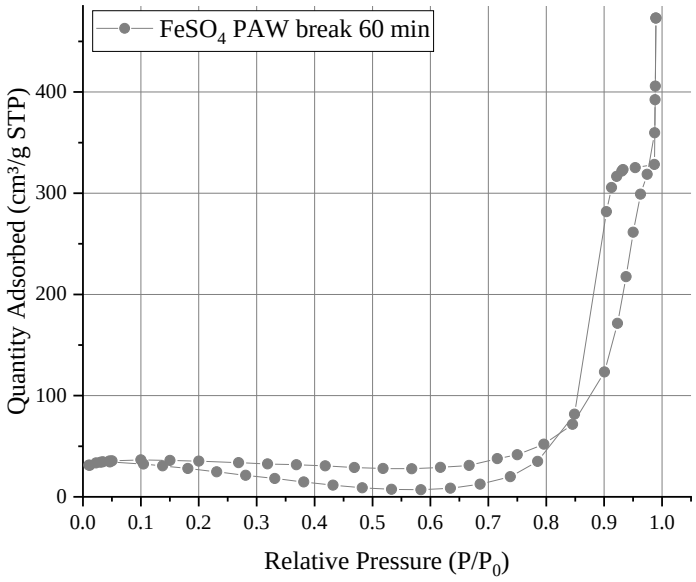
(b)



(c)


FeSO4 PAW break 30 min
Quantity Adsorbed (cm³/g STP)
0
100
200
300
400
0.0
0.1
0.2
0.3
0.4
0.5
0.6
0.7
0.8
0.9
1.0
Relative Pressure (P/P0)

(d)


FeSO4 PAW break 60 min
Quantity Adsorbed (cm³/g STP)
0
100
200
300
400
0.0
0.1
0.2
0.3
0.4
0.5
0.6
0.7
0.8
0.9
1.0
Relative Pressure (P/P0)

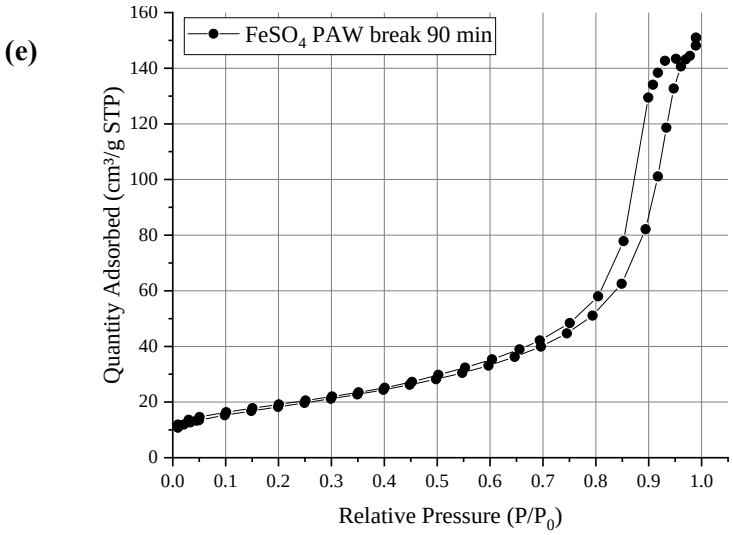


Figure SI.14: Isotherm obtained by N_2-physisorption for solids obtained from $FeSO_4$ (a) by direct exposure, (b) by PAW, (c) by PAW with 30 min break, (d) by PAW with 60 min break and (e) by PAW with 90 min break

SI.15. XRD data of the Au/TiO_2 solids obtained after (non-)exposure to the GP

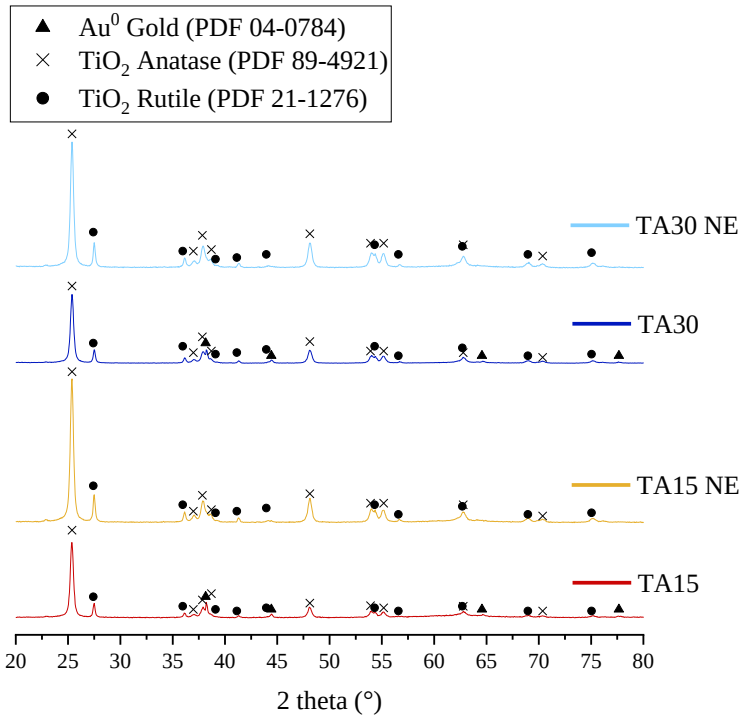
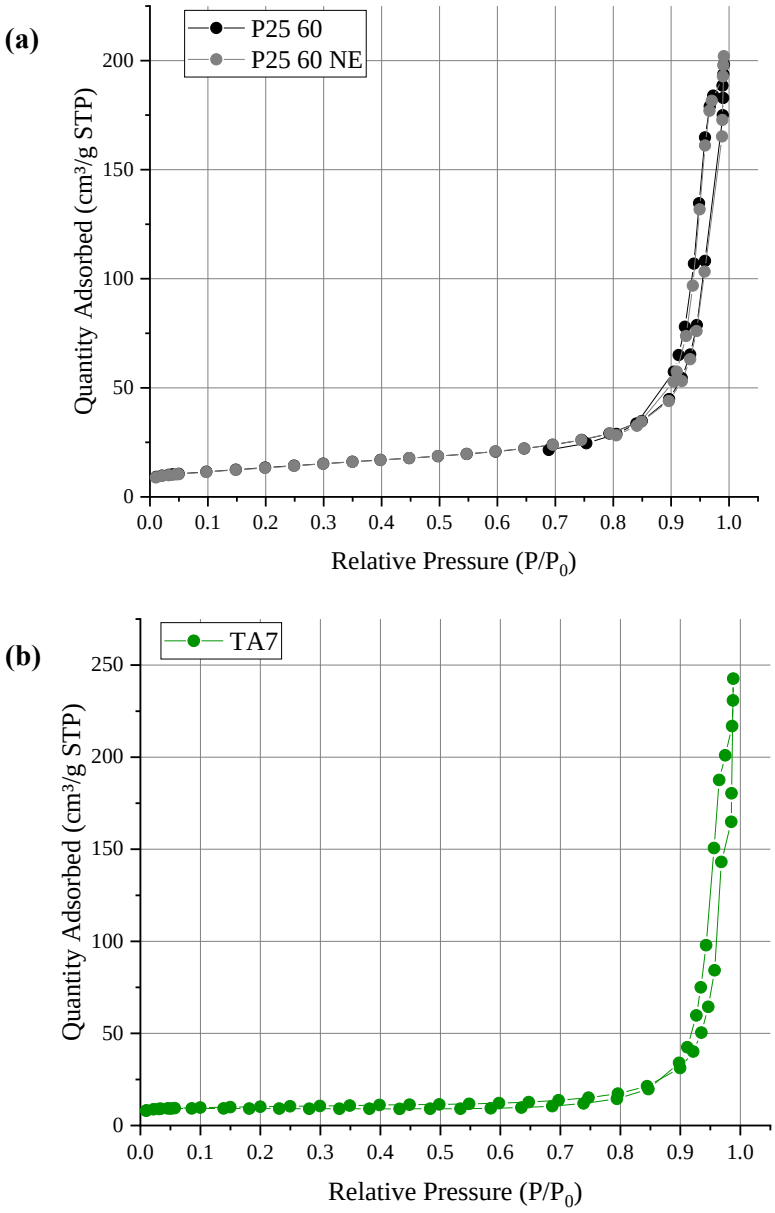
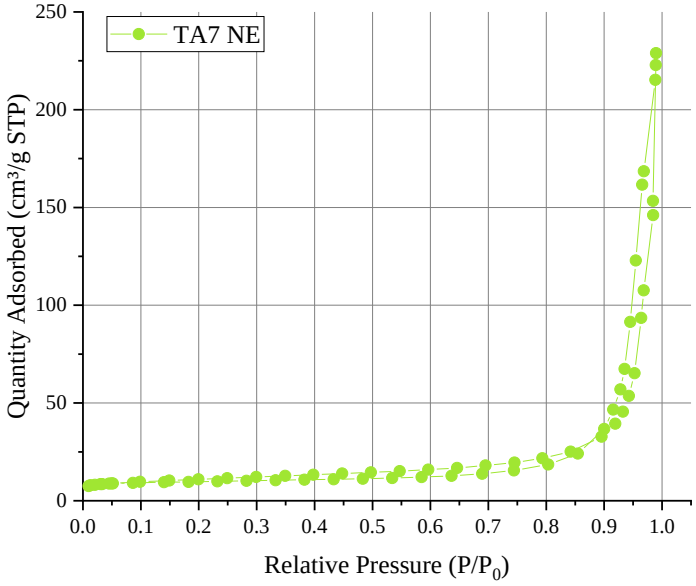


Figure SI.15: XRD data of the Au/TiO_2 solids obtained after (non-)exposure to the GP

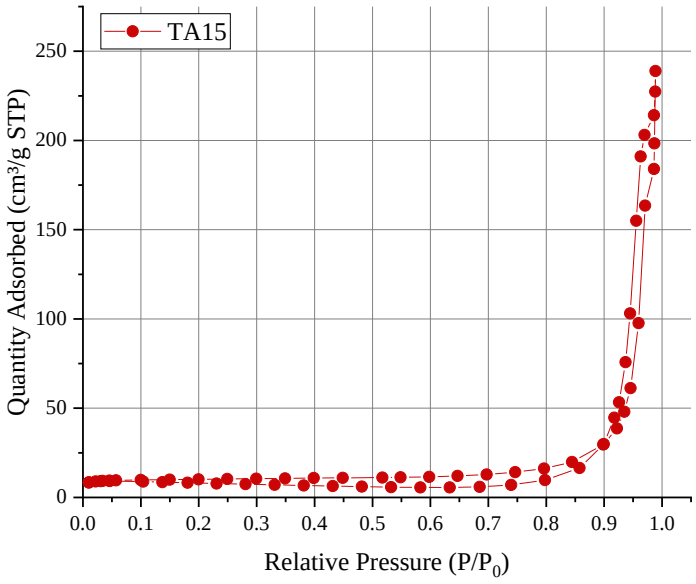
SI.16. Isotherms obtained by N_2-physisorption for solid developed for Au/TiO_2



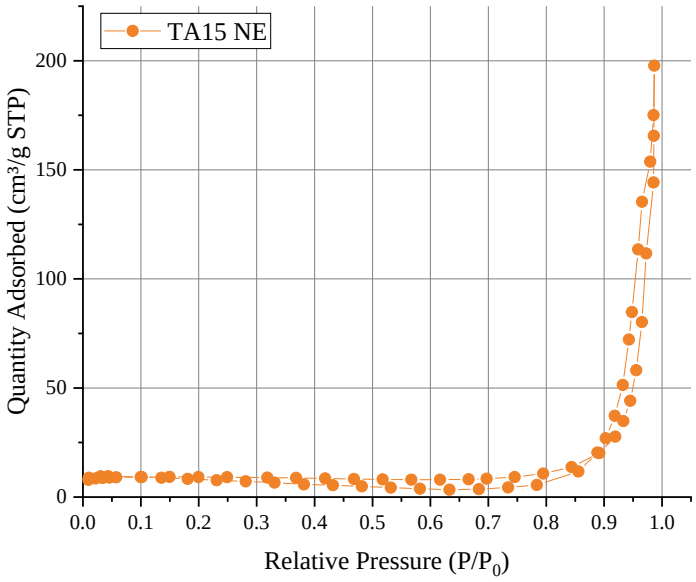
(c)


TA7 NE
Quantity Adsorbed (cm³/g STP)
Relative Pressure (P/P0)
0
50
100
150
200
250
0.0
0.1
0.2
0.3
0.4
0.5
0.6
0.7
0.8
0.9
1.0

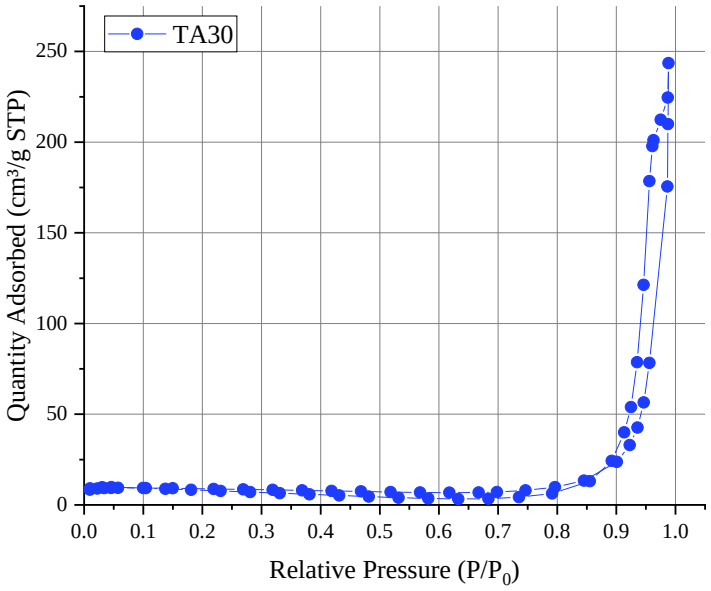
(d)


TA15
Quantity Adsorbed (cm³/g STP)
Relative Pressure (P/P0)
0
50
100
150
200
250
0.0
0.1
0.2
0.3
0.4
0.5
0.6
0.7
0.8
0.9
1.0

(e)


TA15 NE
Quantity Adsorbed (cm³/g STP)
0
50
100
150
200
0.0
0.1
0.2
0.3
0.4
0.5
0.6
0.7
0.8
0.9
1.0
Relative Pressure (P/P0)

(f)


TA30
Quantity Adsorbed (cm³/g STP)
0
50
100
150
200
250
0.0
0.1
0.2
0.3
0.4
0.5
0.6
0.7
0.8
0.9
1.0
Relative Pressure (P/P0)

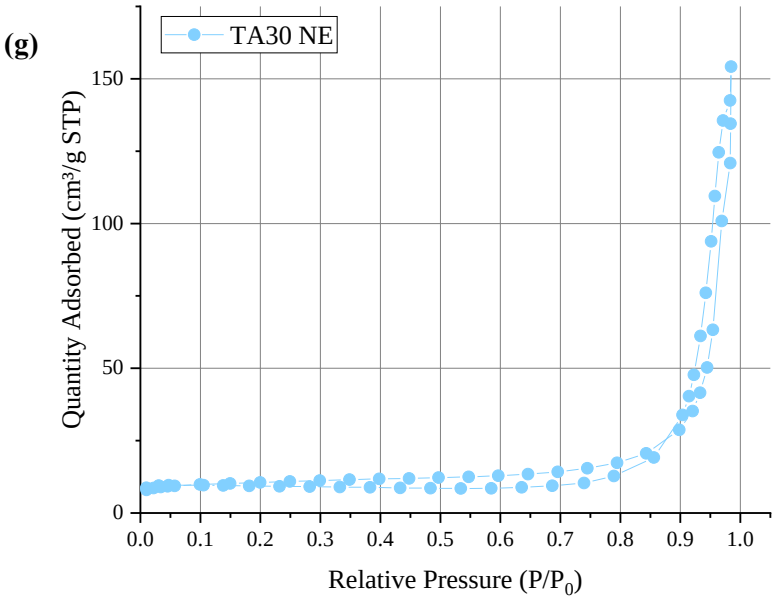


Figure SI.16: Isotherm obtained by N_2-physisorption for solids obtained from (a) P25 60 and P25 60 NE, (b) TA7, (c) TA7 NE, (d) TA15, (e) TA15 NE, (f)TA30 , (g) TA30 NE

SI.17. XPS peaks of Au4f for Au/TiO_2 samples

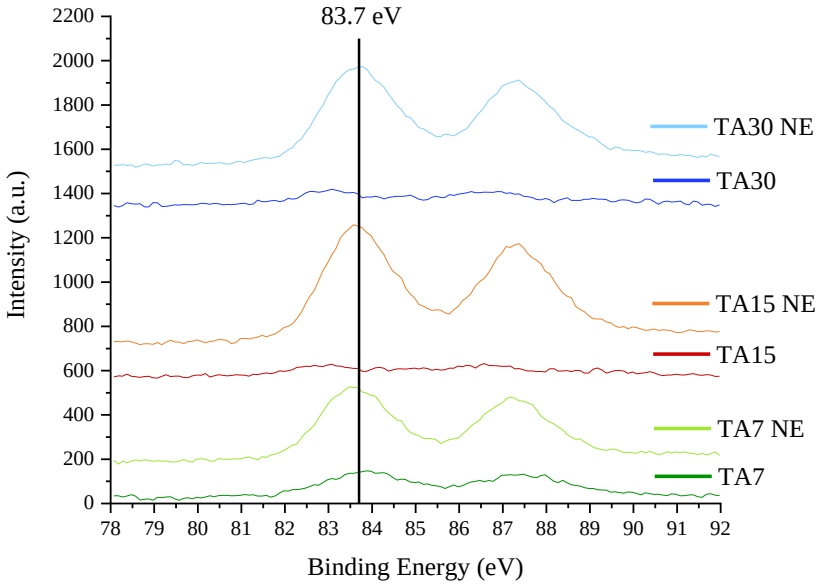
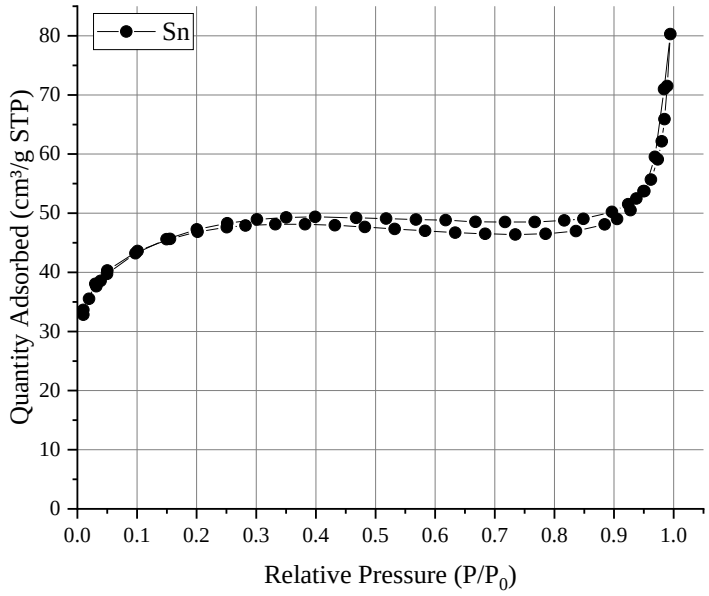


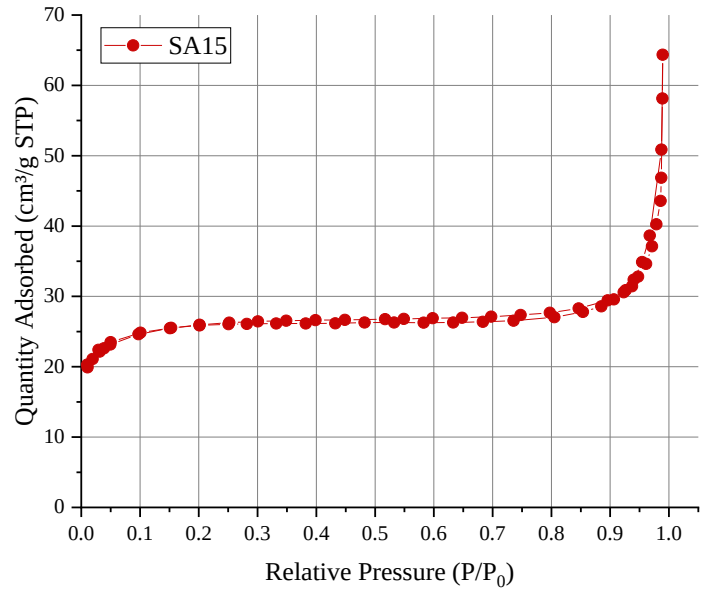
Figure SI.17: XPS peaks of Au4f for Au/TiO_2 samples

SI.18. Isotherms obtained by N_2-physisorption for solid developed for Au/SnO_2

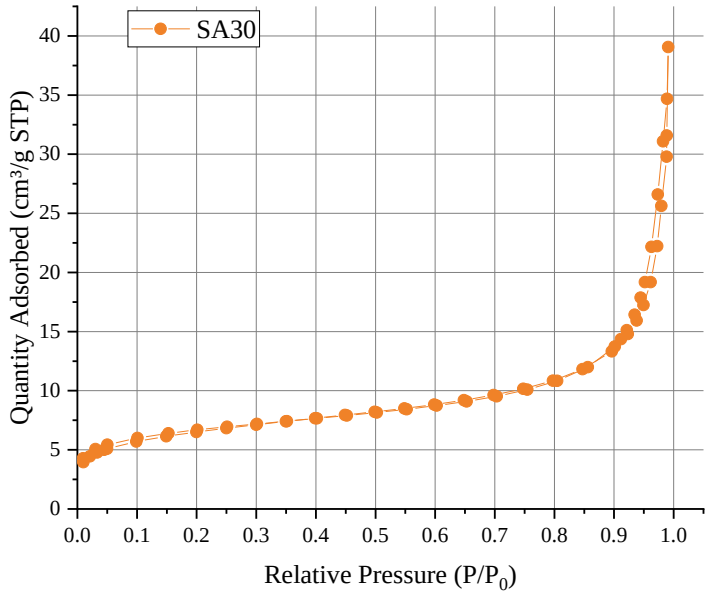
(a)



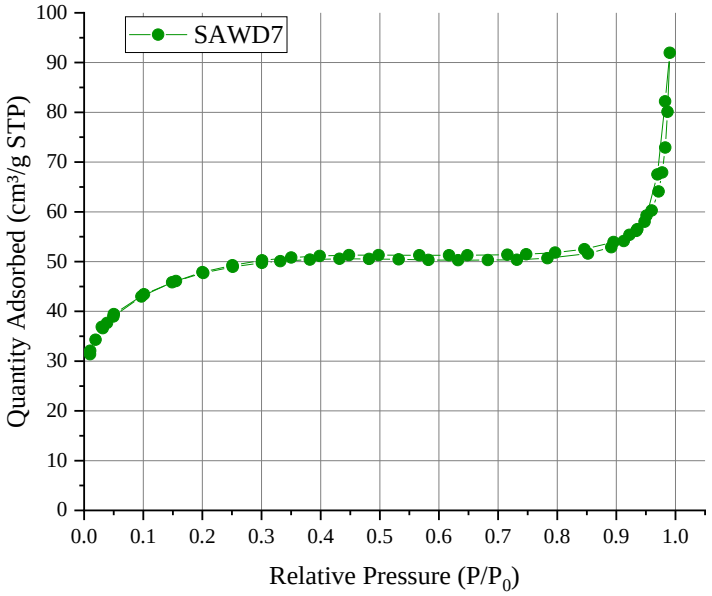
(b)



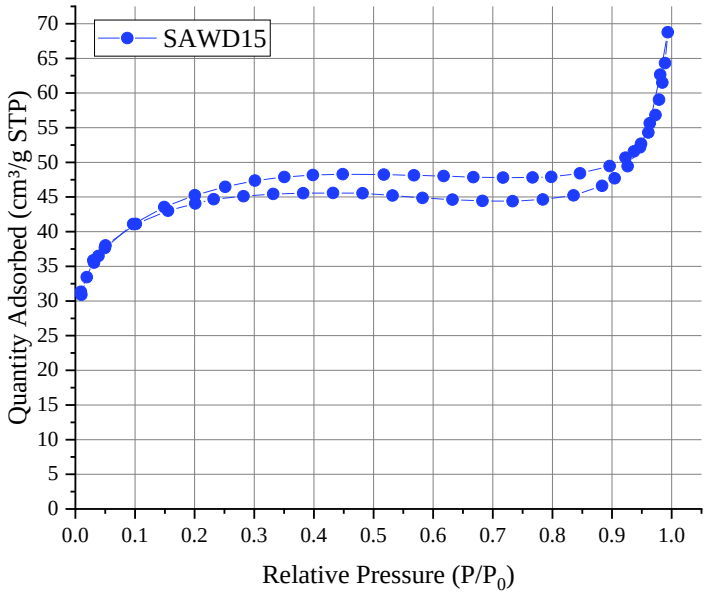
(c)


SA30
Quantity Adsorbed (cm³/g STP)
Relative Pressure (P/P0)
0
5
10
15
20
25
30
35
40
0.0
0.1
0.2
0.3
0.4
0.5
0.6
0.7
0.8
0.9
1.0

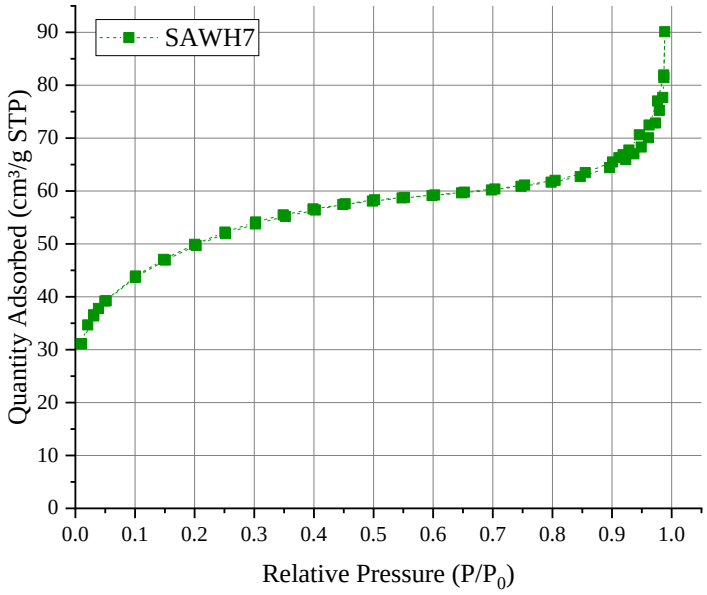
(d)


SAWD7
Quantity Adsorbed (cm³/g STP)
Relative Pressure (P/P0)
0
10
20
30
40
50
60
70
80
90
100
0.0
0.1
0.2
0.3
0.4
0.5
0.6
0.7
0.8
0.9
1.0

(e)


SAWD15
Quantity Adsorbed (cm³/g STP)
Relative Pressure (P/P0)
0
5
10
15
20
25
30
35
40
45
50
55
60
65
70
0.0
0.1
0.2
0.3
0.4
0.5
0.6
0.7
0.8
0.9
1.0

(f)


SAWH7
Quantity Adsorbed (cm³/g STP)
Relative Pressure (P/P0)
0
10
20
30
40
50
60
70
80
90
0.0
0.1
0.2
0.3
0.4
0.5
0.6
0.7
0.8
0.9
1.0

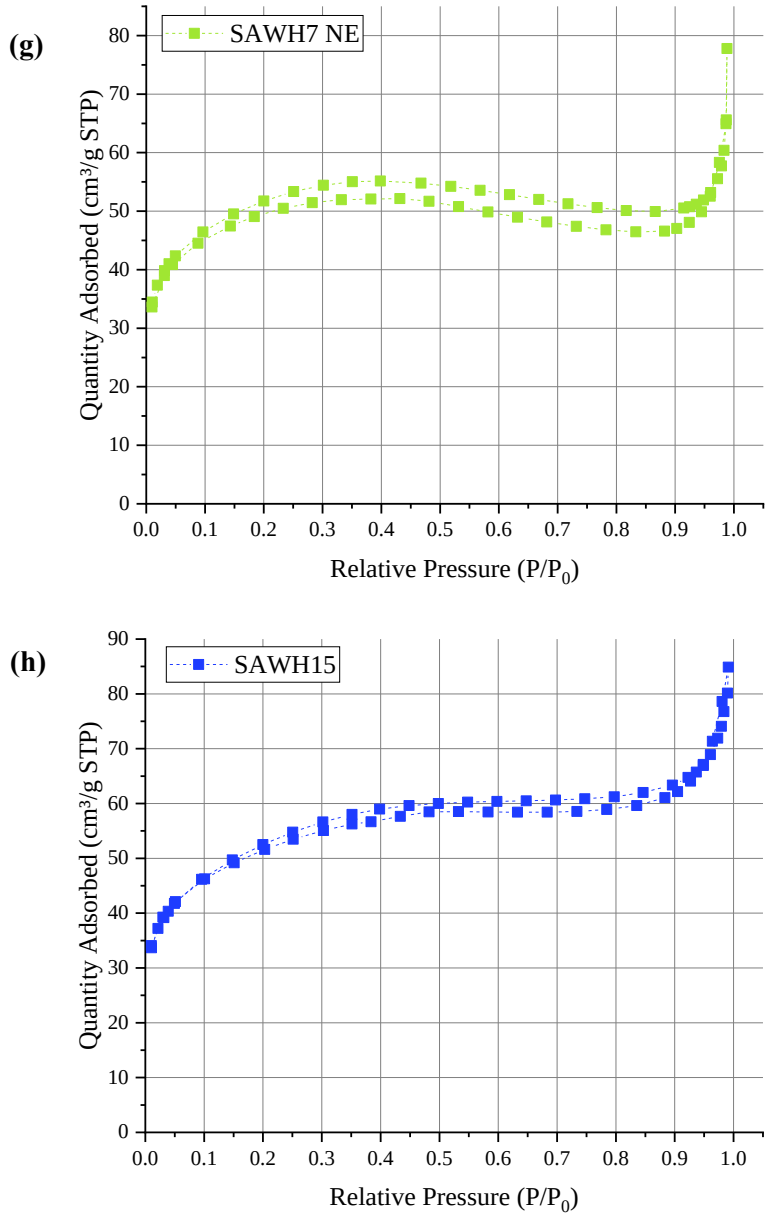


Figure SI.18: Isotherm obtained by N_2-physisorption for solids obtained from (a) Sn, (b) SA15, (c) SA30, (d) SAWD7, (e) SAWD15 , (f) SAWH7, (g) SAWH7 NE and (h) SAWH15

SI.19. Isotherms obtained by N_2-physisorption for solid developed for Au/SnO_2

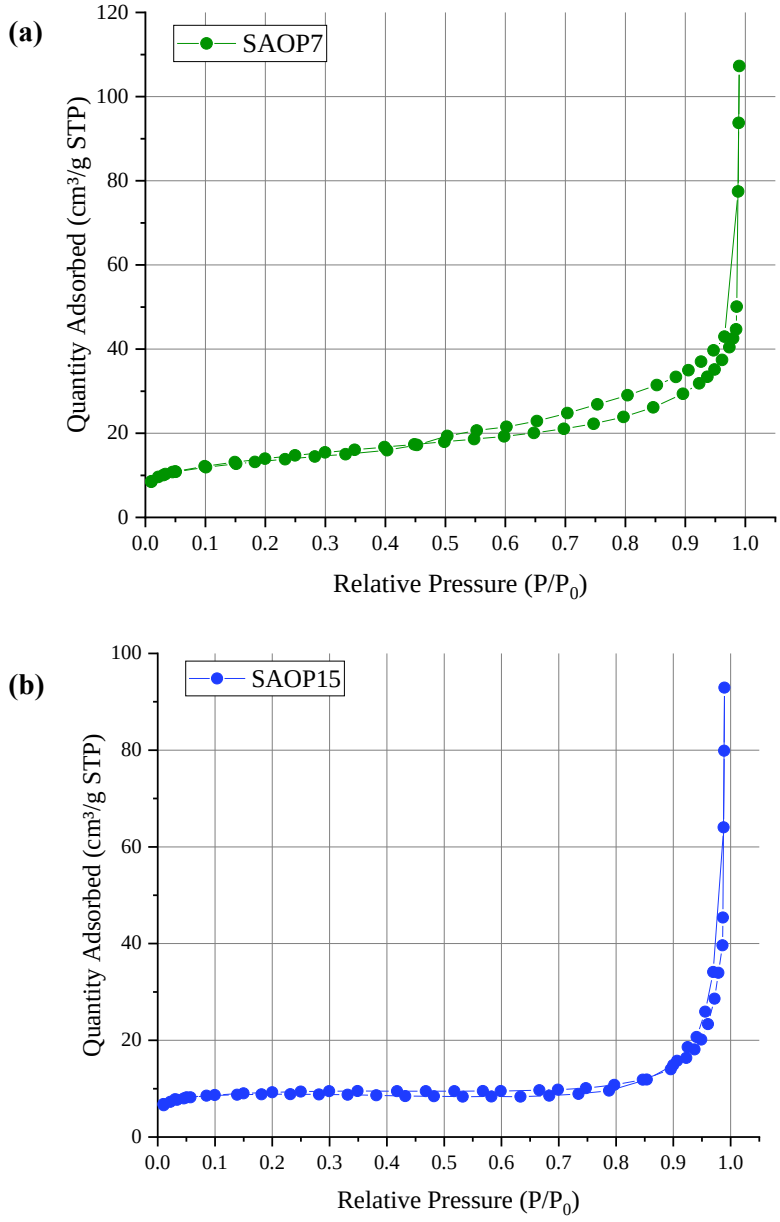


Figure SI.19: Isotherm obtained by N_2-physisorption for solids obtained from (a) SAOP7 and (b) SAOP15

References

[1] J.R.H. Ross, Heterogeneous Catalysis: Fundamentals and Applications, Elsevier, Amsterdam, The Netherlands, 2012.

[2] M. Boudart, B.H. Davis, H. Heinemann, Introduction, in: G. Ertl, H. Knözinger, J. Weitkamp (Eds.), Handb. Heterog. Catal., 1st ed., Wiley, 1997: pp. 1–48. https://doi.org/10.1002/9783527619474.ch1.

[3] M.V. Twigg, Catalyst Handbook, 2nd ed., Wolfe, England, 1989.

[4] C.N. Satterfield, Heterogeneous Catalysis in Industrial Practice, 2nd ed., McGraw-Hill, USA, 1991.

[5] D. Kolb, Catalysis, J. Chem. Educ. 56 (1979) 743–747.

[6] U.S. Department of Energy, DOE Explains...Catalysts, Energy.Gov (n.d.). https://www.energy.gov/science/doe-explainscatalysts (accessed March 18, 2024).

[7] Lumen Learning, Catalysis, (n.d.). https://uen.pressbooks.pub/introductorychemistry/chapter/catalysis/ (accessed March 18, 2024).

[8] L. Lerner, 7 things you may not know about catalysis, Argonne Natl. Lab. (2011). https://www.anl.gov/article/7-things-you-may-not-know-about-catalysis (accessed March 18, 2024).

[9] A.Z. Fadhel, P. Pollet, C.L. Liotta, C.A. Eckert, Combining the Benefits of Homogeneous and Heterogeneous Catalysis with Tunable Solvents and Nearcritical Water, Molecules 15 (2010) 8400–8424. https://doi.org/10.3390/molecules15118400.

[10] J. Védrine, Heterogeneous Catalysis on Metal Oxides, Catalysts 7 (2017) 341. https://doi.org/10.3390/catal7110341.

[11] J. Hagen, Industrial Catalysis, Wiley, Germany, 2005.

[12] F. Devred, P. Dulgheru, N. Kruse, Elementary Steps in Heterogeneous Catalysis, in: Compr. Inorg. Chem. II, Elsevier, 2013: pp. 7–38.

[13] G. Ertl, H. Knözinger, J. Weitkamp, Preparation of Solid Catalysts, Wiley-VCH, New-York, 1999.

[14] C. Perego, P. Villa, Catalyst preparation methods, Catal. Today 34 (1997) 281–305. https://doi.org/10.1016/S0920-5861(96)00055-7.

[15] G.J. Hutchings, J.C. Védrine, Heterogeneous Catalyst Preparation, in: M. Baerns (Ed.), Basic Princ. Appl. Catal., Springer Berlin Heidelberg, Berlin, Heidelberg, 2004: pp. 215–258.

[16] X. Carrier, S. Royer, E. Marceau, Synthesis of metal oxide catalysts, in: Met. Oxides Heterog. Catal., Elsevier, 2018: pp. 43–103.

[17] J.-P. Jolivet, De la solution à l'oxyde, CNRS Editions, Paris, 1994.

[18] J.F. LePage, R. Schlögl, M.S. Wainwright, F. Schü, K. Unger, E.I. Ko, H. Jacobsen, P. Kleinschmit, R.G. Menon, B. Delmon, K. -Y. Lee, M. Misino, S.T. Oyama, Preparation of Solid Catalysts: Sections 2.0 and 2.1, in: G. Ertl, H. Knözinger, J. Weitkamp (Eds.), Handb. Heterog. Catal., 1st ed., Wiley, 1997: pp. 49–138.

[19] S.S. Latthe, A.B. Gurav, C.S. Maruti, R.S. Vhatkar, Recent Progress in Preparation of Superhydrophobic Surfaces: A Review, J. Surf. Eng. Mater. Adv. Technol. (2012) 76–94. https://doi.org/10.4236/jsemat.2012.22014.

[20] J. De Bellis, H. Petersen, J. Ternieden, N. Pfänder, C. Weidenthaler, F. Schüth, Direct Dry Synthesis of Supported Bimetallic Catalysts: A Study on Comminution and Alloying of Metal Nanoparticles, Angew. Chem. Int. Ed. 61 (2022) e202208016. https://doi.org/10.1002/anie.202208016.

[21] K. Köhler, Preparation of Supported Catalysts, (2006).

[22] A. Doubla, É.B. Tsagou-Sobze, D. Moussa, R. Burlica, E. Hnatiuc, J.-L. Brisset, Destruction plasmachimique d'urée et de thiourée par décharge électrique à pression atmosphérique, Rev. Sci. Eau 20 (2007) 265–272. https://doi.org/10.7202/016171ar.

[23] F. Manaigo, Study of a gliding arc discharge for sustainable nitrogen fixation into NOX, Universtity of Mons, University of Antwerp, 2024.

[24] F.W. Boyom Tatchemo, Synthèse par plasma d'arc glissant des dioxydes de manganèse MnO2 : application à la dégradation catalytique de la Tartrazine Jaune dans les eaux usées, Thèse, Université catholique de Louvain, Université de Yaoundé I, 2018.

[25] A. Tiya Djowe, Adsorbants et catalyseurs à base d'argile préparés par voie plasmachimique pour la dépollution des eaux résiduaires industrielles, Thèse, Université catholique de Louvain, Université de Yaoundé I, 2014.

[26] A. Fridman, Plasma Chemistry, Cambridge University Press, Cambridge, 2008.

[27] T.-J. Koyaouili, Etude des procédés plasmas dans l'élimination des polluants organiques persistants dans les effluents aqueux, Université Pierre et Marie Curie, Université de Yaoundé I, 2016.

[28] G. Petitpas, J. Rollier, A. Darmon, J. Gonzalezaguilar, R. Metkemeijer, L. Fulcheri, A comparative study of non-thermal plasma assisted reforming technologies, Int. J. Hydrog. Energy 32 (2007) 2848–2867. https://doi.org/10.1016/j.ijhydene.2007.03.026.

[29] J.C. Whitehead, Plasma–catalysis: the known knowns, the known unknowns and the unknown unknowns, J. Phys. Appl. Phys. 49 (2016). https://doi.org/10.1088/0022-3727/49/24/243001.

[30] A. Czernichowski, Gliding arc: Applications to engineering and environment control, Pure Appl. Chem. 66 (1994) 1301–1310. https://doi.org/10.1351/pac199466061301.

[31] J.-L. Brisset, J. Pawlat, Chemical Effects of Air Plasma Species on Aqueous Solutes in Direct and Delayed Exposure Modes: Discharge, Post-discharge and Plasma Activated Water, Plasma Chem. Plasma Process. 36 (2016) 355–381. https://doi.org/10.1007/s11090-015-9653-6.

[32] G. Kamgang-Youbi, J.-M. Herry, M.-N. Bellon-Fontaine, J.-L. Brisset, A. Doubla, M. Naïtali, Evidence of Temporal Postdischarge Decontamination of Bacteria by Gliding Electric Discharges: Application to Hafnia alvei, Appl. Environ. Microbiol. 73 (2007) 4791–4796. https://doi.org/10.1128/AEM.00120-07.

[33] J.-L. Brisset, D. Moussa, A. Doubla, E. Hnatiuc, B. Hnatiuc, G. Kamgang Youbi, J.-M. Herry, M. Naïtali, M.-N. Bellon-Fontaine, Chemical Reactivity of Discharges and Temporal Post-Discharges in Plasma Treatment of Aqueous Media: Examples of Gliding Discharge Treated Solutions, Ind. Eng. Chem. Res. 47 (2008) 5761–5781. https://doi.org/10.1021/ie701759y.

[34] M.R. Ghezzar, F. Abdelmalek, M. Belhadj, N. Benderdouche, A. Addou, Gliding arc plasma assisted photocatalytic degradation of anthraquinonic acid green 25 in solution with TiO2, Appl. Catal. B Environ. 72 (2007) 304–313. https://doi.org/10.1016/j.apcatb.2006.11.008.

[35] K.C. Sabat, P. Rajput, R.K. Paramguru, B. Bhoi, B.K. Mishra, Reduction of Oxide Minerals by Hydrogen Plasma: An Overview, Plasma Chem. Plasma Process. 34 (2014) 1–23. https://doi.org/10.1007/s11090-013-9484-2.

[36] H. Lesueur, A. Czernichowsky, J. Chapelle, Dispositif de génération de plasma basse température par formation de décharges électriques glissantes, 2639172, n.d.

[37] E.B. Tsagou-Sobze, D. Moussa, A. Doubla, E. Hnatiuc, J.-L. Brisset, Gliding discharge-induced oxidation of a toxic alkaloid, J. Hazard. Mater. 152 (2008) 446–449. https://doi.org/10.1016/j.jhazmat.2007.12.066.

[38] A. Czernichowski, H. Nassar, A. Ranaivosoloarimanana, A.A. Fridman, M. Simek, K. Musiol, E. Pawelec, L. Dittrichova, Spectral and Electrical Diagnostics of Gliding Arc, Acta Phys. Pol. A 89 (1996) 595–603. https://doi.org/10.12693/APhysPolA.89.595.

[39] A. Doubla, L. Boubabello, M. Fotso, J. Brisset, Plasmachemical decolourisation of Bromothymol Blue by gliding electric discharge at atmospheric pressure, Dyes Pigments 77 (2008) 118–124. https://doi.org/10.1016/j.dyepig.2007.03.016.

[40] A. El-Zein, M. Talaat, G. El-Aragi, A. El-Amawy, Electrical Characteristics of Nonthermal Gliding Arc Discharge Reactor in Argon and Nitrogen Gases, IEEE Trans. Plasma Sci. 44 (2016) 1155–1159. https://doi.org/10.1109/tps.2016.2578301.

[41] J. Zhu, J. Gao, A. Ehn, M. Aldén, A. Larsson, Y. Kusano, Z. Li, Spatiotemporally resolved characteristics of a gliding arc discharge in a turbulent air flow at atmospheric pressure, Phys. Plasmas 24 (2017). https://doi.org/10.1063/1.4974266.

[42] F.W.B. Tatchemo, S. Nzali, G. Kamgang Youbi, A. Tiya Djowe, D.K. Saa, E. Acayanka, S. Laminsi, E.M. Gaigneaux, Gliding Arc Plasma Synthesis of MnO2 Nanorods for the Plasma-Catalytic Bleaching of Azoïc Amaranth Red Dye, Top. Catal. 60 (2017) 962–972. https://doi.org/10.1007/s11244-017-0761-9.

[43] J. Cech, L. Prokeš, M. Zemánek, L. Dostál, D. Šimek, J. Valenta, R. Žebrák, L. Zápotocký, P. Sťahel, Rotating Gliding Arc: Innovative Source for VOC Remediation, Plasma Phys. Technol. 6 (2019) 156–160. https://doi.org/10.14311/ppt.2019.2.156.

[44] A. Czernichowski, M. Czernichowski, Further development of plasma sources : the Glidarc-III, (2005).

[45] F. Manaigo, O. Samadi Bahnamiri, A. Chatterjee, A. Panepinto, A. Krumpmann, M. Michiels, A. Bogaerts, R. Snyders, Electrical Stability and Performance of a Nitrogen–Oxygen Atmospheric Pressure Gliding Arc Plasma, ACS Sustain. Chem. Eng. 12 (2024) 5211–5219. https://doi.org/10.1021/acssuschemeng.3c08257.

[46] W. Wang, B. Patil, S. Heijkers, V. Hessel, A. Bogaerts, Nitrogen Fixation by Gliding Arc Plasma: Better Insight by Chemical Kinetics Modelling, ChemSusChem 10 (2017) 2145–2157. https://doi.org/10.1002/cssc.201700095.

[47] S. Van Alphen, H. Ahmadi Eshtehardi, C. O'Modhrain, J. Bogaerts, H. Van Poyer, J. Creel, M.-P. Delplancke, R. Snyders, A. Bogaerts, Effusion nozzle for energy-efficient NOx production in a rotating gliding arc plasma reactor, Chem. Eng. J. 443 (2022) 136529. https://doi.org/10.1016/j.cej.2022.136529.

[48] D. Moussa, H. Vitrac, B.G. Chéron, E. Hnatiuc, A. Addou, J.L. Brisset, Acidity control of the oxidation reactions induced by non-thermal plasma treatment of aqueous effluents in pollutant abatment processes, Eur. Phys. J. Appl. Phys. 29 (2005) 308–312.

[49] R. Burlica, M.J. Kirkpatrick, B.R. Locke, Formation of reactive species in gliding arc discharges with liquid water, J. Electrost. 64 (2006) 35–43. https://doi.org/10.1016/j.elstat.2004.12.007.

[50] B. Benstaali, P. Boubert, B.G. Cheron, A. Addou, J.L. Brisset, Density and Rotational Temperature Measurements of the OH° and NO° Radicals Produced by a Gliding Arc in Humid Air, Plasma Chem. Plasma Process. 22 (2002) 553–571. https://doi.org/10.1023/A:1021371529955.

[51] W. Van Boxem, J. Van der Paal, Y. Gorbanev, S. Vanuytsel, E. Smits, S. Dewilde, A. Bogaerts, Anti-cancer capacity of plasma-treated PBS: effect of chemical composition on cancer cell cytotoxicity, Sci. Rep. 7 (2017) 16478. https://doi.org/10.1038/s41598-017-16758-8.

[52] A. Khlyustova, C. Labay, Z. Machala, M.-P. Ginebra, C. Canal, Important parameters in plasma jets for the production of RONS in liquids for plasma medicine: A brief review, Front. Chem. Sci. Eng. 13 (2019) 238–252. https://doi.org/10.1007/s11705-019-1801-8.

[53] Y. Gorbanev, A. Privat-Maldonado, A. Bogaerts, Analysis of Short-Lived Reactive Species in Plasma–Air–Water Systems: The Dos and the Do Nots, Anal. Chem. 90 (2018) 13151–13158. https://doi.org/10.1021/acs.analchem.8b03336.

[54] P.J. Bruggeman, M.J. Kushner, B.R. Locke, J.G.E. Gardeniers, W.G. Graham, D.B. Graves, R.C.H.M. Hofman-Caris, D. Maric, J.P. Reid, E. Ceriani, D. Fernandez Rivas, J.E. Foster, S.C. Garrick, Y. Gorbanev, S. Hamaguchi, F. Iza, H. Jablonowski, E. Klimova, J. Kolb, F. Krcma, P. Lukes, Z. Machala, I. Marinov, D. Mariotti, S. Mededovic Thagard, D. Minakata, E.C. Neyts, J. Pawlat, Z.L. Petrovic, R. Pflieger, S. Reuter, D.C. Schram, S. Schröter, M. Shiraiwa, B. Tarabová, P.A. Tsai, J.R.R. Verlet, T. Von Woedtke, K.R. Wilson, K. Yasui, G. Zvereva, Plasma–liquid interactions: a review and roadmap, Plasma Sources Sci. Technol. 25 (2016) 053002. https://doi.org/10.1088/0963-0252/25/5/053002.

[55] S.R. Sun, S. Kolev, H.X. Wang, A. Bogaerts, Coupled gas flow-plasma model for a gliding arc: investigations of the back-breakdown phenomenon and its effect on the gliding arc characteristics, Plasma Sources Sci. Technol. 26 (2016). https://doi.org/10.1088/0963-0252/26/1/015003.

[56] A. Tiya-Djowe, M.-A. Dourges, H. Deleuze, Tuning the “O” vacancies density in SnO2 nanocrystals during and after humid air plasma synthesis: implications on the photocatalytic performances under UV light, J. Mater. Sci. 55 (2020) 4792–4807. https://doi.org/10.1007/s10853-019-04335-5.

[57] A. Tiya-Djowe, E. Acayanka, A.P. Mbouopda, W. Boyom-Tatchemo, S. Laminsi, E.M. Gaigneaux, Producing oxide catalysts by exploiting the chemistry of gliding arc atmospheric plasma in humid air, Catal. Today 334 (2019) 104–112. https://doi.org/10.1016/j.cattod.2019.01.008.

[58] R. Seutcha, G. Kamgang-Youbi, E. Acayanka, V. Vermile, F. Devred, E.M. Gaigneaux, S. Laminsi, Plasma-synthesis of various polymorphs of tungsten trioxide nanoparticles using gliding electric

discharge in humid air: characterization and photocatalytic properties, Plasma Sci. Technol. 25 (2023) 125502. https://doi.org/10.1088/2058-6272/ace235.

[59] F.W. Boyom-Tatchemo, F. Devred, G. Ndiffo-Yemeli, S. Laminsi, E.M. Gaigneaux, Plasma-induced redox reactions synthesis of nanosized α-, γ- and δ-MnO2 catalysts for dye degradation, Appl. Catal. B Environ. 260 (2020) 118159. https://doi.org/10.1016/j.apcatb.2019.118159.

[60] A.P. Mbouopda, E. Acayanka, F.W. Boyom-Tatchemo, G.Y. Kamgang, A.M. Nzeufa, S. Laminsi, D. Richard, New-route synthesis of N-doped TiO2 via exposing the TiCl3 precursor to non-thermal quenched plasma at various times, Mater. Chem. Phys. 206 (2018) 224–231. https://doi.org/10.1016/j.matchemphys.2017.12.019.

[61] A. Tiya-Djowe, S. Laminsi, G.L. Noupeyi, E.M. Gaigneaux, Non-thermal plasma synthesis of sea-urchin like α-FeOOH for the catalytic oxidation of Orange II in aqueous solution, Appl. Catal. B Environ. 176–177 (2015) 99–106. https://doi.org/10.1016/j.apcatb.2015.03.053.

[62] E. Acayanka, A. Tiya Djowe, S. Laminsi, C.C. Tchoumkwé, S. Nzali, A. Poupi Mbouopda, P.T. Ndifon, E.M. Gaigneaux, Plasma-Assisted Synthesis of TiO2 Nanorods by Gliding Arc Discharge Processing at Atmospheric Pressure for Photocatalytic Applications, Plasma Chem. Plasma Process. 33 (2013) 725–735. https://doi.org/10.1007/s11090-013-9455-7.

[63] A. Tiya-Djowe, N. Ruth, G. Kamgang-Youbi, E. Acayanka, S. Laminsi, E.M. Gaigneaux, FeOx-kaolinite catalysts prepared via a plasma-assisted hydrolytic precipitation approach for Fenton-like reaction, Microporous Mesoporous Mater. 255 (2018) 148–155. https://doi.org/10.1016/j.micromeso.2017.07.036.

[64] E. Acayanka, D.S. kuete, G.Y. Kamgang, S. Nzali, S. Laminsi, P.T. Ndifon, Synthesis, Characterization and Photocatalytic Application of TiO2/SnO2 Nanocomposite Obtained Under Non-thermal Plasma Condition at Atmospheric Pressure, Plasma Chem. Plasma Process. 36 (2016) 799–811. https://doi.org/10.1007/s11090-016-9699-0.

[65] F.W. Boyom-Tatchemo, F. Devred, S. Laminsi, E.M. Gaigneaux, Temporal post-discharge reactions effect on the oxidative catalytic

properties of plasma-synthesized α-MnO2 nanorods, Appl. Catal. Gen. 616 (2021) 118109. https://doi.org/10.1016/j.apcata.2021.118109.

[66] The International Centre for Diffraction Data, ICDD (2020). http://www.icdd.com/.

[67] Y. Nosaka, A.Y. Nosaka, Comment on "Coumarin as a Quantitative Probe for Hydroxyl Radical Formation in Heterogeneous Photocatalysis," J Phys Chem C (2019). https://doi.org/10.1021/acs.jpcc.9b04190.

[68] K. Ishibashi, A. Fujishima, T. Watanabe, K. Hashimoto, Detection of active oxidative species in Ti02 photocatalysis using the fluorescence technique, Electrochem. Commun. 2 (2000) 207–210. https://doi.org/10.1016/S1388-2481(00)00006-0.

[69] M. Audemar, O. Vallcorba, I. Peral, J.-S. Thomann, A. Przekora, J. Pawlat, C. Canal, G. Ginalska, M. Kwiatkowski, D. Duday, S. Hermans, Catalytic enrichment of plasma with hydroxyl radicals in the aqueous phase at room temperature, Catal. Sci. Technol. 11 (2021) 1430–1442. https://doi.org/10.1039/d0cy01557a.

[70] A. Przekora, M. Audemar, J. Pawlat, C. Canal, J.-S. Thomann, C. Labay, M. Wojcik, M. Kwiatkowski, P. Terebun, G. Ginalska, S. Hermans, D. Duday, Positive Effect of Cold Atmospheric Nitrogen Plasma on the Behavior of Mesenchymal Stem Cells Cultured on a Bone Scaffold Containing Iron Oxide-Loaded Silica Nanoparticles Catalyst, Int. J. Mol. Sci. 21 (2020) 4738. https://doi.org/10.3390/ijms21134738.

[71] B.C. Rutely C., F. Jean-M., T. Walter Z., D.-B. Xochitl, S. Mika, Towards reliable quantification of hydroxyl radicals in the Fenton reaction using chemical probes, RSC Adv. 8 (2018) 5321–5330. https://doi.org/10.1039/c7ra13209c.

[72] V. Leandri, J.M. Gardner, M. Jonsson, Coumarin as a Quantitative Probe for Hydroxyl Radical Formation in Heterogeneous Photocatalysis, J. Phys. Chem. C 123 (2019) 6667–6674. https://doi.org/10.1021/acs.jpcc.9b00337.

[73] S. Nagarajan, N.C. Skillen, F. Fina, G. Zhang, C. Randorn, L.A. Lawton, J.T.S. Irvine, P.K.J. Robertson, Comparative assessment of visible light and UV active photocatalysts by hydroxyl radical

quantification, J. Photochem. Photobiol. Chem. 334 (2017) 13–19. https://doi.org/10.1016/j.jphotochem.2016.10.034.

[74] A. Wafi, E. Szabó-Bárdos, O. Horváth, É. Makó, M. Jakab, B. Zsirka, Coumarin-based quantification of hydroxyl radicals and other reactive species generated on excited nitrogen-doped TiO2, J. Photochem. Photobiol. Chem. 404 (2021) 112913. https://doi.org/10.1016/j.jphotochem.2020.112913.

[75] L. Pinto da Silva, R. Simkovitch, D. Huppert, J.C.G. Esteves da Silva, Combined experimental and theoretical study of the photochemistry of 4- and 3-hydroxycoumarin, J. Photochem. Photobiol. Chem. 338 (2017) 23–36. https://doi.org/10.1016/j.jphotochem.2017.01.032.

[76] G. Louit, S. Foley, J. Cabillic, H. Coffigny, F. Taran, A. Valleix, J.P. Renault, S. Pin, The reaction of coumarin with the OH radical revisited: hydroxylation product analysis determined by fluorescence and chromatography, Radiat. Phys. Chem. 72 (2005) 119–124.

[77] Z. Liu, C. Zhou, D. Liu, T. He, L. Guo, D. Xu, M.G. Kong, Quantifying the concentration and penetration depth of long-lived RONS in plasma-activated water by UV absorption spectroscopy, AIP Adv. 9 (2019) 15–14. https://doi.org/10.1063/1.5037660.

[78] S.B. Singh, Spectroscopic determination of iron by 1,10-phenanthroline method, (2020). https://doi.org/10.13140/RG.2.2.12030.74568.

[79] J. Kim, Y.J. Choe, S.H. Kim, K. Jeong, Enhancing the decomposition of refractory contaminants on SO42--functionalized iron oxide to accommodate surface SO4- generated via radical transfer from OH, Appl. Catal. B Environ. 252 (2019) 62–76. https://doi.org/10.1016/j.apcatb.2019.04.015.

[80] M. Pan, Z. Chen, C. Shan, Y. Wang, B. Pan, G. Gao, Photochemical activation of seemingly inert SO42− in specific water environments, Chemosphere 214 (2019) 399–407. https://doi.org/10.1016/j.chemosphere.2018.09.123.

[81] V.M. Amin, N.F. Olson, Spectrophotometric Determination of Hydrogen Peroxide in Milk, J. Dairy Sci. 50 (1967) 461–464. https://doi.org/10.3168/jds.S0022-0302(67)87447-2.

[82] F. Sandri, M. Danieli, M. Zecca, P. Centomo, Comparing Catalysts of the Direct Synthesis of Hydrogen Peroxide in Organic Solvent: is the Measure of the Product an Issue?, ChemCatChem 13 (2021) 2653–2663. https://doi.org/10.1002/cctc.202100306.

[83] D. Porter, M.D. Poplin, F. Holzer, W.C. Finney, B.R. Locke, Formation of Hydrogen Peroxide, Hydrogen, and Oxygen in Gliding Arc Electrical Discharge Reactors With Water Spray, IEEE Trans. Ind. Appl. 45 (2009) 623–629. https://doi.org/10.1109/07IAS.2007.175.

[84] R. Laurita, D. Barbieri, M. Gherardi, V. Colombo, P. Lukes, Chemical analysis of reactive species and antimicrobial activity of water treated by nanosecond pulsed DBD air plasma, Clin. Plasma Med. 3 (2015) 53–61. https://doi.org/10.1016/j.cpme.2015.10.001.

[85] R. Thirumdas, A. Kothakota, U. Annapure, K. Siliveru, R. Blundell, R. Gatt, V.P. Valdramidis, Plasma activated water (PAW): Chemistry, physico-chemical properties, applications in food and agriculture, Trends Food Sci. Technol. 77 (2018) 21–31.

[86] M. Pourbaix, Atlas of electrochemical equilibria in aqueous solutions, National association of corrosion engineers, Cebelcor, Texas, Bruxelles, 1967.

[87] A Study on the Preparation of Nitrous Acid, Unacademy (n.d.). https://unacademy.com/content/upsc/study-material/chemistry/a-study-on-the-preparation-of-nitrous-acid/ (accessed September 19, 2024).

[88] F. Hanon, S. Hermans, E.M. Gaigneaux, What are the species involved in the gliding arc plasma synthesis of heterogeneous catalysts?, Catal. Today 430 (2024) 114550. https://doi.org/10.1016/j.cattod.2024.114550.

[89] D.H. Ripin, D.A. Evans, pKa Table, (n.d.). chrome-extension://efaidnbmnnnibpcajpcglclefindmkaj/http://ccc.chem.pitt.edu/wipf/MechOMs/evans_pKa_table.pdf.

[90] M. Szabó, G. Bellér, J. Kalmár, I. Fábián, The Kinetics and Mechanism of Complex Redox Reactions in Aqueous Solution: The Tools of the Trade, in: Adv. Inorg. Chem., Elsevier, 2017: pp. 1–61. https://doi.org/10.1016/bs.adioch.2017.02.004.

[91] G. Charlot, L'analyse qualitative et les réactions en solution, 5th ed., Masson & Cie, Paris, 1963.

[92] R. Granados-Fernández, M.A. Montiel, S. Díaz-Abad, M.A. Rodrigo, J. Lobato, Platinum Recovery Techniques for a Circular Economy, Catalysts 11 (2021) 937. https://doi.org/10.3390/catal11080937.

[93] Mettler-Toledo International Inc all rights, Supersaturation and Crystallization, (n.d.). https://www.mt.com/ca/en/home/applications/L1_AutoChem_Applications/L2_Crystallization/Supersaturation_Application.html (accessed May 10, 2024).

[94] Solubility Product Constant and Common Ion Effect - Free Sketchy MCAT Lesson, (n.d.). https://www.sketchy.com/mcat-lessons/solubility-product-constant-and-common-ion-effect (accessed April 24, 2024).

[95] W. Feitknecht, P. Schindler, Solubility constants of metal oxides, metal hydroxides and metal hydroxide salts in aqueous solution, Pure Appl. Chem. 6 (1963). https://doi.org/10.1351/pac196306020125.

[96] T. Rees, The stability of potassium permanganate solutions, J. Chem. Educ. 64 (1987) 1058. https://doi.org/10.1021/ed064p1058.

[97] American Elements, Ruthenium(IV) Oxide, Am. Elem. (n.d.). https://www.americanelements.com/ruthenium-iv-oxide-12036-10-1 (accessed May 11, 2024).

[98] G. Korotcenkov, L.B. Gulina, B. Cho, V. Brinzari, V.P. Tolstoy, Synthesis by successive ionic layer deposition (SILD) methodology and characterization of gold nanoclusters on the surface of tin and indium oxide films, Pure Appl. Chem. 86 (2014) 801–817. https://doi.org/10.1515/pac-2013-1102.

[99] I.V. Mironov, E.V. Makotchenko, Equilibria in the system of aquachlorohydroxogold(III) complexes in aqueous solution, Russ. J. Inorg. Chem. 54 (2009) 2010–2017. https://doi.org/10.1134/S0036023609120298.

[100] A. Deffernez, S. Hermans, M. Devillers, Preparation of carbon-supported Pd and Au-Pd catalysts via optimized adsorption of

metallic complexes, Stud. Surf. Sci. Catal. 162 (2006) 79–86. https://doi.org/10.1016/S0167-2991(06)80893-1.

[101] M.D. Đurović, R. Puchta, Ž.D. Bugarčić, R. van Eldik, Studies on the reactions of $[AuCl_4]^-$ with different nucleophiles in aqueous solution, Dalton Trans 43 (2014) 8620–8632. https://doi.org/10.1039/c4dt00247d.

[102] I.V. Mironov, E.V. Makotchenko, The Hydrolysis of AuCl4− and the Stability of Aquachlorohydroxocomplexes of Gold(III) in Aqueous Solution, J. Solut. Chem. 38 (2009) 725–737. https://doi.org/10.1007/s10953-009-9400-9.

[103] P.K. Gallagher, D.W. Johnson, F. Schrey, Thermal Decomposition of Iron(II) Sulfates, J. Am. Ceram. Soc. 53 (1970) 666–670. https://doi.org/10.1002/jctb.5020260199.

[104] G. Ventruti, G. Della Ventura, M.A. Gomez, G. Capitani, M. Sbroscia, A. Sodo, High-temperature study of basic ferric sulfate, FeOHSO4, Phys. Chem. Miner. 47 (2020) 43. https://doi.org/10.1007/s00269-020-01113-7.

[105] X-ray Photoelectron Spectroscopy (XPS) Reference Pages, (n.d.). http://www.xpsfitting.com/search/label/Sulphur.

[106] H.J. McAulay, G. Podolsky, F. Chan, Low sulfur red iron oxide useful as a catalyst or catalyst component and a process for making low sulfur red iron oxide, US 2007/0014716 A1, 2007.

[107] T. Wang, Y. Jin, Z. Wang, Z. Yu, A study of the morphology of the goethite crystallization process, Chem. Eng. J. 69 (1998) 1–5. https://doi.org/10.1016/S1385-8947(97)00104-6.

[108] R. Ma, L. Xiang, X. Zhao, J. Yin, Progress in Preparation of Sea Urchin-like Micro-/Nanoparticles, Materials 15 (2022) 2846. https://doi.org/10.3390/ma15082846.

[109] B. Wang, H. Wu, L. Yu, R. Xu, T. Lim, X.W. (David) Lou, Template-free Formation of Uniform Urchin-like α -FeOOH Hollow Spheres with Superior Capability for Water Treatment, Adv. Mater. 24 (2012) 1111–1116. https://doi.org/10.1002/adma.201104599.

[110] C. House, G. Kelsall, Potential-pH diagrams for the Sn/H2O-Cl system, Electrochem. Acta 29 (1984) 1459–1464. https://doi.org/10.1016/0013-4686(84)87028-0.

[111] R. Edwards, The stabilities of secondary tin minerals. Part 2*: The hydrolysis of tin(II) sulphate and the stability of Sn30(OH)2SO 4, Mineral. Mag. 60 (1996) 427–432.

[112] E. Kaprara, N. Tziarou, K. Kalaitzidou, K. Simeonidis, L. Balcells, E.V. Pannunzio, A. Zouboulis, M. Mitrakas, The use of Sn(II) oxy-hydroxides for the effective removal of Cr(VI) from water: Optimization of synthesis parameters, Sci. Total Environ. 605–606 (2017) 190–198. https://doi.org/10.1016/j.scitotenv.2017.06.199.

[113] G.G. Graf, Tin, Tin Alloys, and Tin Compounds, in: Wiley-VCH Verlag GmbH & Co. KGaA (Ed.), Ullmanns Encycl. Ind. Chem., Wiley-VCH Verlag GmbH & Co. KGaA, Weinheim, Germany, 2000.

[114] B. Benstaali, D. Moussa, A. Addou, J.-L. Brisset, Plasma treatment of aqueous solutes: Some chemical properties of a gliding arc in humid air, Eur. Phys. J. Appl. Phys. 4 (1998) 171–179. https://doi.org/10.1051/epjap:199825.

[115] R. Cucciniello, A. Intiso, T. Siciliano, A.E. Palomares, J. Martínez-Triguero, J.L. Cerrillo, A. Proto, F. Rossi, Oxidative Degradation of Trichloroethylene over Fe2O3-doped Mayenite: Chlorine Poisoning Mitigation and Improved Catalytic Performance, Catalysts 9 (2019) 747. https://doi.org/10.3390/catal9090747.

[116] J. Li, P. Zhao, S. Liu, SnO –MnO –TiO2 catalysts with high resistance to chlorine poisoning for low-temperature chlorobenzene oxidation, Appl. Catal. Gen. 482 (2014) 363–369. https://doi.org/10.1016/j.apcata.2014.06.013.

[117] M. Li, F. Bi, Y. Xu, P. Hao, K. Xiang, Y. Zhang, S. Chen, J. Guo, X. Guo, W. Ding, Effect of Residual Chlorine on the Catalytic Performance of Co for CO Oxidation, ACS Catal. 9 (2019) 11676–11684. https://doi.org/10.1021/acscatal.9b03797.

[118] A. Ghaderi, S. Abbasi, F. Farahbod, Synthesis of SnO2 and ZnO Nanoparticles and SnO2-ZnO Hybrid for the Photocatalytic Oxidation of Methyl Orange, Irian J. Chem. Eng. 12 (2015).

[119] M.H. Saad, Contribution à l'étude d'un réacteur plasma en post-déchrage N2-H2 appliqué à la stérilisation, (n.d.) 114.

[120] D. Mariotti, J. Patel, V. Švrček, P. Maguire, Plasma-Liquid Interactions at Atmospheric Pressure for Nanomaterials Synthesis

and Surface Engineering: Plasma-Liquid Interactions at Atmospheric Pressure…, Plasma Process. Polym. 9 (2012) 1074–1085.

[121] F. Hanon, E.M. Gaigneaux, Post-discharge: An interesting step to improve heterogeneous catalysts synthesized by glidarc plasma?, Chem. Eng. J. 489 (2024) 151088. https://doi.org/10.1016/j.cej.2024.151088.

[122] J. Wang, H. Li, S. Meng, X. Ye, X. Fu, S. Chen, Controlled synthesis of Sn-based oxides via a hydrothermal method and their visible light photocatalytic performances, RSC Adv. 7 (2017) 27024–27032. https://doi.org/10.1039/c7ra04041e.

[123] E. Ovodok, M. Ivanovskaya, D. Kotsikau, I. Azarko, V. Kormosh, I. Alyaksev, Effect of structure and surface state ofnanocrystalline tin dioxide on its gas sensing properties, Phys. Chem. Appl. Nanostructures (2013) 625–628. https://doi.org/10.1142/9789814460187_0153.

[124] Q.-Y. Han, X. Wen, J.-Y. Gao, C.-S. Zhong, Y.-Y. Ni, Application of plasma-activated water in the food industry: A review of recent research developments, Food Chem. 405 (2023) 134797. https://doi.org/10.1016/j.foodchem.2022.134797.

[125] D.T. Thompson, Using gold nanoparticles for catalysis, Nano Today 2 (2007) 40–43. https://doi.org/10.1016/S1748-0132(07)70116-0.

[126] C.W. Corti, R.J. Holliday, D.T. Thompson, Progress towards the commercial application of gold catalysts, Top. Catal. 44 (2007) 331–343. https://doi.org/10.1007/s11244-007-0307-7.

[127] J. Gong, Structure and Surface Chemistry of Gold-Based Model Catalysts, Chem. Rev. 112 (2012) 2987–3054. https://doi.org/10.1021/cr200041p.

[128] T. Takei, T. Akita, I. Nakamura, T. Fujitani, M. Okumura, K. Okazaki, J. Huang, T. Ishida, M. Haruta, Heterogeneous Catalysis by Gold, in: Adv. Catal., Elsevier, 2012: pp. 1–126. https://doi.org/10.1016/B978-0-12-385516-9.00001-6.

[129] R. Zanella, S. Giorgio, C.R. Henry, C. Louis, Alternative Methods for the Preparation of Gold Nanoparticles Supported on TiO_2, J. Phys. Chem. B 106 (2002) 7634–7642. https://doi.org/10.1021/jp0144810.

[130] P.N. Njoki, I.-I.S. Lim, D. Mott, H.-Y. Park, B. Khan, S. Mishra, R. Sujakumar, J. Luo, C.-J. Zhong, Size Correlation of Optical and Spectroscopic Properties for Gold Nanoparticles, J. Phys. Chem. 111 (2007) 14664–14669. https://doi.org/10.1021/jp074902z.

[131] K. O'Connell, J.R. Regalbuto, High Sensitivity Silicon Slit Detectors for 1 nm Powder XRD Size Detection Limit, Catal. Lett. 145 (2015) 777–783. https://doi.org/10.1007/s10562-015-1479-6.

[132] C. Cellier, Catalytic removal of nitrogen- and sulfur-containing volatile organic compounds/Destruction catalytique des composés organiques volatils contenant de l'azote ou du soufre, UCLouvain, 2003.

[133] S. Ivanova, C. Petit, V. Pitchon, A new preparation method for the formation of gold nanoparticles on an oxide support, Appl. Catal. Gen. 267 (2004) 191–201. https://doi.org/10.1016/j.apcata.2004.03.004.

[134] P. Fernández-Ibáñez, F.J. de las Nieves, S. Malato, Titanium Dioxide/Electrolyte Solution Interface: Electron Transfer Phenomena, J. Colloid Interface Sci. 227 (2000) 510–516. https://doi.org/10.1006/jcis.2000.6917.

[135] K.P. De Jong, Synthesis of Solid Catalysts, Weinheim, Germany, 2009.

[136] S. Ivanova, V. Pitchon, C. Petit, H. Herschbach, A. Dorsselaer, E. Leize, Preparation of alumina supported gold catalysts: Gold complexes genesis, identification and speciation by mass spectrometry, Appl. Catal. Gen. 298 (2006) 203–210. https://doi.org/10.1016/j.apcata.2005.10.018.

[137] C. Cellier, S. Lambert, E.M. Gaigneaux, C. Poleunis, V. Ruaux, P. Eloy, C. Lahousse, P. Bertrand, J.-P. Pirard, P. Grange, Investigation of the preparation and activity of gold catalysts in the total oxidation of n-hexane, Appl. Catal. B Environ. 70 (2007) 406–416. https://doi.org/10.1016/j.apcatb.2006.01.026.

[138] R. Zanella, C. Louis, Influence of the conditions of thermal treatments and of storage on the size of the gold particles in Au/TiO2 samples, Catal. Today 107–108 (2005) 768–777. https://doi.org/10.1016/j.cattod.2005.07.008.

[139] A. Alshammari, V.N. Kalevaru, Supported Gold Nanoparticles as Promising Catalysts, in: N.K. Mishra (Ed.), Catal. Appl. Nano-Gold Catal., InTech, 2016. https://doi.org/10.5772/64394.

[140] A. Corma, H. Garcia, Supported gold nanoparticles as catalysts for organic reactions, Chem. Soc. Rev. 37 (2008) 2096. https://doi.org/10.1039/b707314n.

[141] A.S. Alshammari, Heterogeneous Gold Catalysis: From Discovery to Applications, Catalysts 9 (2019) 402. https://doi.org/10.3390/catal9050402.

[142] M. Van Der Verren, Innovative aerosol-based synthesis of nanostructured catalysts for the direct upgrading of glycerol, UCLouvain, 2023.

[143] J.-J. Zou, Y. Zhang, C.-J. Liu, Reduction of Supported Noble-Metal Ions Using Glow Discharge Plasma, Langmuir 22 (2006) 11388–11394. https://doi.org/10.1021/la061795b.

[144] M. Kosmulski, Isoelectric points and points of zero charge of metal (hydr)oxides: 50years after Parks' review, Adv. Colloid Interface Sci. 238 (2016) 1–61. https://doi.org/10.1016/j.cis.2016.10.005.

[145] D. Moussa, F. Abdelmalek, B. Benstaali, A. Addou, E. Hnatiuc, J.-L. Brisset, Acidity control of the gliding arc treatments of aqueous solutions: application to pollutant abatement and biodecontamination, Eur. Phys. J. Appl. Phys. 29 (2005) 189–199.

[146] Dynamic Light Scattering DLS, (n.d.). https://www.malvernpanalytical.com/en/products/technology/light-scattering/dynamic-light-scattering (accessed November 8, 2024).

[147] Mössbauer Spectroscopy, Methods (n.d.). https://serc.carleton.edu/msu_nanotech/methods/mossbauer.html (accessed November 8, 2024).

[148] Auger Electron Spectroscopy, Methods (n.d.). https://serc.carleton.edu/msu_nanotech/methods/aes.html (accessed November 8, 2024).

List of publications, communications and awards

Publications

- "What are the species involved in the gliding arc plasma synthesis of heterogeneous catalysts?", Fanny Hanon, Sophie Hermans, Eric M. Gaigneaux, Catalysis Today, Volume 430, 2024, 114550 https://doi.org/10.1016/j.cattod.2024.114550

- "Post-discharge: An interesting step to improve heterogeneous catalysts synthesized by glidarc plasma?", F. Hanon, E.M. Gaigneaux, Chemical Engineering Journal, Volume 489, 2024, 151088 https://doi.org/10.1016/j.cej.2024.151088

- "Improving the synthesis of heterogeneous catalysts by gliding arc plasma using the "no-cooling system"", Fanny Hanon, Eric M. Gaigneaux, Applied Materials Today, Volume 40, 2024, 102408 https://doi.org/10.1016/j.apmt.2024.102408

- "Towards the Understanding of Parameters Allowing to Anticipate the Precipitation Reaction of Metallic Precursors in Humid Air Gliding Arc Plasma Reactor", Fanny Hanon, Michel Devillers, Eric M. Gaigneaux, Plasma Chemistry and Plasma Processing, 2024 https://doi.org/10.1007/s11090-024-10516-1

- "Mn and Co decorated biomorphic ceria fiber catalysts for soot and benzene total oxidation", M. Rodriguez, F. Hanon, F. Devred, E.M. Gaigneaux, E.E. Miró, V.G. Milt, Chemosphere, Volume 359, 2024, 142247 https://doi.org/10.1016/j.chemosphere.2024.142247

- "Plasma-assisted deposition of Mn and Fe phases on CeO2 biomorphic fibers for soot combustion and CO oxidation", M. Rodriguez, S.A. Leonardi, F. Hanon, E.E. Miró, V.G. Milt, E.M. Gaigneaux, Catalysis Today, Volume 431, 2024, 114457 https://doi.org/10.1016/j.cattod.2023.114457

Conference communications

1. Oral communications

- "Synthesis of metal oxides oxidation catalysts by glidarc plasma", F. Hanon, E.M. Gaigneaux, oral presentation at World Congress on Oxidation Catalysis, Cardiff (Wales), 4-8 September 2022

- "Synthesis of heterogeneous oxides catalysts by humid air glidarc plasma: effect of the post-discharge", F. Hanon, E.M. Gaigneaux, oral presentation at ChemCYS, Blankenberge (Belgium), 12-14 October 2022

- "The glidarc plasma: an innovative method for the synthesis of heterogeneous catalysts", F. Hanon, E.M. Gaigneaux, oral presentation at International Symposium on Plasma Chemistry 25, Kyoto (Japan), 22-26 May 2023

- "Synthèse de catalyseurs hétérogènes par plasma glidarc", F. Hanon, E.M. Gaigneaux, oral presentation at GECat, Dunkerque (France), 6-9 June 2023

- "Synthesis of heterogeneous catalysts by humid air glidarc plasma", F. Hanon, E.M. Gaigneaux, oral presentation at Prepa13, Louvain-la-Neuve (Belgium), 10-13 July 2023

- "Humid air glidarc plasma: an innovative method for heterogeneous catalysts synthesis", F. Hanon, E.M. Gaigneaux, oral presentation at PhD Student's Day 2024, Louvain-la-Neuve (Belgium), 24 May 2024

- "Humid air glidarc plasma: an innovative method for heterogeneous catalysts synthesis", F. Hanon, E.M. Gaigneaux, oral presentation at International Congress on Catalysis, Lyon (France), 14-19 July 2024

2. Poster communications

- "Synthesis of heterogeneous catalysts by humid air glidarc plasma", F. Hanon, E.M. Gaigneaux, poster at SRC Day, Bruxelles (Belgium), 14 October 2021

- "Synthesis of heterogeneous oxides catalysts by humid air glidarc plasma: effect of the post-discharge", F. Hanon, E.M. Gaigneaux, poster at PhD Student's Day 2022, Louvain-la-Neuve (Belgium), 25 May 2022

- "Effect of the post-discharge (PD) on the synthesis of metal oxide catalysts by humid air glidarc plasma", F. Hanon, E.M. Gaigneaux, poster at Prepa13, Louvain-la-Neuve (Belgium), 10-13 July 2023

- "What are the species involved in the gliding arc plasma synthesis of heterogeneous catalysts", F. Hanon, E.M. Gaigneaux, poster at International Congress on Catalysis, Lyon (France), 14-19 July 2024

- "Synthesis of gold supported catalysts by humid air glidarc plasma", F. Hanon, E.M. Gaigneaux, poster at International Congress on Catalysis, Lyon (France), 14-19 July 2024

Awards

IACS Award 2024 (Young researcher Support for Attending ICC) at International Congress on Catalysis, in Lyon (France), 14-19 July, 2024.

The writing of this thesis was assisted by the AI language model ChatGPT, developed by OpenAI. The use was strictly limited to spelling and grammar checks. All content has been thoroughly reviewed and verified by the author.